Report No. FAA-RD-72-81

AD 749845

# ACOUSTIC ANALYSIS OF AIRCRAFT VORTEX CHARACTERISTICS


Martin Balser

Arthur E. Nagy

C. McNary

XONICS, INC.

6837 Hayvenhurst Ave.

Van Nuys, Calif. 91406


JULY 1972

FINAL REPORT

TASK II

Availability is unlimited. Document may be released to the National Technical Information Service, Springfield, Virginia 22151, for sale to the public.

Prepared for

DEPARTMENT OF TRANSPORTATION

FEDERAL AVIATION ADMINISTRATION

Systems Research & Development Service

Washington, D.C. 20591


Reproduced by

NATIONAL TECHNICAL INFORMATION SERVICE

U S Department of Commerce

Springfield VA 22151

The contents of this report reflect the views of the contractor who is responsible for the facts and the accuracy of the data presented herein. The contents do not necessarily reflect the official views or policy of the Department of Transportation. This report does not constitute a standard, specification or regulation.

ACCESSION for
NTIS White Section
DDC Buff Section
UNANNOUNCED
JUSTIFICATION
BY
DISTRIBUTION/AVAILABILITY CODES
Dist. AVAIL. and/or SPECIAL
A

TECHNICAL REPORT STANDARD TITLE

| | | |
|---|---|---|
| 1. Report No. FAA-RD-72-81 | 2. Government Accession No. | 3. Recipient's Catalog No. |
| 4. Title and Subtitle Acoustic Analysis of Aircraft Vortex Characteristics | | 5. Report Date July 1972 |
| | | 6. Performing Organization Code |
| 7. Author(s) M. Balser, C. McNary, A. Nagy | | 8. Performing Organization Report No |
| 9. Performing Organization Name and Address Xonics, Incorporated 6837 Hayvenhurst Avenue Van Nuys, Calif. 91406 | | 10. Work Unit No. 214-531-00 |
| | | 11. Contract or Grant No. DOT-FA72-WA-2843 |
| 12. Sponsoring Agency Name and Address Department of Transportation Federal Aviation Administration 800 Independence Ave SW Washington, D.C. 20592 | | 13. Type of Report and Period Covered Task II Final Report |
| | | 14. Sponsoring Agency Code |

15. Supplementary Notes

None

16. Abstract

A program of field measurements at NAFEC and related analysis has been carried out as part of the development of acoustic radar for aircraft vortex turbulence detection. Spectra of acoustic signals scattered from the vortices were found to agree in form with those derived from a model, and yielded velocities that generally agreed with those observed by the NAFEC tower instrumentation. Consistent quantitative measurements of circulation, the quantity most closely related to hazard, were obtained for a number of different aircraft. Confident vortex tracks were obtained for aircraft (a DC-6) altitudes up to 1500 ft, with the vortex detected at about 1300 ft and tracked for about a minute until it passed out of the coverage region. A preliminary system analysis shows the sensor characteristics and configuration that could provide coverage for a single runway approach.

| | |
|---|---|
| 17. Key Words Wake Vortices Bistatic acoustic radar Acoustic Scattering Normalized Velocity | 18. Distribution Statement Availability is unlimited. Document may be released to National Technical Information Service. Springfield, Va. 22151, for sale to public. |

| 19. Security Classif. (of this report) | 20. Security Classif. (of this page) | 21. No. of Pages | 22. Price |
|---|---|---|---|
| UNCLASSIFIED | UNCLASSIFIED | 197 | |

Form DOT F 1700.7 (8-69)

ACKNOWLEDGMENT

Those named as authors of this report, of necessity a small number, should be understood to represent all of the people whose work made the report possible. The overall program was conducted under the general supervision of Martin Balser. The field tests were conducted by a team under Arthur Nagy, who was ably assisted by Frank Ambler, Jack Swoboda and David Eby. The processing and analysis efforts were led by Charles McNary, and substantial contributions were made by Zanoni Schwarzbein, Teodoro Azzarelli, Kenner Knight, Thomas Hanrahan and Dennis Anderson. Thanks are due to many other members of the company, too numerous to mention individually, who helped achieve success in the program.

We are all, in turn, grateful to those outside the company whose co-operation made the task not only possible but pleasant. These include Cliff Hay of the FAA, Leo Carodz of NAFEC, Mark Gorstein of TSC, and all of their associates whose efforts expedited the work and helped make it stimulating.

Preceding page blank

TABLE OF CONTENTS


| Section | | Page |
|---|---|---|
| 1 | INTRODUCTION | 1-1 |
| 2 | VORTEX MODELS | 2-1 |
| 3 | STUDY OF XONICS DATA FROM PREVIOUS TESTS | 3-1 |
| 4 | RECENT TOWER COMPARISON TESTS | 4-1 |
| 5 | EXTENDED TRACKING TESTS | 5-1 |
| 6 | PRELIMINARY SYSTEM ANALYSIS | 6-1 |
| 7 | CONCLUSIONS | 7-1 |
| 8 | REFERENCE | 8-1 |


Preceding page blank

## 1. INTRODUCTION

The work described in this report was carried out as part of a continuing acoustic radar program whose goal is the development of an operational Airport Turbulence Alert System. The technique of observing acoustic signals scattered from aircraft wake turbulence and subsequently analyzing their doppler velocity spectra to detect, track and assess the potential hazard of the turbulent vortices has been worked out by Xonics personnel during the past three years. The internally funded initial sensor development culminated in a series of tests during the spring of 1971 in which vortices were observed regularly on commercial traffic at Ontario and Los Angeles International Airports[1]. In the fall of 1971, tests were conducted at NAFEC under FAA sponsorship. Spectra of the received signals were analyzed for the velocity content of the observed vortices, which were generated by a DC-7 under controlled conditions (low-altitude flybys of an instrumented tower). In other tests conducted during that series, vortices generated at altitudes up to 800 feet were tracked by the acoustic radar[2].

The program covering the work reported in this document was carried out under FAA Contract No. DOT-FA72WA-2843. Four tasks were specified in the Statement of Work. The first consisted of a more thorough examination of the data gathered in the earlier NAFEC tests[2], with two principal objectives. One is to relate the observed spectral data through a scattering model to the flow distribution in the observed vortex; the other is to formulate potential "discriminants", i.e., parameters deduced from the observed data that are used to assess the circulation, and hence the hazard of the vortex. These discriminants, a key element in an operational system, are then to be tested in the field tests that are included in the second task of this program. The work of this first task is presented in Sections 2 and 3 of the report.

The second task covered a new series of flight tests involving a further comparison of Xonics data with those obtained by the NAFEC

tower. Two features of these tests distinguish them from the previous series[2]. A significant difference was the planned use of various size aircraft — DC-7, C-141, and C-5A — as the vortex generators to provide data for testing proposed discriminants (and probably suggest new ones). (Unfortunately, the full range of expected data were not to be realized, due to curtailment of the C-5A availability.) The second feature is the closer spacing (1 ft) between the tower sensors that allows a more complete and valid comparison between the two data sources than could be made in the earlier tests. The acoustic data from these new tests are analyzed by comparison with the corresponding tower data, and also with respect to the evaluation of the proposed discriminants. This work is reported in Section 4.

The third task called for tracking of vortices at altitudes up to perhaps 1700 ft, approximately the maximum altitude of an aircraft on approach at the outer marker. Improvements in the acoustic equipment made since last fall were expected to produce an increased range over the 800 ft altitude capability demonstrated at that time. (Again, the lack of a large aircraft for these tests restricted their utility in evaluating performance.) The results are given in Section 5.

Section 6 describes the results of a brief system analysis called out as the fourth task. In essence, the analysis describes the basic configuration and coverage of an acoustic vortex sensor network for one runway approach, and gives approximate sensor parameters that meet the stipulated requirements.

Finally, Section 7 gives the major conclusions of this phase of the program.

## 2. VORTEX MODELS

One of the major objectives of this study is an understanding of the connection between the flow that constitutes a vortex and the spectrum of the acoustic signal scattered by that vortex. This understanding, based on a combination of analytic and heuristic reasoning and augmented by the experimental observations themselves, can then serve to suggest those spectral parameters, which we shall call discriminants, that most simply and reliably measure the hazard-related characteristics of the vortex, such as its circulation. This section is an examination of the vortex models that appear to be most appropriate for use in the study.

### 2.1 Current Physical Understanding

#### 2.1.1 General Vortex Description

To support its weight an aircraft accelerates air downwards. The velocity shear between the outside air (beyond the wing tips) and that with a downward velocity component results in a pair of vortices that is left trailing along the flight path. One may rather consider the pressure system around a finite lifting wing. The pressure below the wing exceeds that on the upper surface. Near the wing tip the air tends to flow from the bottom around the tip to equalize the pressure. The resulting circulation contributes to the vortex. A more detailed discussion of this, with graphical aids, can be found in Goldstein[3].

Several qualitative features of the vortex history might be noted. After a very short transition region, a vortex core is formed somewhat inboard of the wing tip. It has a diameter of the order of 1m or more for large aircraft. A rotating flow in approximately solid-body motion and, in the absence of engine exhaust entrainment, an associated low pressure and temperature region exist within this core. There is also a large axial velocity component. The flow is in some sense turbulent, although radial velocity perturbations are likely to be strongly suppressed by the rapid rotation (since turbulence tends to be dampened

by stretching of vortex lines). Outside of the core, the rotational velocity decreases with increasing radius. In the classical model, the region outside the core is in potential flow so that all the circulation is contained in the core; in fact, the circulation may increase slowly with increasing radius, depending on the specific actual radial dependence of velocity.

In addition to the air in the immediate vicinity of the wing tip, the turbulent boundary-layer flow over the wing and the hot turbulent exhaust from the jet engines are eventually ingested into the vortices. This also is true of any secondary vortices (as from the flaps or horizontal tail surfaces). Boundary layers from the body surfaces are also within the induced velocity field of the tip vortices, and roll up to add to the complexity of vortex flow.

It is clear from an extensive review of the available literature that although these general ideas are understood, a detailed comprehension has not been reached. Mean velocity fields have been measured for only a handful of cases (often with probes which may interfere with the flow), but the temperature and turbulent fields have not been measured at all. As a result, we have virtually no way of constructing quantitatively realistic scattering models at the present time.

### 2.1.2 Radial Velocity Profile

The circulation in the vortex is related to the lift on the wing. From "infinite-lifting-line" theory, the lift per unit length is

$$\frac{dL}{dy} = \rho U \Gamma \tag{2-1}$$

where $\rho$ is the air density, U the free-stream velocity and $\Gamma$ the circulation, given by the integral around a closed path

$$\Gamma = \oint \vec{v} \cdot d\vec{s} \tag{2-2}$$

A finite wing of elliptical loading has a circulation of $\Gamma_o$. For the lift equal to the aircraft weight, from equation (2-1) (see reference 2)

$$\Gamma_o = \frac{4W}{\pi\rho U b} \tag{2-3}$$

where b is the wingspan and W the weight.

The vortices are shed from the aircraft wing tips, then roll up to a smaller spacing $b'<b$. There seems to be little data on the value of $b'$. Donaldson[4] implies that $b' = \pi b/4$. Photos by Garodz[5] show the vortex cores closing to $b' \approx b/2$, then spreading again as air is entrained[6].

### 2.1.2 Radial Profile of Tangential Velocity

For an ideal inviscid vortex, the circulation outside the infinitesimal vortex filament measured in a centered coordinate system is independent of r, i.e., $\Gamma(r) \equiv \Gamma_o$. For the case of cylindrical symmetry, the tangential velocity is given by

$$v(r) = \Gamma_o/2\pi r \tag{2-4}$$

The singular behavior at $r = 0$ is not expected in the real fluid. If at $t = 0$ in a fluid of kinematic viscosity $\nu$ we have $v(r)$ given by equation (2-4), at a later time t we find[7]

$$v(r) = \frac{\Gamma_o}{2\pi r}\left(1 - e^{-r^2/4\nu t}\right) \tag{2-5}$$

This allows us to define a core radius $r_c = 2\sqrt{\nu t}$. For a core that is not laminar one must consider $\nu$ to be an effective kinematic viscosity (or eddy viscosity).

Donaldson[4] has shown that a theory due to Betz[8] agrees more closely with data taken by Garodz[5] than does equation (2-5). Betz matches three moments of the vorticity distribution in the wake to that in the wing;

hence, his theory also has a better physical foundation than that resulting in equation (2-5), which is applied to a laminar, isolated vortex. The Betz theory results in a velocity distribution

$$v(r) = \frac{\Gamma_o}{2\pi r} \left[6 \frac{r}{b} - 9 \left(\frac{r}{b}\right)^2 \right]^{1/2} \qquad 0 < \frac{r}{b} < \frac{1}{3}$$

$$= \Gamma_o/2\pi r \qquad \frac{r}{b} > \frac{1}{3} \qquad (2\text{-}6)$$

where $\Gamma_o$ is the circulation for large r.

McCormick et al[9] have measured trailing vortices by flight testing and by wind tunnel tests. They claim the model tests to be "of limited value" due to the Reynolds-number dependence (the full-scale tests were on a small single-engine aircraft). In those tests, they found the circulation outside the core increased with r in a logarithmic fashion, given by

$$\Gamma(r) = \Gamma(r_c) \left[1 + \ln (r/r_c)\right] \qquad (2\text{-}7)$$

Hoffmann and Joubert[10] had earlier found in their wind tunnel tests that the measured circulation of turbulent line vortices correlated with the form of equation (2-7). From this one finds

$$v(r) = \frac{\Gamma(r)}{2\pi r}$$

$$= \frac{\Gamma(r_c)}{2\pi r} \left[1 + \ln (r/r_c)\right] \qquad (2\text{-}8)$$

To find $\Gamma(r_c)$, McCormick[9] notes that for much of the data $\Gamma(r_c) = 0.16\ \Gamma_o$. He also notes that the maximum circumferential velocity at the wing tip $v_o = \frac{5}{8} C_L U$, where $C_L$ is the aircraft lift coefficient and U is its velocity. McCormick has also considered the growth of the vortex with distance behind the aircraft. Letting $v_m$ denote the peak velocity in

the vortex, McCormick notes from his data that

$$\frac{v_o}{v_m} = 1 + 0.0065 \frac{x}{\bar{c}} \tag{2-9}$$

where $\bar{c}$, the mean chord, is the quotient of wing area S divided by wing-span b, and x is the distance behind the aircraft.

Figure 2-1 shows a comparison between the data of Garodz and the theory of Betz, reproducing the results of Donaldson. The values were obtained from an assumed weight for the observed aircraft, a Convair 880, of 140,000 pounds, a velocity of 220 knots, and a sea level density of 0.002378 slugs/cu ft. We have added the result of equation (2-5) for $r_c$ = 1 ft. Note that the 1/r dependence is too strong, if one is to judge from this comparison. The McCormick method of calculating the vortex structure is used to calculate the "log profile 80 seconds after passage" curve. This can be compared to the "log profile at wing tip" case which fits the data somewhat better, even though it should not.

### 2.1.3 Axial Flow

A number of observations of the axial flow in the core have been made, including the notable experiments of Logan[11] and of Olson[12]. Logan observes the core velocity to be as high as 70 percent of the free-stream velocity, but his measurements are only 10 and 26 chord-lengths behind the wing.

Olsen's measurements are more appropriate in this respect, as his experiment, a towed wing in a water tank, allows observation of the core motion at over a hundred chord lengths behind the wing. He shows a strong dependence on Reynolds number and a linear dependence on the angle of attack. If one is so rash as to try to extrapolate to full-scale conditions, one finds the core velocity 1/2 mile behind a 747 may be as high as 55 knots. It is very important to note however, that towed models induce a net forward axial momentum in the medium; while

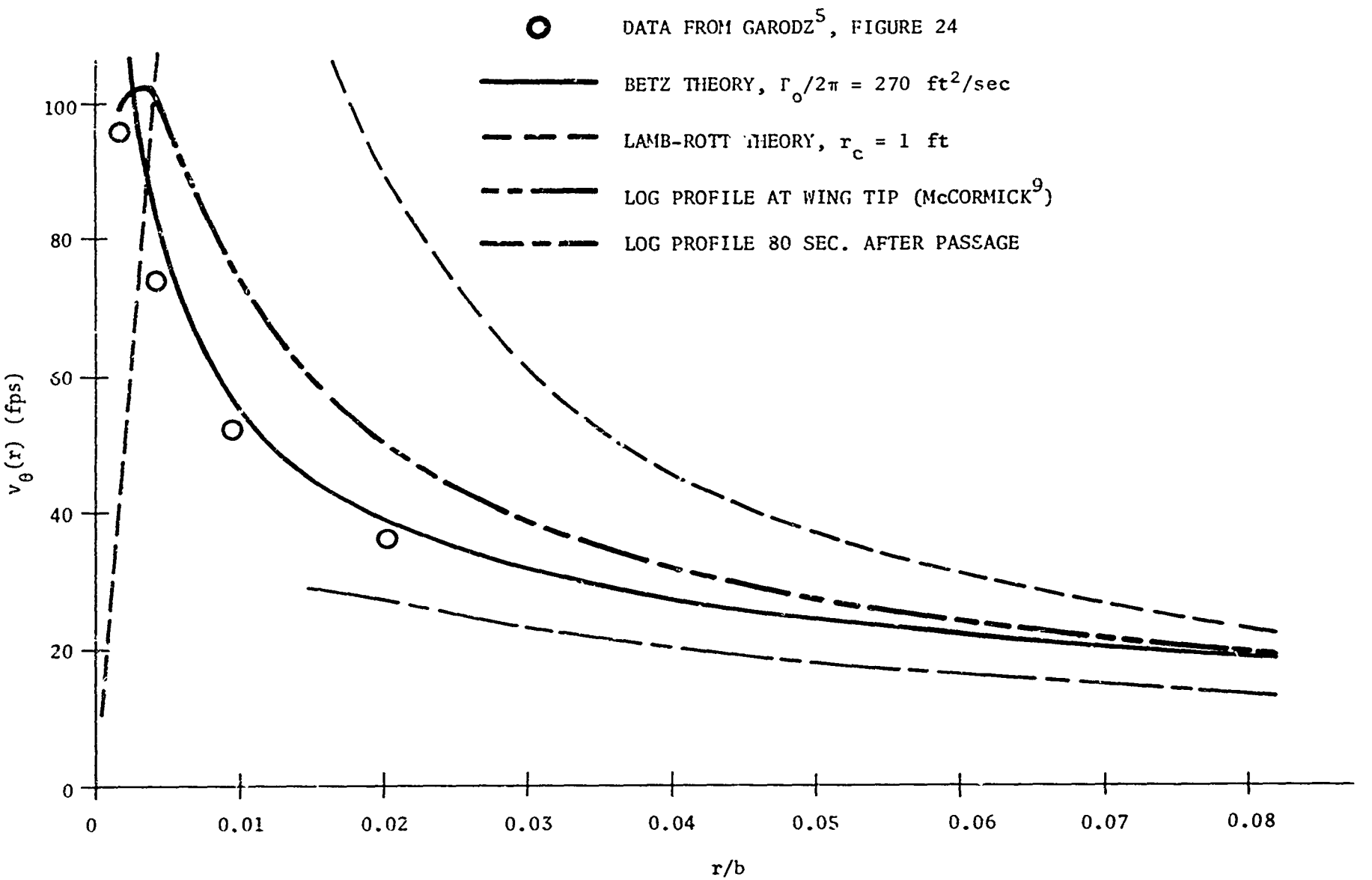


Figure 2-1. Vortex Theories Compared to Observed Data

self-propelled bodies, such as aircraft, do not. Here again, the available information may be only indicative of the conditions encountered in aircraft flight, and detailed full-scale measurements alone will provide the required data.

## 2.2 Simplified Scattering Model

### 2.2.1 General Expression for the Frequency Spectrum of the Scattered Signal

When a single-frequency acoustic signal, transmitted in a direction defined by the unit vector $\vec{n}_1$, is scattered by a vortex, the signal received in some other direction $\vec{n}_2$ consists of a superposition of waves having a continuous spectrum of frequencies. The frequency spectrum of the scattered wave can be most easily related to the flow pattern and geometry of the vortex if one accepts the (reasonable) assumption that the scattering is caused by small-scale inhomogeneities of the order of a wavelength that are simply carried along by the larger-scale flow and therefore act as a "stain" to make that flow observable. Small-scale, turbulent, fluctuating velocities and the temperature-density fluctuations are, in fact, the principal mechanisms which contribute to the scattering of the acoustic wave[13]. If we adopt this view, then each infinitesimal element of volume of the illuminated portion of the vortex can be treated as an independent scatterer moving with a velocity $\vec{v}(\vec{r},t)$. Again, the velocity $\vec{v}(\vec{r},t)$ denotes the systematic local mean flow velocity of the vortex, and not the instantaneous velocity which is known to contain turbulent fluctuations about the mean.

The received scattered signal from an elementary cell located at $\vec{r}$ will have a Doppler shift in its frequency given by

$$\Delta\omega = (\vec{k}_1 - \vec{k}_2) \cdot \vec{v}(\vec{r},t) \equiv \vec{k} \cdot \vec{v}(\vec{r},t) \qquad (2\text{-}10)$$

where $\vec{k}_1$ and $\vec{k}_2$ are, respectively, the wave vectors of the transmitted and the received signals, i.e.,

$$\vec{k}_i = \frac{2\pi\vec{n}_i}{\lambda_o} = \frac{\omega_o}{c_o}\,\vec{n}_i \qquad i = 1,2 \qquad (2\text{-}11)$$

and where $\lambda_o$ and $\omega_o$ are the wavelength and the (circular) frequency of the incident wave, and $c_o$ denotes the velocity of sound.

If we decompose the total received signal into its frequency (Fourier) components, the portion of the spectrum between two adjacent frequencies (see Figure 2-2) $\omega$ and $\omega + \Delta\omega$ is the contribution due to that portion of the vortex which lies in the illuminated volume and which has coordinates $\vec{r}$ such that the relation

$$\omega < \vec{k} \cdot \vec{v}(\vec{r},t) < \omega + \Delta\omega \qquad (2\text{-}12)$$

is satisfied.

If we now examine a frequency spectrum such as the one depicted in Figure 2-2, it is clear that the area under the spectrum curve from $\omega = -\infty$ to an arbitrary value $\omega$, is proportional to the integral

$$I(\omega,t) = \int_{V_o} d\vec{r}\; W(\vec{r})\; \Theta(\omega - \vec{v}(\vec{r},t) \cdot \vec{k}) \qquad (2\text{-}13)$$

where $V_o$ denotes the total illuminated volume, $\Theta(x)$ is the unit step function, and $W(\vec{r})$ is a weighting function of position which takes into account the fact that different locations in the vortex may scatter with different intensities. The spectrum $S(\omega)$ is given by definition as

$$S(\omega,t) \equiv \frac{dI(\omega,t)}{d\omega} = \int_{V_o} d\vec{r}\; W(\vec{r})\; \delta(\omega - \vec{v}(\vec{r},t) \cdot \vec{k}) \qquad (2\text{-}14)$$

where $\delta(x)$ is the Dirac delta function.

In equation (2-14), the illuminated portion of the vortex, or effective scattering volume, is treated as a sharply defined volume

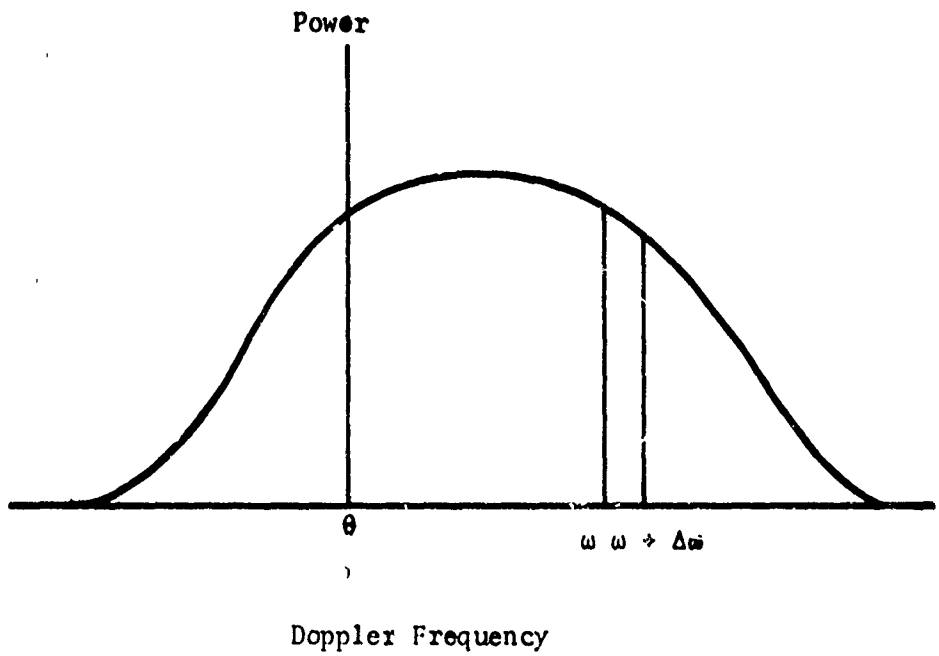


Figure 2-2. Idealized Spectrum of the Scattered Signal

$V_0$, whereas in actual fact the gain or shape of the beam lobes weight the returns from different parts of their common volume differently. This condition may be accounted for by multiplying the integral in equation (2-14) by an effective lobe-gain weighting function $G(\vec{r})$. Thus the spectrum can be more generally represented by

$$S(\omega,t) = N \int d\vec{r}\, G(\vec{r})\, W(\vec{r})\, \delta(\omega - \vec{k} \cdot \vec{v}(\vec{r},t)) \tag{2-15}$$

where in addition to the weighting function $G(\vec{r})$, which accounts for the intensity pattern of both the incident and the receiving intersecting beams, we have also introduced a convenient normalization factor N given by

$$\frac{1}{N} = \int d\vec{r}\, G(\vec{r})\, W(\vec{r}) \tag{2-16}$$

This choice of N normalizes the total power spectrum to unity, i.e.,

$$\int_{-\infty}^{\infty} S(\omega)\, d\omega = 1 \tag{2-17}$$

The normalization required to compare a measured spectrum with one derived from the model is to divide the measured spectrum by the total cross-section.

The general expression for the spectrum $S(\omega)$ stated in equation (2-15) is based on two tacit simplifying assumptions that deserve further comment. First, by treating each element of the vortex as an independent scatterer, we have neglected second- and higher-order scattering processes. This is a reasonable assumption that is not likely to affect greatly the results of the model. Another approximation has to do with the quasi-stationarity of the mean flow velocity. The time dependence of equation (2-15) is treated parametrically, that is, the spectrum of the observed signal is assumed to be essentially constant over the time interval required to estimate the spectrum, and to change slowly with respect to that interval. If that is not the

case, the spectrum for a given estimation interval may be synthesized by superposing the spectra for a number of shorter subintervals that do satisfy the quasi-stationarity condition. (In this connection, see Section 2.3.2.4). Further, we neglect refraction effects by the vortex flow itself on the incident wave. (For the observed velocities, this should not cause large errors; this point is discussed in Section 2.3.2.8).

### 2.2.2 Vortex Geometry

The geometric configuration employed in the model calculations is shown in Figure 2-3. The z-axis has been chosen in the direction $\vec{n}_1 - \vec{n}_2$, i.e., it is taken to coincide with the bisector of the incident and the receiving beams. The y-axis is taken to be perpendicular to the plane of propagation, i.e., to both $\vec{n}_1$ and $\vec{n}_2$, and passing through the intersection of the two beam centers. The effective scattering volume is taken to be sharply defined, and chosen to be a segment of a cylinder of length 2h and radius $R_o$. The axis of this cylinder is coincident with the y-axis, and its center is at the origin 0 of the adopted coordinate system. Finally, the vortex axis is assumed normal to the plane of propagation, centered at some point $(x_o, z_o)$.

It can be easily shown that the velocity field v(x,t) of the vortex is given, in the coordinate system centered at 0, by

$$v_x = \frac{(z-z_o)}{\rho} \; v(\rho) + \dot{x}_o \tag{2-18}$$

$$v_y = 0$$

$$v_z = -\frac{(x-x_o)}{\rho} \; v(\rho) + \dot{z}_o$$

where $\rho = \sqrt{(x-x_o)^2 + (z-z_o)^2}$ is the radial distance from the vortex center, $\dot{x}_o$, $\dot{z}_o$ denote the components, in the plane (x,z), of the

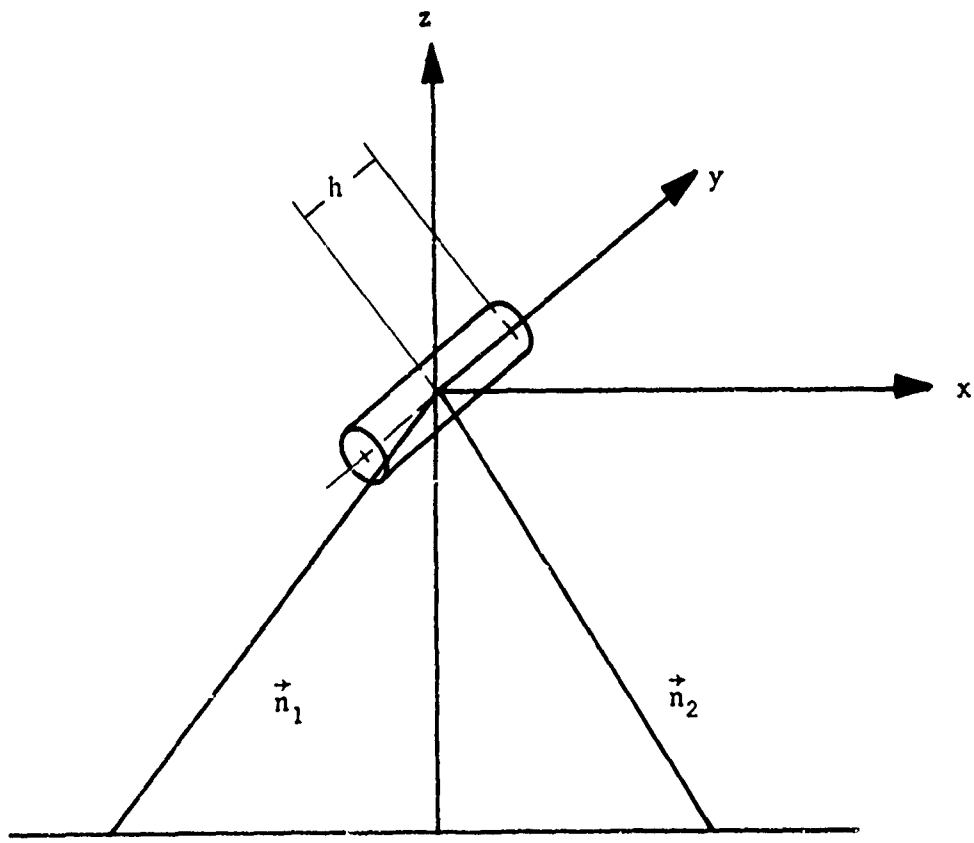


Figure 2-3. Scattering Geometry

translational velocity of the vortex, and $v(\rho)$ denotes its tangential velocity profile, assumed cylindrically symmetric, i.e., a function of $\rho$ alone. It is also reasonable to assume that the weighting function $W(\vec{r})$, which accounts for the varying scattering intensity in different parts of the vortex, is a function of the radius $\rho$ only.

From equation (2-14) we can now write the Doppler spectrum as follows:

$$S(\omega) = 2Nh \int_{A_o} dx\, dz\, W(\rho)\, \delta(\omega - \frac{2\pi}{\lambda_o} [\dot{z}_o - \frac{x-x_o}{\rho} v(\rho)]) \qquad (2\text{-}19)$$

where $A_o$ denotes the area inside the circle of radius $R_o$. If we introduce polar coordinates,

$$x-x_o = \rho \cos\theta \qquad\qquad z-z_o = \rho \sin\theta \qquad (2\text{-}20)$$

$S(\omega)$ can be written as

$$S(\omega) = 2Nh \int_{A_o} d\theta\, d\rho\, \rho\, W(\rho)\, \delta(\omega' + 2\pi \frac{\cos\theta}{\lambda_o} v(\rho)) \qquad (2\text{-}21)$$

where $\omega' = \omega + 2\pi \frac{\dot{z}_o}{\lambda_o}$.

Using the unit step function $\Theta(x)$, to account for the boundaries of the area $A_o$, we get

$$S(\omega) = 2Nh \int_0^\infty d\rho\, \rho\, W(\rho) \int_0^{2\pi} d\theta\, \delta(\omega' + \frac{2\pi \cos\theta}{\lambda_o} V(\rho))$$

$$\Theta(R_o^2 - (x_o + \rho \cos\theta)^2 - (z_o + \rho \sin\theta)^2) \qquad (2\text{-}22)$$

By making appropriate changes of variables and integrating out the delta function, it can be shown that equation (2-22) can be written as

$$S(\omega) = S_1(\omega';\ x_o,z_o) + S_1(-\omega';-x_o,z_o) + S_1(\omega';x_o,-z_o)$$

$$+ S_1(-\omega';-x_o,-z_o) \tag{2-23}$$

where $S_1(\omega';x_o,z_o)$ is given by

$$S_1(\omega';x_o,z_o) = \frac{\lambda_o hN\Theta(\omega')}{\pi} \int_o \frac{d\rho\ \rho\ W(\rho)}{\sqrt{v^2(\rho) - q^2}} \Theta(v(\rho)-q)$$

$$\Theta[R_o^2 - (x_o^2+z_o^2) - \rho^2 + \frac{2\rho}{v(\rho)} \{x_o q + z_o\sqrt{v^2(\rho) - q^2}\}] \tag{2-24}$$

with

$$q = \frac{\lambda_o \omega'}{2\pi} \tag{2-25}$$

For the special case $x_o = z_o = 0$ (centered vortex) we get

$$S(\omega) = 2[S_1(\omega';0,0) + S_1(-\omega';0,0]$$

$$= \frac{2\lambda_o hN}{\pi} \{\Theta(\omega') \int_o^{R_o} \frac{W(\rho)\ \rho\ d\rho}{\sqrt{v^2(\rho) - q^2}} \theta(v(\rho)-q)$$

$$+ \Theta(-\omega') \int_o^{R_o} \frac{W(\rho)\ \rho\ d\rho}{\sqrt{v^2(\rho) - q^2}} \Theta(v(\rho)-q)\} \tag{2-26}$$

The normalization coefficient N can be obtained by integrating equation (2-24) over $\omega$ and applying the condition of equation (2-17), giving

$$\frac{1}{N} = 2h \int_0^{R_o} d\rho\ \rho \int_0^{2\pi} d\theta\ W(\sqrt{(\rho\ \cos\theta + x_o)^2 + (\rho\ \sin\theta + z_o)^2}) \qquad (2\text{-}27)$$

For the special case $x_o = z_o = 0$, equation (2-27) reduces to

$$\frac{1}{N} = 4\pi h \int_0^{R_o} d\rho\ \rho\ W(\rho) \qquad (2\text{-}28)$$

### 2.2.3 Assumed Vortex Model

We will now calculate the spectrum $S(\omega)$ for a specific choice of the functions $W(\rho)$ and $v(\rho)$. Certain features of the earlier acoustic vortex observations seem to suggest that the scattering strength does not vary greatly with position. (For some further discussion of this point, see Section 2.3.2.2.) Accordingly, we have chosen constant scattering strength, $W(\rho) \equiv 1$. For the radial velocity profile, we have chosen

$$v(\rho) = \frac{\rho}{r_c}\ v_m \qquad \rho < r_c$$

$$= \frac{r_c}{\rho}\ v_m \qquad \rho < r_c \qquad (2\text{-}29)$$

where $r_c$ denotes the radius of the vortex core. The physical significance of this profile is straightforward. For $\rho < r_c$, the velocity increases linearly to its maximum value $v(r_c) = v_m$, i.e., the core is taken to rotate like a solid body; for $\rho > r_c$, the velocity falls off proportional to $1/\rho$, which implies a constant circulation for all radial distances outside the core. These assumptions form the basis

for the simplified vortex and scattering model; the effects of modifying these assumptions are considered in Section 2.3.

The expression for the function $S_1(\omega;x_o,z_o)$ for this model is found to be

$$S_1(\omega;x_o,z_o) = \frac{\lambda_o\Theta(\omega)}{2\pi^2R_o^2}\left\{\int_0^{r_c}\frac{d\rho\,\rho}{\sqrt{v_m^2\frac{\rho^2}{r_c^2}-q^2}}\,\Theta\left(v_m\frac{\rho}{r_c}-q\right)\right.$$

$$\times\,\Theta\left(R_o^2-(x_o^2+z_o^2)-\rho^2+\frac{2r_c}{v_m}\left[x_oq+z_o\,v_m^2\frac{\rho^2}{r_c^2}-q^2\right]\right)$$

$$+\int_{r_c}^{\infty}\frac{d\rho\,\rho}{\sqrt{v_m^2\frac{r_c^2}{\rho^2}-q^2}}\,\Theta\left(v_m\frac{r_c}{\rho}-q\right)$$

$$\times\,\Theta\left(R_o^2-(x_o^2+z_o^2)-\rho^2+\frac{2\rho^2}{r_cv_m}\left[x_oq+z_o\sqrt{v_m^2\frac{r_c^2}{\rho^2}-q^2}\right]\right)$$

(2-30)

Making the change of variable $\rho = r_c\eta$ and introducing the non-variable $k = \frac{q}{v_m} = \frac{\lambda_o\omega}{2\pi v_m}$ and the non-dimensional parameters $\xi_o = \frac{x_o}{R_o}$, $\zeta_o = \frac{z_o}{R_o}$, $\mu = \frac{r_c}{R_o}$ we get

$$S_1(k;\xi_o,\zeta_o) = \left\{\int_0^1\frac{d\eta}{\eta^2-k^2}\,\Theta(\eta-k)\,\Theta\left(1-(\xi_o^2+\zeta_o^2)-\eta^2\mu^2+2\mu\left[\xi_ok+\zeta_o\sqrt{\eta^2-k^2}\right]\right)\right.$$

$$+\int_1^{\infty}\frac{d\eta\,\eta^2}{\sqrt{1-k^2\eta^2}}\,\Theta(1-k\eta)\,\Theta\left\{1-(\xi_o^2+\zeta_o^2)-\eta^2\mu^2\right.$$

$$\left.\left.+2\mu\eta^2\left[\xi_ok+\frac{\zeta_o}{\eta}\sqrt{1-k^2\eta^2}\right]\right\}\right. \qquad (2\text{-}31)$$

In going from equation (2-30) to equation (2-31), we have also renormalized the spectrum by dividing it by the quantity $\frac{\lambda_o}{2\pi v_m}$, so that when the spectrum is plotted as a function of the non-dimensional quantity $k = \frac{\lambda_o \omega}{2\pi v_m}$, the total power is normalized to unity.

The numerical evaluation of the spectrum $S(k;\xi_o,\zeta_o)$ as given by equations (2-23) and (2-31) was performed for numerous values of the three available parameters $\mu$, $\xi_o$ and $\zeta_o$. A number of representative samples from these plots will now be presented.

Figures 2-4 through 2-7 illustrate the development with time of the spectrum for a vortex whose center moves through the center of the observation volume (i.e., $\zeta_o = 0$). The core radius $r_c$ was chosen in this case so that $\mu = r_c/R_o = 0.25$. At a time when the center of the vortex is still well outside the observation volume ($x_o = 1.75\ R_o$), only low-velocity components are observed (Figure 2-4). As the vortex center approaches to a distance $R_o$, higher-velocity components appear (Figure 2-5), as do velocities in the opposite direction after the core has crossed into the observation volume (Figure 2-6). Finally, when the vortex is centered in the observation volume, the spectrum is symmetric (Figure 2-7). This shape is characteristic of the centered spectrum. It can be shown that the local maxima correspond to the velocity at $R_o$, which, by virtue of the large size of the scattering volume at the maximum radius and the relatively low velocity there, appears with peak amplitude in the spectrum. The implication of this feature for discrimination is exploited in Section 3.4.

The time history proceeds symmetrically to this sequence as the vortex continues along its path beyond the centered position.

Figure 2-8 gives the spectrum for $\mu = 0.5$. Since the velocity at $R_o$ is now half the peak velocity, or twice what is was in the preceding case, the maxima for this case are correspondingly further

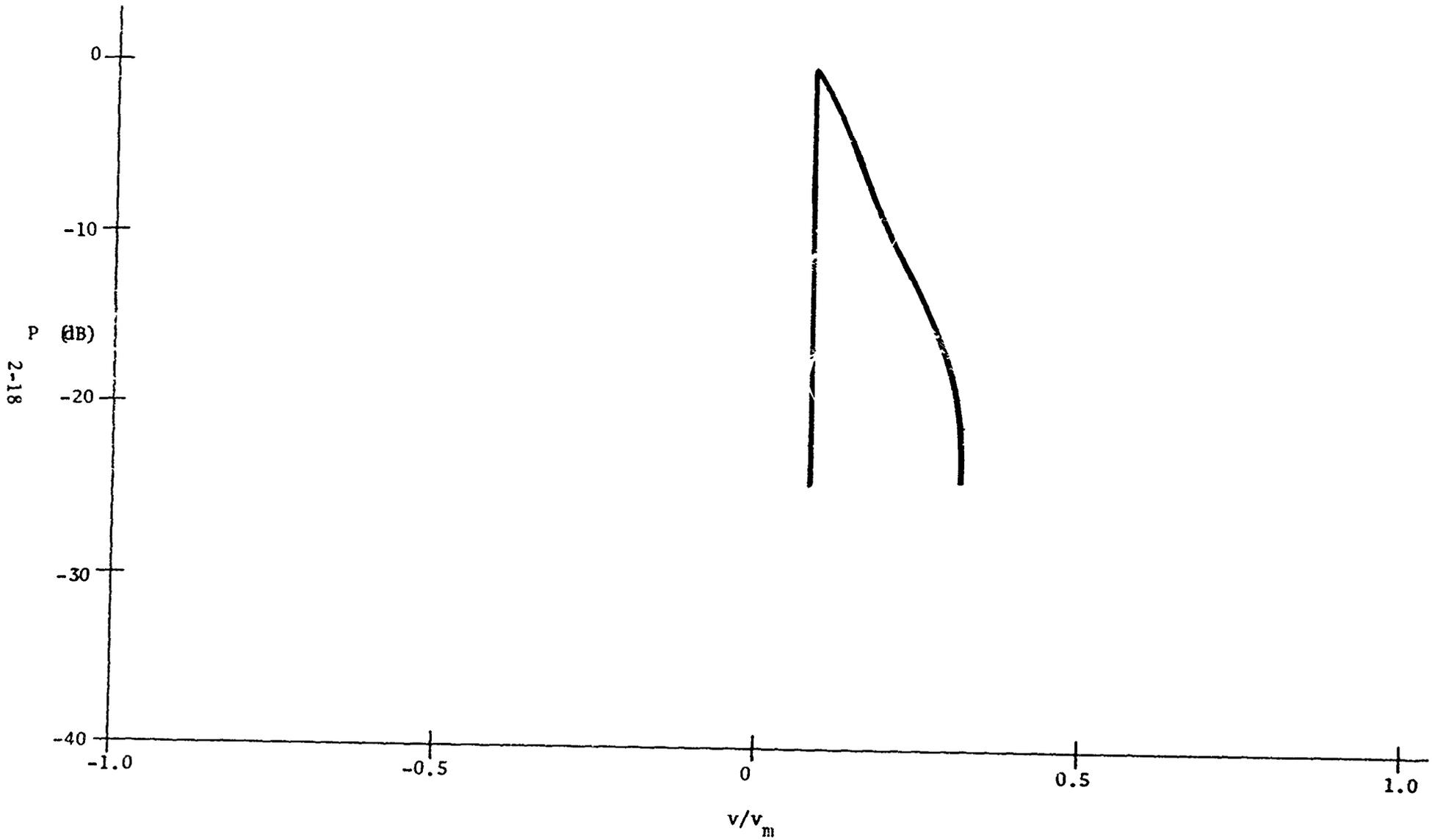


Figure 2-4. Calculated Spectrum, $\mu$=0.25, $\xi_o$=1.75, $\zeta_o$=0

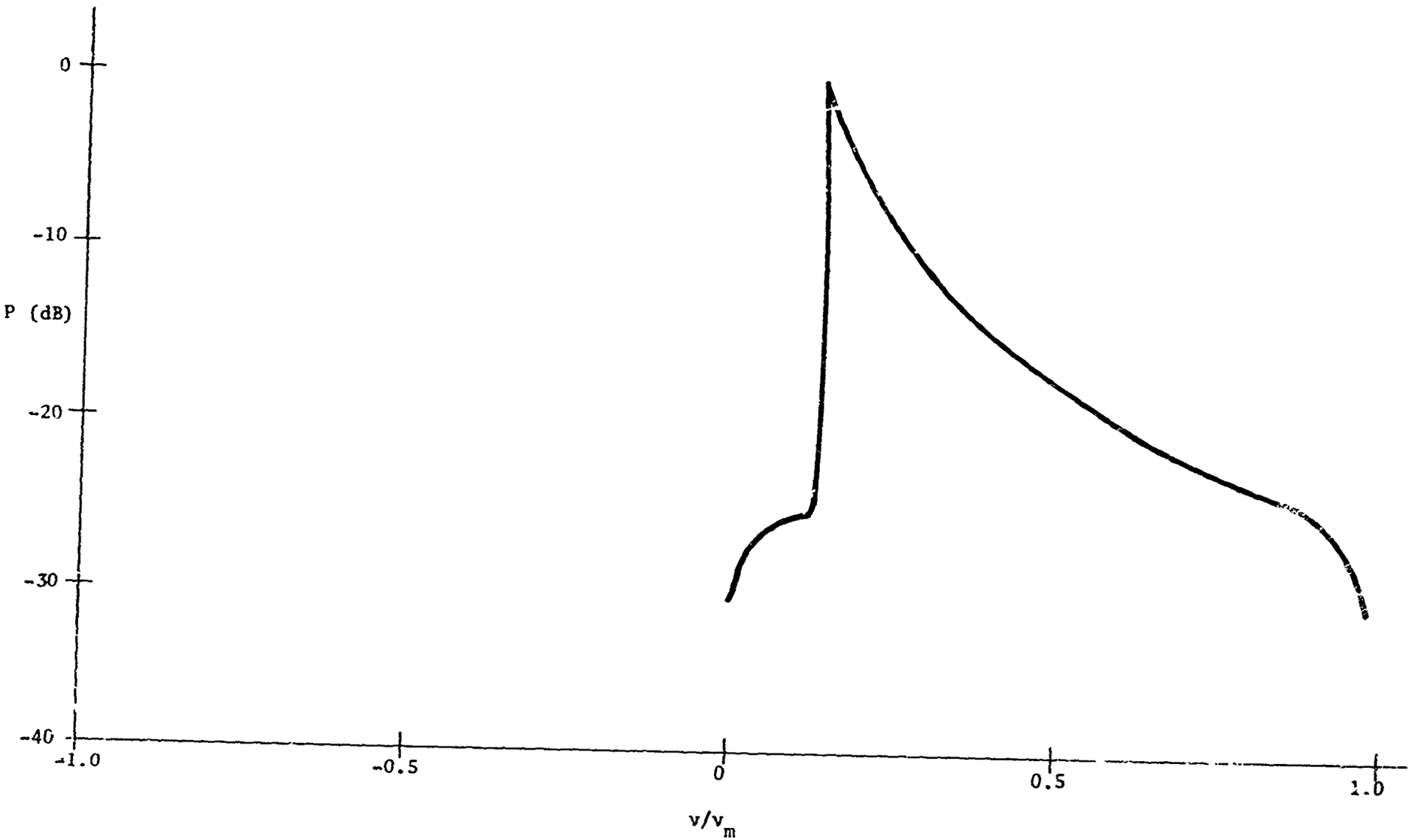


Figure 2-5. Calculated Spectrum, $\mu$=0.25, $\xi_o$=1.0, $\zeta_o$=0

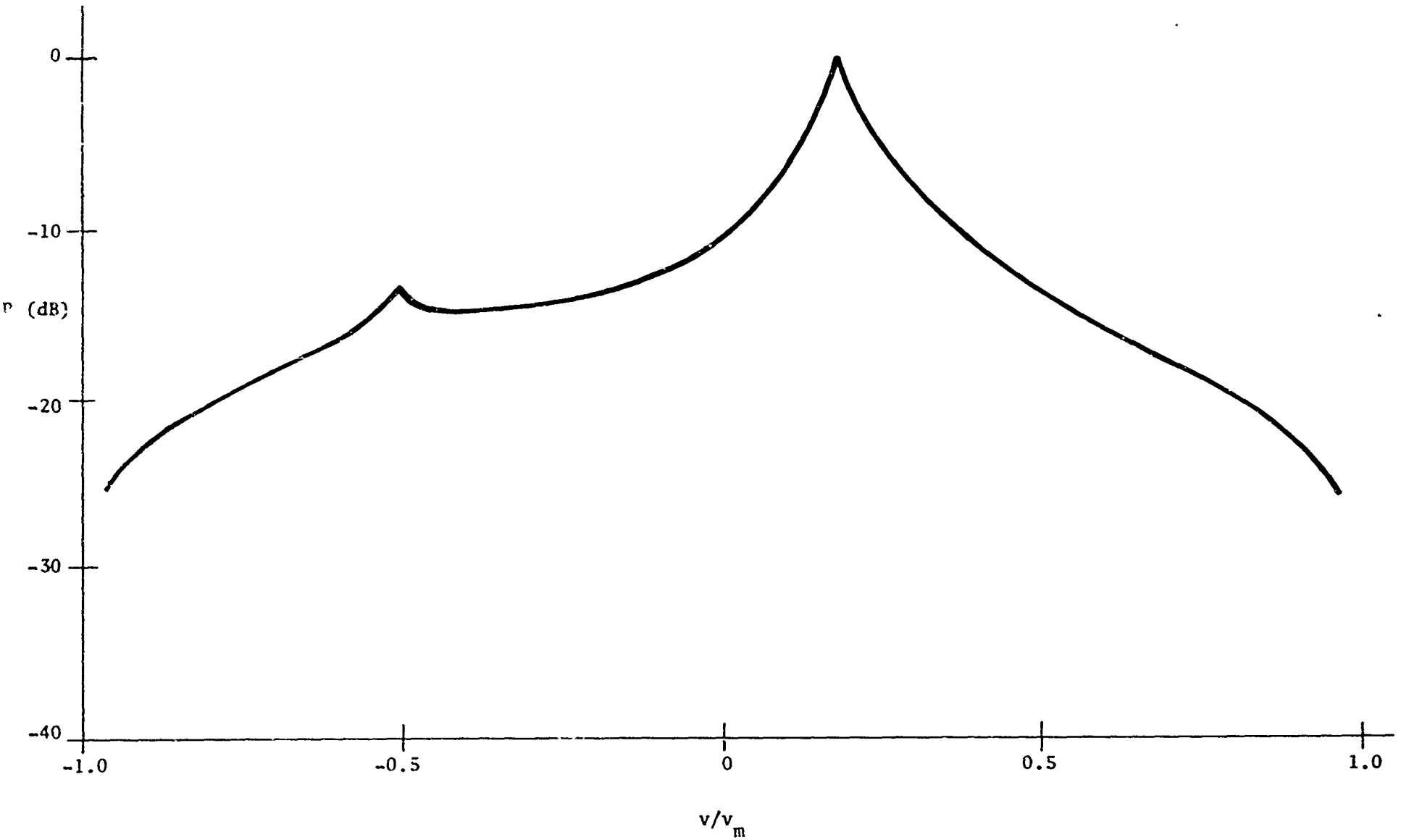


Figure 2-6. Calculated Spectrum, $\mu=0.25, \xi_o=0.5, \zeta_o=0$

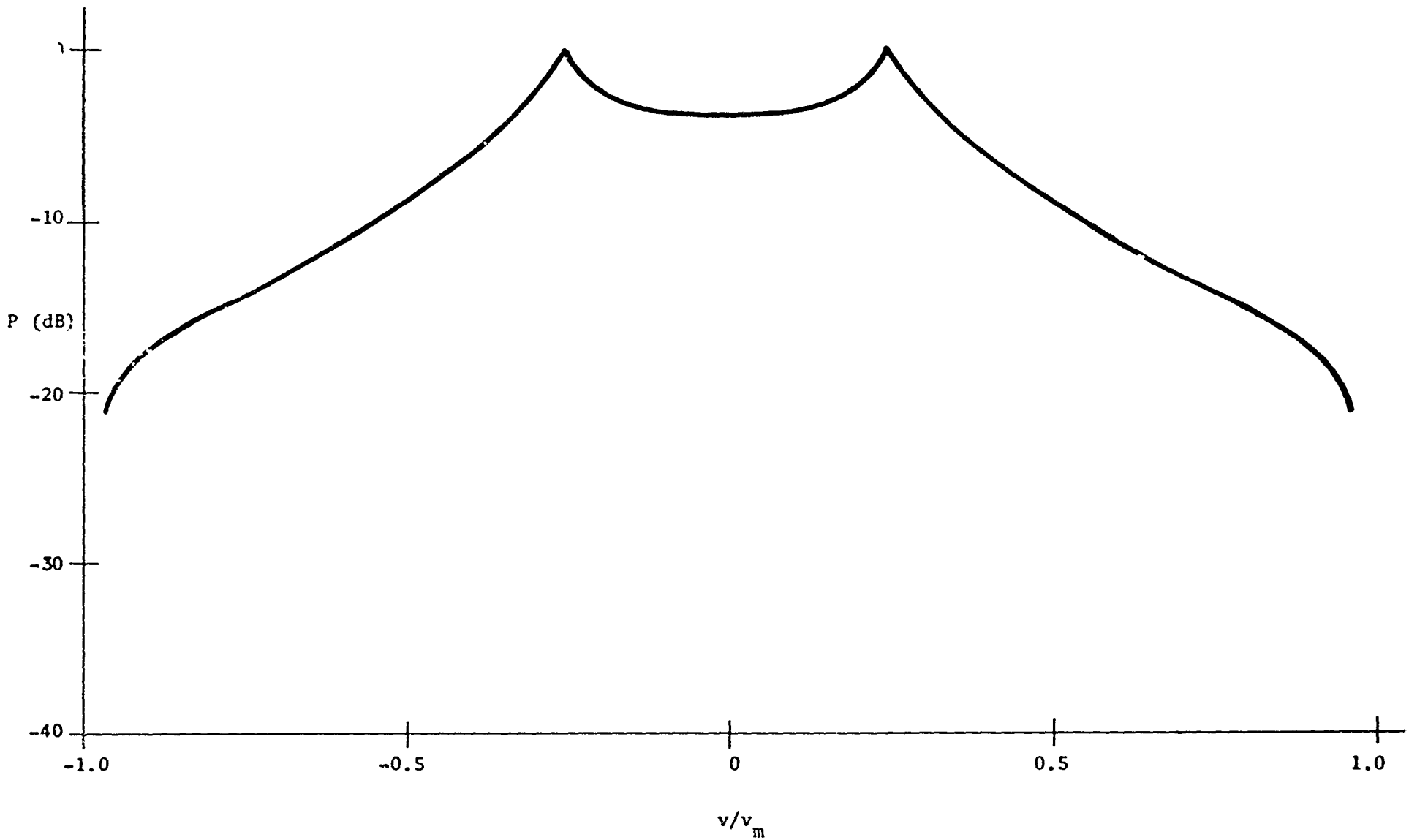


Figure 2-7. Calculated Spectrum, $\mu$=0.25, $\xi_o$=0, $\zeta_o$=0

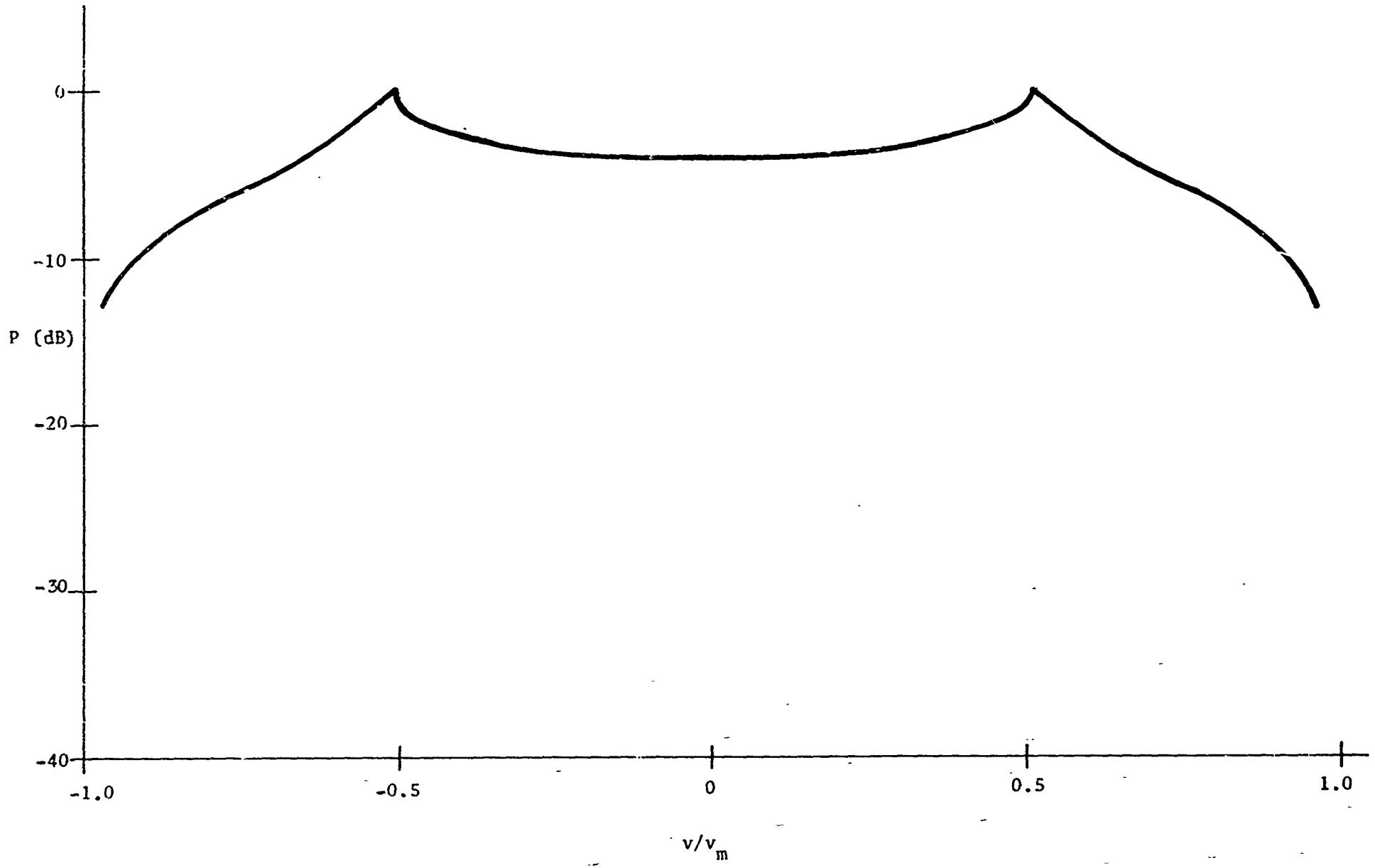


Figure 2-8. Calculated Spectrum, $\mu$=0.5, $\xi_o$=0, $\zeta_o$=0

out. Finally, Figure 2-9 shows the change in the spectral shape when the vortex center does not pass through the center of the observation volume. When $\zeta_0 = 0.5$, i.e., the vortex center is halfway up toward the edge of the coverage, the main effect appears to be that the depression between the two maxima disappears, and the maxima are instead observed merely as "shoulders" or break points in the spectrum.

The character of the spectral shape changes somewhat when the core radius becomes larger than the radius of the observation volume. As an example, Figures 2-10 and 2-11 are the calculated spectra for a vortex whose core radius is twice that of the observation volume ($\mu$=2) for $\xi$=0 and 1.75 respectively, i.e., when the vortex center coincides with that of the observation volume and when it is 1.75 observation radii removed from the center. It should be kept in mind that the velocity scales are normalized to the maximum velocity, which for a very large core radius is proportionately lower for a given circulation. Thus on an absolute scale, the spectra in Figures 2-10 and 2-11 are considerably narrower than those shown earlier. It can be seen that each spectrum represents essentially a band of velocities, corresponding to the rather well resolved part of the vortex being examined at that time.

## 2.3 Discussion of Improved Models

A set of calculated spectra was presented in Section 2.2 that was derived from a simplified model of the vortex flow and its acoustic scattering properties. While it is difficult to ascertain the degree to which the real case differs from the idealized situation, it is worthwhile to examine the assumptions upon which the calculations were based, and to determine insofar as possible to what extent the results are sensitive to each assumption. For those variations that do not produce significant changes in the calculated spectral shape, the simplified analysis is adequate for practical purposes; to the contrary, where a change in the assumption substantially affects the spectral

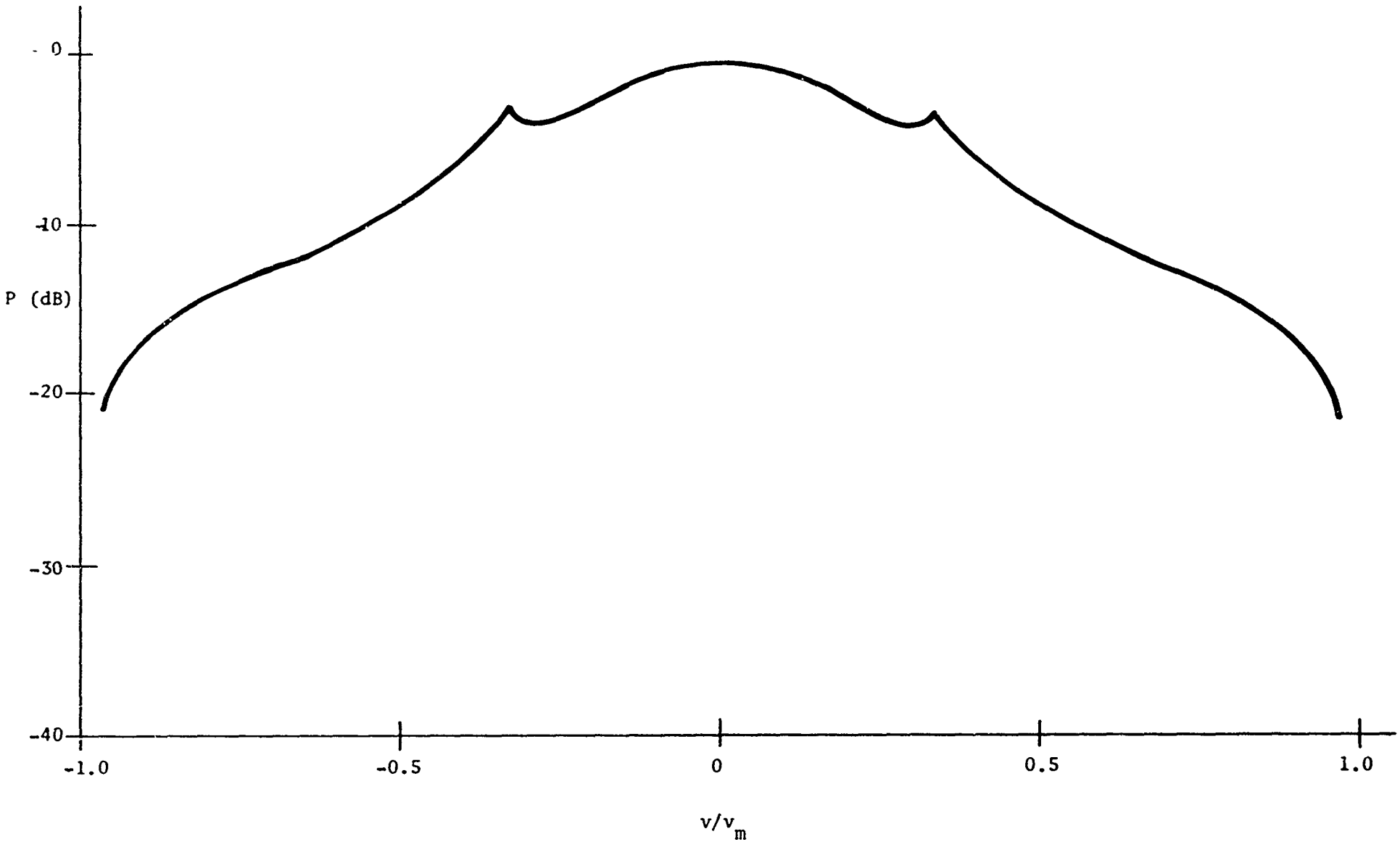


Figure 2-9. Calculated Spectrum, $\mu$=0.25, $\xi_o$=0, $\zeta_o$=0.5

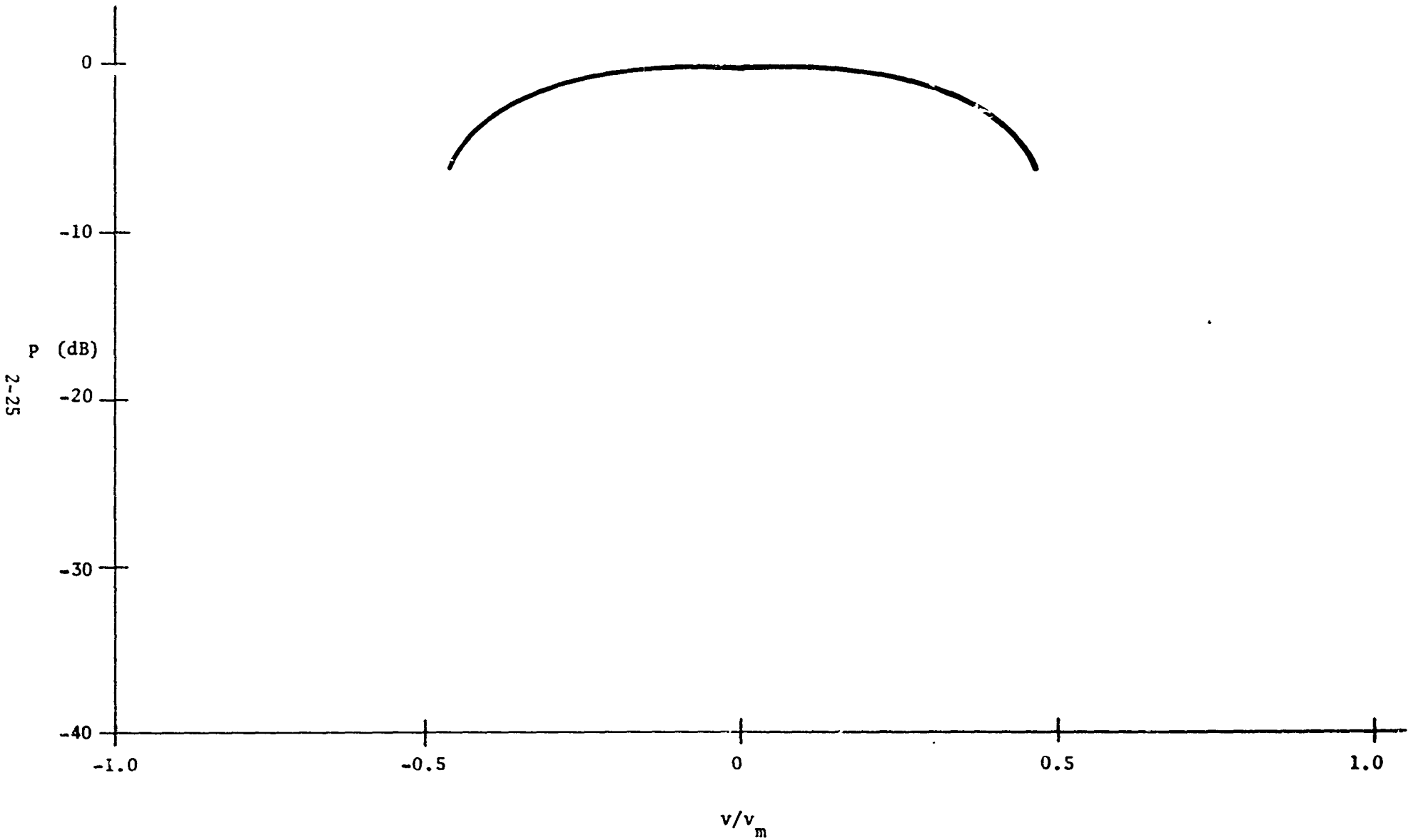


Figure 2-10. Calculated Spectrum, $\mu=2$, $\xi_o=0$, $\zeta_o=0$

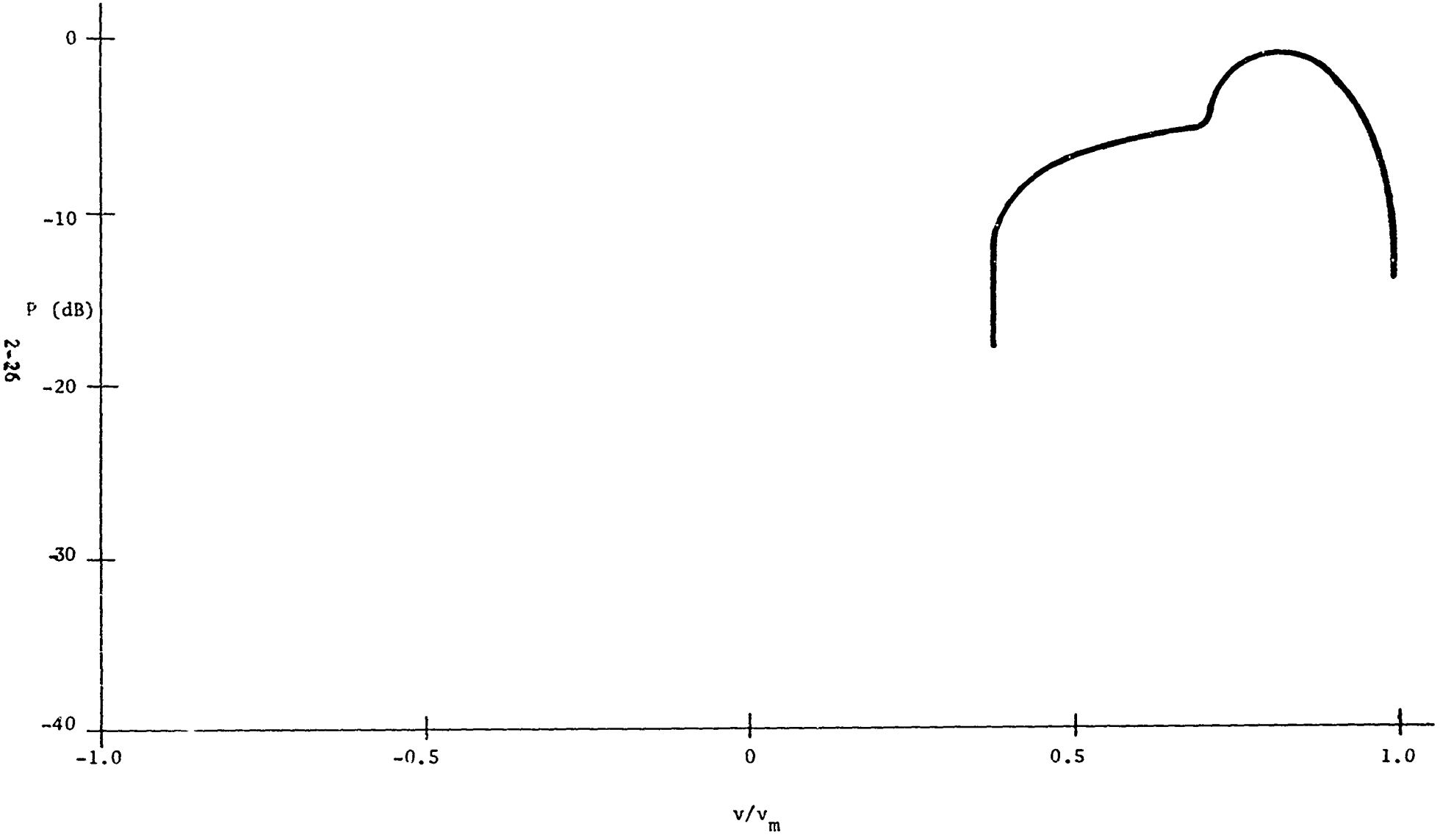


Figure 2-11. Calculated Spectrum, $\mu=2$, $\xi_o=1.75$, $\zeta_o=0$

shape, further investigation to establish the actual condition is indicated. This section is an attempt to determine those factors to which the spectral shape may be sensitive.

### 2.3.1 Assumptions to be Examined

The major assumptions employed in the simplified analysis and the (possibly realistic) deviations from those assumptions are as follows:

a. A specific radial dependence was assumed for the vortex (solid core and potential flow outside the core). Consider the effect of other radial dependences.

b. The weighting function of scattering per unit volume was taken to be constant. Suppose it varies over the vortex.

c. The scattering volume was assumed to be sharply defined. Realistic beam illumination may change the result.

d. The scattering model was essentially a static one. Consider the effect of vortex motion during the integration interval.

e. The vortex axis was taken to be perpendicular to the plane of propagation. Assume now that this is not the case.

f. Only tangential velocities were considered in the calculations. Determine the effect of axial velocity.

g. The effect on the spectrum of the turbulence embedded in the systematic flow was neglected. Determine how significant the turbulent temperature, density and velocity fluctuations are in altering the spectral shapes.

h. Propagation was in all cases taken to be rectilinear. Consider refraction effects.

### 2.3.2 Effects of Variations in Assumptions

The questions raised in Section 2.3.1 will now be examined in turn.

2.3.2.1 Radial Velocity Dependence. The assumed velocity dependence for the simplified model is given in equation (2-29). The Betz model described in equation (2-6) is substantially different in form. With the proposed modification to account for a core, it may be approximated (since r<<b in the observation volume containing the core) as

$$v(r) = \frac{\sqrt{6}\,\Gamma_o}{2\pi\sqrt{rb}}\left(1 - e^{-r^2/r_1^2}\right) \qquad (2\text{-}32)$$

Note that the core does not undergo solid-body rotation in this model, and that circulation increases with increasing radius even outside the core.

The solid curve in Figure 2-12 is the centered simplified model case for $\mu = 0.25$. The dashed spectrum in Figure 2-12 is calculated from equation (2-32) for the case where $r_1$ was chosen so that the maximum velocity occurs at 0.25 $R_o$. In addition, $\Gamma_o$ has been changed by a factor of 2.2 to match the velocities for the two cases at the edge of the beam. It is seen that the effect of varying the radial velocity dependence is not a major one if the velocity at the edge of the beam (hence the circulation over that scale) is kept constant. Stated differently, the interpreation of the significant feature in the spectrum, i.e., the peak or shoulder, as the velocity at the edge of the beam is not sensitive to assumed changes in the radial velocity profile.

2.3.2.2 Scattering Weighting Function. There is little evidence available on which to base a choice of weighting function W(r) other than the uniform weighting that was chosen. Qualitative physical reasoning might lead one to suppose that turbulence would be most strongly generated in the vicinity of the core, where velocity gradients are strongest. On the other hand, to the extent that the inhomogeneities are residual from entrained jet exhaust and other turbulent flow, they would presumably be widely distributed through the vortex.

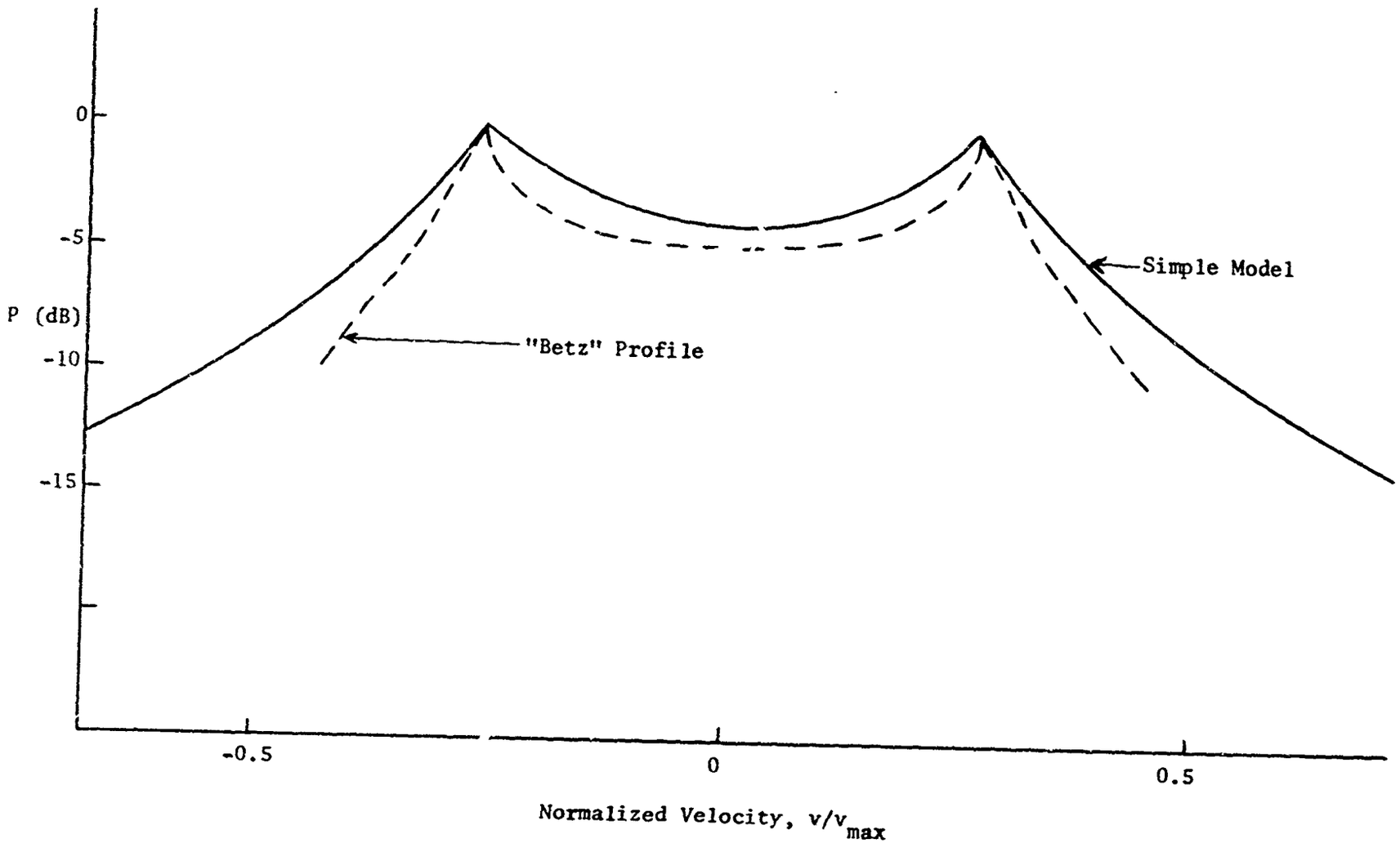


Figure 2-12. Comparison of Spectra with Different Radial Velocity Profiles

Two observations from the earlier acoustic returns from vortices tend to suggest that the latter situation is closer to correct, and thereby support the supposition of uniform scattering strength. It was noted that at a distance of a few beam positions away from that containing the core the scattered signal was still strong, in fact comparable to the strength of the central beam. Perhaps more to the point, in that central beam, the spectral strength fell off very rapidly with increasing velocity. If the scattering strength were very much greater around the core radius, the highest-velocity returns would have been correspondingly emphasized and seen more prominently in the spectrum, which does not appear to be the case. This point will be considered further in later sections in connection with vortices for which the core size is comparable to or exceeds the dimension of the scattering volume.

Figure 2-13 shows the result of replacing $W(r) \equiv 1$ with the function

$$W(r) = 2,3 \qquad 0 < r < 1.5\ r_c$$

$$W(r) = 1 \qquad r > 1.5\ r_c \qquad (2\text{-}33)$$

for the case $r_c/R_o = 0.25$. As might be expected, the change in the spectrum is not very great for a moderate increase in scattering strength at the core when the core represents a relatively small part of the total return in the scattering volume. Clearly, the spectral shape will be altered if the weighting is changed substantially over a large fraction of the scattering volume.

2.3.2.3 Boundary of the Scattering Volume. The illumination of the scattering volume was taken to be uniform out to the radius $R_o$, and zero beyond. For the case of the centered vortex, a modification for non-uniform illumination $G(r)$ (equation (2-15)) is clearly equivalent to a similar modification in the weighting function $W(r)$, and the conclusion might be expected to be similar to that in the previous

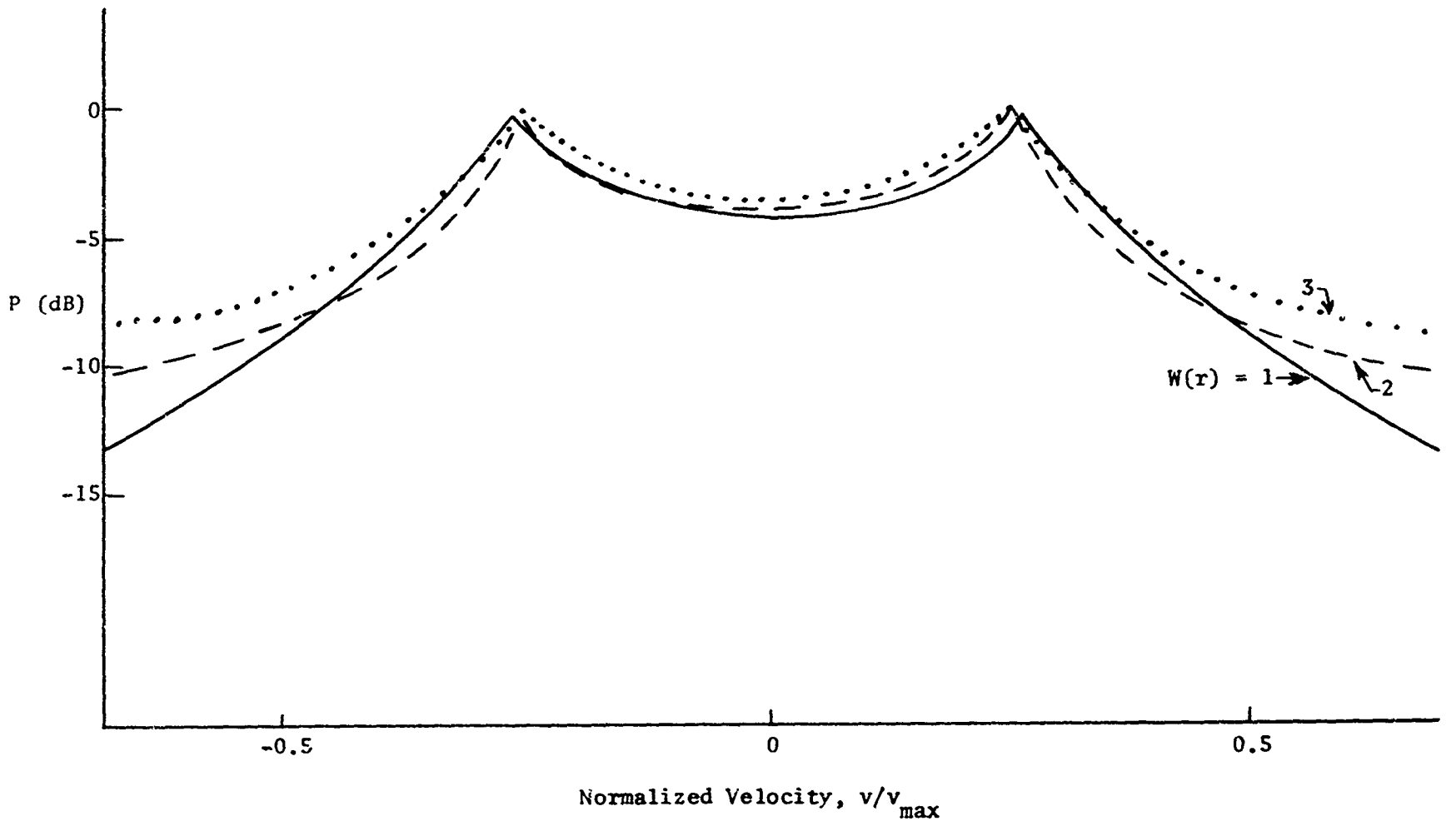


Figure 2-13. Effect of Various Weighting Functions on the Spectral Shape. For $0 < r < 1.5\ r_c$, W(r) is as indicated for each curve. For $r > 1.5\ r_c$, $W(r) \cong 1$ for all curves.

subsection. The result of taking the more realistic beam pattern

$$G(r) = \frac{\sin^2\left(\frac{k\pi r}{R_o}\right)}{\left(\frac{k\pi r}{R_o}\right)^2} \tag{2-34}$$

with $k = 0.6$ is compared with the case for uniform illumination with $r_c = 0.25\ R_o$ in Figure 2-14. The results are seen to be similar, due to the fact that the velocity in the largest effective scattering volume is about the same. In particular, $G(R_o) = 0.25$, so the "effective" edge velocity is seen to correspond to the point illuminated 6 dB down from the peak.

Another sense in which the assumption of a uniform circular illumination can be violated is in the circularity rather than the uniformity. Figure 2-15 shows the spectrum for the case of a uniformly illuminated rectangle with a base-to-height ratio of 2, with the scattering direction perpendicular to the base. This curve is compared with the simple case for $r_c = 0.25\ R_o$, where the area of the circle, $\pi R_o^2$ is equal to the rectangular area. As should be anticipated, the amplitude of the zero (and small) doppler components is reduced, since the rectangular volume encloses less of the velocity field contributing to these amplitudes. Also, the peak amplitude is shifted to smaller velocities since the largest amplitude contribution results from scattering at the extreme ends of the long dimension of the rectangle. As before, the chief spectral feature is associated with the velocity at the edge of the beam.

2.3.2.4 Dynamic Effects. The model considerations presented in Section 2.2 account for the fact that the acoustic radar is not a point sensor, but rather responds simultaneously to the velocity distribution throughout its antenna beam coverage. In addition to this spatial averaging, observed spectra are the result also of averaging

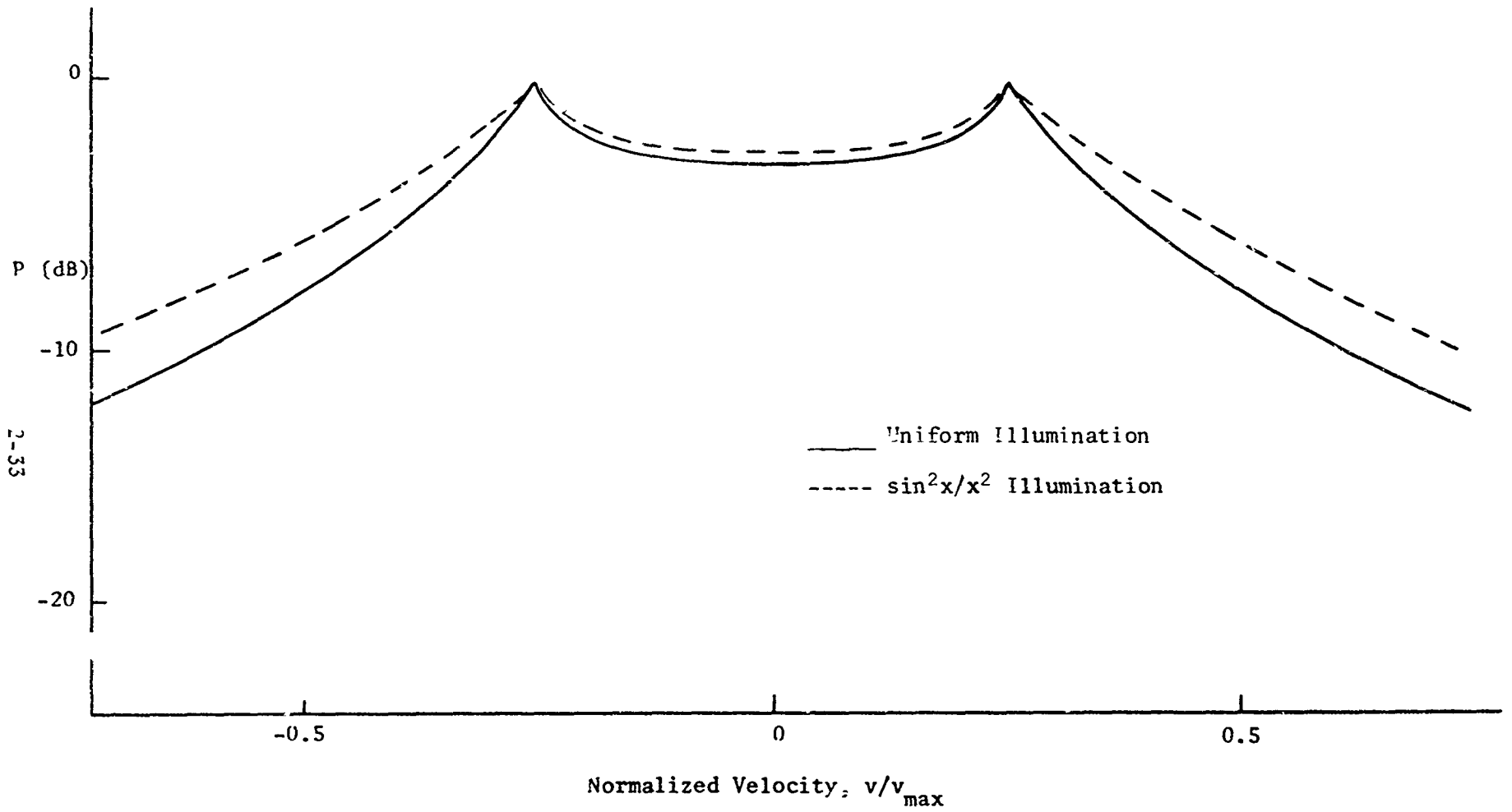


Figure 2-14. Effect of Beam Illumination of the Spectral Shape

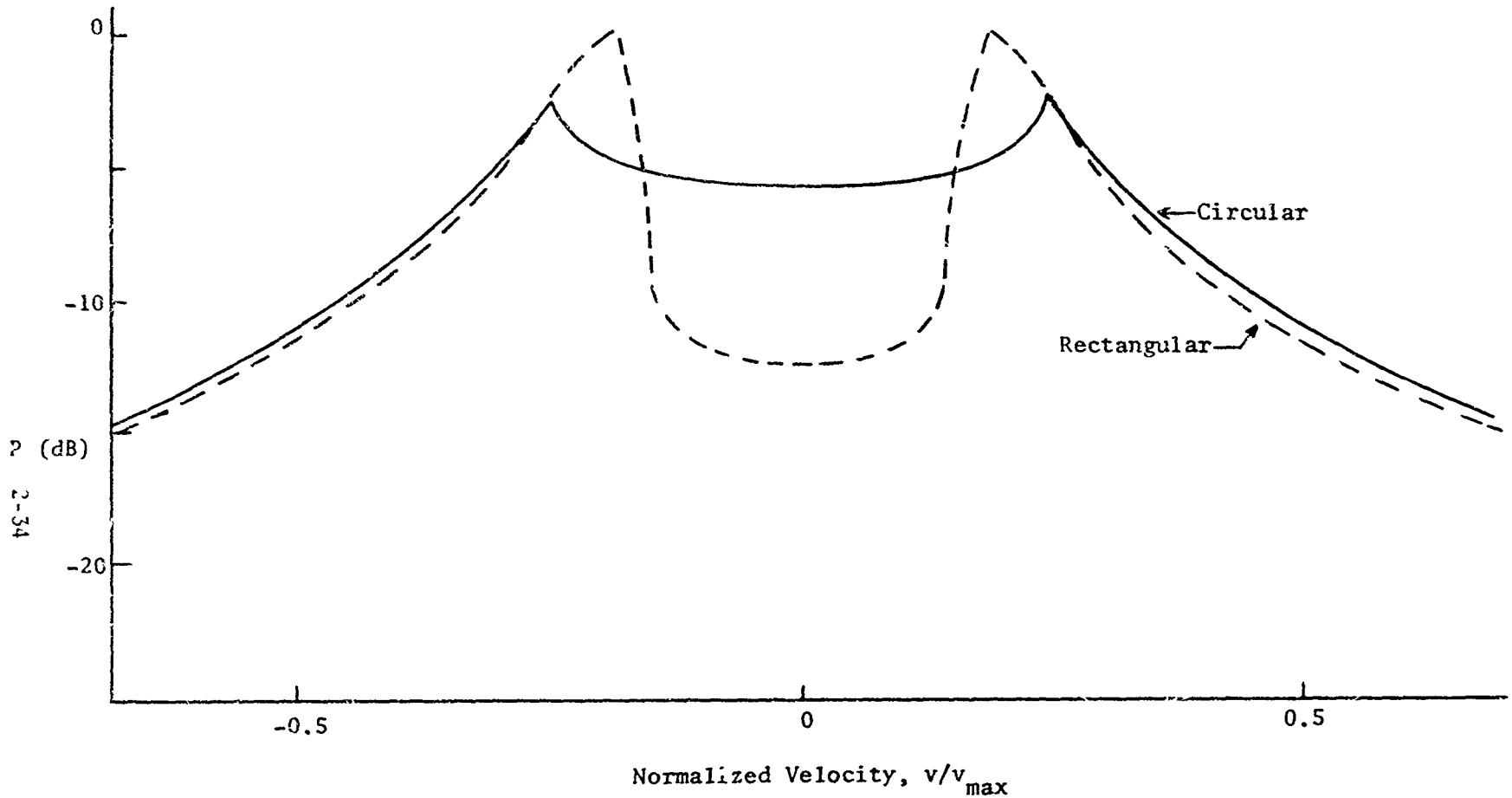


Figure 2-15. Effect of Observation Volume Shape on the Spectrum

in time over the interval of the integration period employed for the spectral analysis. While this interval is under the control of the analyst, the desired velocity resolution prevents the choice of arbitrarily short integration periods. For relatively high (but for these tests frequently encountered) winds, the vortex may be displaced a significant fraction of the dimension of the observation volume during the integration interval, typically taken as 0.2 seconds.

A good idea of the dynamic effect on the observed spectrum that would be expected by this translational motion can be obtained simply by averaging over the static spectra that cover the spatial interval corresponding to the translational motion during an integration period.

Figures 2-16 through 2-18 show the results of averaging sets of neighboring spectra for the case $r_c/R_o = 0.25$ and $z_o/R_o = 0$. Figure 2-16 is the average for $\xi_o = x_o/R_o = 0.0$, 0.25 and 0.5, representing a motion of the vortex center from the center of the observation area to halfway out toward the edge. Figure 2-17 is a similar average for $\xi_o = 0.5$, 0.75 and 1.0, and Figure 2-18 for $\xi_o = 1.0$, 1.25 and 1.5. The solid curves in each figure indicate the respective averages, while the dashed curves are the spectral shapes for the center position of each average, i.e., $x_o/R_o = 0.25$, 0.75, and 1.25 respectively. From these results, it is apparent that even with small vortex size ratios ($r_c/R_o = 0.25$ which corresponds roughly to a DC-7 vortex) vortex displacements of a large fraction of the observation volume dimension are necessary for significant dynamic effects on the spectra.

2.3.2.5 Vortex Orientation. To a reasonable degree of approximation, the component of velocity that produces a Doppler shift in the received acoustic signal is vertical. (This is very nearly true for anticipated operating configurations. For the tower tests, the scattering vector is typically 20 to 25 degrees away from the vertical, which affects Doppler shifts but little since the cosine of such

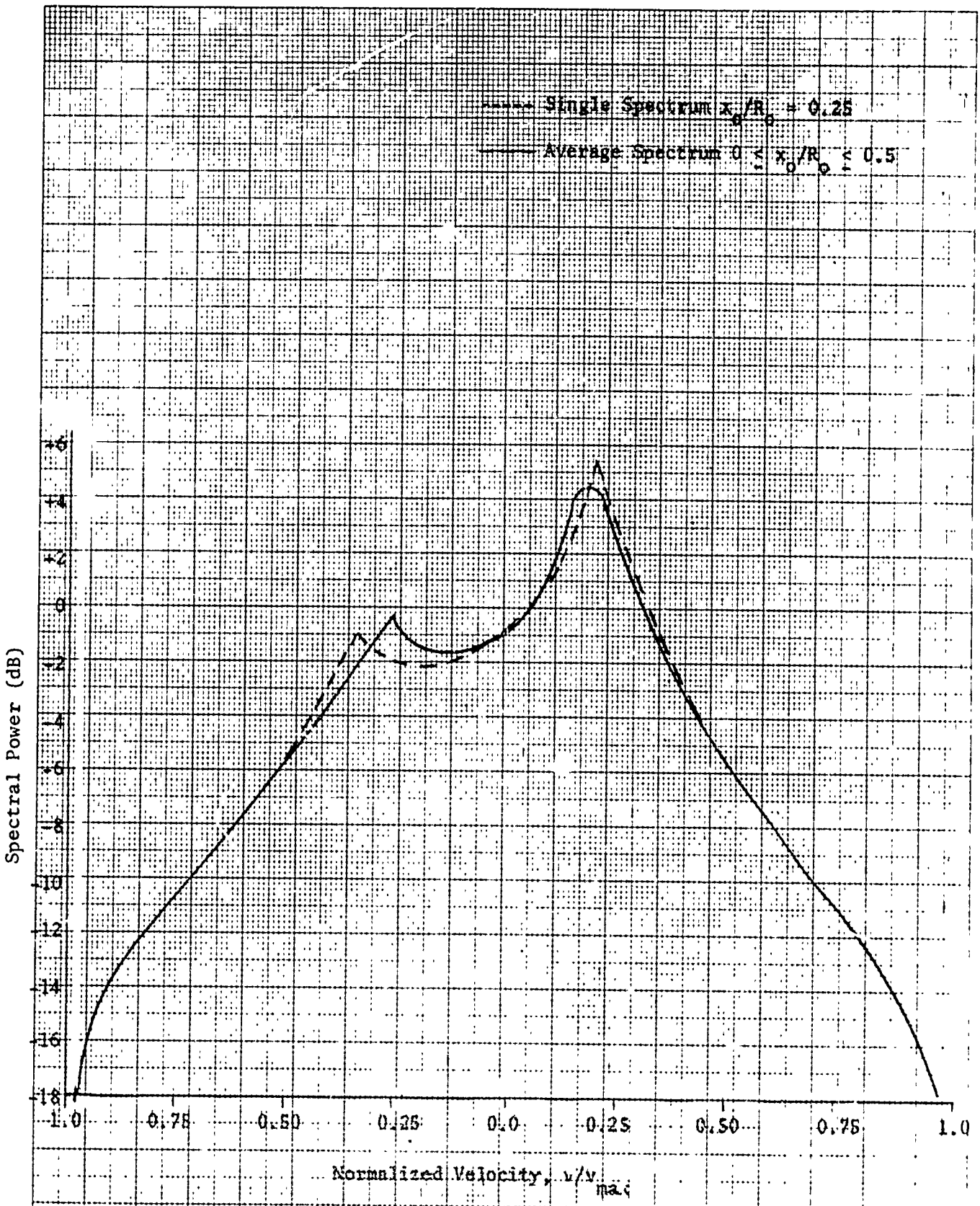


Figure 2-16. Effect of Vortex Motion through the Observation Volume

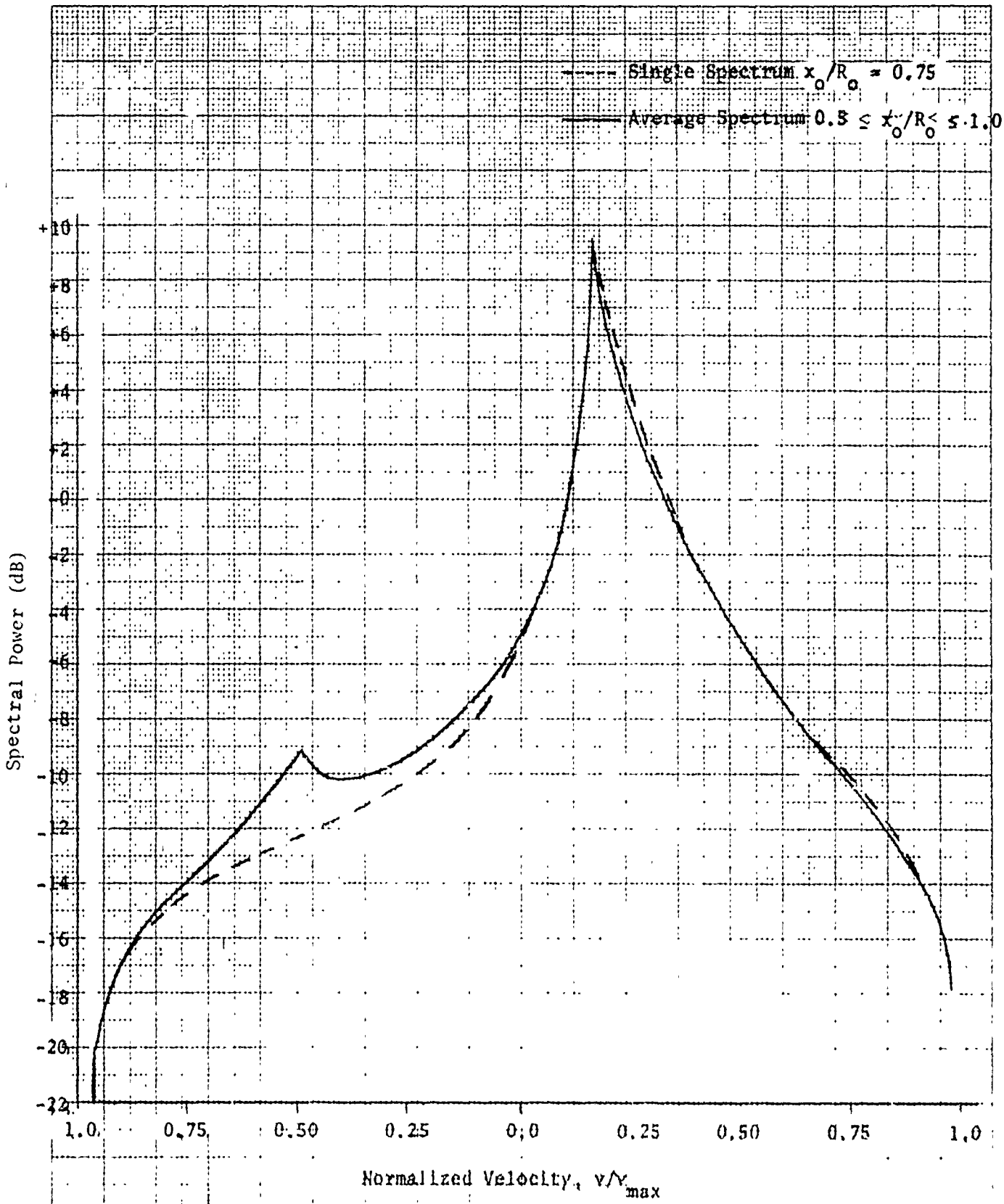


Figure 2-17. Effect of Vortex Motion through the Observation Volume

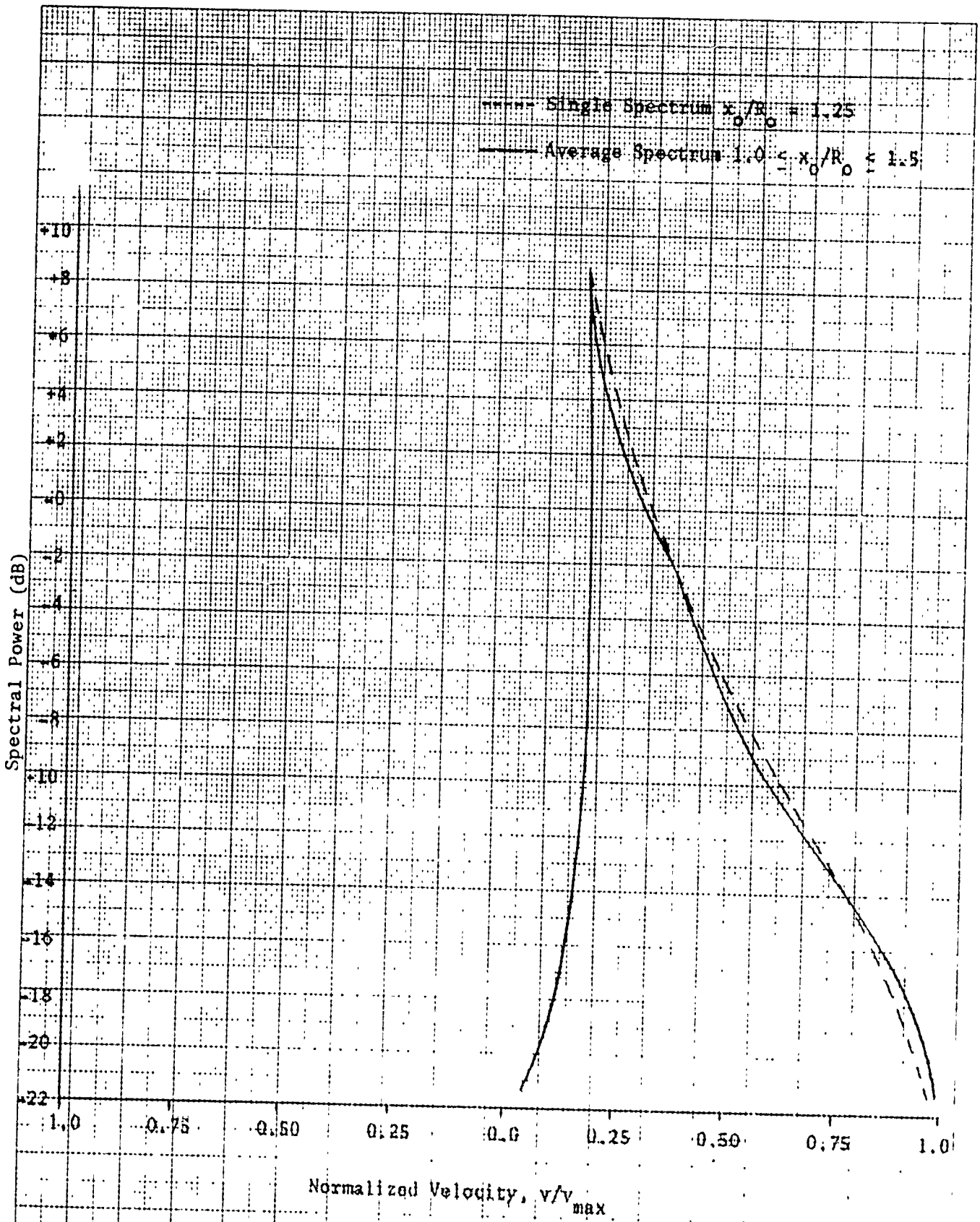


Figure 2-18. Effect of Vortex Motion through the Observation Volume

angles is about 0.9.) To that same degree of approximation then, there should be no difference in the spectrum of a horizontal vortex, whatever the orientation of its (horizontal) axis with respect to the plane of propagation, since the vertical component of the tangential velocity remains the same under such a rotation. (Again, some distinction will be noticed for the tower case since the radar responds to a lesser extent to a horizontal component in the plane of propagation.)

The principal effect of vortex orientation, and this includes a moderate incline of the vortex axis to the horizontal, is that the cylindrical symmetry of the scattering configuration is destroyed. To the extent that the scattering volume is cylindrical, as in Figure 2-3, a vortex which is not aligned in the volume will have its axis at different locations $x_o$, $z_o$ of that volume at the same time. This problem is thus reduced to the one discussed in Section 2.3.2.4, which treated just such a superposition of returns. To the extent that the scattering volume can not be represented ideally in this way, the beam-shape modifications investigated in Section 2.3.2.3 would come into play. Thus the effects of vortex orientation are expected to be similar to and of the same order as effects described in the preceding two sections.

2.3.2.6 Axial Velocity. The preceding section considered the effect of the orientation of the vortex axis, but restricted its attention to tangential motion. Even where the scattering vector, hence the observed doppler component, is not vertical (as in the tower tests), the cylindrical symmetry of the motion minimizes any changes in spectral shape. This situation is changed for the case of axial (predominantly horizontal) velocity, which is systematically in one direction. There would therefore clearly be an effect on the spectrum if the acoustic scattering vector has a significant horizontal component, as it does in the tower test configuration. That effect

can be seen to be a shift in the doppler velocity of the return from the affected region, the shift itself corresponding to the doppler component of the axial velocity.

One might expect that a significant axial velocity would be confined to the core of the vortex (see Section 2.1.3). For very small cores, such as those observed in the DC-7, the observable effect of the axial velocity, along with that of the core in general, would also be small. If the axial velocity is more widespread, and in any case when the core fills the observation volume (as is expected for large aircraft) the shift should be observable. The most notable distinction should occur between two receivers displaced in perpendicular directions from the transmitter, particularly when the vortex axis points toward one of those receivers.

In the case of anticipated operational configurations, where the scattering vector is predominantly vertical, the effect of axial velocity, particularly since the aircraft path will normally be perpendicular to the plane of propagation, is expected to be negligible.

2.3.2.7 Turbulent Spreading. It was assumed throughout the modeling study that the return from a given portion of the vortex suffered a doppler shift determined solely by the mean, or systematic, flow velocity at that location. In fact, the scattering is understood to be caused by small-scale irregularities that are carried along in the flow. Some of the energy is scattered by temperature fluctuations. If these are relatively frozen in the flow over the integration period, the local velocity is the mean velocity, and the spectrum calculated on the basis of mean velocity is valid. Velocity fluctuations that contribute to the scattering also introduce local velocity changes about the mean that will result in a certain amount of spreading in the spectrum of even a small region over which the mean velocity is essentially constant. This spreading is random in

nature, corresponding to the statistical characteristics of the turbulent fluctuations, in contrast with the deterministic quality of the mean motion.

An estimate of the expected modification of the spectral shape may be inferred from the typical value of turbulent velocities that may be generated in momentum-less wake flows behind self-propelled bodies[14]. Measured turbulent intensities in these flows have been fit with the curve

$$\frac{\tilde{u}}{U} \approx 0.4 \left(\frac{x}{D}\right)^{-0.85} , \qquad (2\text{-}35)$$

where

$\tilde{u}$ = the maximum turbulent intensity

$U$ = the aircraft velocity

$x$ = the distance behind the aircraft

$D$ = the aircraft wing thickness

Nominal values of the turbulent intensity 10 seconds after the aircraft passage are seen to be a very few tenths of a foot per second. The spreading introduced by this turbulence may be thought of as a smoothing filter in the frequency domain, with a bandwidth corresponding to a fraction of a ft/sec. Thus, even if turbulent velocity fluctuations generated by the vortex flow represent a substantial part of the source of scattering, the modification of the spectrum on their account is clearly minor compared to many of the other effects being discussed in this section.

2.3.2.8 Refraction. The equation governing the trajectory of an acoustic ray in a medium with varying velocity is

$$\frac{d\vec{n}}{dl} = -\vec{n} \times \nabla \times (\vec{v}/c) \qquad (2\text{-}36)$$

In a region of irrotational flow ( $\nabla \times \vec{v} = 0$), it is seen that no refraction occurs. In our simplified model, the flow outside the core, which decays as 1/r, is irrotational. Thus, no refraction takes place outside the core, so the calculation of most of the return is valid.

Should the radial dependence of the vortex velocity outside the core not be precisely 1/r (see Section 2.3.2.1), some refraction would take place there. The effect of such refraction is three-fold. First, the scattering angle can be changed from that for rectilinear propagation. Second, the direction of the scattering vector, and hence of the sensed doppler velocity component, is changed. Finally, some beam focusing may occur, resulting in varying illumination over the target. It would appear that the departure of the true radial profile from the 1/r dependence is slight enough so that these changes, already second-order effects, would be negligible compared with other effects discussed here. This tentative conclusion should, however, be re-examined when more definitive radial velocity profiles become available, particularly from the tests of large aircraft.

### 2.3.3 Conclusions

Eight assumptions underlying the simplified model were listed at the beginning of Section 2.3, and the result of modifying each of those assumptions in some reasonable manner was examined in turn. The result can be stated to be that the effect on the spectrum of a "realistic", as opposed to an idealized, assumption is not very great, with one important understanding. The predominant feature in the calculated spectra is the pair of peaks or shoulders that correspond to the velocity at the edge of the observation volume; if that value is held constant, the spectral shape is not substantially affected. Put more generally, the spectrum for all the modified assumptions retains the characteristic association of peaks with the velocity at the edge of the observation volume This conclusion will continue to be tested as more definitive information becomes available on each of the assumptions.

## 3. STUDY OF XONICS DATA FROM PREVIOUS TESTS

The first set of tests conducted by Xonics in September 1971 at NAFEC in conjunction with the instrumented tower demonstrated the capability of the acoustic radar to locate vortices in space and time, in agreement with similar observations by the tower. Some study was made of the spectra obtained by processing the scattered signal, and these agreed qualitatively with the shapes expected as a function of time as the vortex passed the observation volume. The only quantitative comparison of internal vortex motion that was made between data from the two sensors in that initial examination had to do with the peak observed vortex velocity. That choice was unfortunate, since neither sensor was really suitable for measuring peak velocity, owing to the very small vortex core diameters, of the order of 1 to 2 feet, generated by the DC-7. The acoustic radar measures the velocity distribution in a volume several feet on a side, so that the very small volume occupied by the highest velocities of a small vortex appears in the spectrum with a strength far down from the peak, in fact below the noise level. The 4-foot spacing between tower sensors frequently allowed the core to pass between adjacent sensors, so that the maximum observed velocity was far lower than the true maximum.

As part of the initial phase of this continuing study, it was agreed that a re-examination of the acoustic data from those earlier tests was in order before the new data generated by the further field testing became available. Three important purposes would be served by this re-examination; it would

a. Provide an early indication of the validity and shortcomings of the models of vortex structure and acoustic scattering.

b. Suggest potential discriminants for estimating the hazard posed by a vortex.

c. Expedite the schedule of the new tests by virtue of the experience in processing and analysis gained from the old ones, leading to improved plans and methods.

This section describes the study of the earlier acoustic spectra.

## 3.1 Review of the Earlier Tests

Details of the tests conducted at NAFEC in September 1971 and the results of the first processing of the data are contained in reference 2. Briefly, the data were obtained by a bistatic radar system configured as shown in Figure 3-1. The transmitter dish generated a vertical acoustic beam parallel to the instrumented tower and displaced from it by about 20 feet; the transmitted signal was an unmodulated sine wave (cw). The receiving dish produced a fan of 12 individual receiving beams that intersected the transmitted beam in a series of scattering volumes along the height interval of interest. The individual signals received in each beam, resulting from the energy scattered in the corresponding common volumes at known altitudes, were recorded onto a 14-track magnetic tape.

The tracks on the tape were then examined individually using an analog spectrum analyzer whose output was displayed on an oscilloscope. Relevant sections of the signal so observed were filmed by a movie camera, and the data were then manually scaled off the film frames. This rather rudimentary system of data processing, though tedious, in fact proved quite effective in producing the first round of results rapidly. Perhaps its major shortcoming was the relative inflexibility in integration interval and difficulty in accurately fixing and varying start times that limited the analyst's freedom to pursue certain lines of inquiry.

## 3.2 Description of Spectral Processing

As a result of the limitations of the early processing technique, it was decided that digitization of the data and subsequent processing on a computer would offer a most worthwhile improvement in flexibility, repeatability and convenience. Accordingly, a playback unit was set up at Xonics that is shown schematically in Figure 3-2.

Figure 3-1. Bistatic Acoustic Radar Configuration Employed in Tower Tests

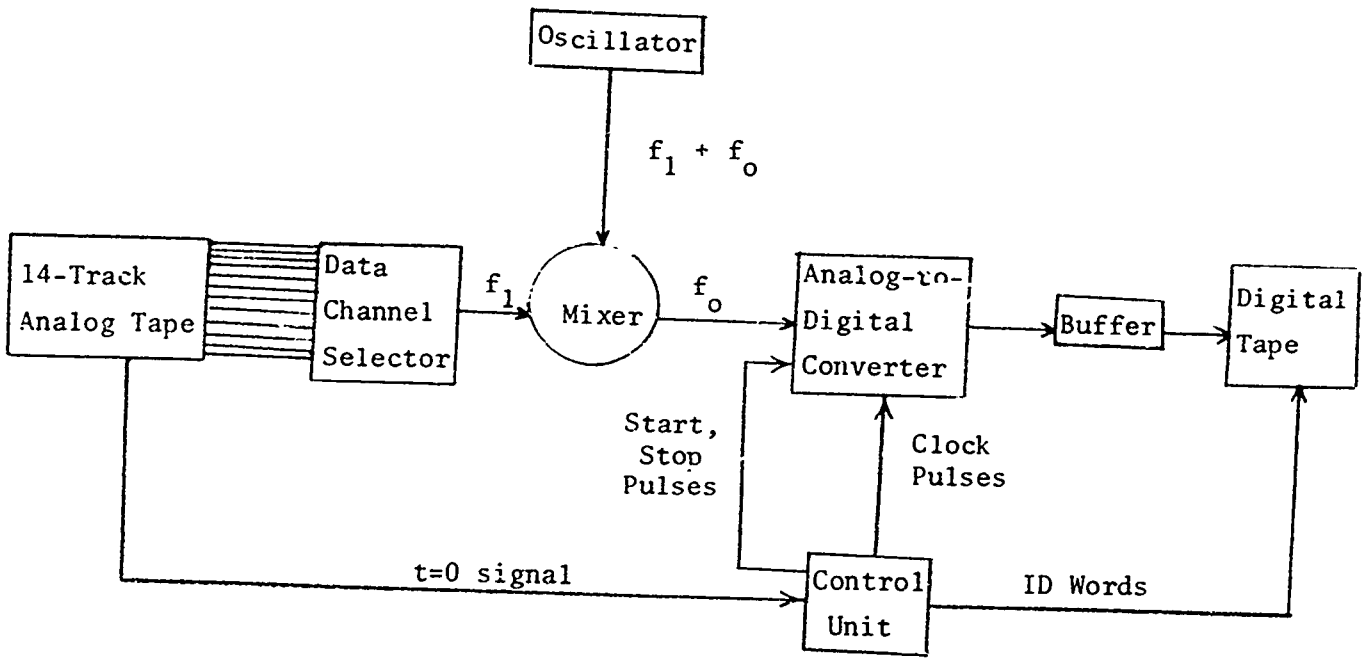


Figure 3-2. Data Digitization System

The digitization system processes one channel at a time, so the channel of interest is selected and processed, and the procedure is then repeated for other channels if desired. First, the signal, originally transmitted at a frequency $f_1$ (which may be changed for different experiments) is mixed with a frequency $f_1 + f_o$, so that the signal actually processed occupies a frequency range around a standard frequency $f_o$. It has so far been found convenient and sufficient to take $f_o = 1.25$ kHz.

The digitizing operation is under the control of a control unit. A pulse recorded on a non-data tape channel initiates the cycle. (This pulse, supplied by NAFEC, occurs as the aircraft passes the tower, and is always taken as the t = 0 reference). Preset start and stop times determine the segment of data to be digitized. The clock pulses fix the rate at which the signal is sampled. Consistent with a center frequency $f_o = 1.25$ kHz, the sampling frequency has been taken to be 5 kHz, allowing an unambiguous frequency interval of 2.5 kHz to be examined. (All of these values can be easily changed.) Next, the sampled voltage is digitized and stored in a buffer. Finally, the stored samples are read out onto digital tape in record blocks of 1024 words (samples) each. Header records and words for identification of data are supplied to the digital tape by a bank of manually set switches in the control unit.

The digital tape is now ready to be used as input data for a digital computer, and it can then be processed as desired. In this case, the processing virtually always takes the form of spectral analysis. The specific program used on the data presented in this report is a Fast Fourier Transform operating on an unweighted segment of data, i.e., no filtering, such as Hamming weighting, has been applied. The resulting frequency spectrum is displayed graphically as line-printer output. An example both of the format of this output and of the frequency filter response of the processing is shown in

Figure 3-3, which was traced from the computer printout of the spectrum of a test sine wave. A 0.2 second interval of data was analyzed, resulting in a frequency resolution of 5 Hz between neighboring points along the abcissa. A power scale (in dB) is given for the ordinate.

Data from many of the analog tapes recorded during the tower tests of September 1971 were processed in this manner. The integration period of about 3/4 second used to examine the data in reference 2 was judged to be too long for detailed analysis and comparison with model spectra. A period of 0.2 second seemed a reasonable compromise on obtaining acceptable time resolution without compromising the desired frequency (velocity) resolution. The integration period is an input parameter in the program, and is of course changeable at the discretion of the analyst.

Another feature of the program is designed to decrease the large statistical fluctuations inherent in spectral estimation of noise-like signals such as those scattered from vortices. Smoothing is applied by averaging a number of adjacent points, typically four, and plotting one point for each set so averaged. The resolution in frequency is reduced thereby to 20 Hz, but this resolution appears to be quite sufficient, and the smoothing greatly facilitates the observation of detailed spectral shape. This whole procedure was applied to the digitized data, and a considerable data bank was thereby developed for further study.

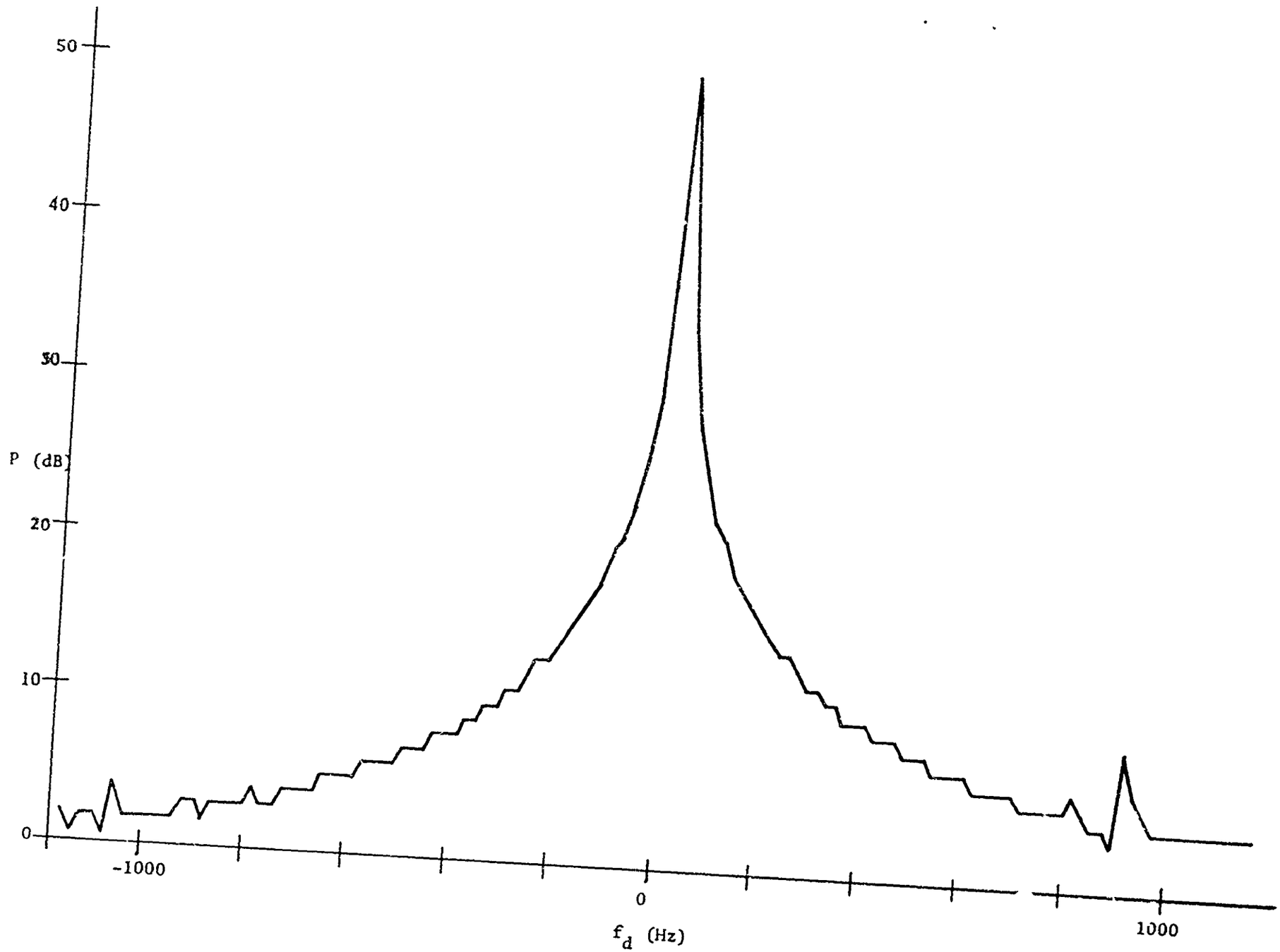


Figure 3-3. Typical Frequency Filter Response

### 3.3 Comparison of Observed Spectra with the Model

The scattered power spectrum of the vortex signal S(f) is obtained as a function of the Doppler frequency f by the signal processing technique of fast Fourier transformation as discussed in Section 3.2. The power spectrum associated with a given resolution cell or receiver beam is displayed as a function of Doppler frequency at time intervals corresponding to the integration time of the Fourier processing, which is 0.2 second for the data considered here.

The spectrum of the scattered signal changes in time as the vortex is transported across a given observation volume by a combination of its natural motion of falling and separation in ground effect, and convection by the wind. The expected spectral shapes as a function of time have been discussed in detail in Section 2 for a simplified model and to some extent for modifications to that model that may make it more realistic. Generally speaking, the observed data display the features shown by the calculated spectra and a few other features that should be mentioned. One is the addition of noise, which puts a "floor" on the useful data. Another is the presence of a "feed-through" signal, the result of the reception of a signal directly from the transmitter to the receiver through sidelobes of both antennas. This signal always appears with no Doppler shift, as would be expected. Finally, the spectra are modified by the ambient wind, which produces three effects. The first effect is that scattering occurs from turbulent fluctuations in the ambient wind stream, so that a peak in the scattered spectrum is produced at the Doppler frequency corresponding to the wind velocity even in the absence of a vortex or other disturbance. When the vortex arrives, the wind shifts the center frequency of the vortex spectrum to that of the Doppler frequency corresponding to the component of the wind velocity in the direction of the scattering vector. Lastly, the wind velocity $v_w$ causes the vortex center to move an additional distance

$x = v_w \tau$ along the trajectory during the integration time $\tau$ of the signal processing. This distance may amount to as much as 2 feet for the cases under consideration. Therefore, the processed spectra may display the results of a spatial averaging of the instantaneous, fixed position spectra, as was discussed in Section 2.3.2.4.

Figures 3-4 through 3-10 show the processed power spectra for Run 104, Beam 9, h = 59 feet. The figures are arranged in chronological order to show the time development sequence of spectra comparable to Figures 2-4 through 2-7. Many intervening spectra have been omitted in the interest of brevity. The base of the curve is the noise level. The central peak in Figure 3-4 is the spectrum associated with the direct-path feed-through signal. On the subsequent figures in this series, this narrow feed-through at zero Doppler frequency has been truncated to make the shape of the scattered spectrum easier to observe. No vortex activity is apparent yet in Figure 3-4, which very closely matches the filter response of Figure 3-3. Figure 3-5 signals the appearance of the vortex by the narrow peak to the right of the zero frequency shift. (Time of observation following aircraft passage is given for each figure.) Figures 3-6 and 3-7 display the progressive broadening towards higher Doppler frequencies that occurs as the core approaches the center of the scattering volume. Figure 3-8 displays the symmetric spectrum that results when the vortex center coincides with the center of the resolution cell. Figures 3-9 and 3-10 depict the decreasing velocities in the opposite direction as the core recedes from the observation volume.

Several of these figures compare quite favorably with the sequence of calculated spectra shown in Section 2.2. For example, the curve in Figure 2-7, the centered case, is shown superimposed on Figure 3-8. Similarly, (the mirror image of) Figure 2-6, for the vortex somewhat displaced from the center, is superimposed on Figure 3-9. Figure 2-5, with the core at the edge of the observation volume is drawn on Figure 3-7, while Figure 2-4, still further out, is drawn on Figure 3-10.

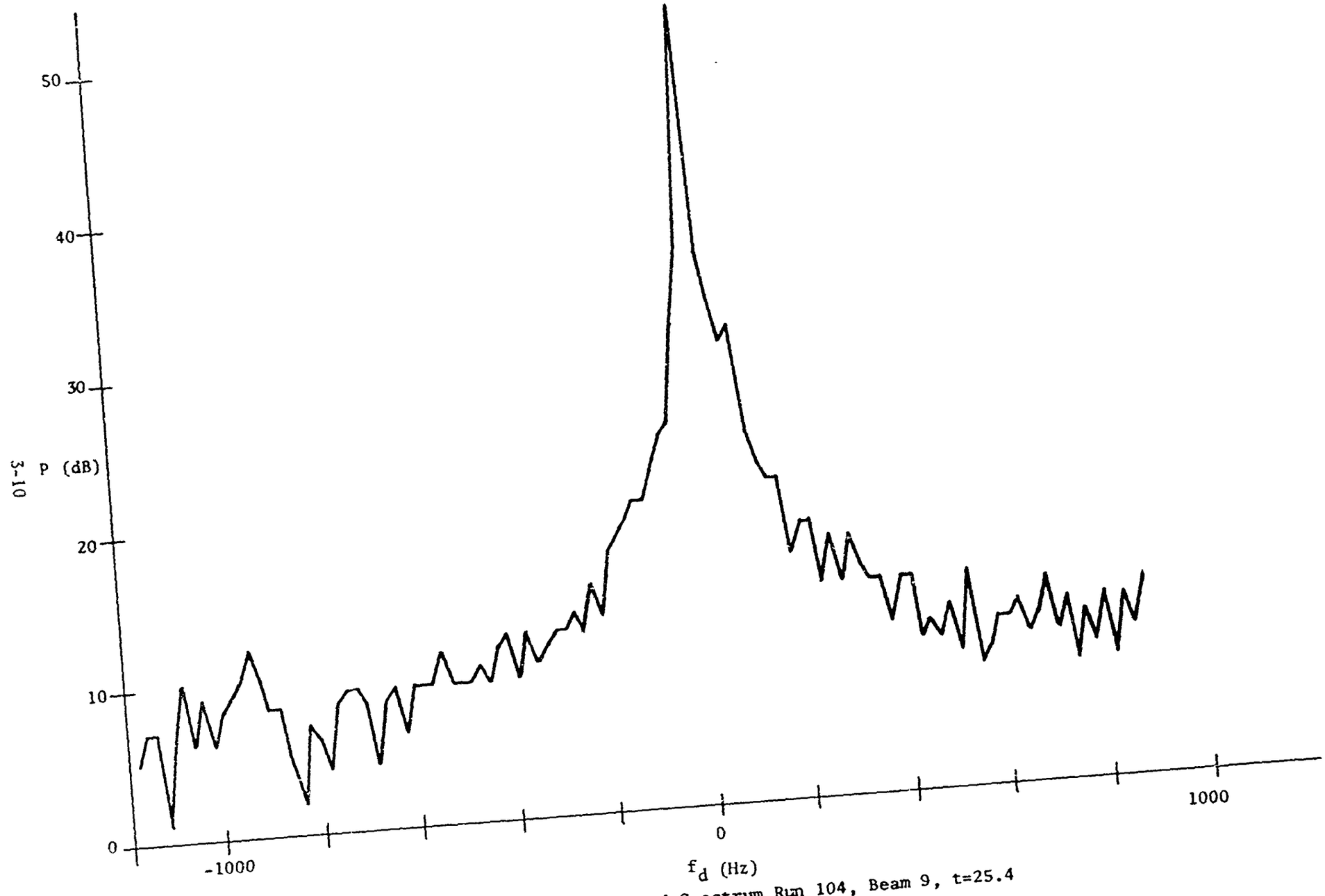


Figure 3-4. Observed Spectrum, Run 104, Beam 9, t=25.4

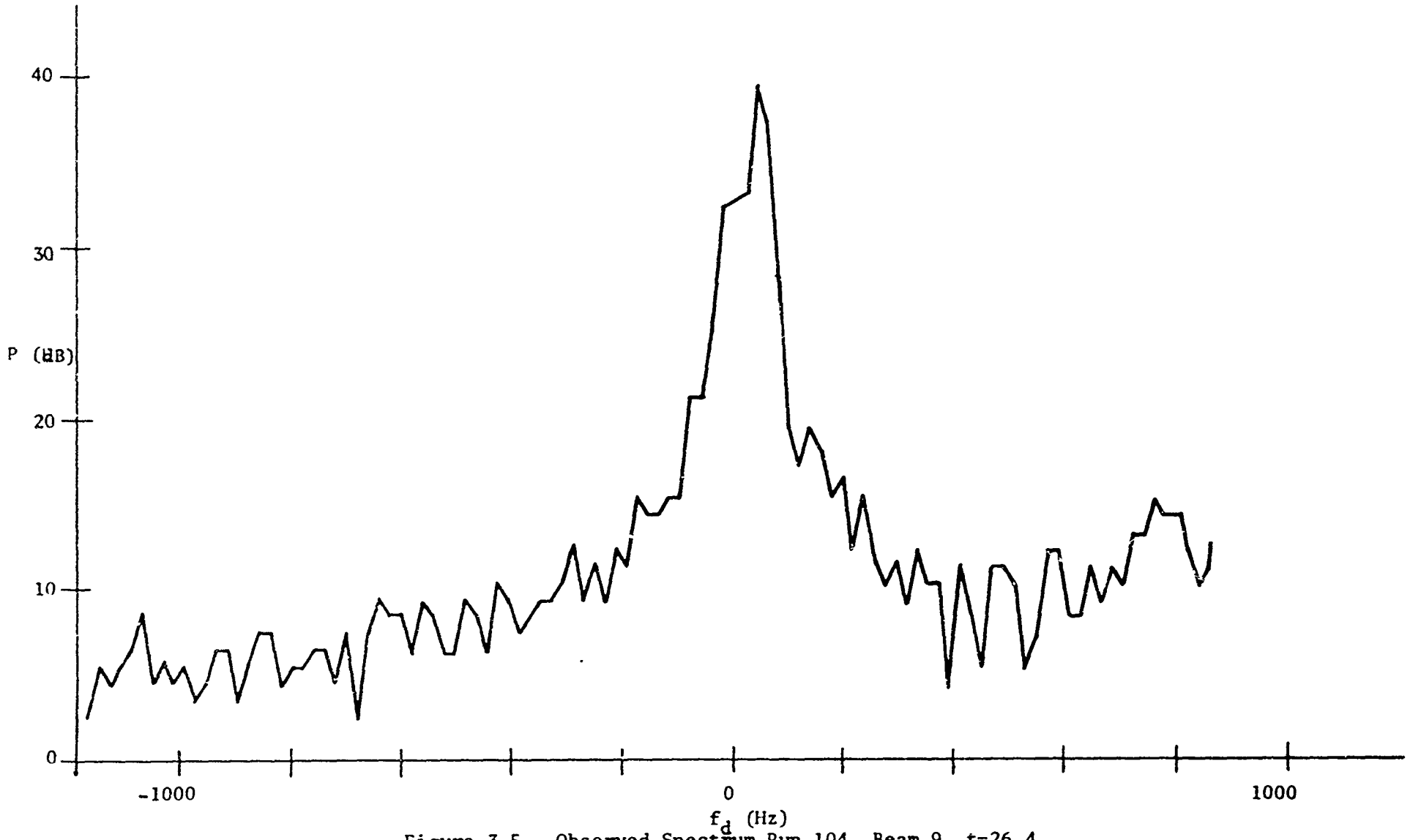


Figure 3-5. Observed Spectrum, Run 104, Beam 9, t=26.4

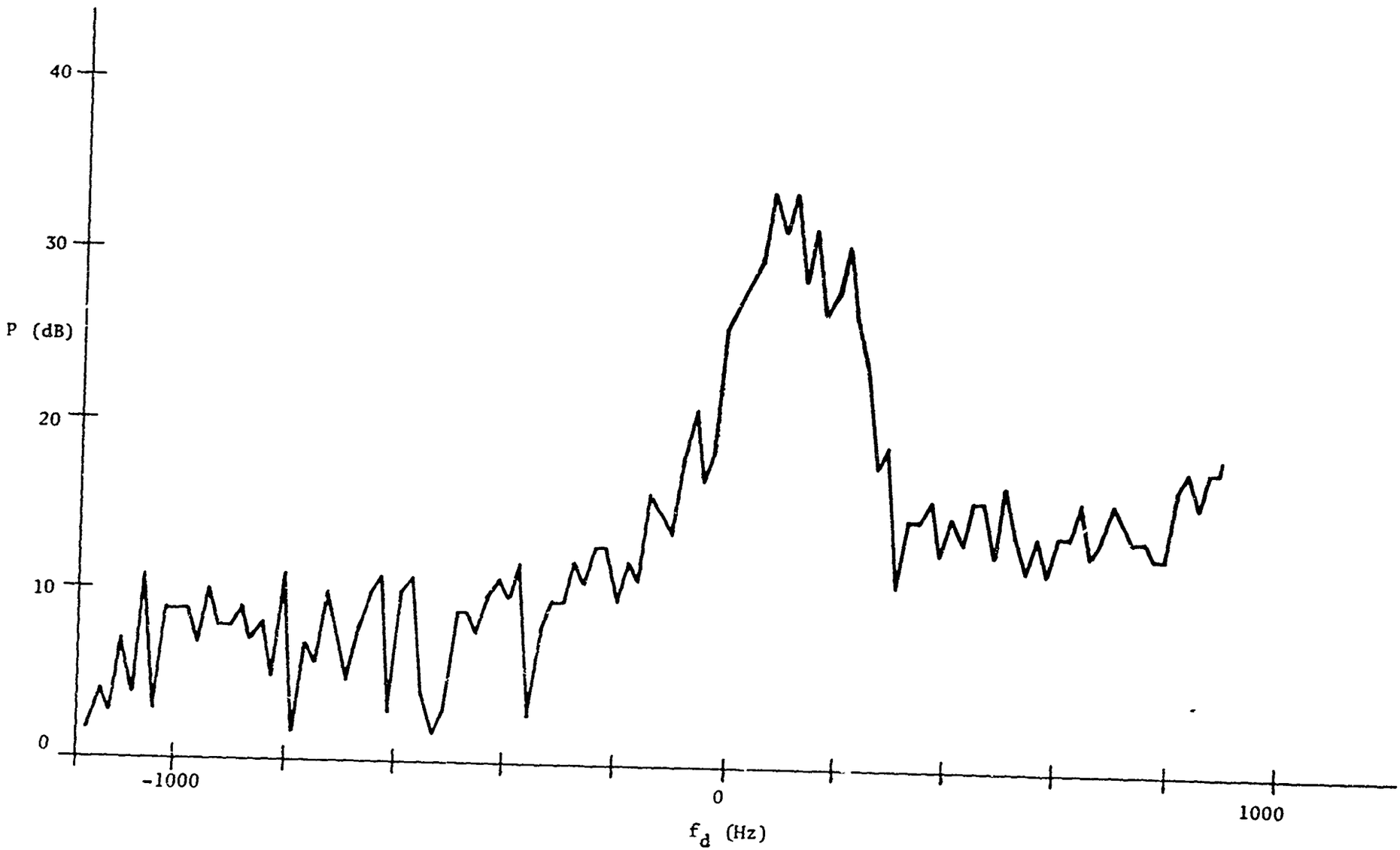


Figure 3-6. Observed Spectrum, Run 104, Beam 9, t=27.7

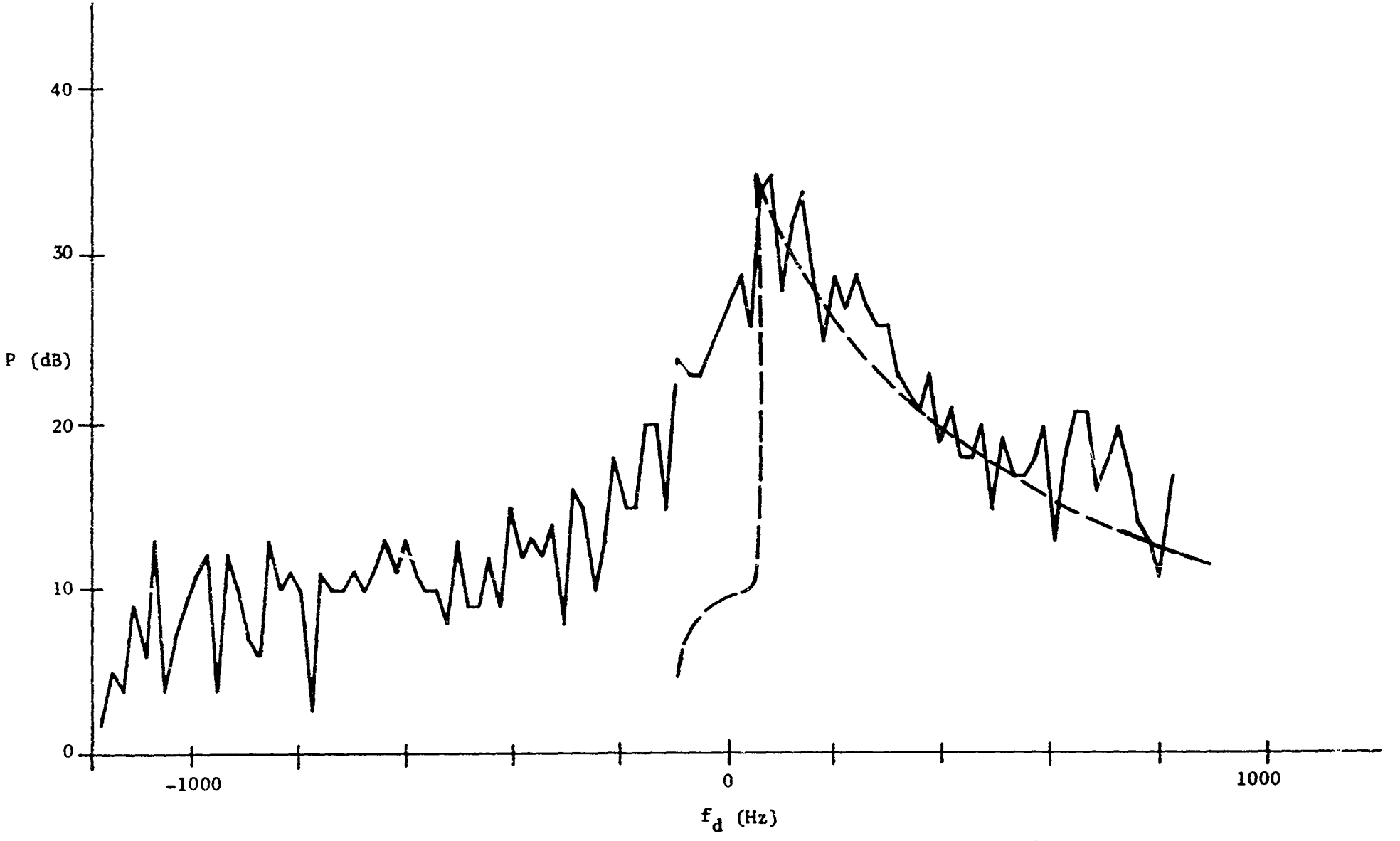


Figure 3-7. Observed Spectrum, Run 104, Beam 9, t=28.3

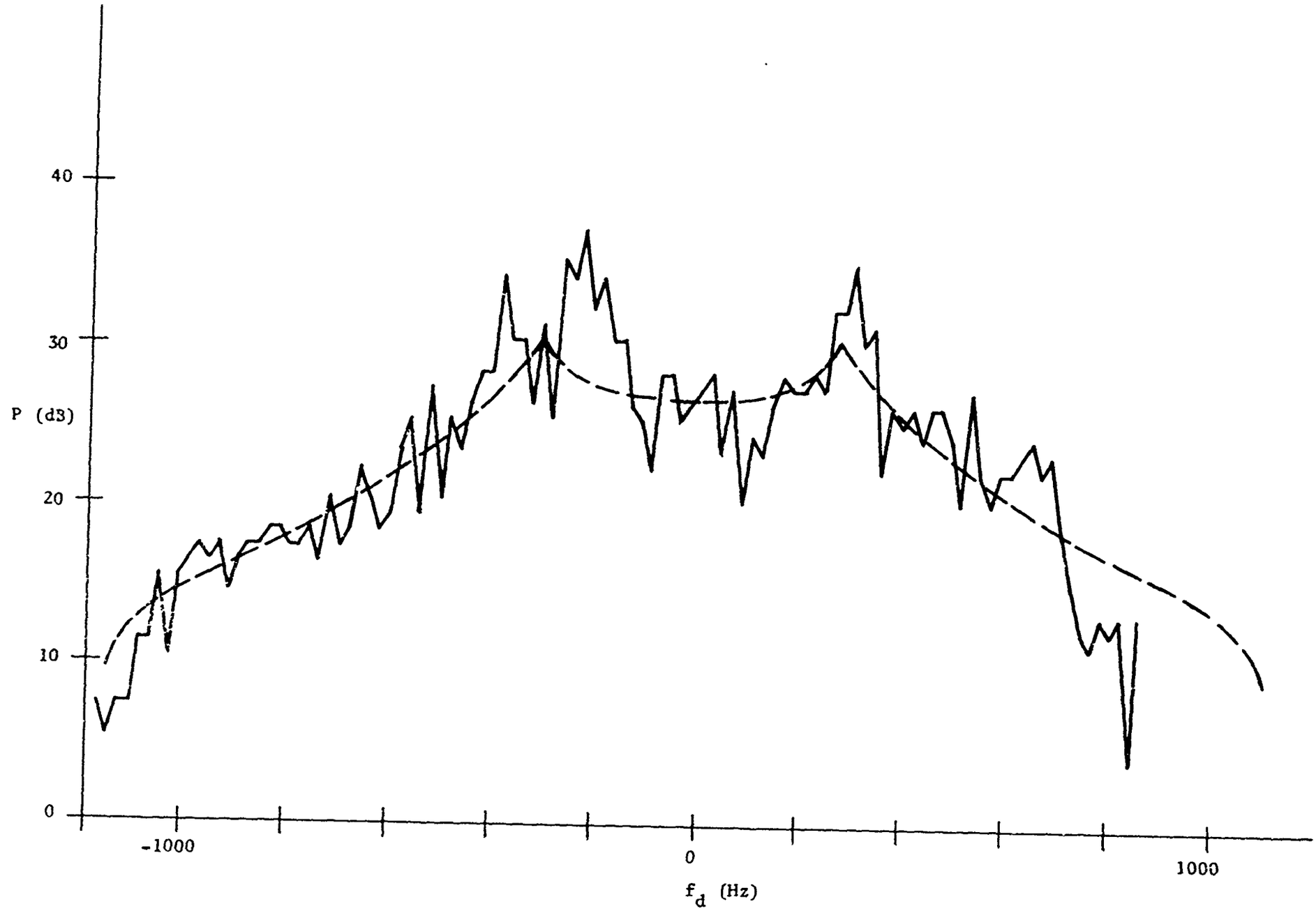


Figure 3-8. Observed Spectrum, Run 104, Beam 9, t=28.9

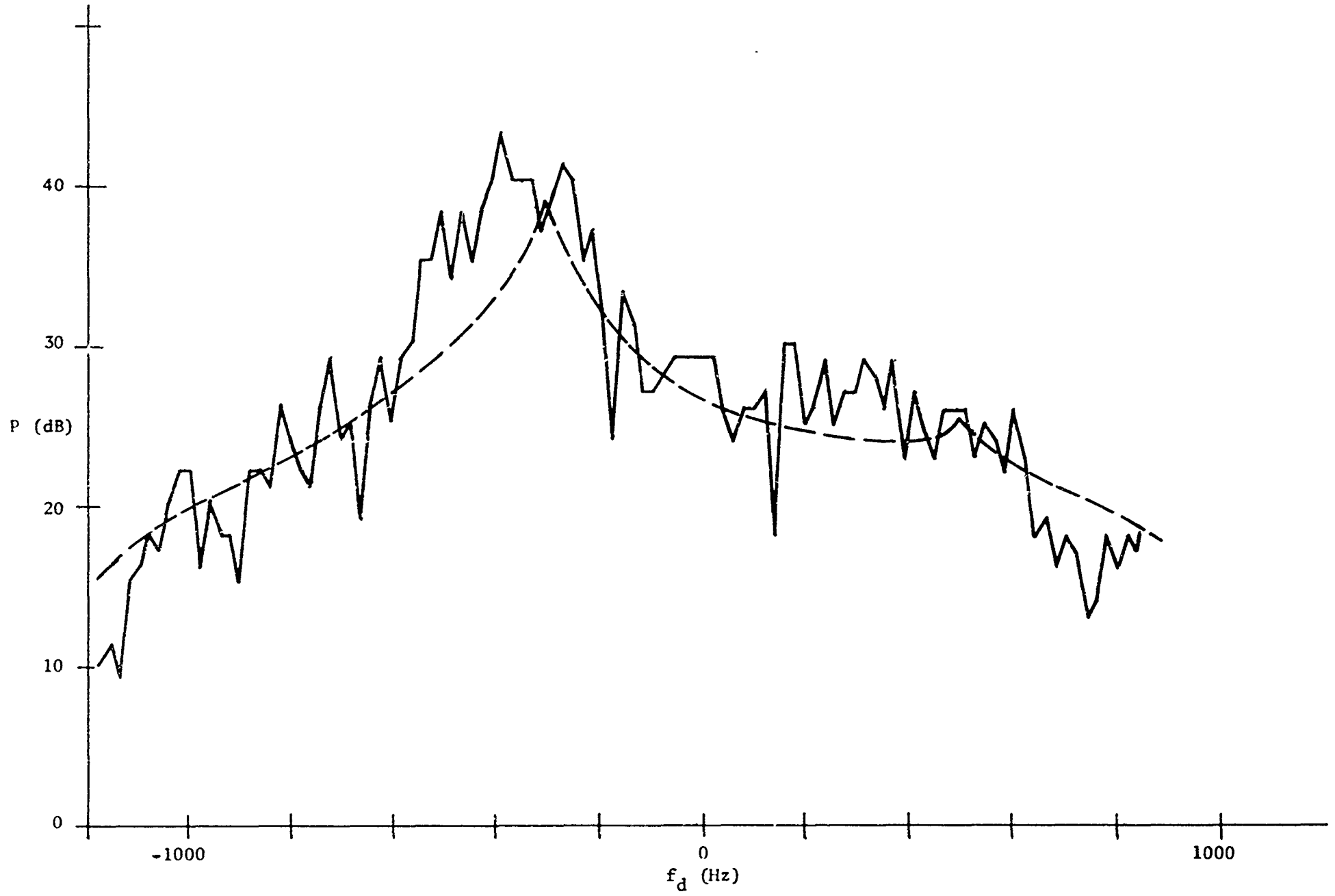


Figure 3-9. Observed Spectrum, Run 104, Beam 9, t=29.1

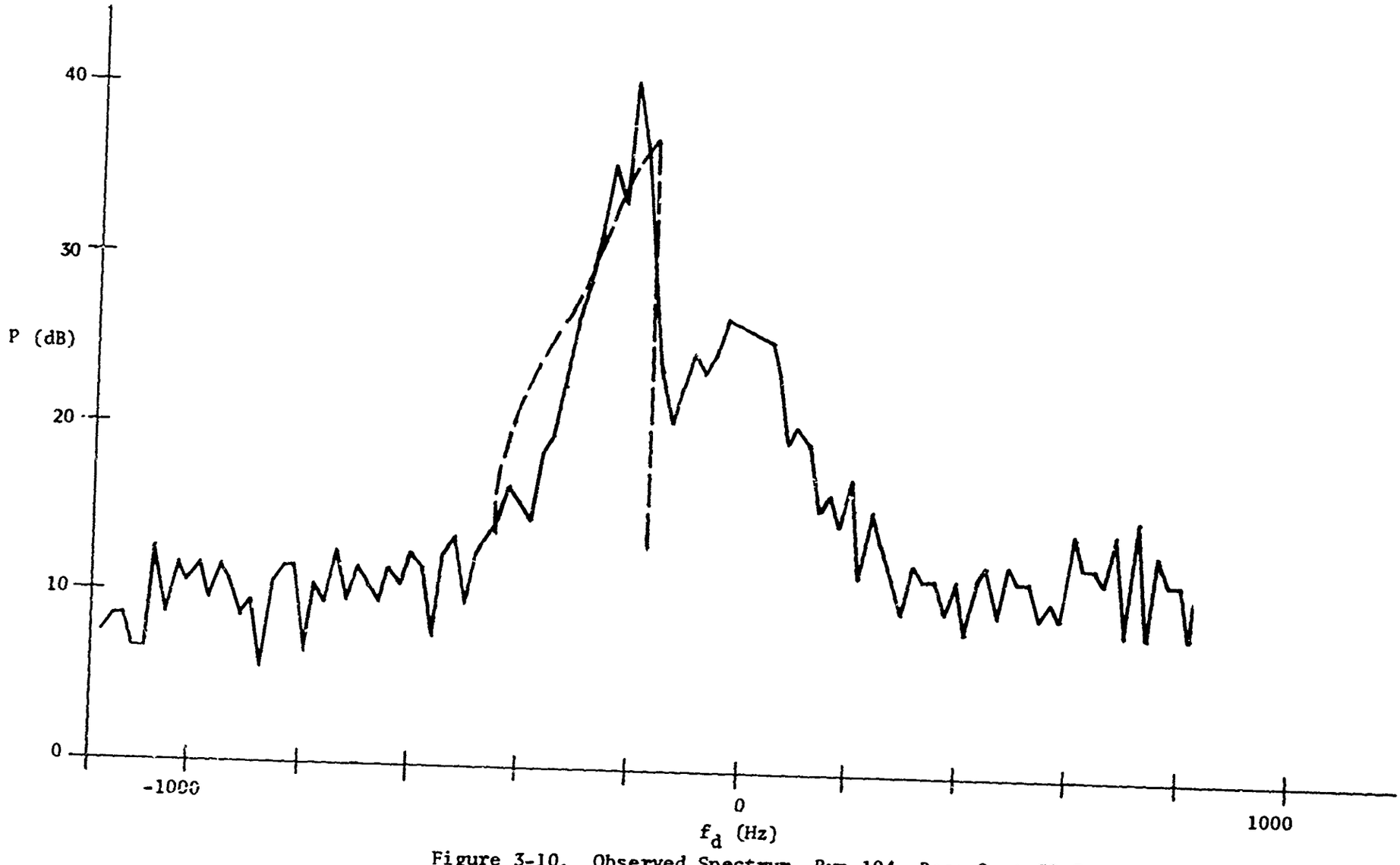


Figure 3-10. Observed Spectrum, Run 104, Beam 9, t=30.3

The matches between the two sets of figures is quite good, considering the simplifying assumptions used in the model calculations.

Figure 3-11 shows the symmetric spectrum from Run 13. Many of the runs showed spectra which, like this one, had no pronounced peaks such as the ones in Figure 3-8. This is the characteristic to be expected when the core passes through the observation volume at some distance from its center. That is the case considered in the model spectrum of Figure 2-9, which is redrawn in Figure 3-11 with its velocity scale compressed slightly. Figure 3-12 is the spectrum for Run 83, which shows least evidence of peaks or shoulders; the conjecture that it passed far from the center of the beam was checked by examining the neighboring beams. Indeed, the spectrum in one of these was virtually the same as shown in Figure 3-12, thereby lending further weight to this interpretation of the spectral shape.

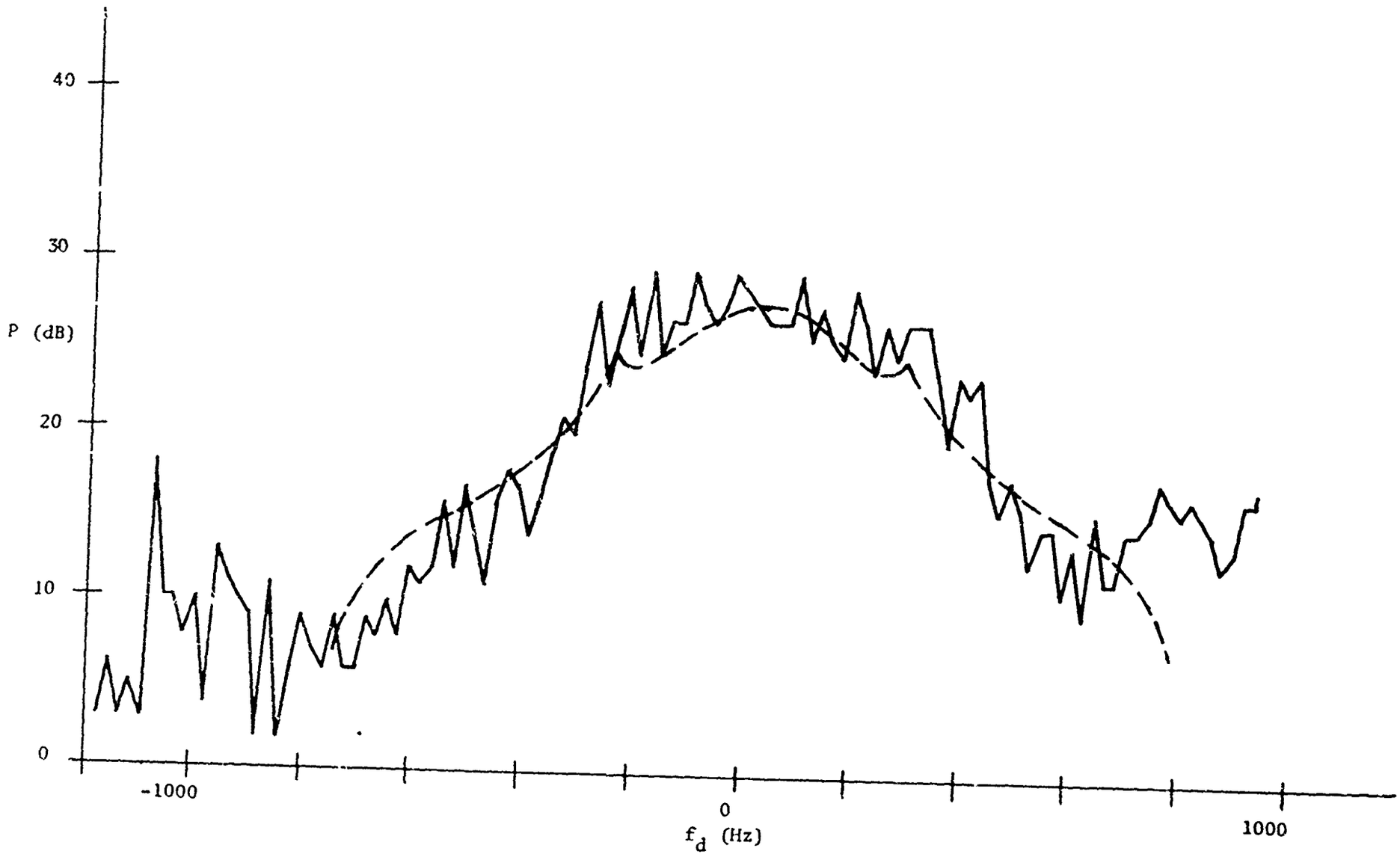


Figure 3-11. Observed Spectrum, Run 13, Beam 3, t=16.9

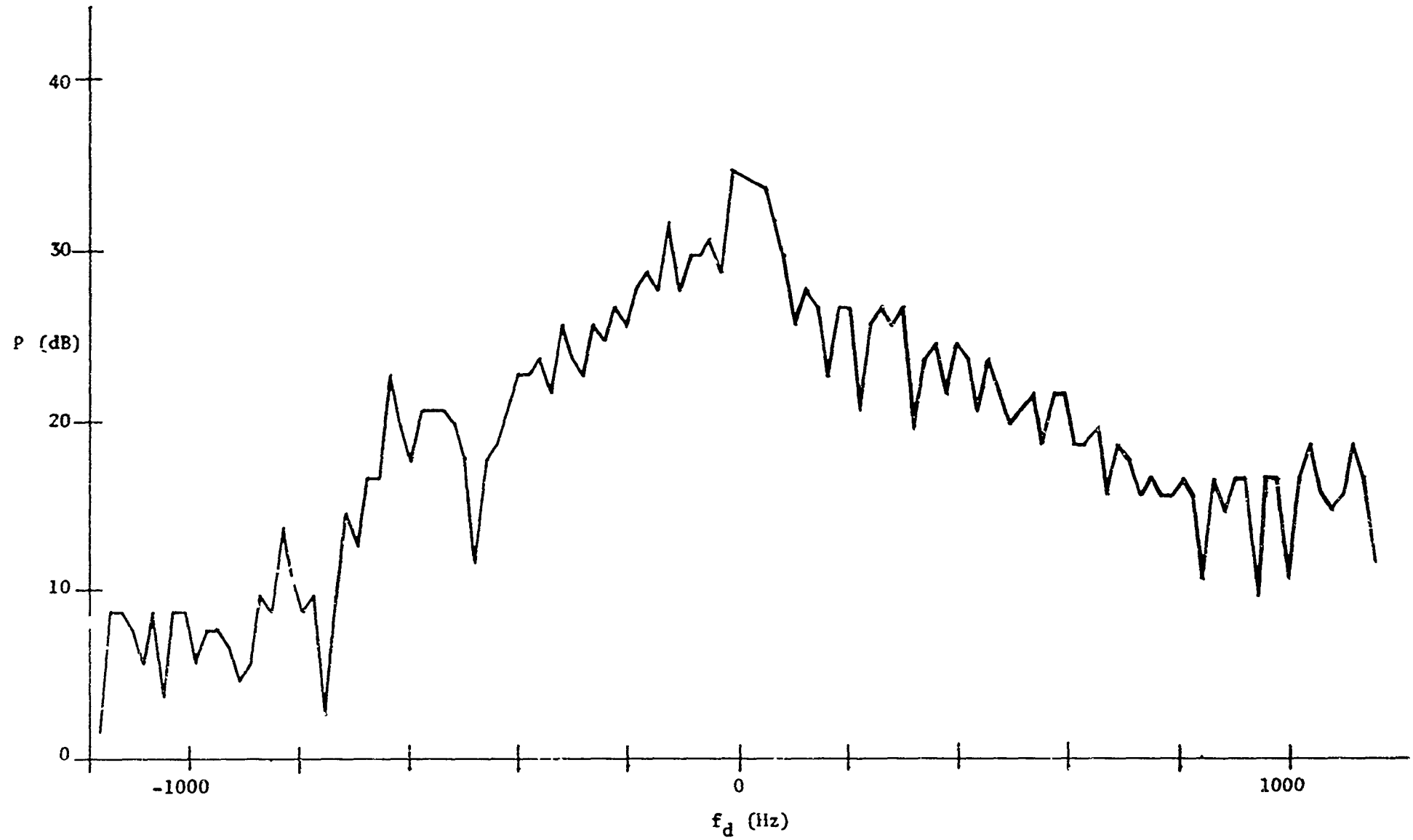


Figure 3-12. Observed Spectrum, Run 83, Beam 8, t=39.1

## 3.4 Proposed Discriminants

The effectiveness of a warning system rests ultimately on its ability to provide an assessment of the threat with sufficient reliability and accuracy so that appropriate action can be taken to nullify the threat with high confidence. The central issue in threat assessment is the process of discrimination, which is the procedure for estimating the severity of the threat from the observables.

### 3.4.1 Basis of Discrimination

In the case of a vortex threat to an aircraft, full analysis of the hazard involves not only some description of the vortex flow that characterizes its severity, but also the reaction of the aircraft in encountering the flow. The latter type of calculation is not included in this study. It appears from other work[13] however that to the level of current capability to analyze aircraft-vortex interaction, the most practical first-order description of the threat is given by the circulation of the vortex over a scale comparable to the wingspan of the encountering aircraft, since to first order that quantity will determine the applied rolling moment. The aim of this discrimination analysis is therefore to estimate the vortex circulation over a scale of many feet.

The distinction between circulation over a relatively large scale and other vortex descriptions such as core size and maximum velocity is an important one. It is illustrated in Figure 3-13, which shows schematically three radial velocity profiles and their corresponding profiles of circulation $\Gamma(r)$ contained within a distance r from the center. Upon comparing profiles 1 and 2, it can be seen that profile 2 represents a much more compact core containing much higher peak velocities than does profile 1. On the other hand, at the radius R of interest, both vortices have the same velocity, hence the same circulation and corresponding threat. Vortex profile 3 has a peak velocity considerably lower than than of vortex 2, but can be seen to be a much greater threat because of its much greater circulation over the scale of interest. In other

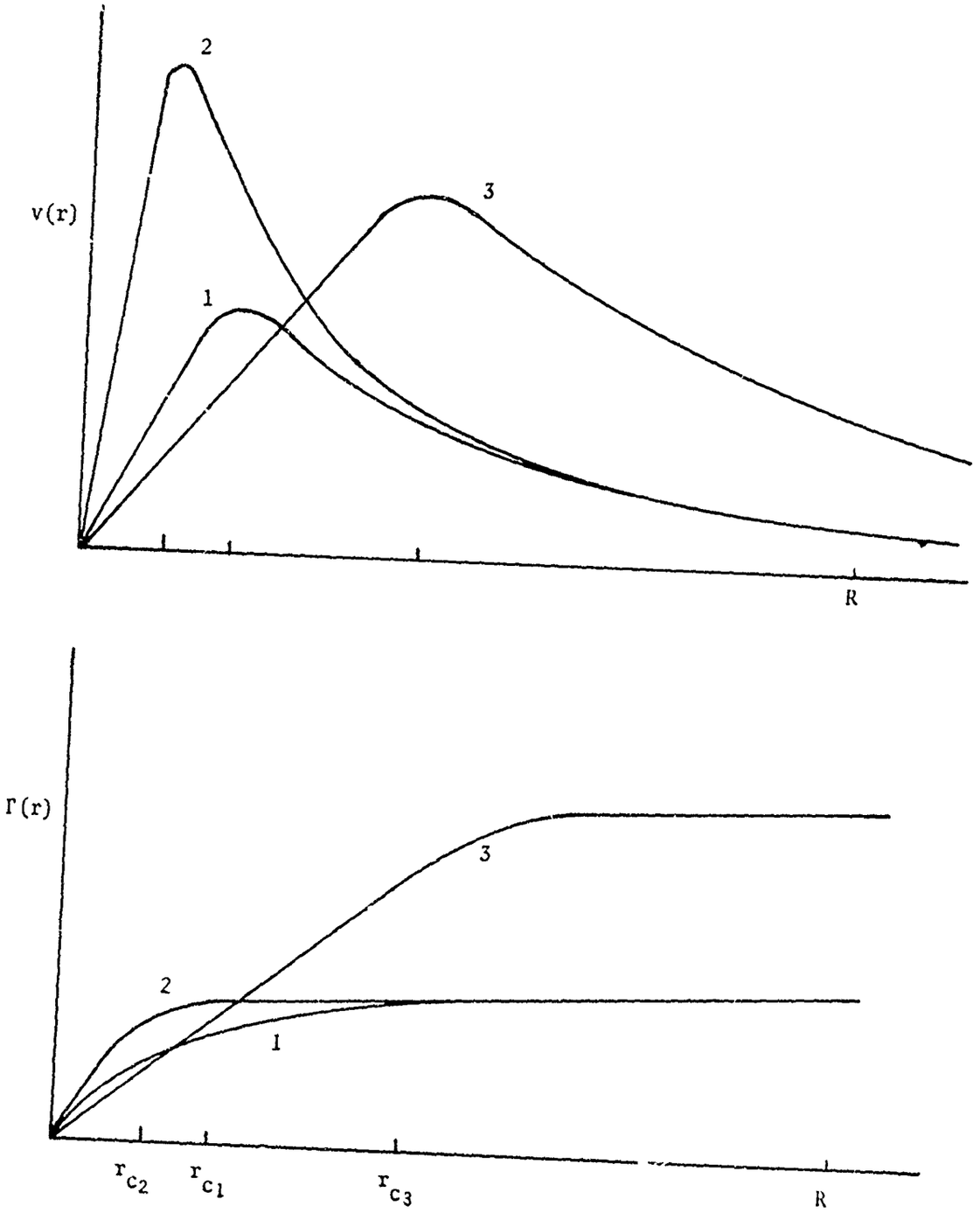


Figure 3-13. Three Schematic Vortex Tangential-Velocity Profiles and Their Corresponding Radial Circulation Profiles

words, small-scale vortex properties such as core parameters may be irrelevant, indeed misleading, as discriminants of the threat.

This discussion is not intended to discourage the study of fine-scale vortex structure with high-resolution instruments. Such study is invaluable in attempting to understand the dynamics of vortices and relate the vortex properties to details of the generating aircraft and the atmospheric environment. It is important to emphasize the difference in goals between a program aimed at understanding physical phenomena and one aimed at a system application of the phenomena. While they can (and ideally do) have much in common, they do not coincide. In fact, very effective system designs can and have been made on the basis of heuristic or limited understanding of the detailed phenomena.

With this in mind, this section concentrates on those aspects of the model and data that bear upon the question of estimating vortex circulation at radii generally greater than that of the core.

### 3.4.2 Discrimination in Scattering Volumes Containing the Core

Attempting to derive the circulation from the spectrum of the signal including scattering from the core is the severest discrimination test, since all the complications of the spectral structure as well as sensitivity of that structure to details of vortex position, beam shape, etc., are emphasized in this situation. Certain features of the spectrum suggested by the model studies should however provide the basis for a discriminant here. While the size of the observation volume in the tower tests is small compared with the distances of interest, perhaps the estimation of the small DC-7 vortices in that small volume will provide insight into the more realistic problem of a full-size core in an operational scattering volume, which will have a dimension commensurate with the desired distance.

The following approach has been employed to extract the value of the circulation from observed spectra. The time development history of the spectra for the resolution cell whose spectra show maximum frequency spread is studied. The particular spectrum from the time history which most nearly conforms to the centered configuration is selected for analysis. The Doppler frequencies corresponding to maximum amplitude are measured when the spectrum shows two peaks (see for example, Figure 2-8). When the peak response of the spectrum appears flat, the frequencies are measured where the average slope of the spectrum appears to be discontinuous (see for example, Figure 3-11). The average value of the absolute frequencies, $\bar{f}$, i.e., half the spread between the two points, is computed, as is the corresponding velocity.

The identification of this peak or shoulder velocity with the velocity at the effective edge of the beam, i.e., at a radius $R_o$, has been made in Section 2.2 on the basis of the model. Since the value $R_o$ is known from the system configuration, it is a straightforward matter to compute an estimate of circulation at that radius by the expression

$$\frac{\Gamma(R_o)}{2\pi} = R_o \, v(R_o) \ , \tag{3-1}$$

where $v(R_o)$ is derived from the observed doppler shift in the standard manner.

Table [illegible] lists 16 DC-7 runs which were analyzed to obtain estimates of circulation. Each run number is followed by a 1 or 2, denoting which vortex is considered, by the aircraft configuration for that run (L = landing, T = take-off) and the central beam. The next column gives the measured vortex velocity $v(R_o)$ estimated by the procedure just described.

Table 3-1. Estimates of Vortex Velocity for Centered Vortices

| Run | Beam | Configuration | $v(R_o)$ (ft/sec) | $\frac{U}{U_o}\frac{\Gamma(R_o)}{2\pi R_o}$ ($ft^2$/sec) |
|---|---|---|---|---|
| 13-1 | 3 | T | 25 | -- |
| 89-1 | 6 | L | 28 | 30 |
| 89-2 | 11 | L | 31 | 33 |
| 94-1 | 4 | T | 21 | 24 |
| 104-1 | 9 | L | 27 | 29 |
| 139-1 | 8 | T | 30 | 32 |
| 144-1 | 5 | T | 32 | 34 |
| 146-1 | 4 | L | 23 | 24 |
| 148-2 | 11 | L | 23 | 23 |
| 174-2 | 6 | T | 36 | 39 |
| 176-2 | 10 | T | 30 | 32 |
| 180-2 | 3 | L | 30 | 31 |
| 184-1 | 8 | L | 36 | 36 |
| 187-1 | 4 | T | 22 | 23 |
| 194-1 | 7 | L | 40 | 41 |
| 196-2 | 7 | L | 30 | 30 |

In accordance with the expected dependence (see equation (2-3)) of circulation on (the known) aircraft velocity, estimates of the circulation at $R_o$ are given in the final column of Table 3-1, normalized to a standard velocity of 118 kts (200 ft/sec) and to $R_o$ itself. It is easily seen that the tabulated quantity is just $(U/U_o)\ v(R_o)$.

A related case of special interest occurs when the vortex center is located just at the edge of the observation volumen, i.e., $r = R_o$ or $\xi = 1$, the model of which is given in Figure 2-5. The feature that makes this situation recognizable by examination of the series of spectra is that it marks the appearance of doppler components on the opposite side of zero from the side they occupied previously. This of course corresponds to the appearance in the observation volume of the oppositely directed air motion on the other side of the vortex center. It can be shown that for this situation the peak spectral return occurs (again see Figure 2-5) at the velocity $v(2R_o)$. While this procedure cannot be said to afford quite the same degree of confidence as the preceding one for estimating $v(R_o)$, it was carried out for most of the same runs. The results are listed in Table 3-2.

Returning to the discrimination application, it can be seen in Tables 3-1 and 3-2 that the variation in velocity estimates covers a narrower range of values than do the estimates of maximum velocity for these same tests as given in reference 2. Perhaps more significant is that the estimates of maximum velocity, clearly related to core structure, separated into two distinct populations corresponding to landing and take-off configuration, while these estimates of velocity show no such correlation with configuration.

### 3.4.3 Discrimination in Scattering Volumes Not Containing the Core

In some respects, discrimination should be simplest when the velocity sample is taken at large distance from the core. The velocity change

Table 3-2. Estimates of Vortex Velocity at Zero Frequency Crossing

| Run | Beam | $v(2R_o)$ (ft/sec) |
|---|---|---|
| 89-1 | 6 | 22 |
| 89-2 | 11 | 25 |
| 94-1 | 4 | 16 |
| 104-1 | 9 | 20 |
| 139-1 | 8 | 29 |
| 144-1 | 5 | 20 |
| 146-1 | 4 | 22 |
| 148-2 | 11 | 24 |
| 150-1 | 3 | 24 |
| 174-2 | 6 | 19 |
| 176-2 | 10 | 17 |
| 180-2 | 3 | 19 |
| 187-1 | 4 | 23 |
| 194-1 | 7 | 18 |
| 196-2 | 7 | 20 |

over a distance the size of an observation volume is relatively small, leading to a clearer measurement of the doppler shift. For the DC-7 tower tests under review, the most straightforward interpretation would be made by examining the spectra in the channel that does contain the core, but at times before and after the passage of the core through the observation volume. These spectra represent the vortex returns from regions removed from the core and where the flow is predominantly vertical, so that the doppler component is the full tangential velocity. Conversion of the time scale to a distance is accomplished through multiplication by a drift velocity, as described below. For the small-scale DC-7 vortices, this is a rather tricky process, since the range of radii that are large compared with the core radius, yet over which the vortex velocity is considerably larger than the wind velocity, is quite limited.

This procedure was carried out for a number of tests, listed in Table 3-3. The radial distance from the center of the vorte is obtained by recording the times when the off-center vortex spectrum is measured and when the vortex is centered within the resolution cell. R is determined by multiplying the time difference by the translational velocity of the vortex. The latter quantity is gotten by dividing the diameter of the resolution cell by the time difference between zero frequency crossings in the time development history of the spectra associated with the vortex. The tangential vortex velocity at the radial distance R is obtained by measuring the frequency associated with maximum amplitude in the spectrum at the time corresponding to R. The frequency, when substituted into the Doppler equation, yields the velocity. T ambiguity in the position of the zero Doppler frequency due to the wind was taken into consideration by averaging the frequencies associated with maximum amplitude before and after the vortex had passed through the resolution cell at times separated by equal intervals from the centered time. The circulation in column 5 is computed from the product of R and v in columns 3 and 4.

Table 3-3. Estimates of Velocity and Circulation for Vortices Outside the Resolution Cell

| Run | Beam | $R/R_o$ | v (ft/sec) | $\Gamma/2\pi R_o$ (ft/sec) |
|---|---|---|---|---|
| 13-1 | 3 | 2.5 | 18 | 45 |
| 89-1 | 6 | 2.0 | 23.5 | 47 |
| | | 4.0 | 10 | 40 |
| 89-2 | 11 | 2.5 | 17 | 42 |
| | | 3.8 | 14 | 53 |
| 94-1 | 4 | 2.5 | 14 | 35 |
| | | 3.8 | 17 | 64 |
| | | 4.2 | 15 | 63 |
| 104-1 | 9 | 2.0 | 20 | 40 |
| | | 2.5 | 17 | 43 |
| | | 3.1 | 14 | 43 |
| 139-1 | 8 | 2.4 | 16.5 | 39 |
| | | 6.4 | 11 | 70 |
| 144-1 | 5 | 4.0 | 15 | 60 |
| 146-1 | 4 | 2.8 | 18 | 50 |
| 148-2 | 11 | 3.8 | 16 | 61 |
| | | 5.4 | 11 | 60 |
| 150-1 | 3 | 4.3 | 14 | 60 |
| | | 7.1 | 9 | 64 |
| 176-2 | 10 | 2.5 | 12.5 | 31 |
| 187-1 | 4 | 5.1 | 13 | 65 |
| 194-1 | 7 | 3.4 | 9.5 | 33 |
| 196-2 | 7 | 4.3 | 11 | 47 |
| | | 5.6 | 9 | 50 |

Figure 3-14 displays the measured circulation as a function of radial distance from the vortex center, both quantities normalized to $R_o$. The circulation values given in Table 3-3 are the circled points. Also plotted in Figure 3-14 at $R_o$ and $2R_o$ are the mean values and standard deviations of the estimated circulations obtained in Tables 3-1 and 3-2. It is observed that the circulation values in Table 3-3 appear to be radially dependent, generally increasing with radial distance. (Note particularly runs 94, 104 and 139, where estimates were made at different times for the same vortex.) This increase would not occur if the tangential vortex velocity decreased inversely with radial distance outside the core.

Two curves are drawn through the data plotted in Figure 3-14. One is of the form given by equation (2-6) for the velocity according to the Betz model. The other follows the logarithmic form in equation (2-8) of the Hoffmann-Joubert model. No definitive choice can be made on the basis of these results. The total circulation $\Gamma_o$ may be derived from these curves by assigning a value to $R_o$, the radius of the observation volume. Since the dish that generates the transmitted beam is 10 ft in diameter, and from comparison of acoustic results with the NAFEC probe data (see Section 4.2), it appears that $R_o$ = 5 ft represents the best estimate. The total circulation (divided by $2\pi$) is then seen to grow to an ultimate value of just over 300 $ft^2$/sec, with values of about 210 $ft^2$/sec and 290 $ft^2$/sec at radii of 10 and 20 ft respectively. The value of total circulation computed from equation (2-3) for the DC-7 at our standard velocity is 310 $ft^2$/sec.

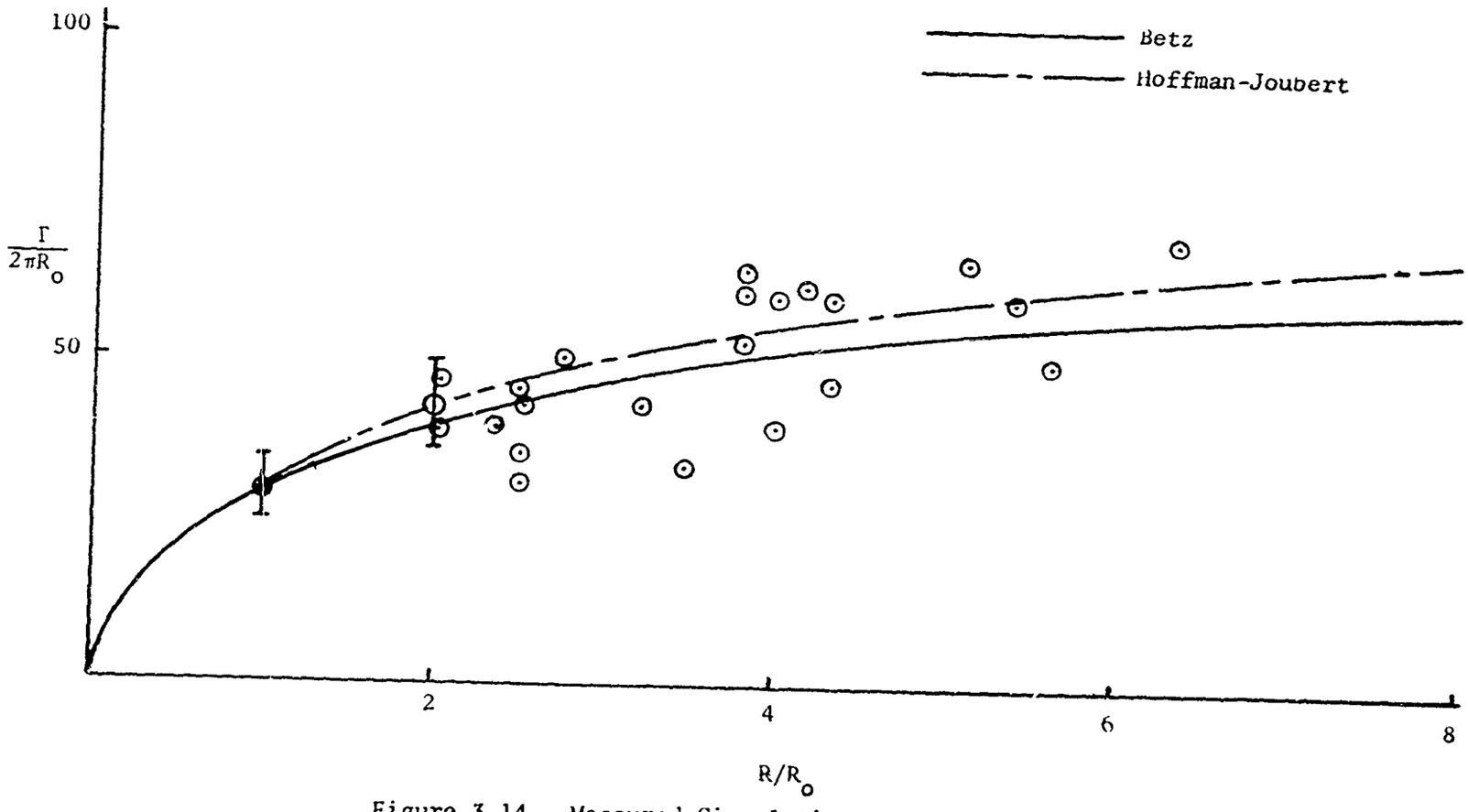


Figure 3-14. Measured Circulation as a Function of Radial Distance for DC-7

## 4. RECENT TOWER COMPARISON TESTS

A new series of tower comparison tests, i.e., observations both by the Xonics acoustic radar and by the NAFEC instrumented tower, of vortices generated by aircraft flying by the tower for that purpose, were conducted under the current effort during April and May 1972. The intent of these tests was primarily to supplement in two important respects the tests conducted last fall and the subsequent modeling analysis described in Sections 2 and 3. First of all, the hot-wire anemometer spacing of 4 ft that was employed on the tower at that time hampered the analysis of small-cored vortices because of the uncertainty in core location relative to the sensors. This situation was rectified by increasing the number of sensors so that the separation was reduced to 1 ft, thereby insuring coverage of even the smallest known cores. Second, and at least equally important, all of the earlier tests involved DC-7 vortices, and it was desired that aircraft with a large range of weights that would generate vortices of greatly different strength be included in the test program. This was done not only to observe the variations in character of the vortex structure and its scattering properties, but to determine the extent to which discriminants based on the observables could be tested for consistency and reliability. Unfortunately, the second objective was not fully accomplished for reasons to be given in the discussion that follows.

### 4.1 Test Description

The entire test configuration for the new series of tower tests as well as the data processing procedures were the same as those described in Section 3, with a few minor exceptions. As just noted, the NAFEC instrumentation was augmented so that the sensor separation was reduced to 1 ft. The acoustic transmitter that illuminated the vertical column of space parallel to the tower was moved to a distance of 30 ft from the tower (an increase of 10 ft) to reduce the effects of scattering

from the tower itself and noise generated on the tower, such as by smoke grenades. In addition, some modifications were made to the acoustic equipment, mostly aimed at reducing sidelobes of the receiving antenna so as to increase the observed signal-to-noise ratio of the vortex returns.

The original intention was to conduct a test series that would result in approximately 10 processed runs on each of three aircraft — one in the 100,000 lb class, one in the 300,000 lb class and one in the 600,000 lb class. The first was to be a DC-7, which would in addition provide a link of common data to the previous tests. The other aircraft were to be a C-141 and a C-5A, to be supplied by the Air Force for these tests. Testing was completed with a satisfactory quantity of data accumulated for both the DC-7 and the C-141. C-5A tests were conducted for one morning on which there was virtually no wind at all; the resulting data were very unsatisfactory, since the vortex structure is studied in this test configuration by both the acoustic and tower instrumentation through the regular translation of the vortex across the sensor. Subsequent tests to satisfy the requirement were found to be impossible because of Air Force operational exigencies.

Other tower fly-bys beside those originally planned were monitored by the acoustic equipment. A number of CV-880 tests were observed, as were some DC-9 tests being conducted for other purposes entirely.

In summary, the test schedule on which data were actually collected by the acoustic radar is as follows:

| Aircraft | Date(s) |
|---|---|
| DC-7 | 18, 19, 20 April |
| C-141 | 2 May |
| C-5A | 6 May |
| CV-880 | 1, 5 May |
| DC-9 | 11 May |

Prior to the testing period, a series of calibrations was executed to verify the antenna patterns and beam pointing angles for the receiving antenna. All of these were found to be close to the nominal values expected from the design. In addition, as a result of design changes in the receiving antenna feed, the far sidelobes at angles exceeding 45 degrees were found to be 40 dB below the response of the main beam. As a consequence, the measured noise level at the receiver was reduced by an estimated 10 dB or more compared with that in the previous set of tests. A number of tests were also conducted to determine the interference level produced by the noise from smoke grenades on the tower as a function of pointing angle of the receiving antenna with respect to the direction from that antenna to the tower. These too produced results that were consistent with the measured sidelobe pattern of the receiving antenna.

Data processing for these tests was carried out just as described in Section 3 for the earlier tests. For each run, the central beam, i.e., the one through which the center of the vortex passed, was identified by the greatest observed velocity excursions in the doppler spectrum. The data from the central beam, as well as two or more contiguous beam positions, were digitized for several seconds around the passage of the vortex core. Two-tenths-second segments were then spectrum-analyzed on a digital computer. The resulting individual power estimates with 5-Hz resolution were averaged in groups of 4 points each to arrive finally at doppler-velocity spectra with 20-Hz resolution, which were printed out for further analysis.

## 4.2 DC-7 Results

The appearance as a function of time of the DC-7 vortex spectra obtained in the earlier tests and their explanation in terms of the postulated model have been described in considerable detail in Sections 2 and 3. The spectra observed in this new series of DC-7 tests appeared in all respects to follow the same pattern, and differed only in having a

somewhat higher signal-to-noise ratio as a result of the antenna modification carried out during the intervening period.

An illustrative sequence of spectra, chosen from run 103, vortex 2, is shown in Figures 4-1 through 4-6. Figure 4-1 shows a very narrow peak corresponding to the downdraft velocity between vortices. (The other peak at zero doppler is due to the direct transmitter-to-receiver feedthrough-signal; it has been truncated for clarity in the remaining figures in this series.) As the (second) vortex core approaches the observation volume, the spectrum begins to extend toward higher velocities and spread in width as the range of velocities contained within the observation volume grows. This process is shown in Figures 4-2 and 4-3, and culminates in Figure 4-4, the case for the core close to the center of the observation volume. A most interesting feature of this spectrum is the peak at about -120 Hz, which is due to a coherent return from the strong gradient in index of refraction at the tight DC-7 core. This doppler shift therefore corresponds to the systematic translational velocity of the vortex, and the output thus provides this piece of tracking information as a byproduct of the coherent processing. Figures 4-5 and 4-6 continue and complete the sequence with the spectra observed just after and well after the passage of the vortex core.

Quantitative doppler frequency information was scaled off a number of these frames in two different ways (as was done previously in Section 3 for the earlier DC-7 data). For those cases well removed from the time when the core is centered in the observation volume, the spectrum is relatively narrow, and a distinct peak can be identified. Figures 4-1, 4-2 and 4-6 are clear examples of this situation. Figure 4-3 is only marginally within the category, due to the evident spreading, but a peak is still identifiable and has been included. The doppler frequencies so obtained are plotted as a function of time in Figure 4-7 for the second vortex of run 103. The second type of observation is associated with the centered core. For this vortex,

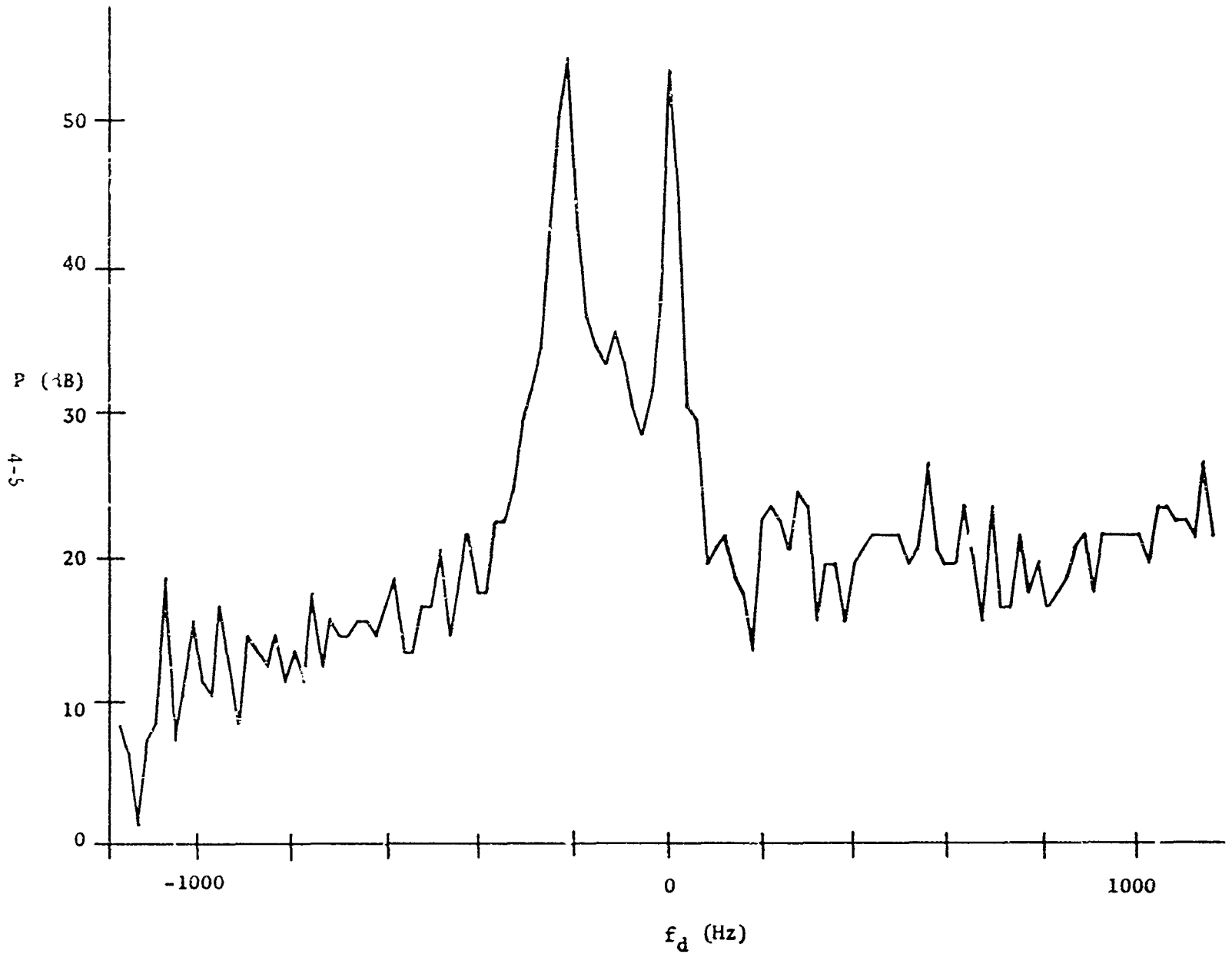


Figure 4-1. DC-7 Vortex Spectrum, Run 103-2, t = 14.2

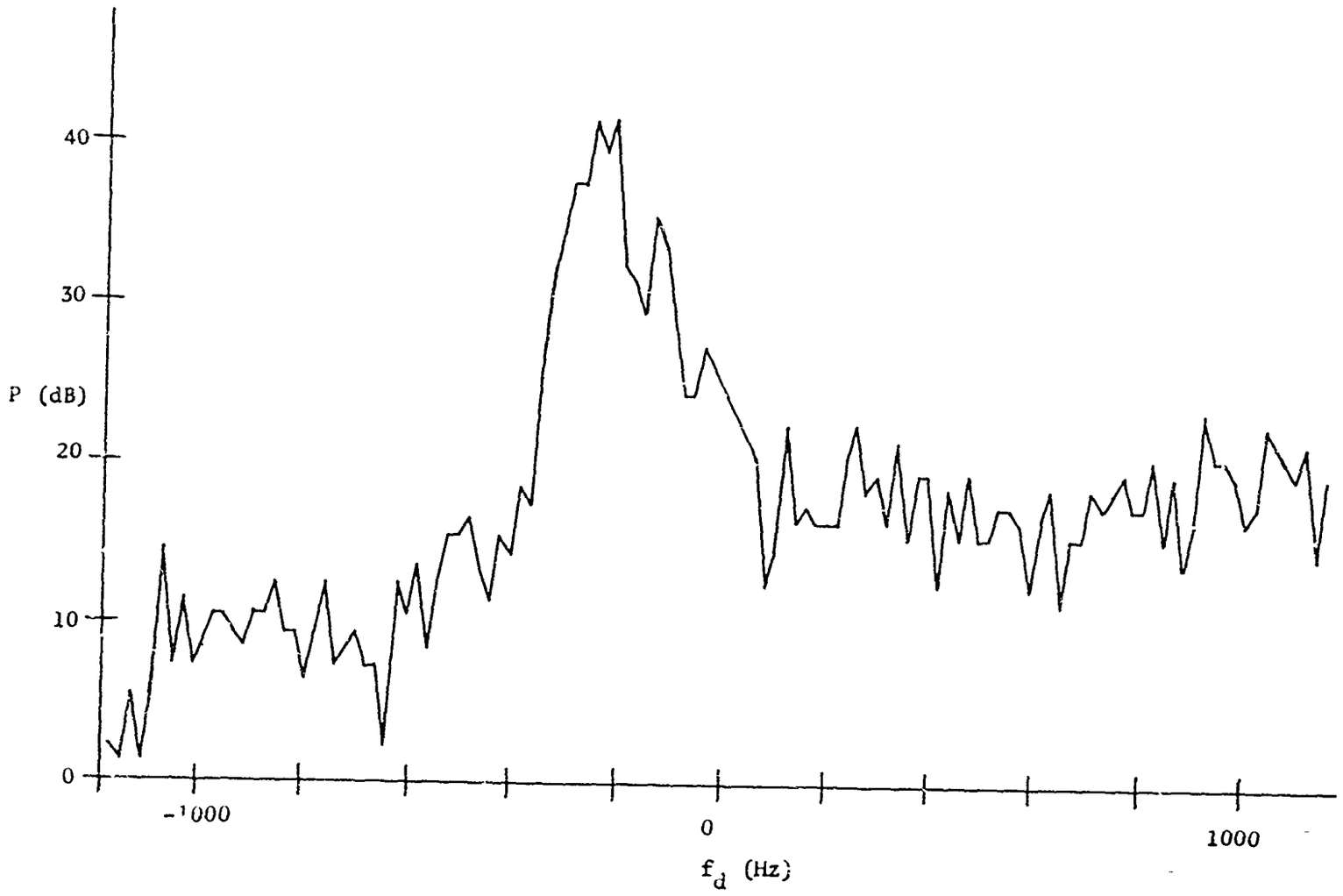


Figure 4-2. DC-7 Vortex Spectrum, Run 103-2, t = 14.6

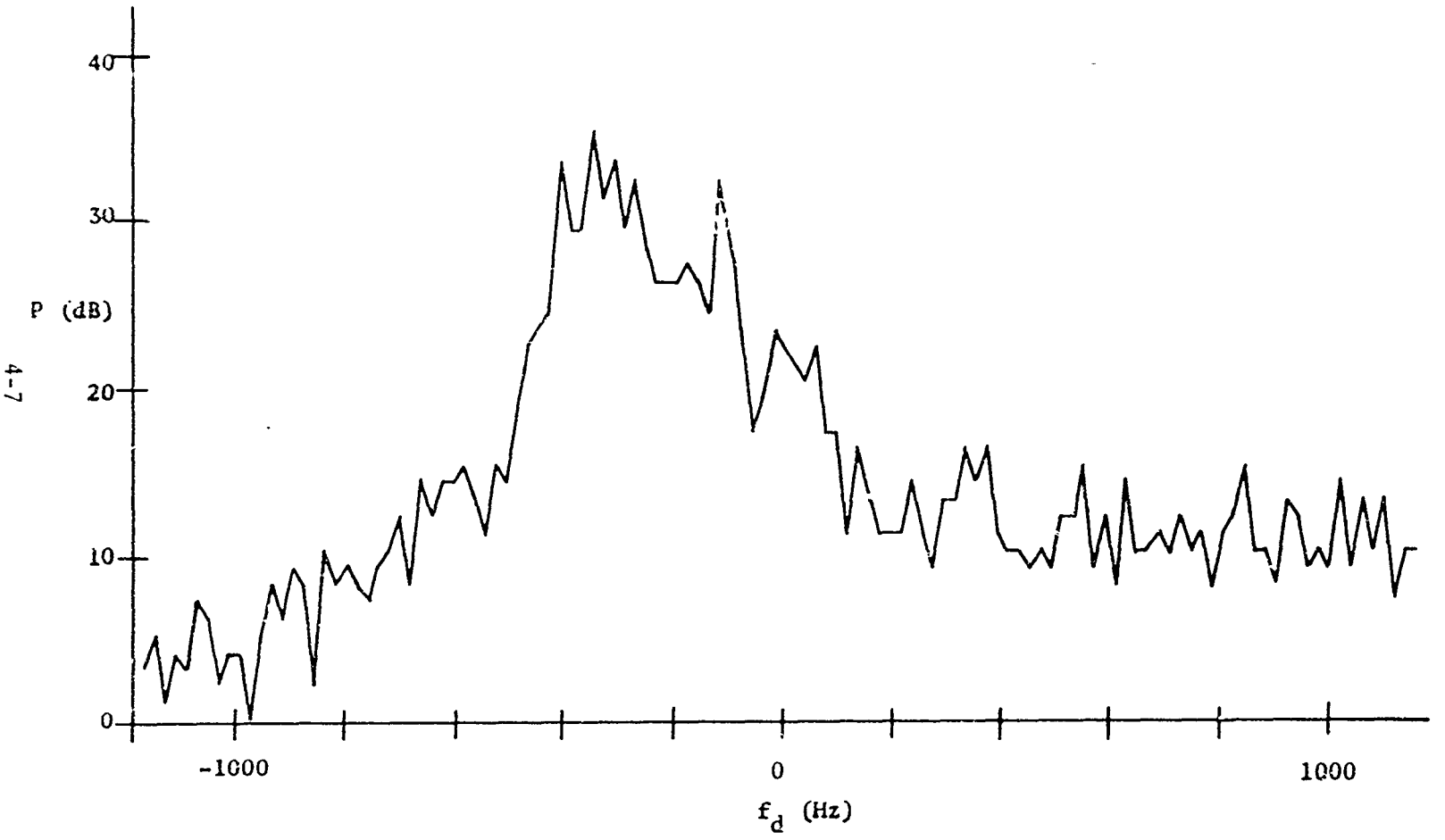


Figure 4-3. DC-7 Vortex Spectrum, Run 103-2, t = 15.0

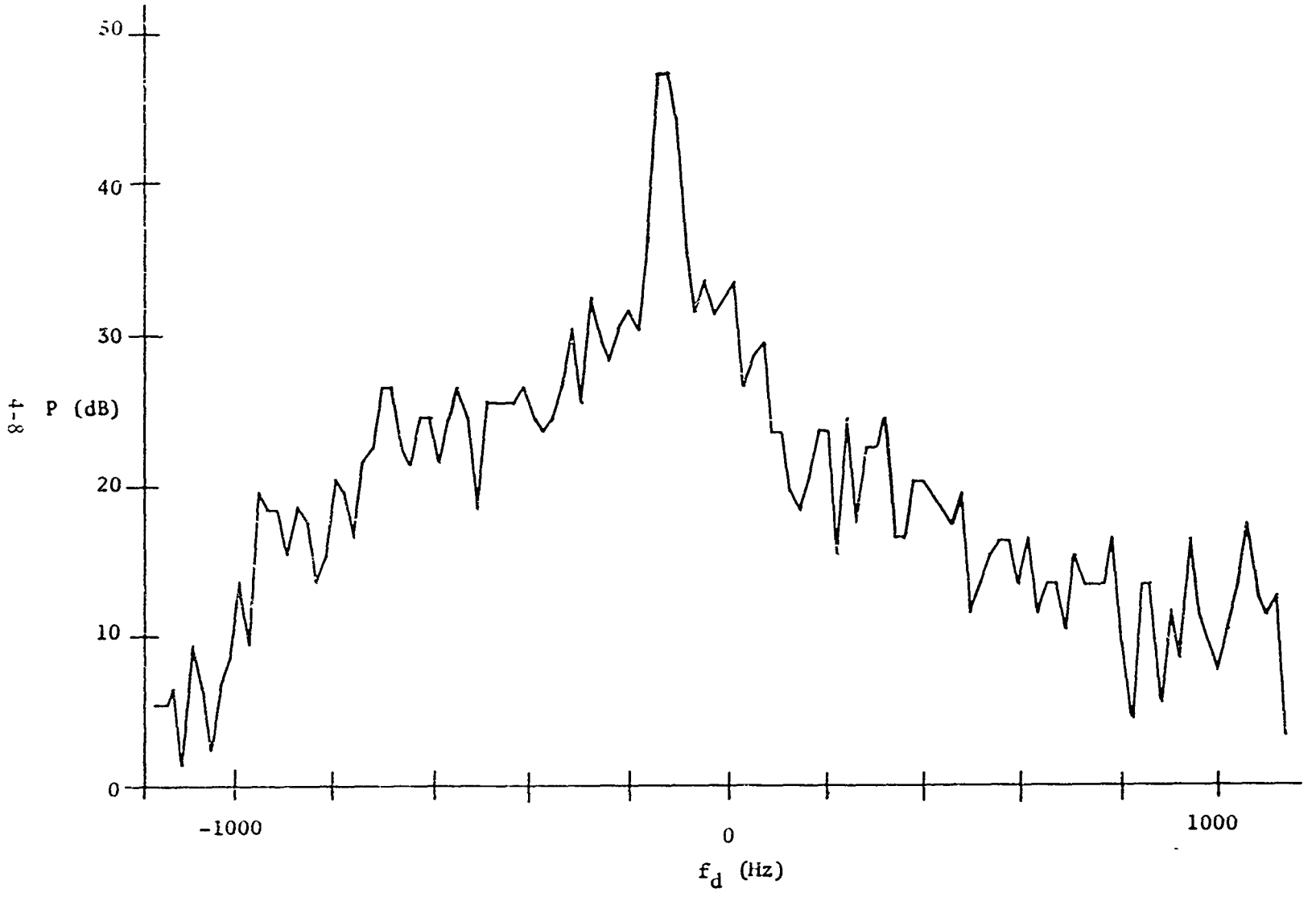


Figure 4-4. DC-7 Vortex Spectrum, Run 103-2, t = 15.4

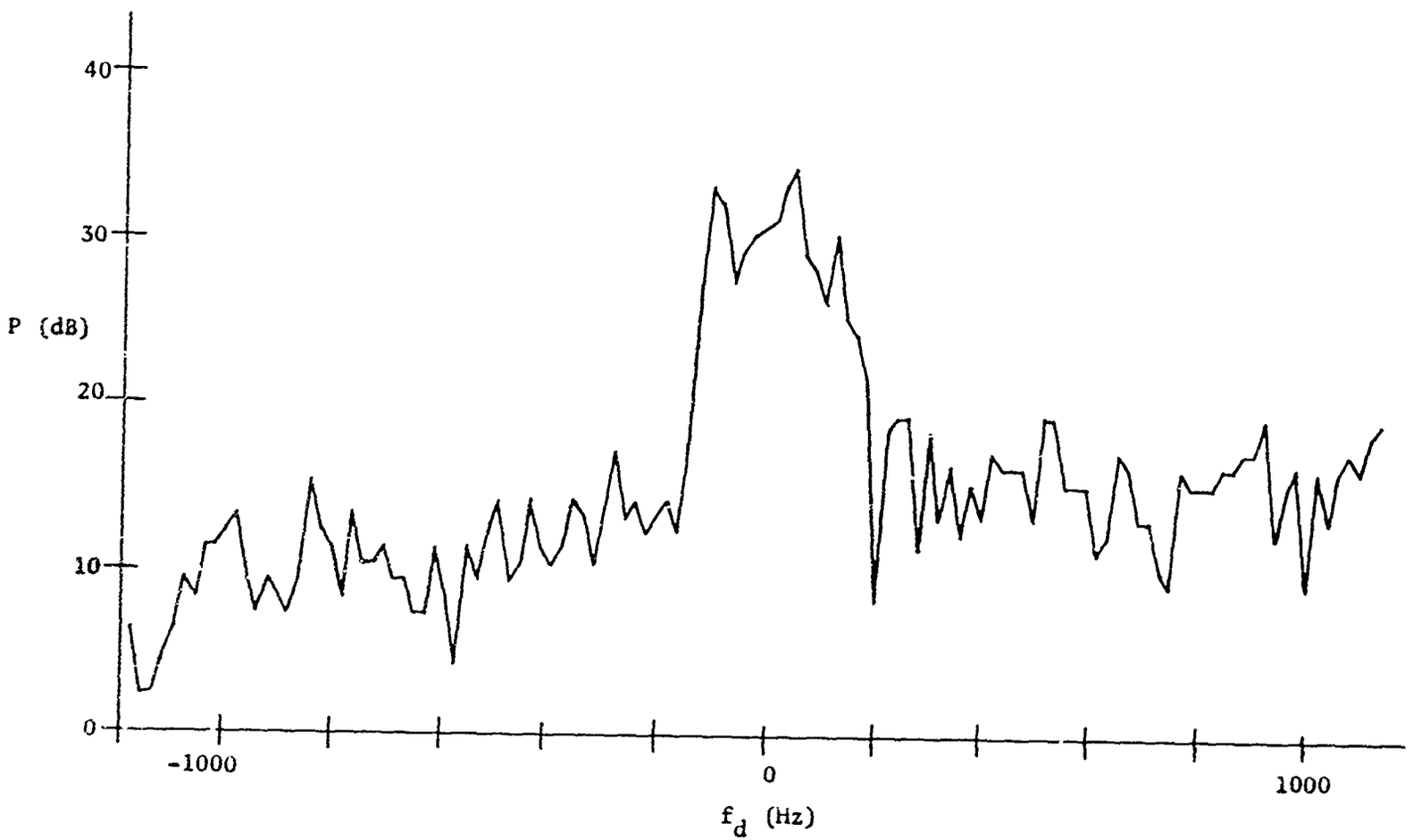


Figure 4-5. DC-7 Vortex Spectrum, Run 103-2, t = 15.8

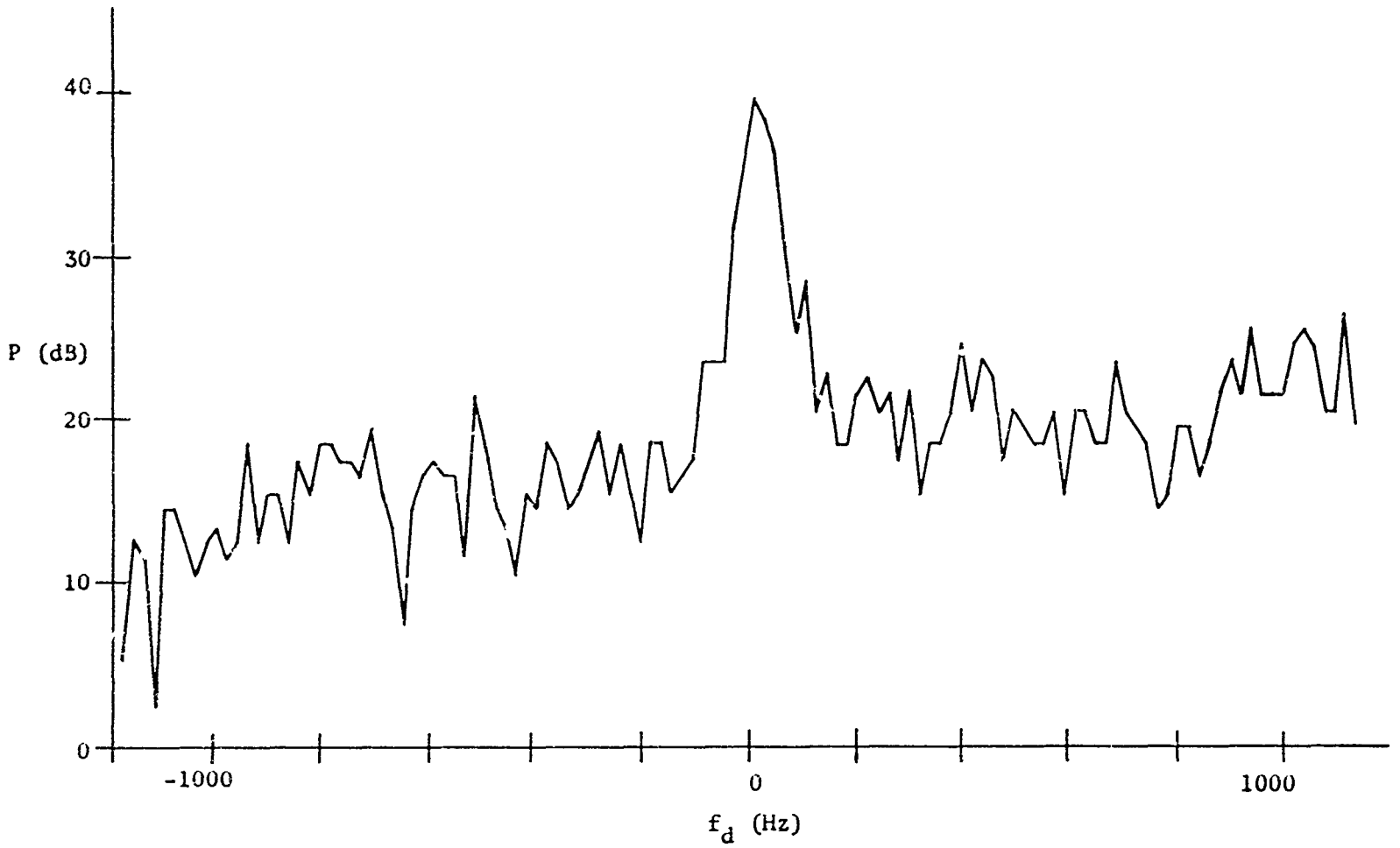


Figure 4-6. DC-7 Vortex Spectrum, Run 103-2, t = 16.2

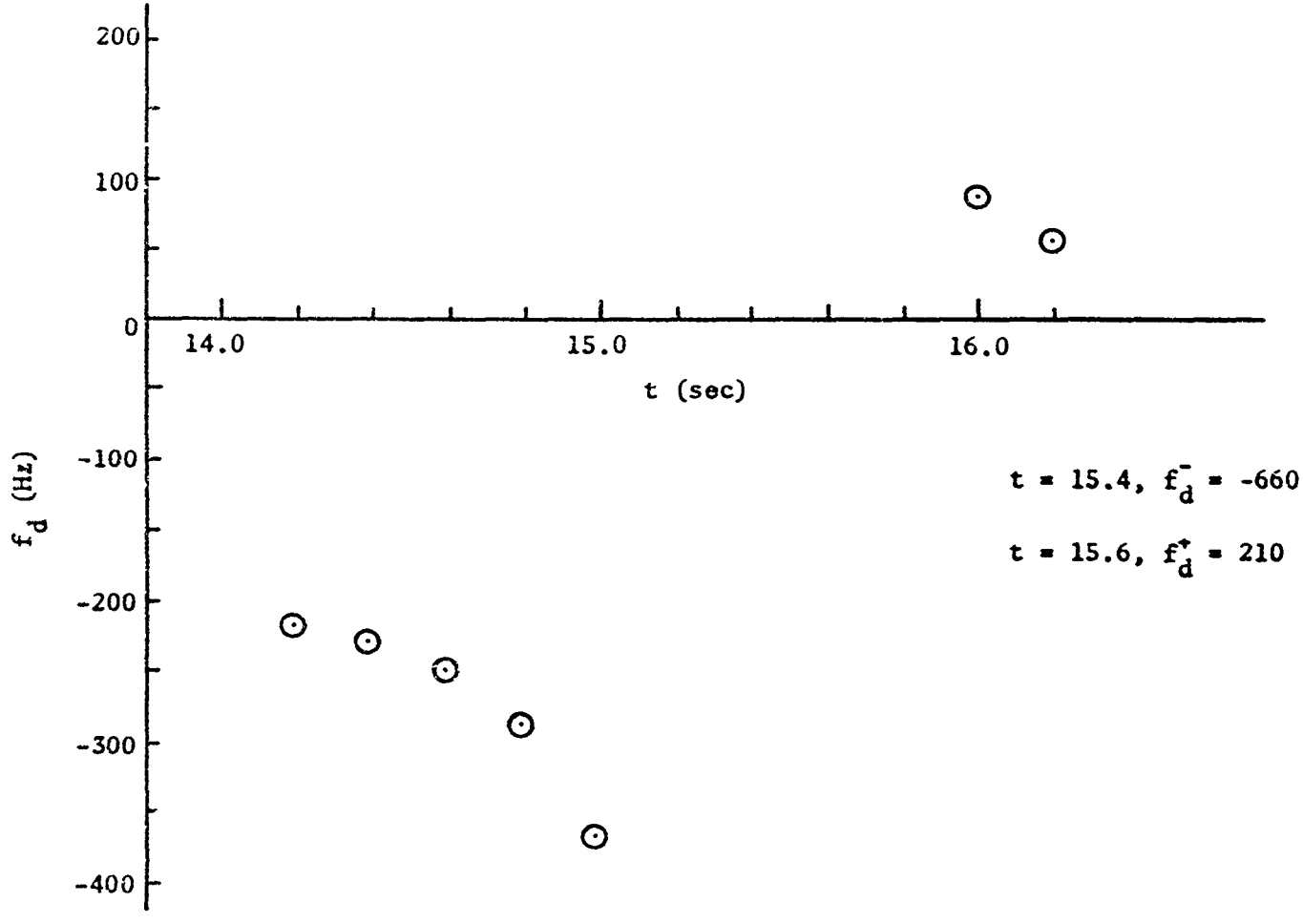


Figure 4-7. Scaled Doppler Frequency Results, Run 103-2

timing of the integration intervals was such that the two shoulders in the spectrum that correspond to the velocities at the edge of the observation volume appeared most clearly one each in two consecutive spectra, rather than in a single frame. The times and the corresponding shoulder frequencies are also indicated on Figure 4-7. Plots similar to Figure 4-7 were generated from the spectra for a number of observed vortices. They serve in effect as a condensed form for examining the raw spectral data, in the sense that the plotted points are simply doppler frequencies read in a straightforward manner at the given times, and no significant assumptions or interpretations have yet been applied.

The final step in the data processing consists of transforming this information to a profile of vortex tangential velocity vs radial distance. This velocity profile, derived from the Xonics acoustic radar processing technique is the physical quantity of interest. It was further desired that the acoustic velocity data be compared and combined with the corresponding probe data taken by NAFEC on the instrumented tower to achieve a single consistent description of vortex structure.

Replotting the points such as those shown in Figure 4-7 onto a velocity-vs-distance format requires a transformation of the time axis into a distance axis. The transformation of time to distance is readily seen to be given by the velocity with which the vortex is being transported across the observation volume. For practical purposes, this transport velocity is taken to be the measured wind velocity. (Deviations due to ground and other effects do not seem to be significant, a conclusion supported by the fact that the time interval between the two vortices on a given run was generally consistent with the transport by the wind over a distance of approximately a wingspan.) Two other observations internal to the acoustic data yielded results consistent with the wind velocity. One of them, rather apparent in Figure 4-7 and even clearer in other runs, is that the doppler frequency

curves are symmetrically arrayed not around zero doppler frequency, but about a frequency (in this case) of about -120 Hz. This displacement of all doppler frequencies is the result of the translation of the entire vortex across the observation volume. The other observation, made on a number of the runs, is the coherent return, described in connection with the spectrum of Figure 4-4. The coherent return provides direct confirmation of the actual instantaneous velocity, which in this case agrees with that inferred from the axis of symmetry and the measured wind. It should be kept in mind however that the wind is not absolutely steady, and fluctuations in the wind can effect substantial changes in the local transport velocity. It is further worth noting tha that the transport velocity is one of the fundamental quantities of interest in tracking; it is given here as an outgrowth of the coherent doppler processing, even through the radar configuration makes no geometric provision for providing tracking information.

Given now that the radial distance corresponding to the time displacement from the center crossing is established, the vortex velocity profile can be plotted by relabeling the ordinates as velocities rather than doppler frequencies. The constant of proportionality that defines the conversion is easily obtained from the operating frequency and the geometric scattering angle. One other point, the velocity at the edge of the observation volume, can also be plotted for each vortex. The velocity is obtained from the shoulder frequencies for the centered spectrum by the same constant of proportionality, but some uncertainty has existed in determining the distance to assign the edge of the beam. It may be recalled that the transmitted beam is created by a driver feeding a 10-ft dish. Due to the special nature and configuration of these tower tests, the observation volumes generally fell well within the near field of the antenna. It is therefore most difficult to determine the actual illumination along the beam, and indeed it is very likely to be somewhat different at different altitudes.

It appears from these results, both from internal evidence and from comparison with the NAFEC probe data that $R_o$ = 5 ft represents the best and most consistent estimate of the radius of the observation volume. This figure is also quite consistent with the dish diameter. The points for the centered vortex have therefore all been plotted at that distance.

Figures 4-8 through 4-31 show the resulting plots of vortex velocity vs radial distance. Each figure shows a point at r = 5 ft, obtained from the spectrum of the centered vortex, and a number of points at greater distance, scaled from the points such as those shown in Figure 4-7. When two points appeared at a given distance but on opposite sides of the center position, their average was plotted at that distance. Most of the figures also show a solid curve, derived for comparison from the preliminary velocity profiles provided by NAFEC for those runs. The NAFEC data from which the curves were taken are plots of v vs h, i.e., the velocity (corrected for wind) recorded at each of the sensors (with 1-ft spacing) at the time the center of the vortex passed the tower. In order to compare with a single velocity profile that contains all the velocity information for a cylindrically symmetric vortex, the two curves above and below the center of the vortex were averaged (which would also tend to average out any error in the wind estimate). The same assumption of cylindrical symmetry provides the justification for comparing the vertical cut through the vortex given by the NAFEC data with the horizontal cut analyzed for the acoustic data. The assumption is probably valid for all practical purposes for distances small compared with the intervortex separation, but clearly breaks down for distances comparable to that separation. In particular, along the axis connecting the two cores, the velocity does not continue to decay indefinitely, but rather builds up again after passing through a minimum. Evidence of this effect is seen in Figures 4-16 and 4-24, where relatively high velocities are seen to persist to great distances

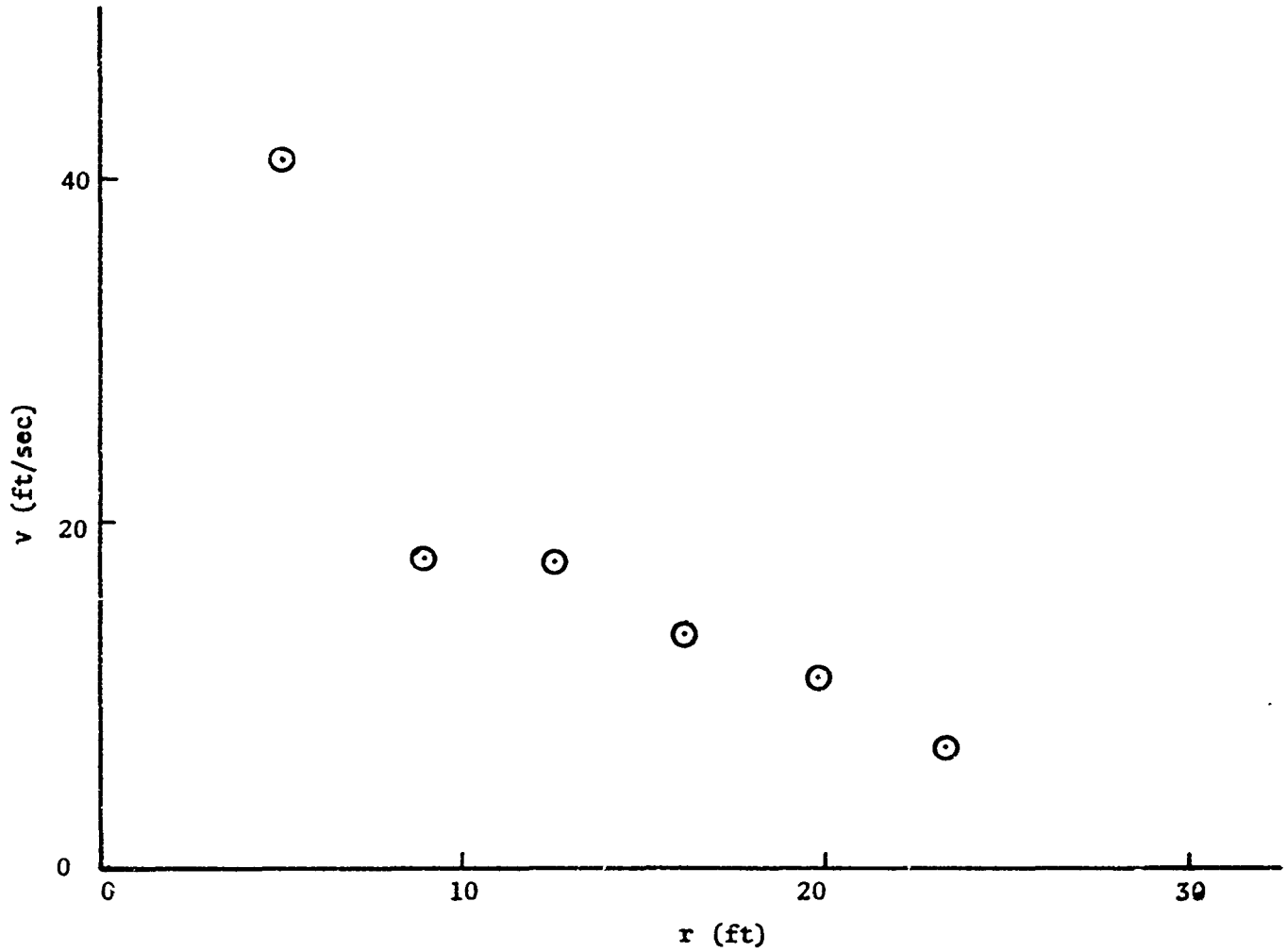


Figure 4-8. Radial Velocity Profile for DC-7, Run 95-1

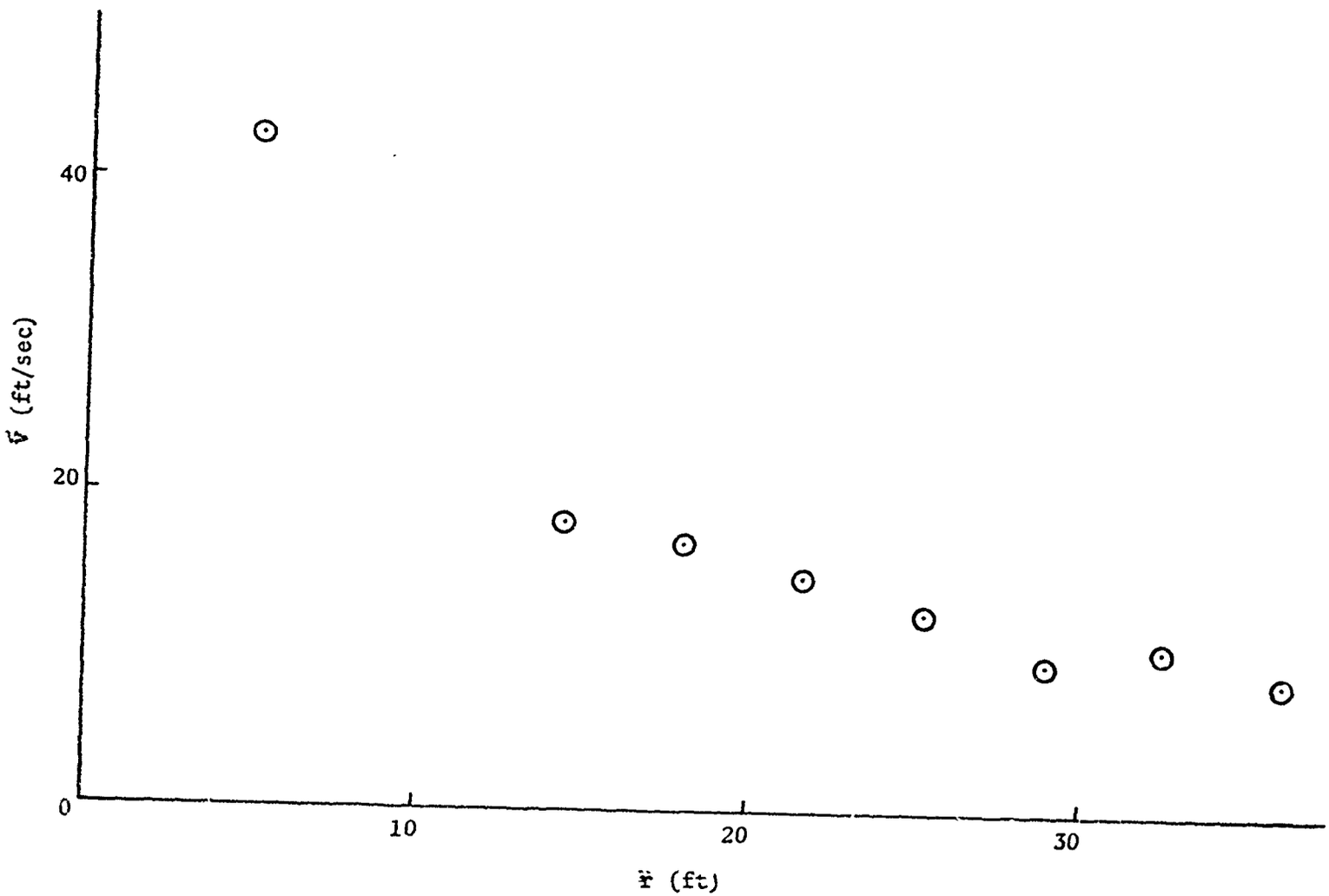


Figure 4-9. Radial Velocity Profile for DC-7, Run 95-2

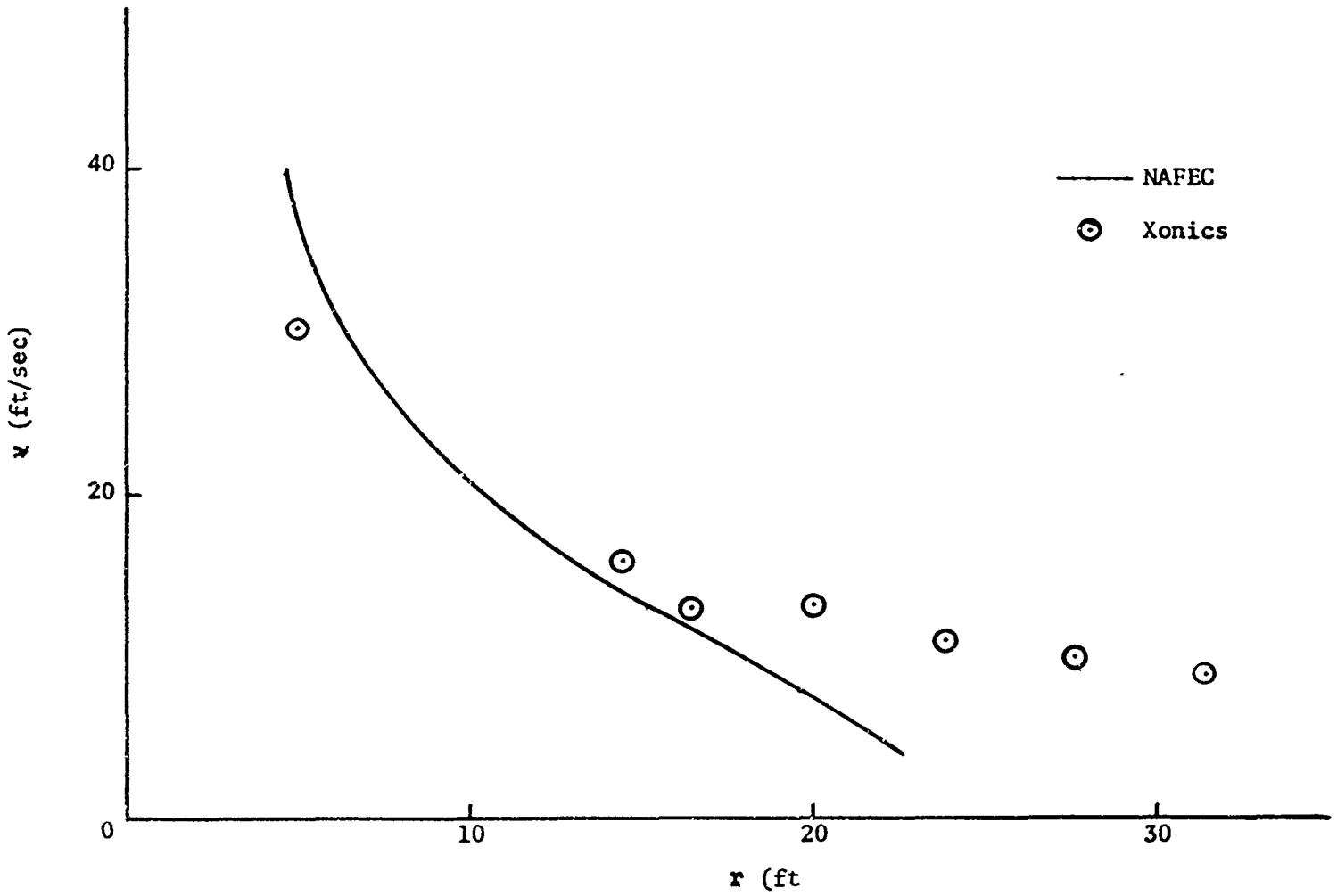


Figure 4-10. Radial Velocity Profile for DC-7, Run 96-1

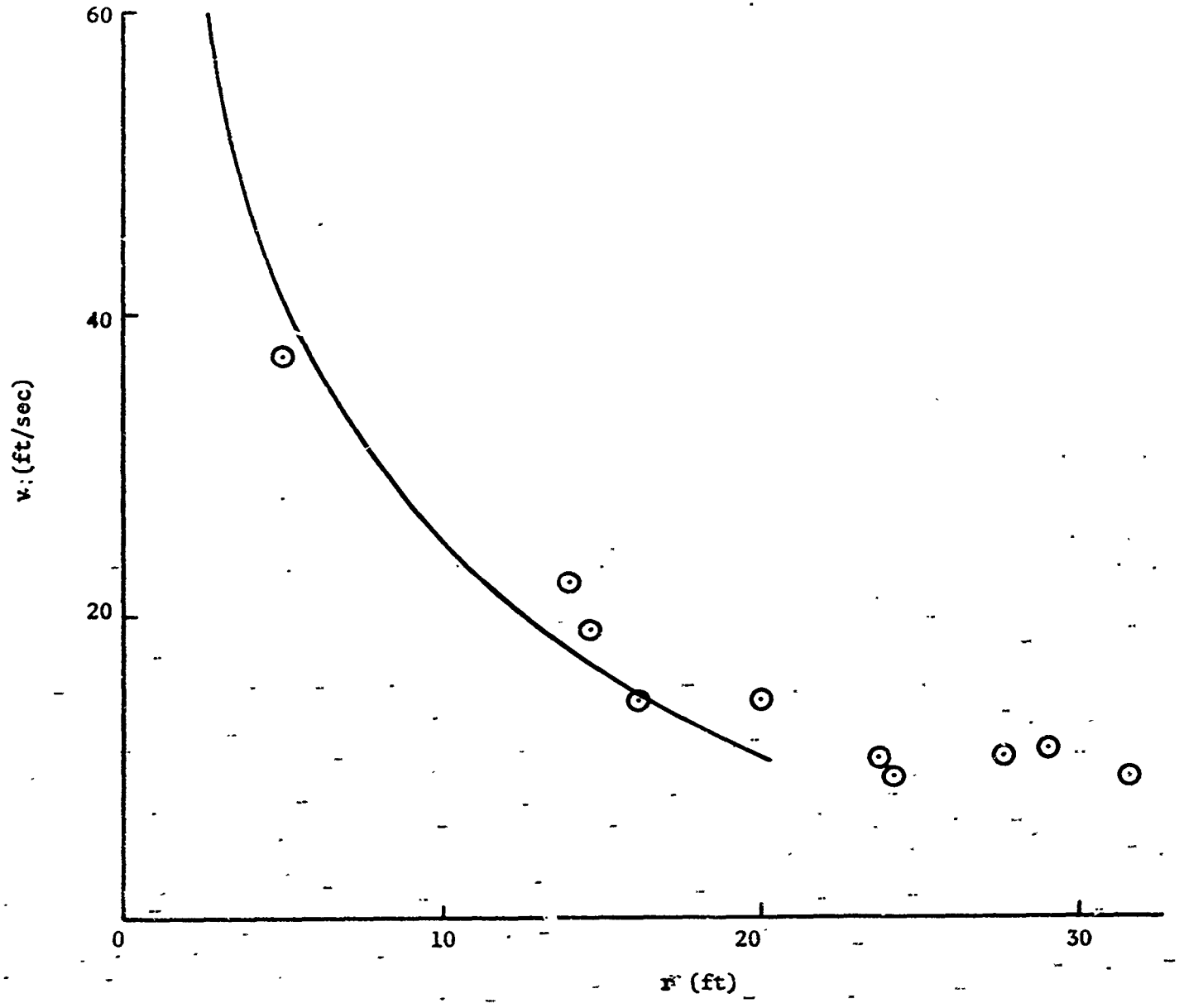


Figure 4-11. Radial Velocity Profile for DC-7, Run 96-2

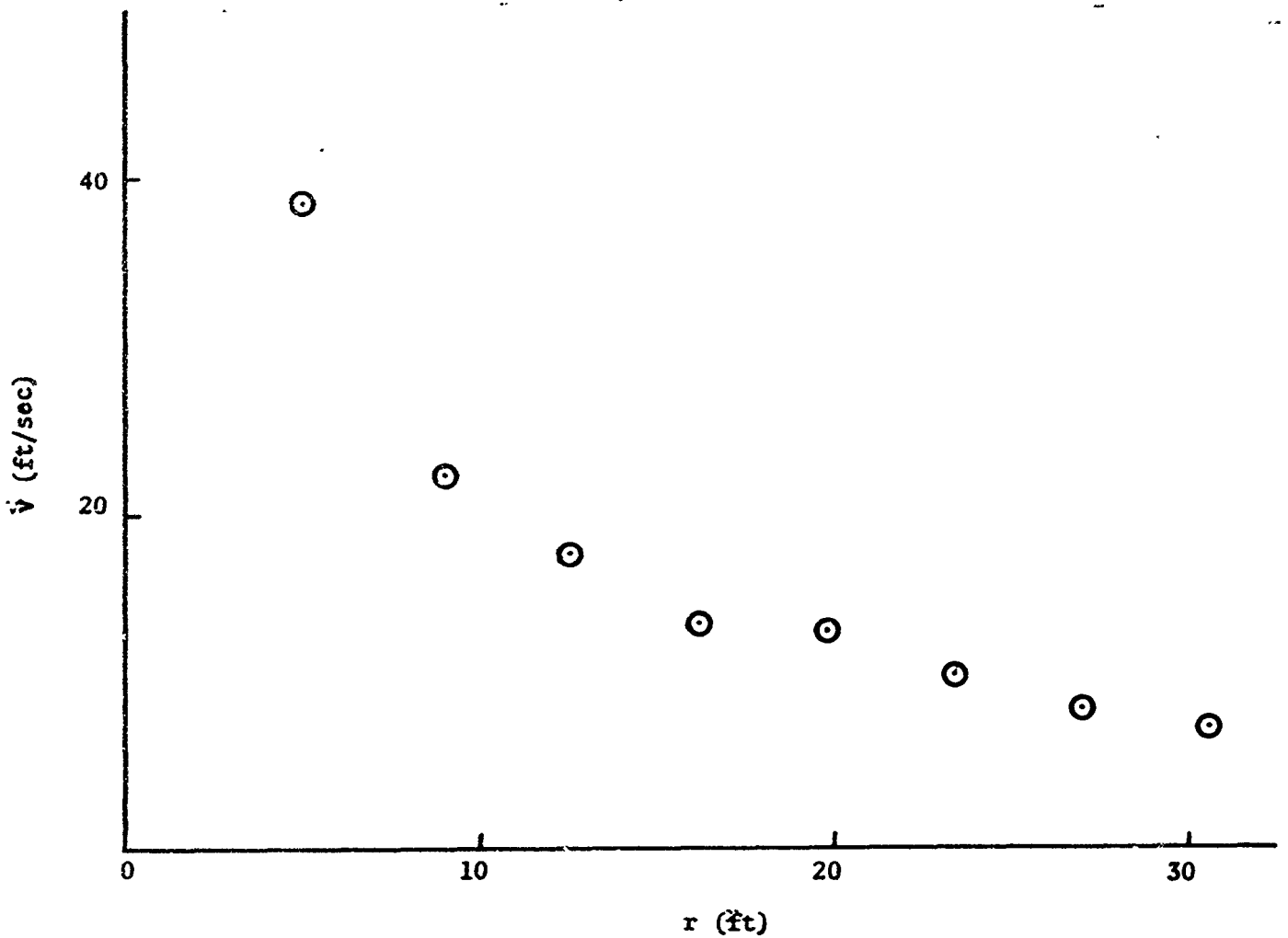


Figure 4-12. Radial Velocity Profile for DC-7, Run 97-1

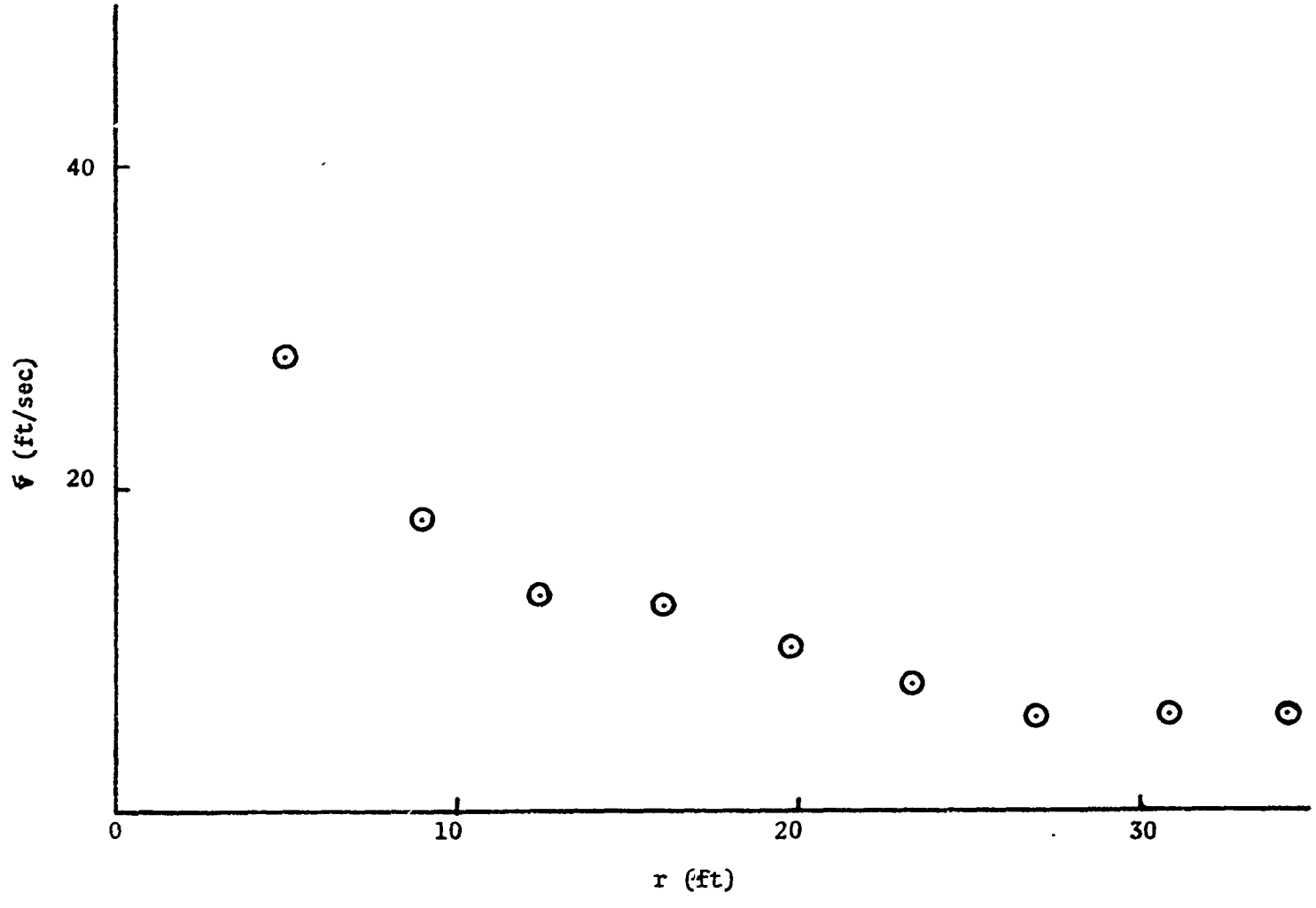


Figure 4-13. Radial Velocity Profile for DC-7, Run 97-2

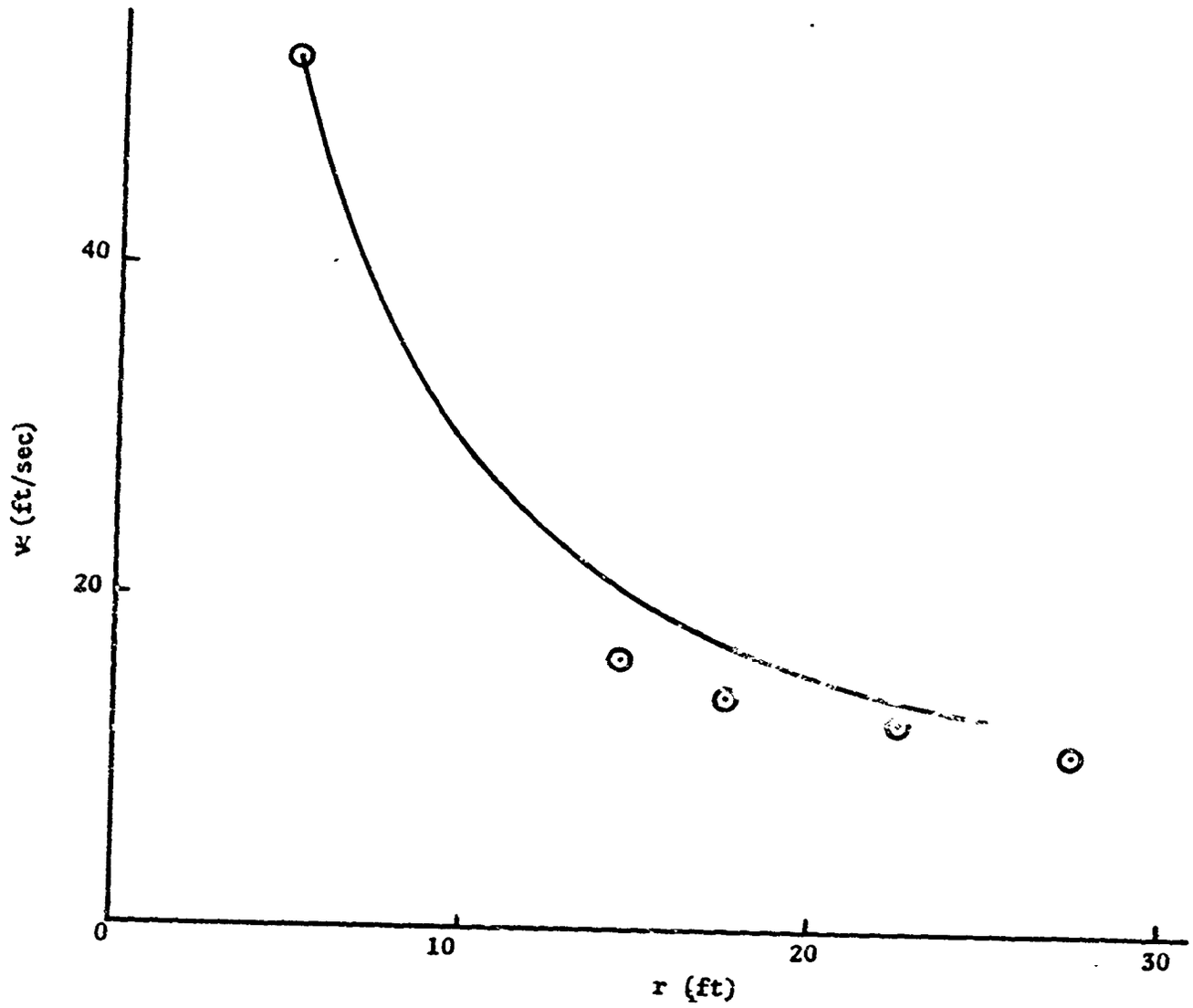


Figure 4-14. Radial Velocity Profile for DC-7, Run 103-1

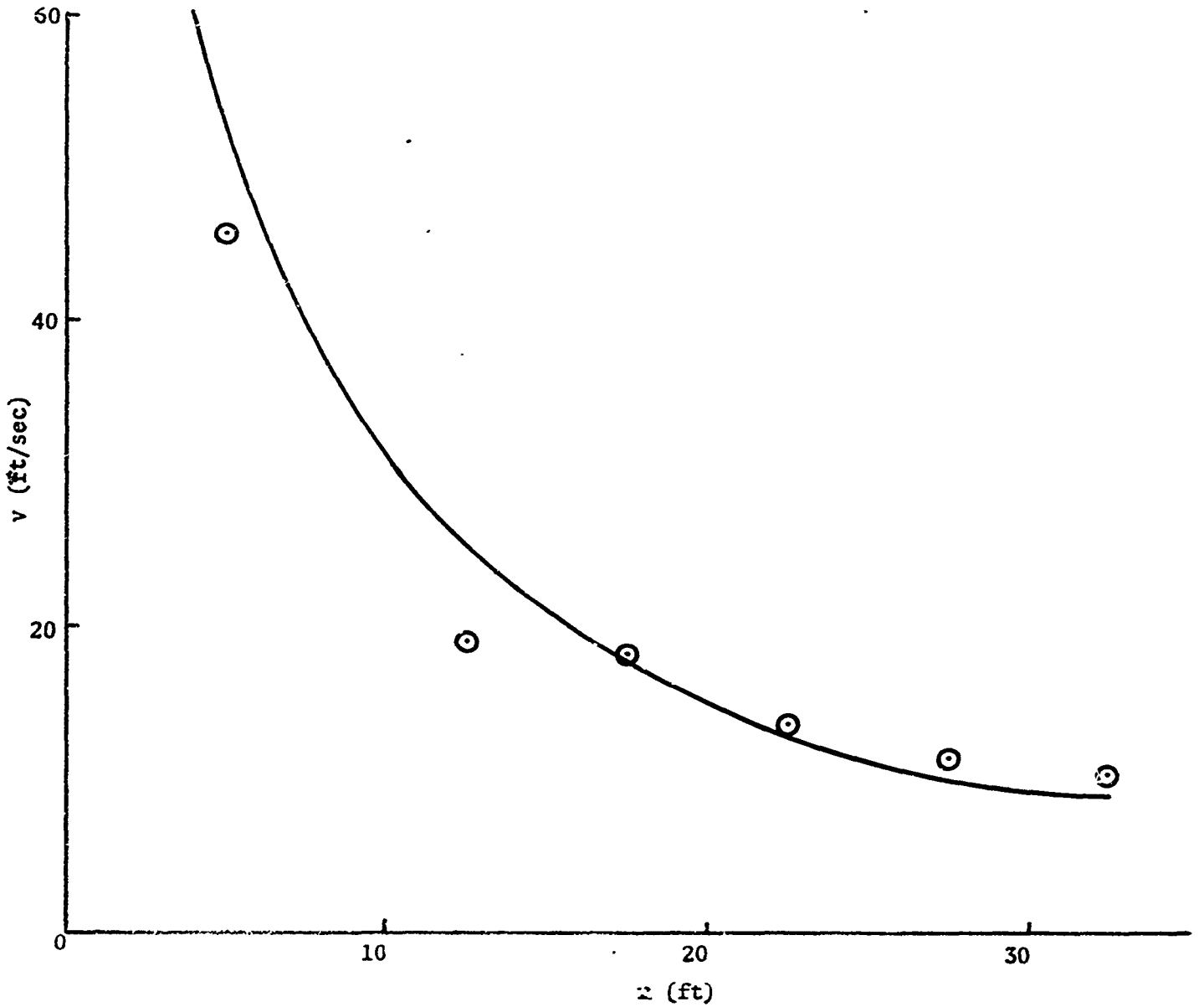


Figure 4-15. Radial Velocity Profile for DC-7, Run 103-2

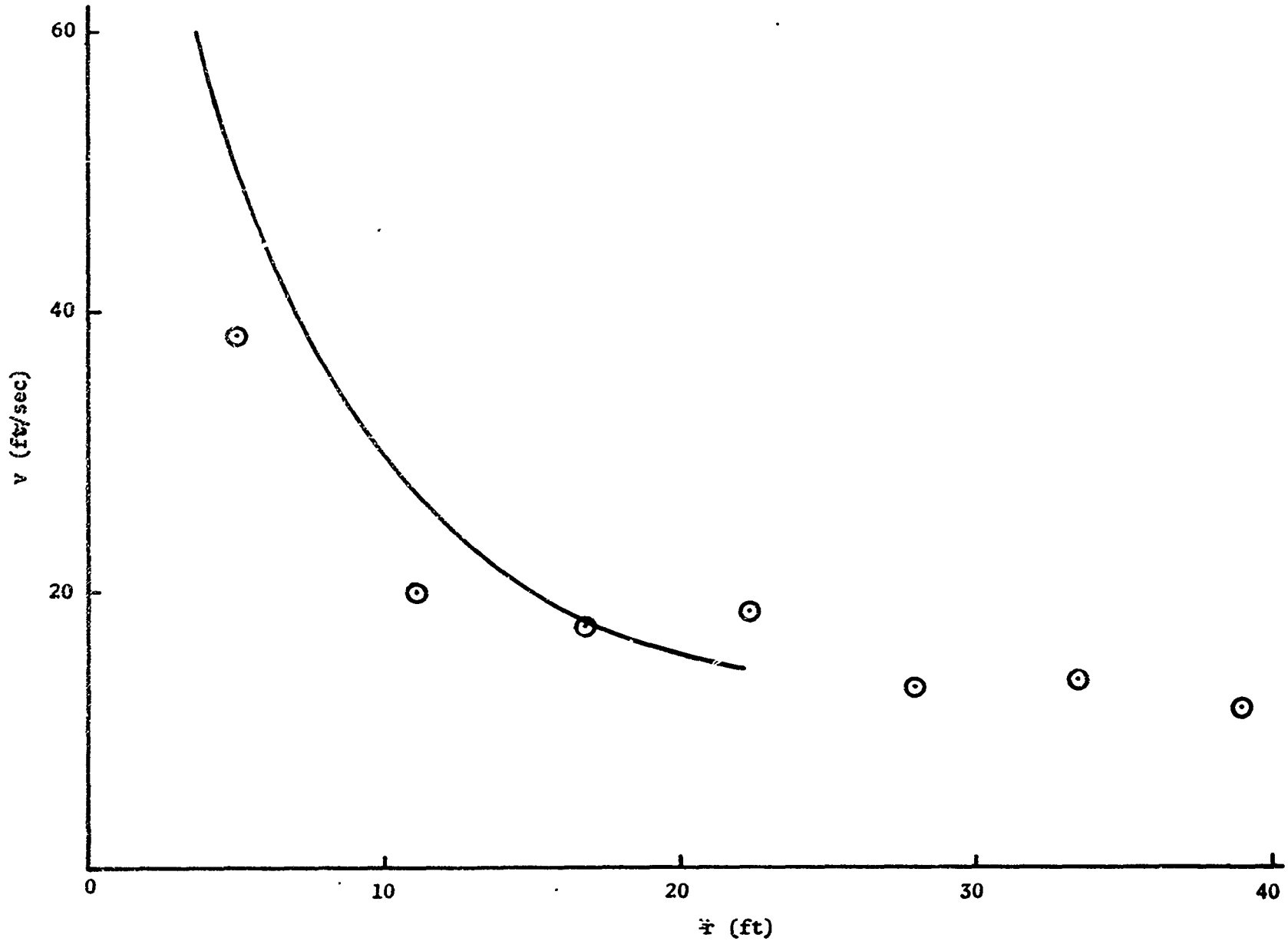


Figure 4-16. Radial relocity Profile for DC-7, Run 105-1

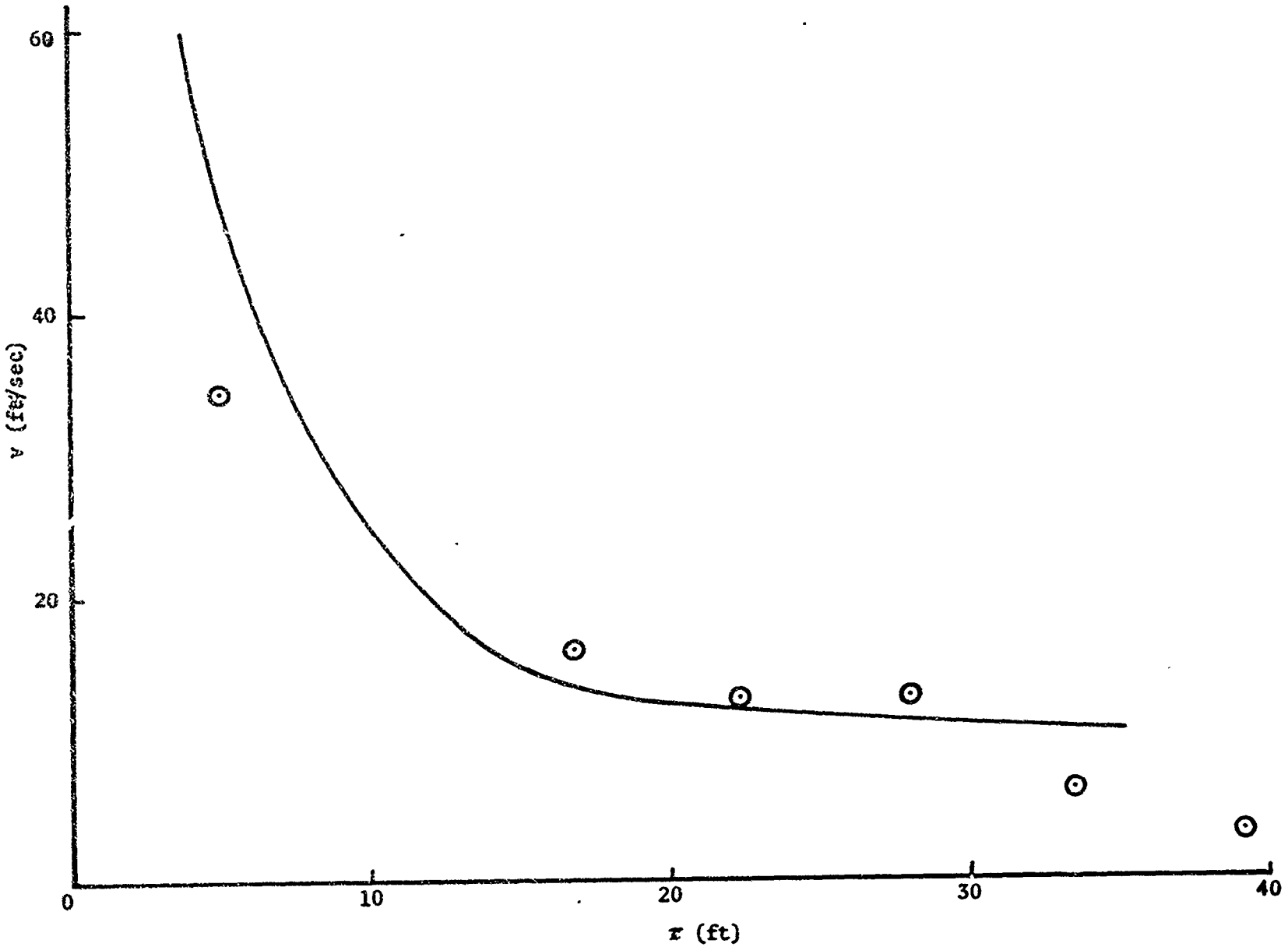


Figure 4-17: Radial Velocity Profile for DC-7, Run 105-2

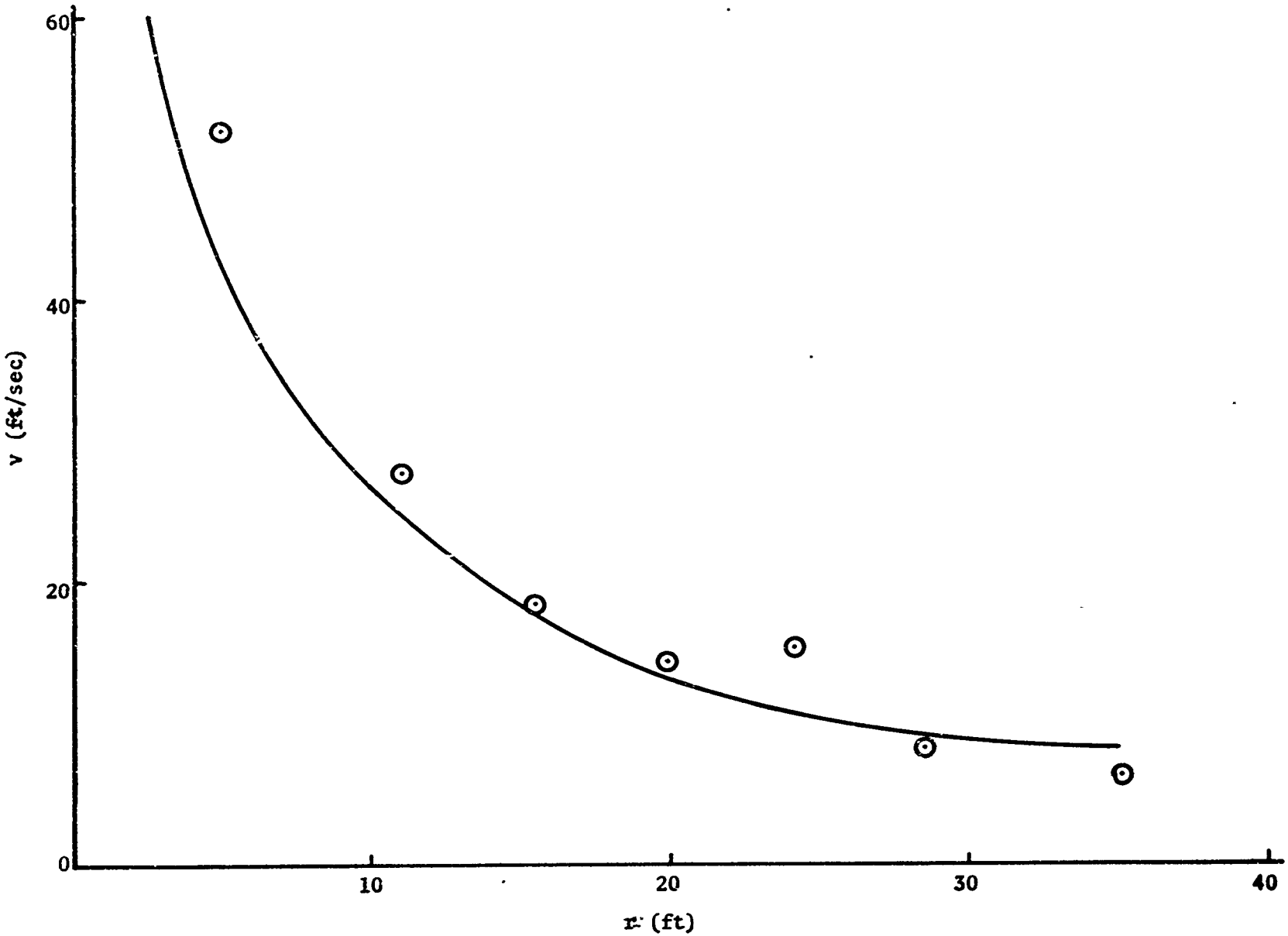


Figure 4-18. Radial Velocity Profile for DC-7, Run 107-1

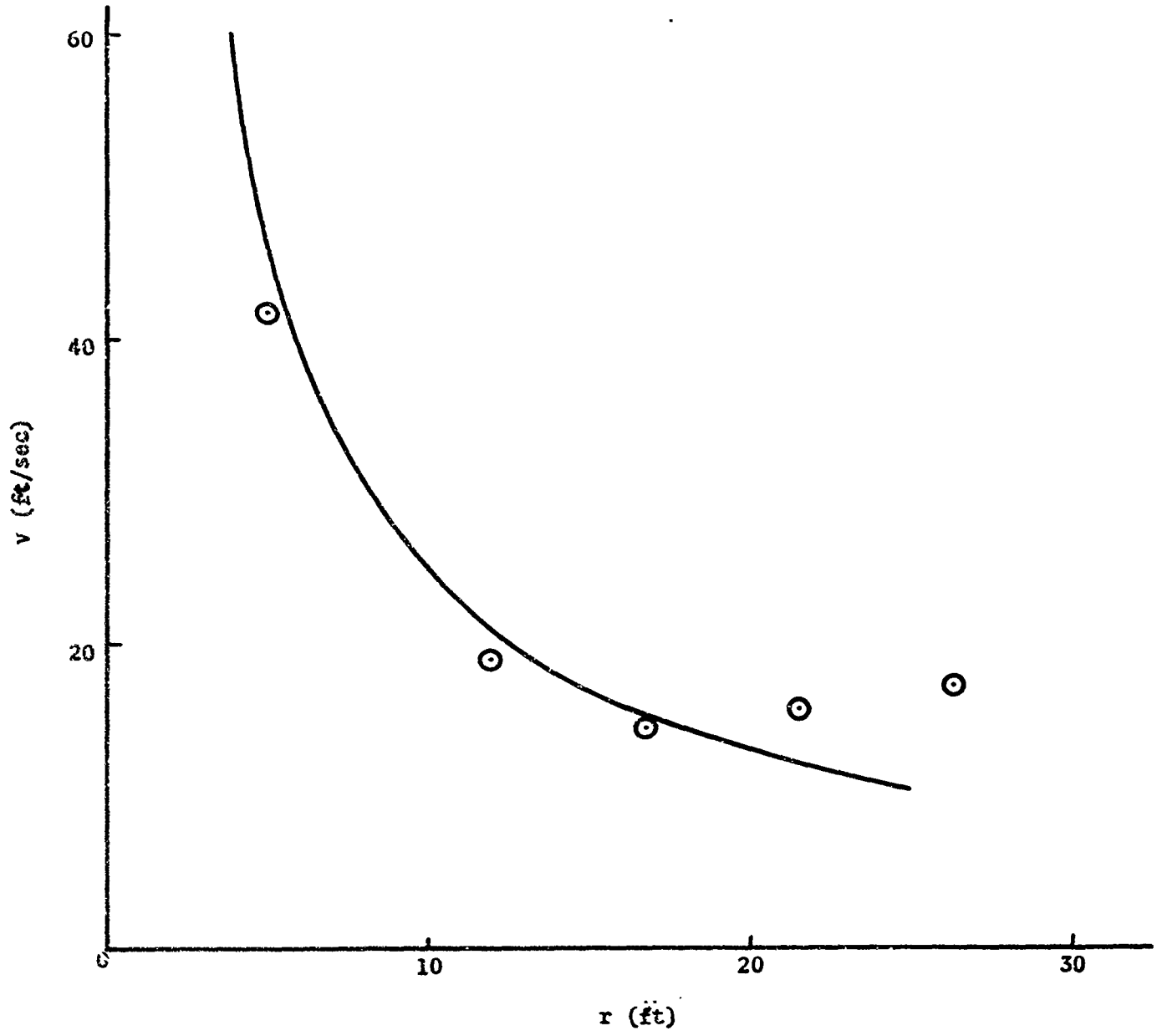


Figure 4-19. Radial Velocity Profile for DC-7, Run 107-2

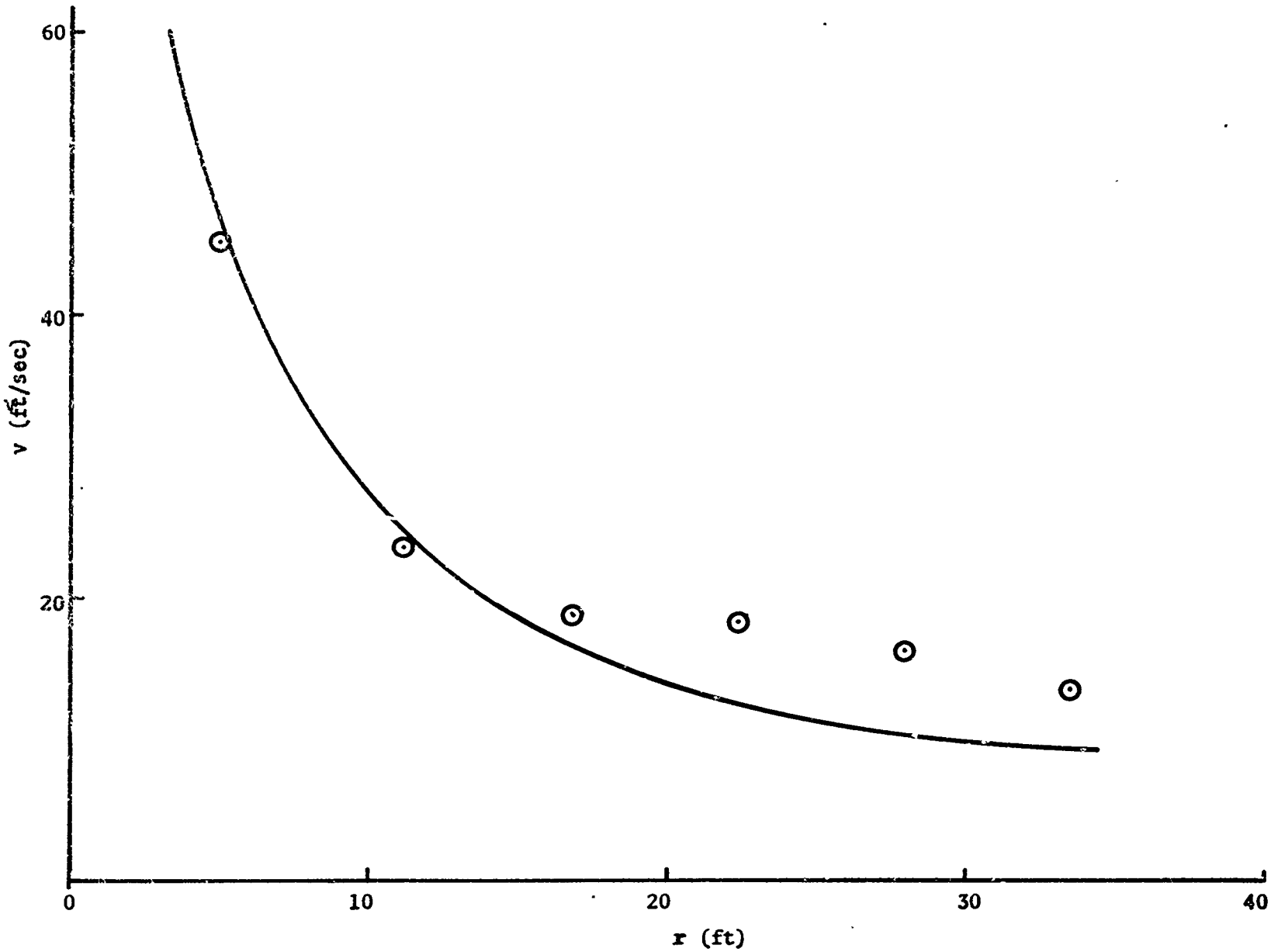


Figure 4-20. Radial Velocity Profile for DC-7, Run 109-1

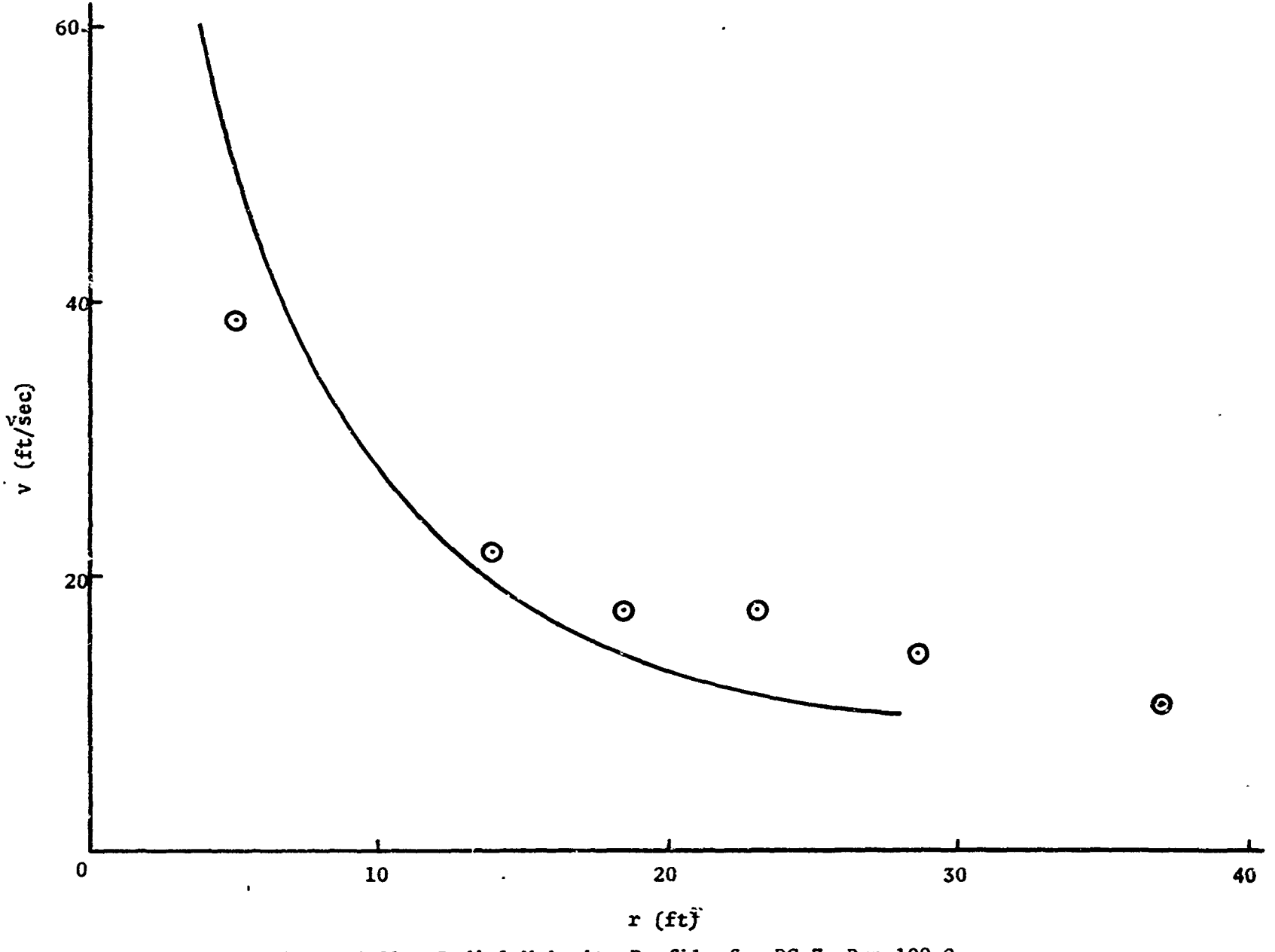


Figure 4-21. Radial Velocity Profile for DC-7, Run 109-2

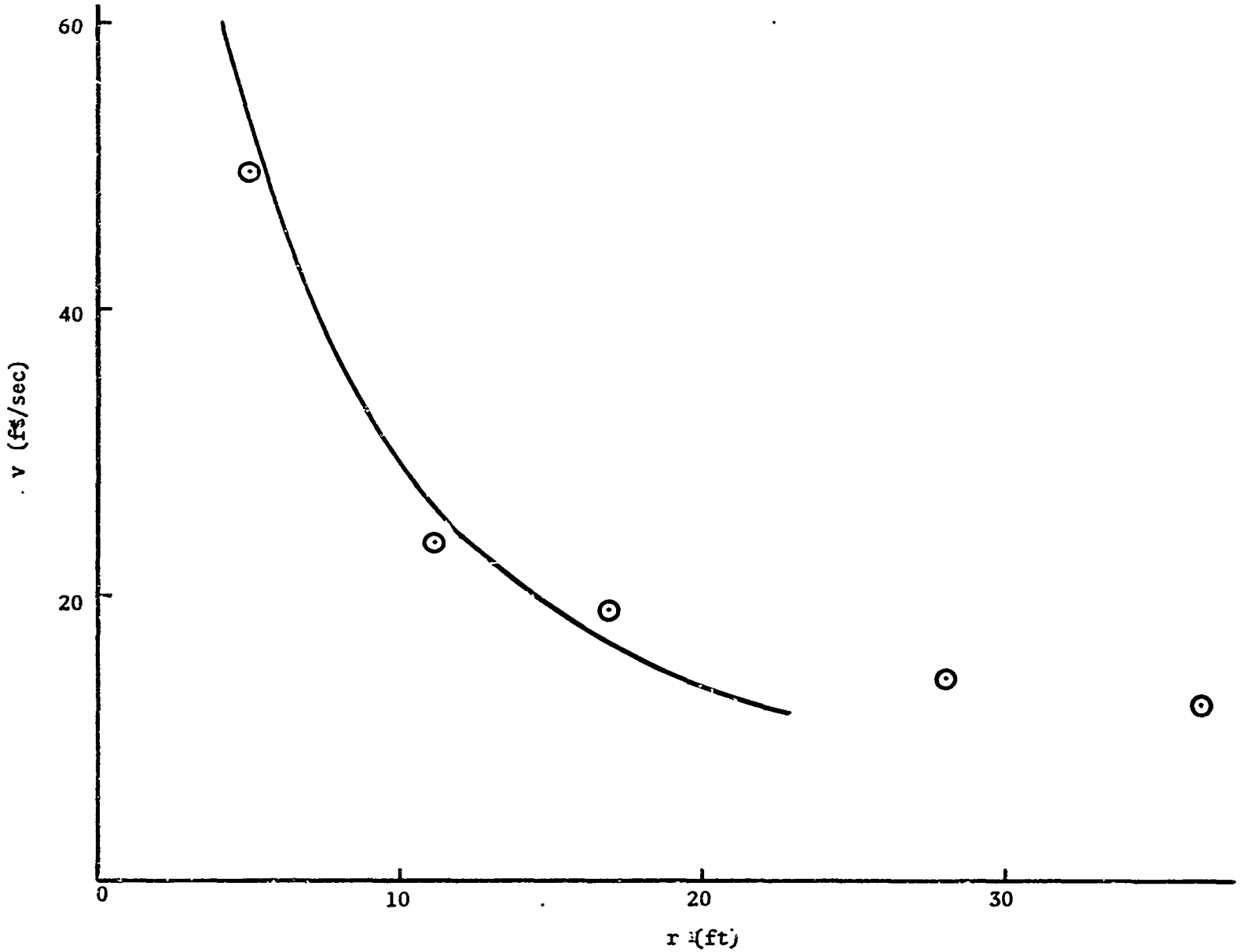


Figure 4-22. Radial Velocity Profile for DC-7, Run 115-1

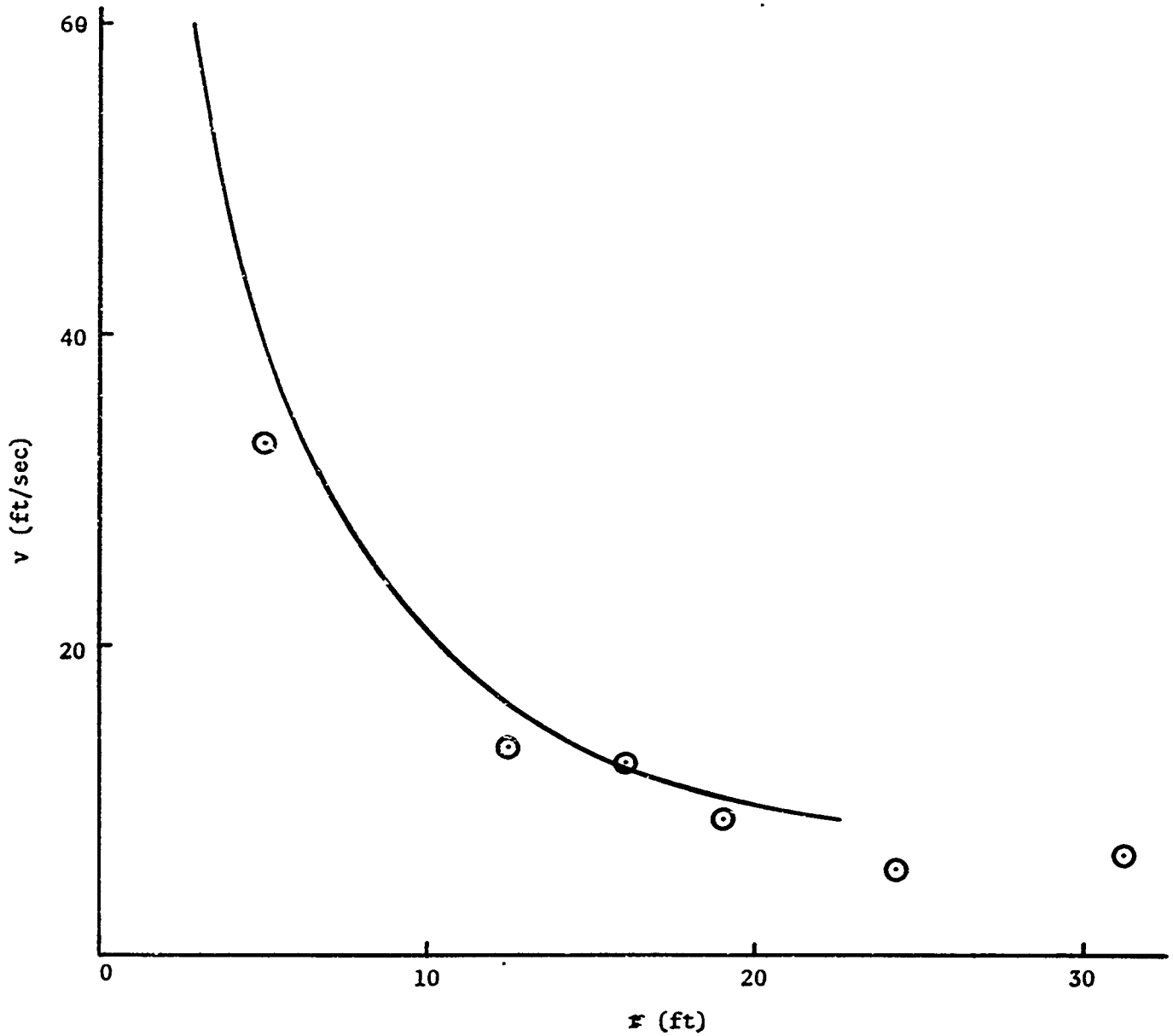


Figure 4-23. Radial Velocity Profile for DC-7, Run 129-1

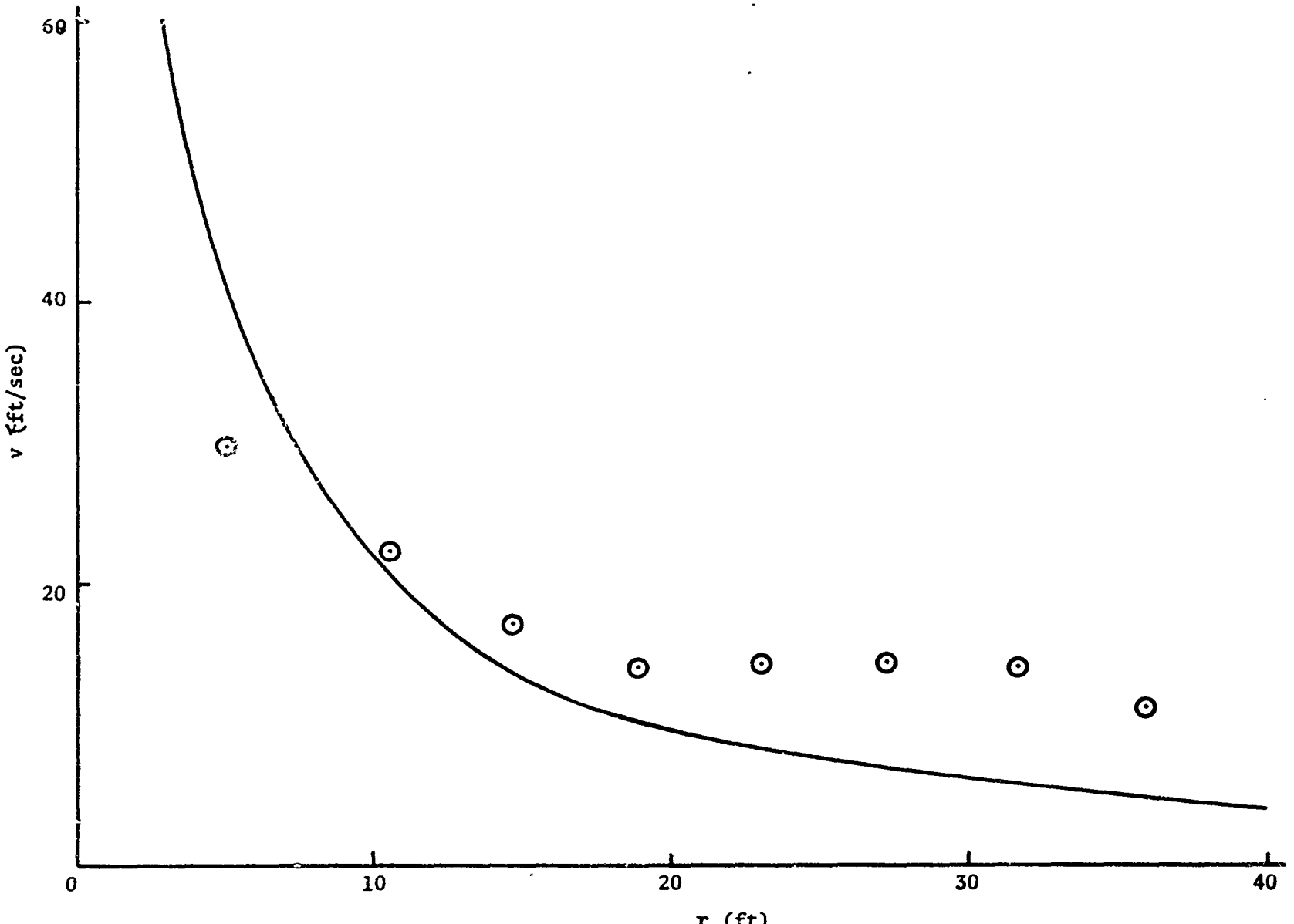


Figure 4-24. Radial Velocity Profile for DC-7, Run 129-2

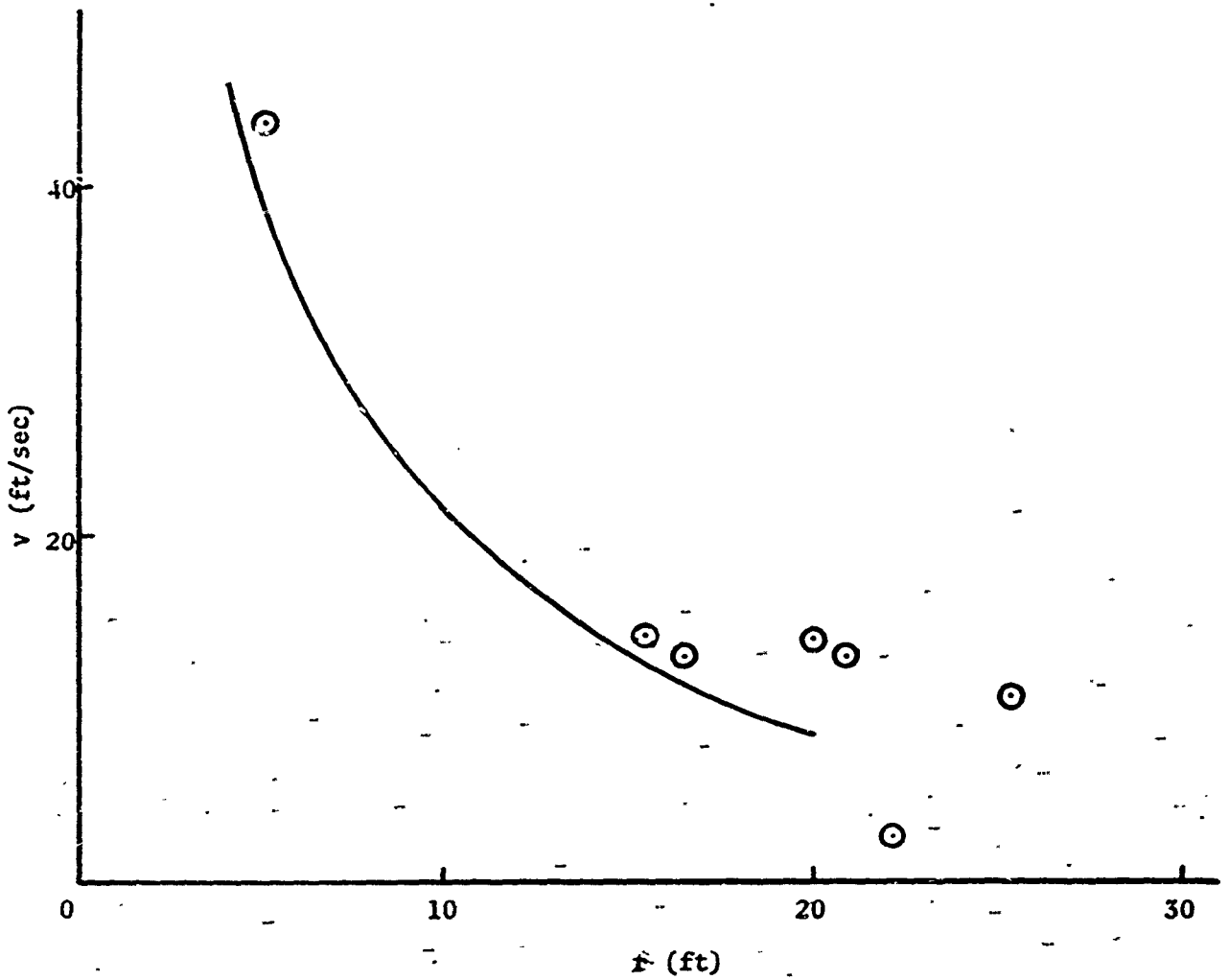


Figure 4-25. Radial Velocity Profile for DC-7, Run 151-1

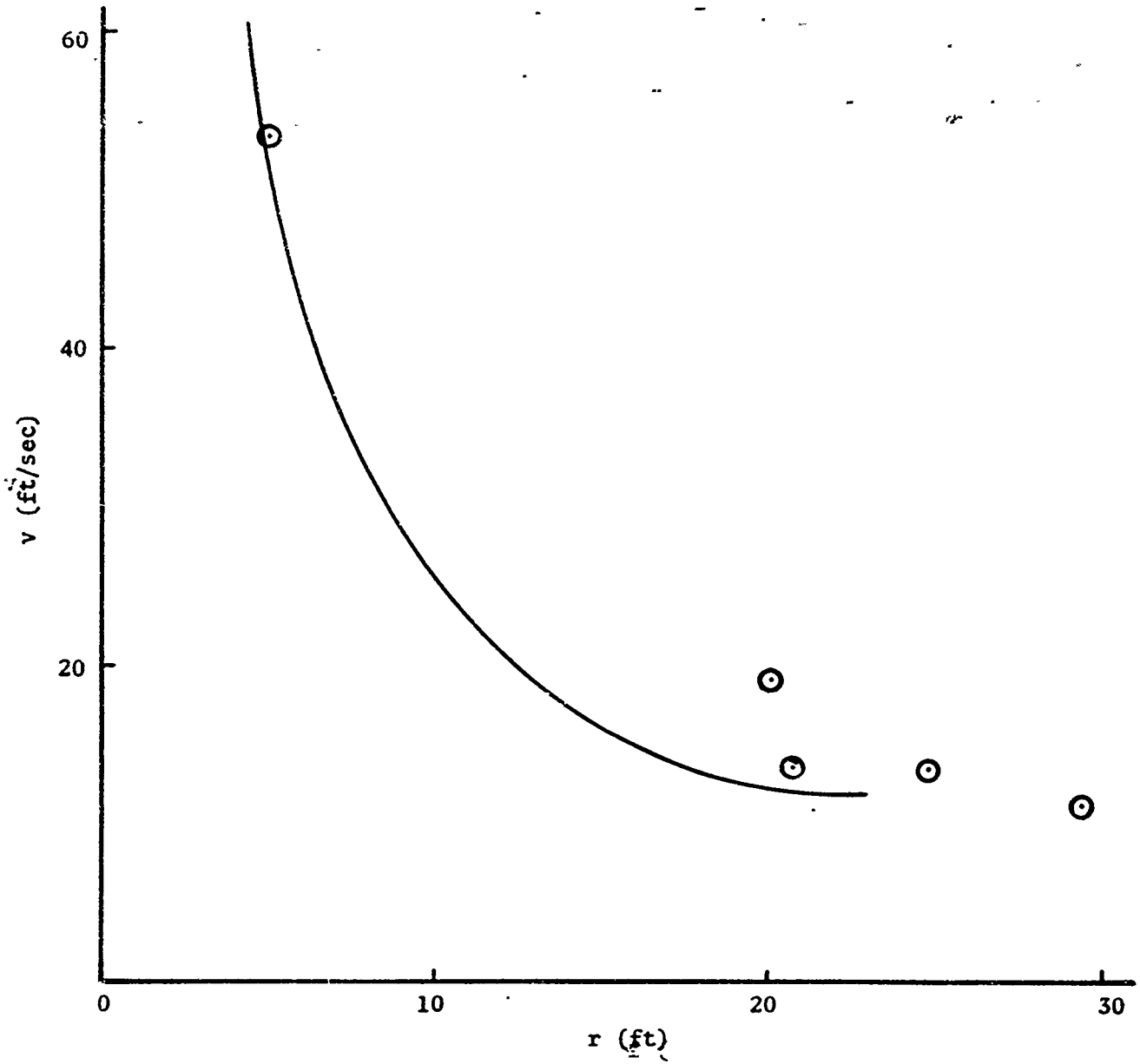


Figure 4-26. Radial Velocity Profile for DC-7, Run 151-2

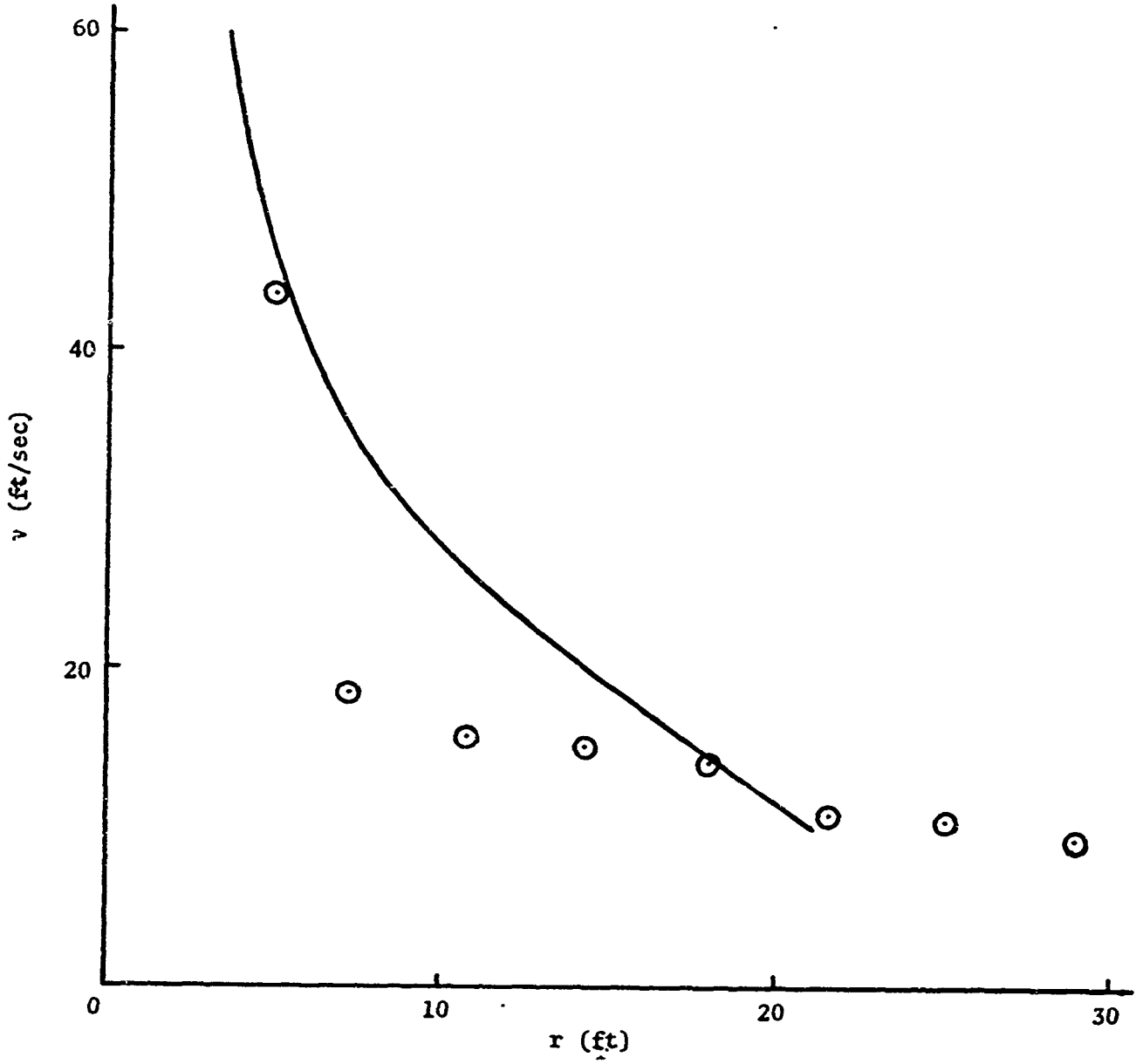


Figure 4-27. Radial Velocity Profile for DC-7, Run 157-1

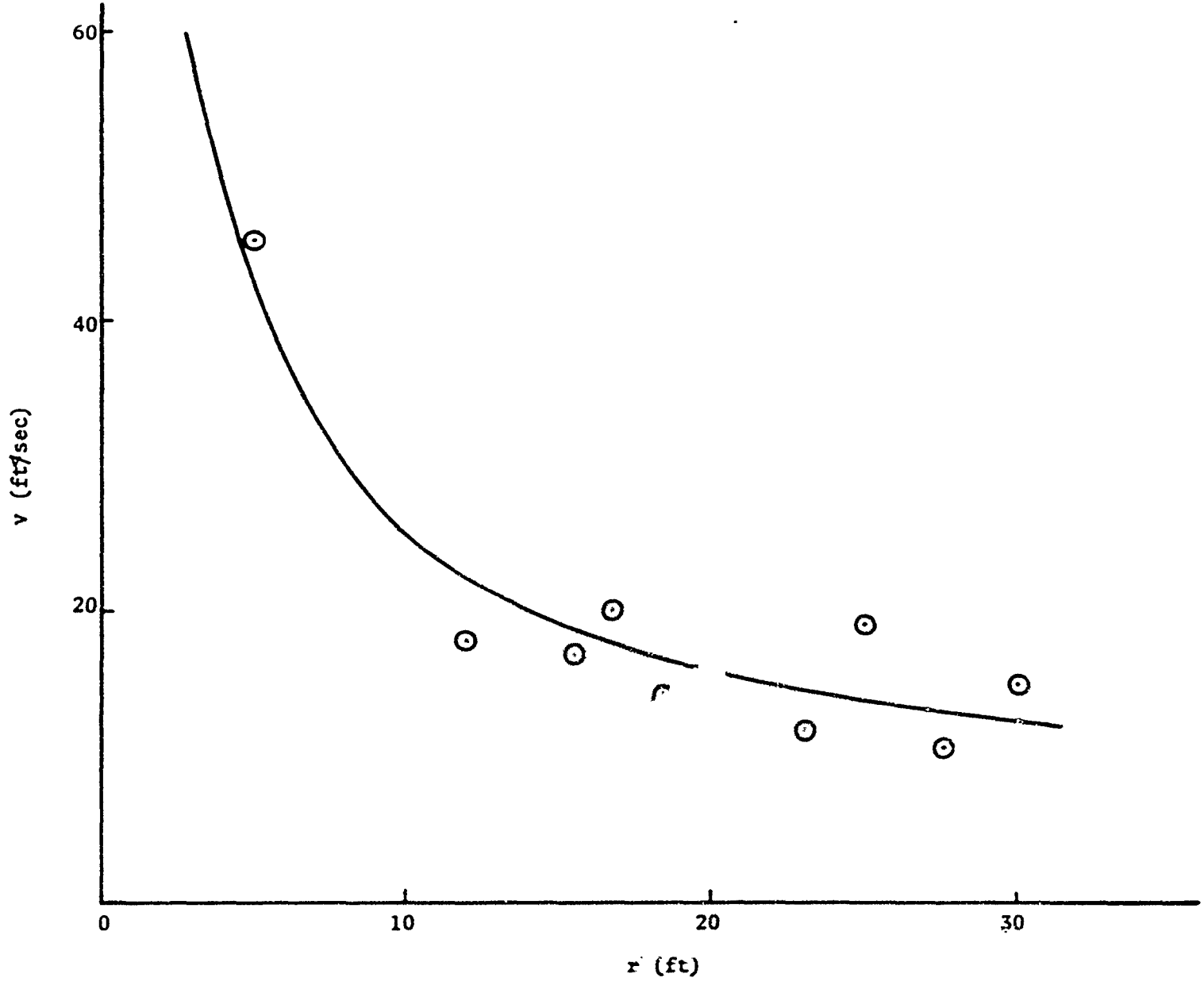


Figure 4-28. Radial Velocity Profile for DC-7, Run 165-1

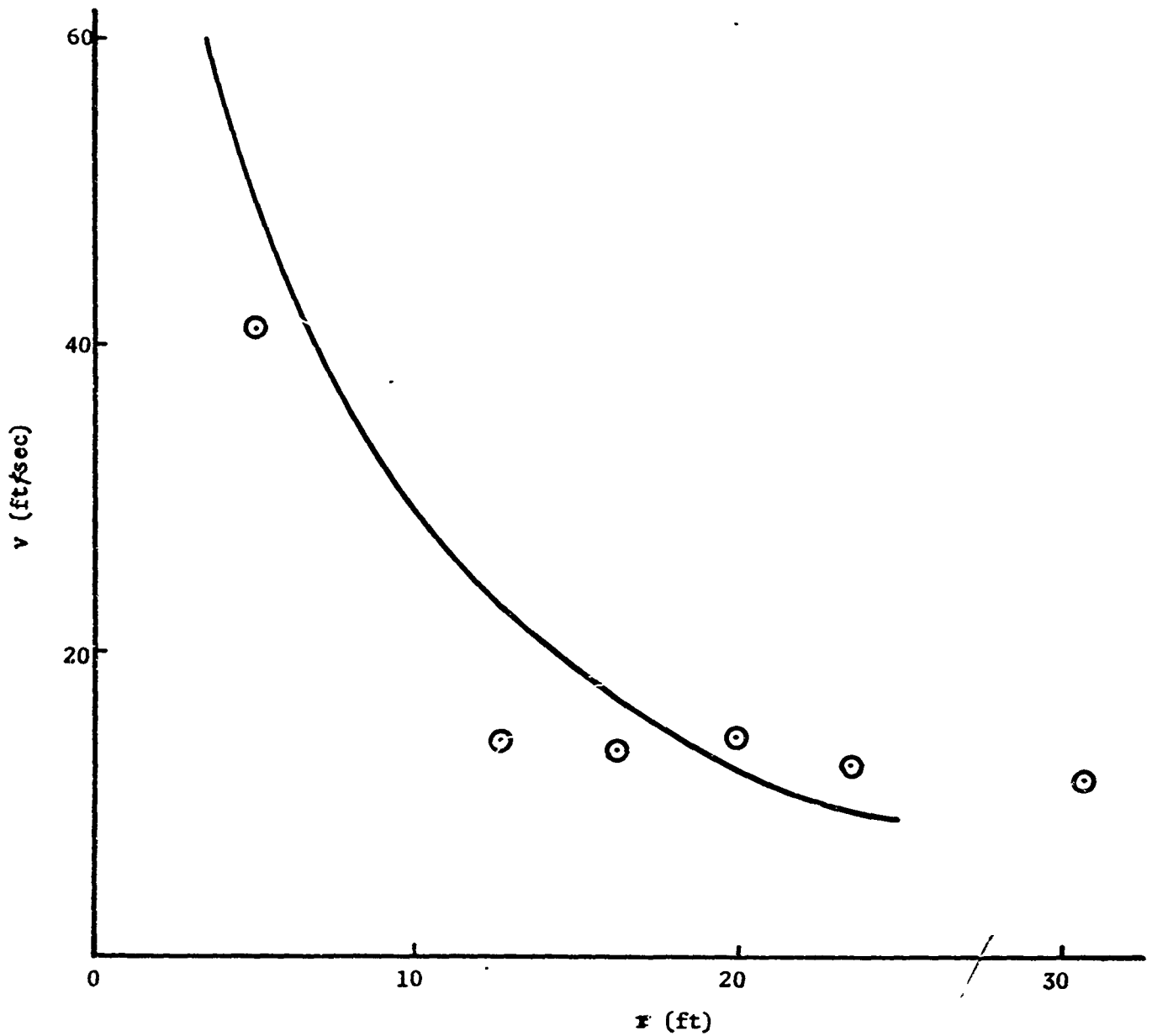


Figure 4-29. Radial Velocity Profile for DC-7, Run 165-2

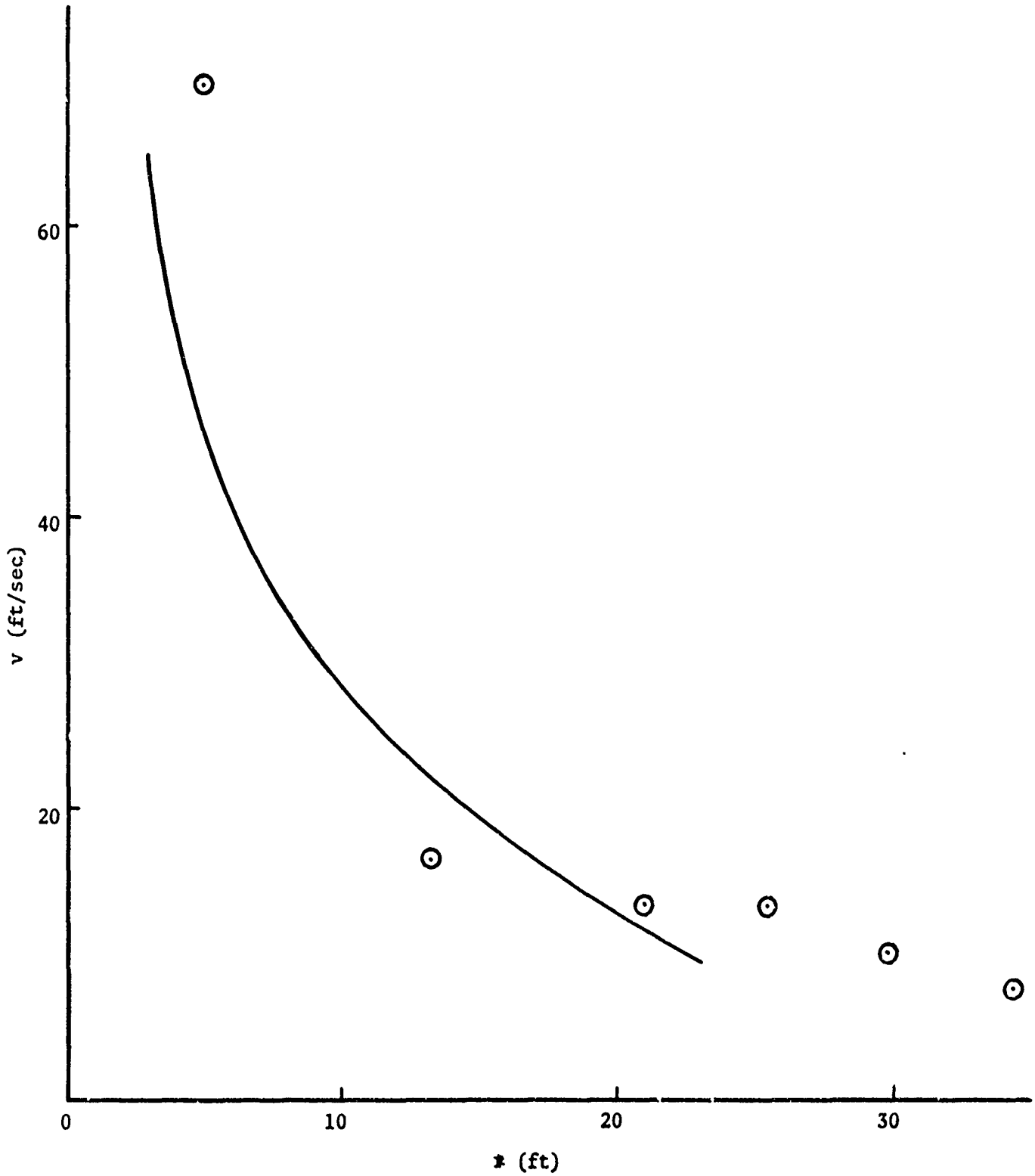


Figure 4-30. Radial Velocity Profile for DC-7, Run 169-1

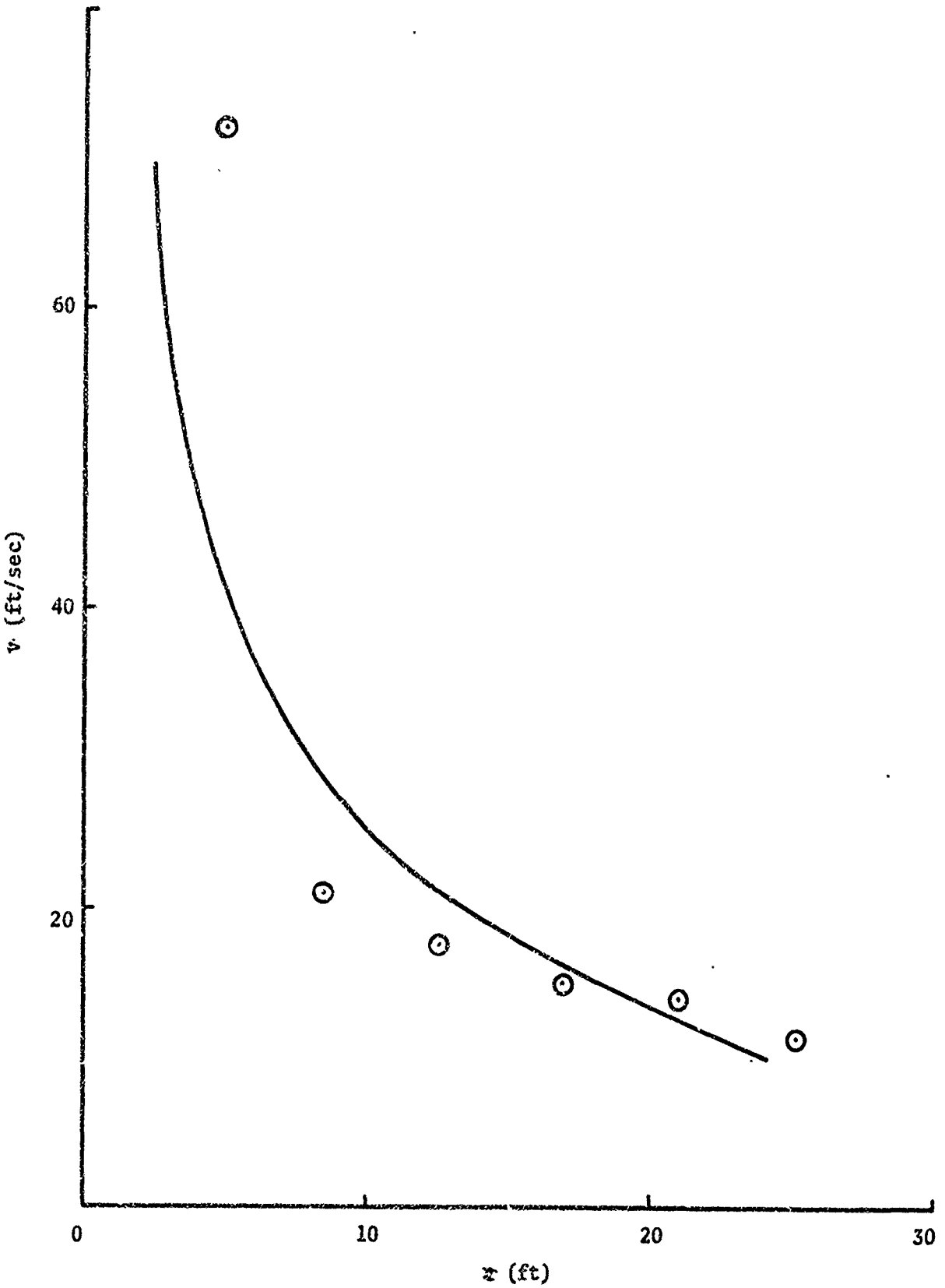


Figure 4-31. Radial Velocity Profile for DC-7, Run 169-2

Considering the probable experimental errors involved in the two sensor systems, compounded by the differences between the quantities measured (such as the physical separation and the considerations just discussed), the data from the two sensors can be used with confidence to supplement each other as tools for studying vortex structure and dynamics in the areas where each is especially suited - the tower to detailed, high-resolution measurements, the acoustic radar to remote observations at all altitudes.

## 4.3 C-141 Results

The contrast in structure between a DC-7 vortex and that of a C-141 is immediately evident from visual observation (aided by smoke grenades) of the respective flow fields. The small-scale, high-velocity core of the DC-7 vortex is lacking in the C-141 vortex, which consists rather of a large-scale rotation with very much lower peak velocity. These differences are directly reflected in the acoustic spectra obtained from the C-141 runs. Examples of calculated spectrum shapes as predicted by the model for vortices whose core diameters are larger than the observation volume were shown in Figures 2-10 and 2-11. Their principal distinguishing characteristic is that they have a relatively flat top and sharply defined sides, the sides corresponding to the highest and lowest velocities present at that time within the observation volume. In effect, for large-scale vortices, the acoustic sensor takes on some of the character of a point sensor, and in the limit of a very large vortex would measure a single, well-defined velocity at any time.

The expected shape is, in fact, the one exhibited by the spectra obtained from the C-141 observations. A sequence of representative spectra, from run 2, vortex 2, is shown in Figures 4-32 through 4-36, which traces the history as the center of the vortex approaches, passes through the observation volume, and recedes. This sequence should be compared and contrasted with the DC-7 sequence of Figures 4-1 through 4-6. The sharper sides of the C-141 spectra, the much lower maximum

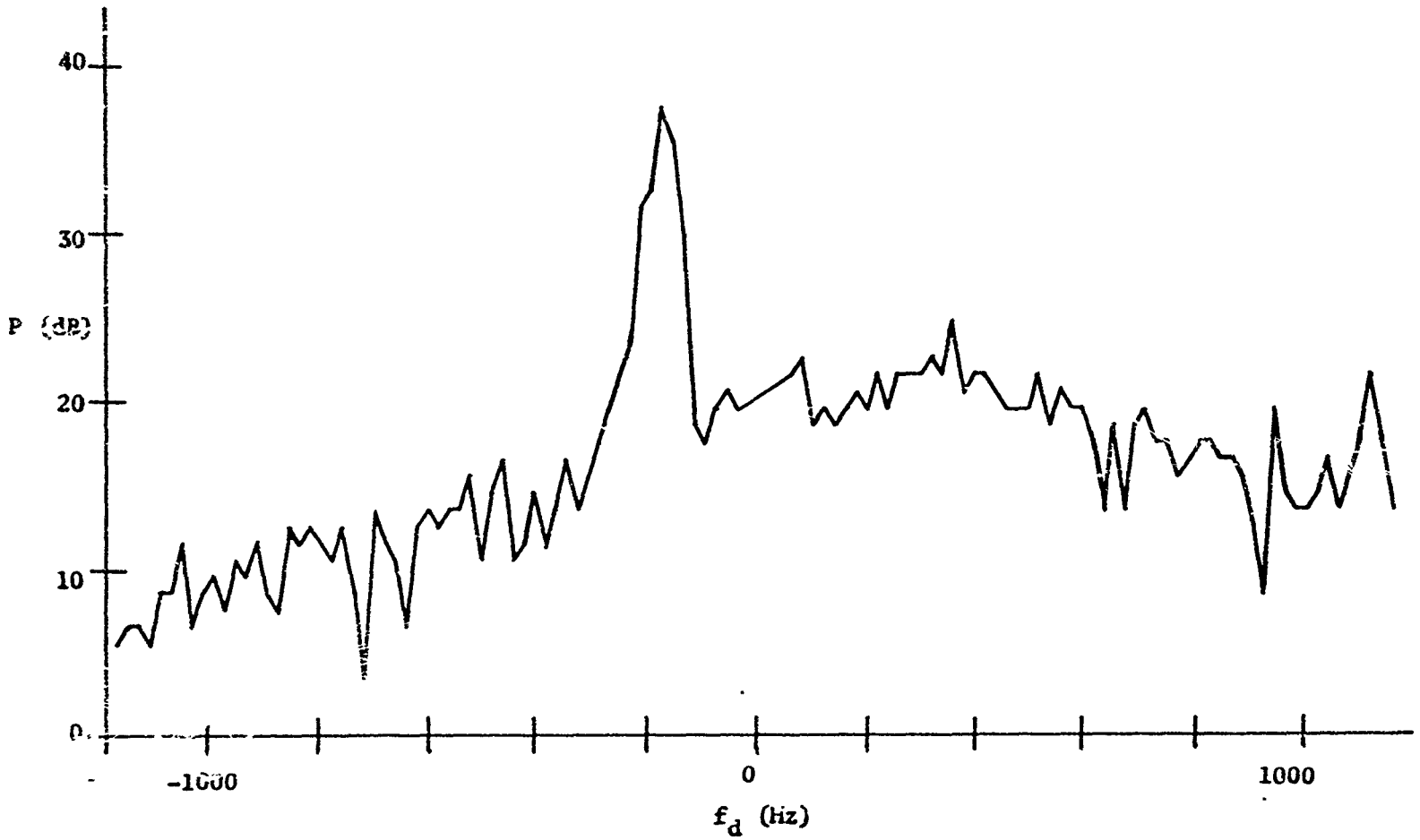


Figure 4-32. C-141 Vortex Spectrum, Run 2-2, t = 17.8

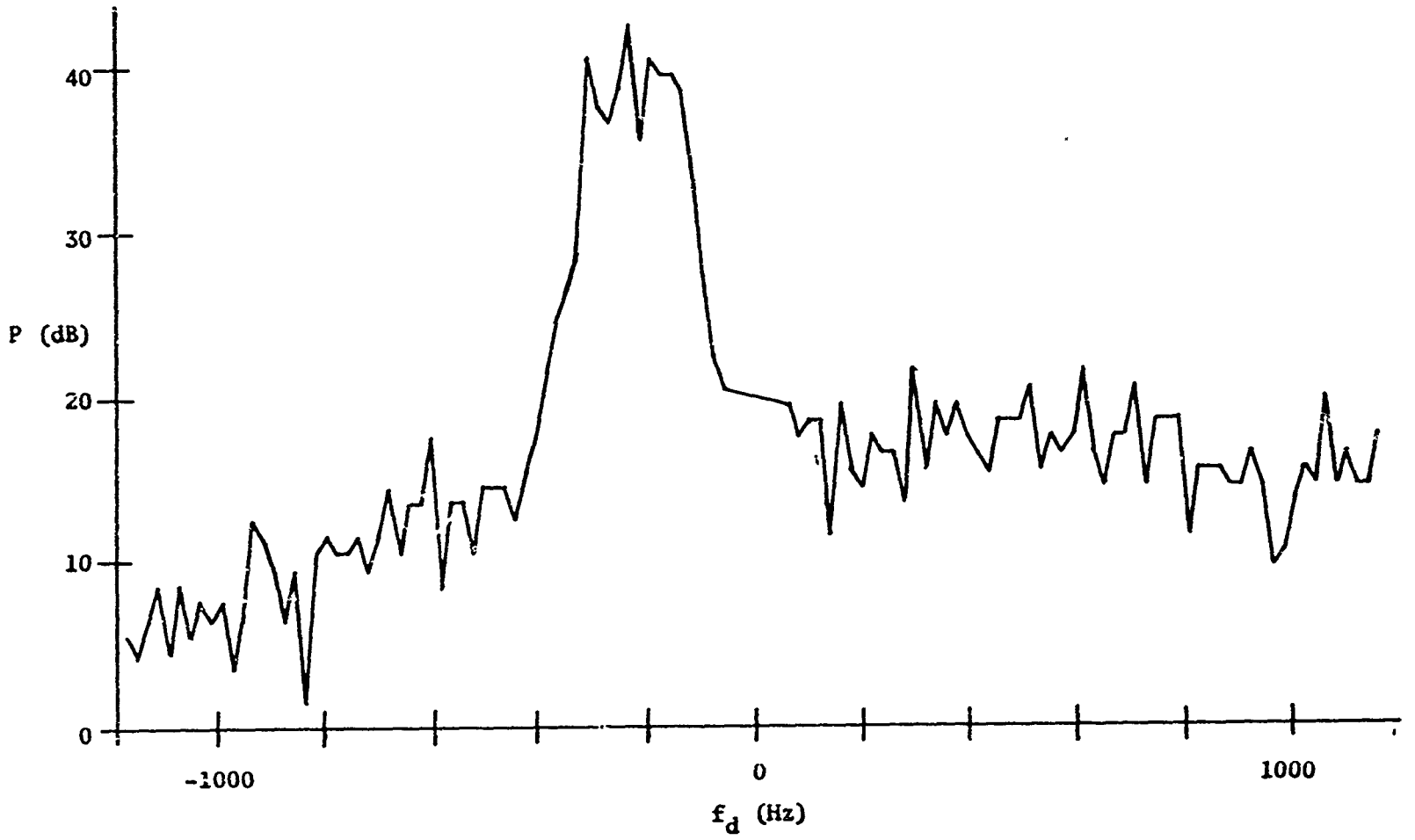


Figure 4-33. C-141 Vortex Spectrum, Run 2-2, t = 20.1

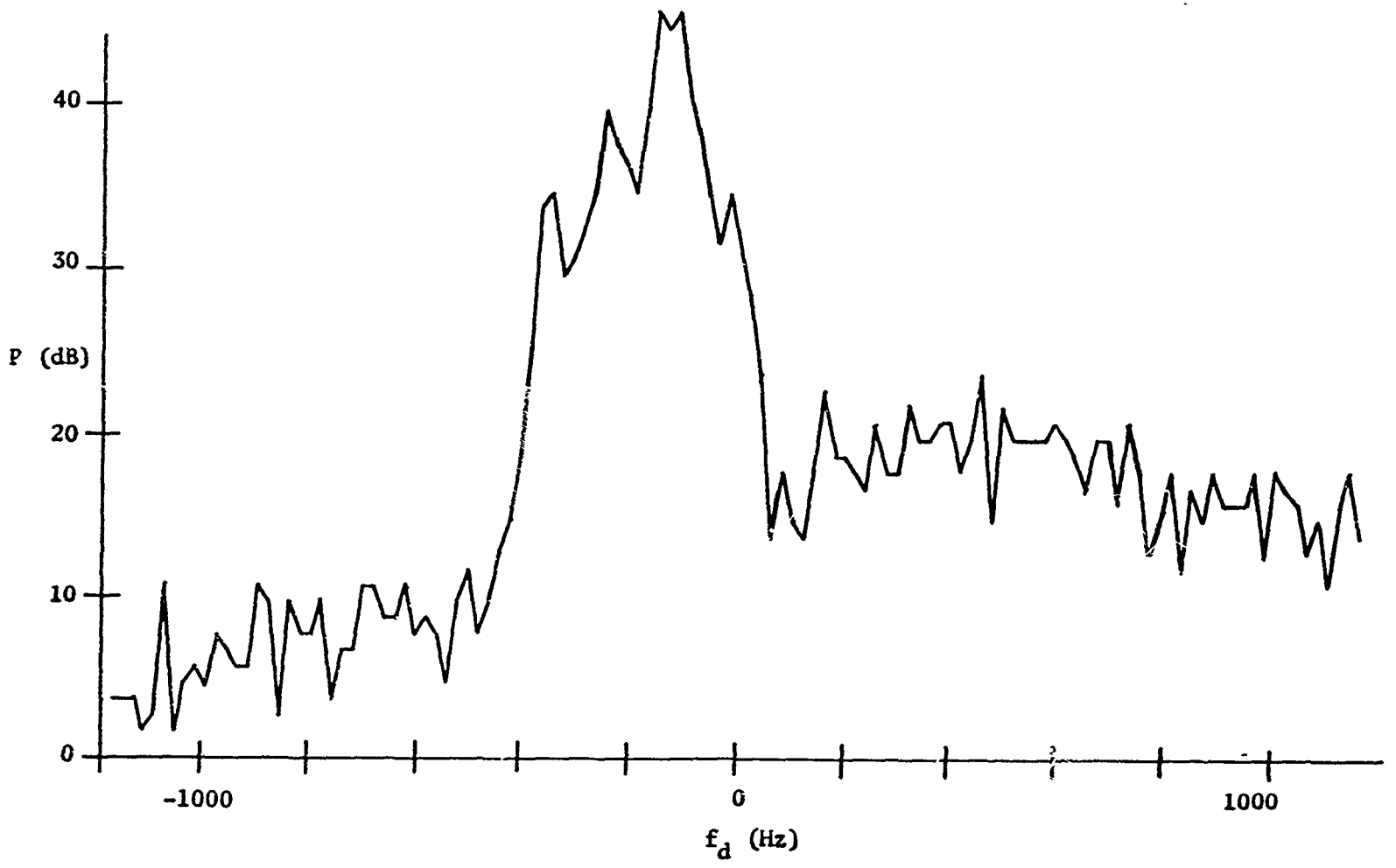


Figure 4-34. C-141 Vortex Spectrum, Run 2-2, t = 20.7

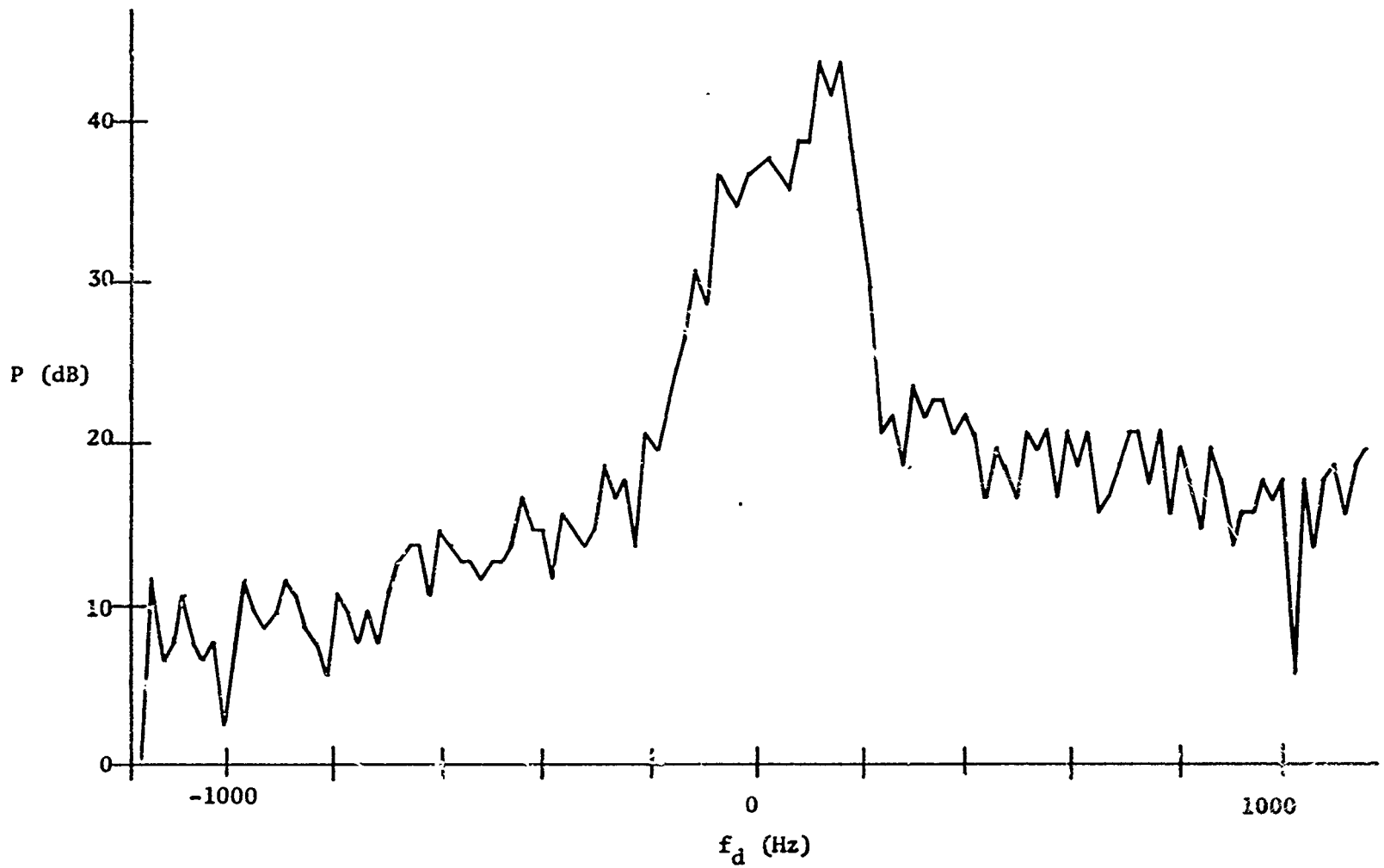


Figure 4-35. C-141 Vortex Spectrum, Run 2-2, t = 22.1

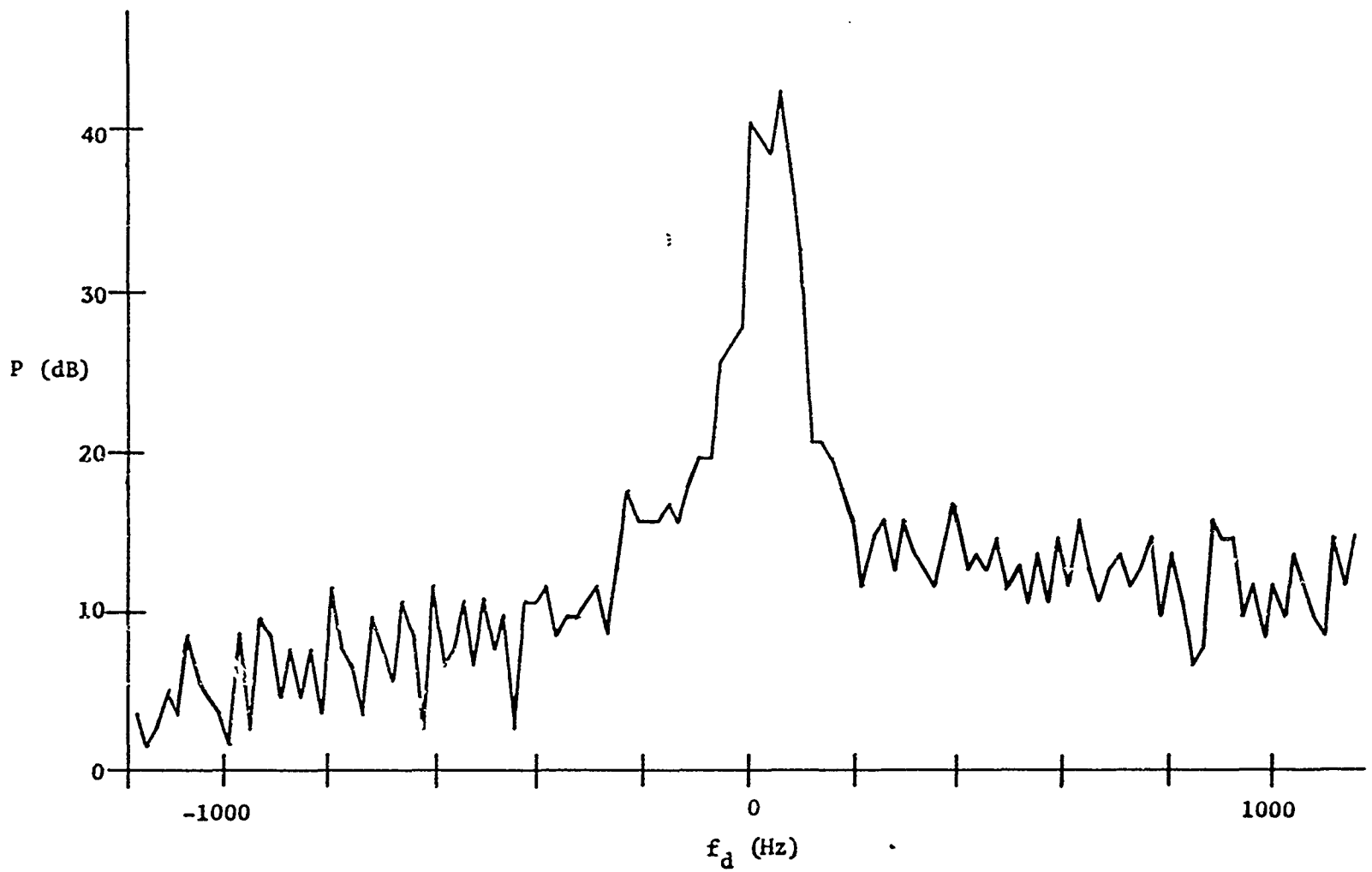


Figure 4-36. C-141 Vortex Spectrum, Run 2-2, t = 23.3

frequency displacement (hence velocity), and the lack of a sudden increase in frequency spread as the center passes all reflect the greatly different nature of the vortex as regards its scale relative to the observation volume.

Because of some of these striking differences in the appearance of the data (the NAFEC probe data were of course correspondingly affected) it was decided that a somewhat different presentation of the velocity-vs-distance curves would be more instructive. The transformation of the time axis to a distance axis through the wind velocity and of the doppler frequency axis to a vortex velocity axis were accomplished just as with the DC-7. Instead of showing a single velocity however, the two velocities corresponding to the (usually sharp) sides of the spectrum were plotted. Outside the core, these represent the maximum and minimum velocities in the observation volume. Inside the core, they show the range of velocities within the volume. The resulting plots are shown for a number of observed C-141 vortices in Figures 4-37 through 4-47. Note that the distance axis is shown in both directions from the origin; the assumption of cylindrical symmetry was not used to combine the two sides of the vortex.

Many of these figures also show a set of points taken from the curves of velocity vs height provided by NAFEC from their probe data. (Note that in the DC-7 figures, the points were Xonics data and the solid curves NAFEC data; in the C-141, these roles are reversed). Again, it must be recalled that the NAFEC probe data provide a vertical cut through the vortex center, the acoustic radar data a horizontal cut. In some cases, a velocity bias was added to the NAFEC data to make them more symmetric. The biases, of the order of a few ft/sec, could have been due to changes in wind velocity, which assume greater importance when the maximum vortex velocity is only a few times that amount.

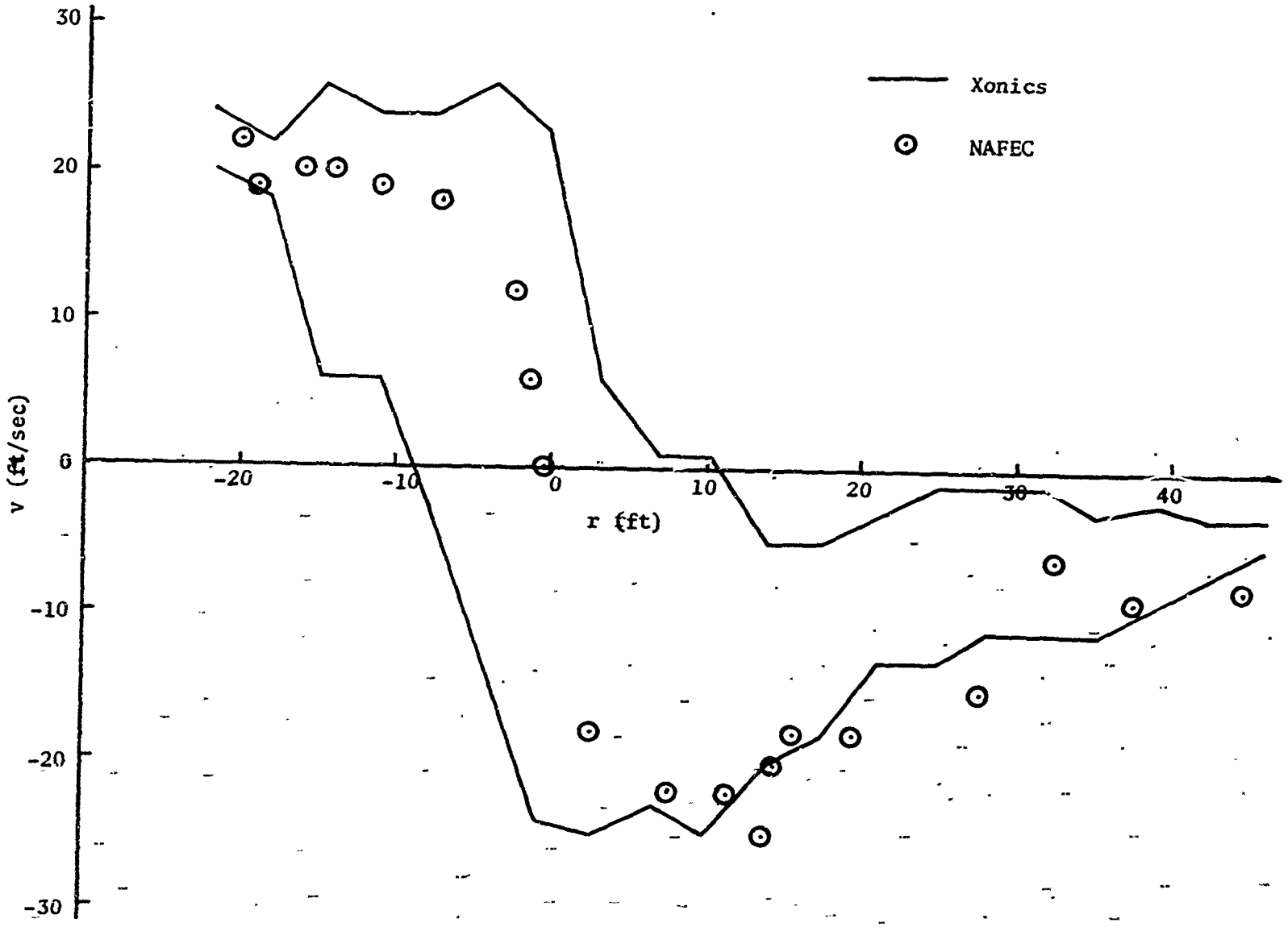


Figure 4-37. Velocity vs Radial Distance for C-141, Run 2-1

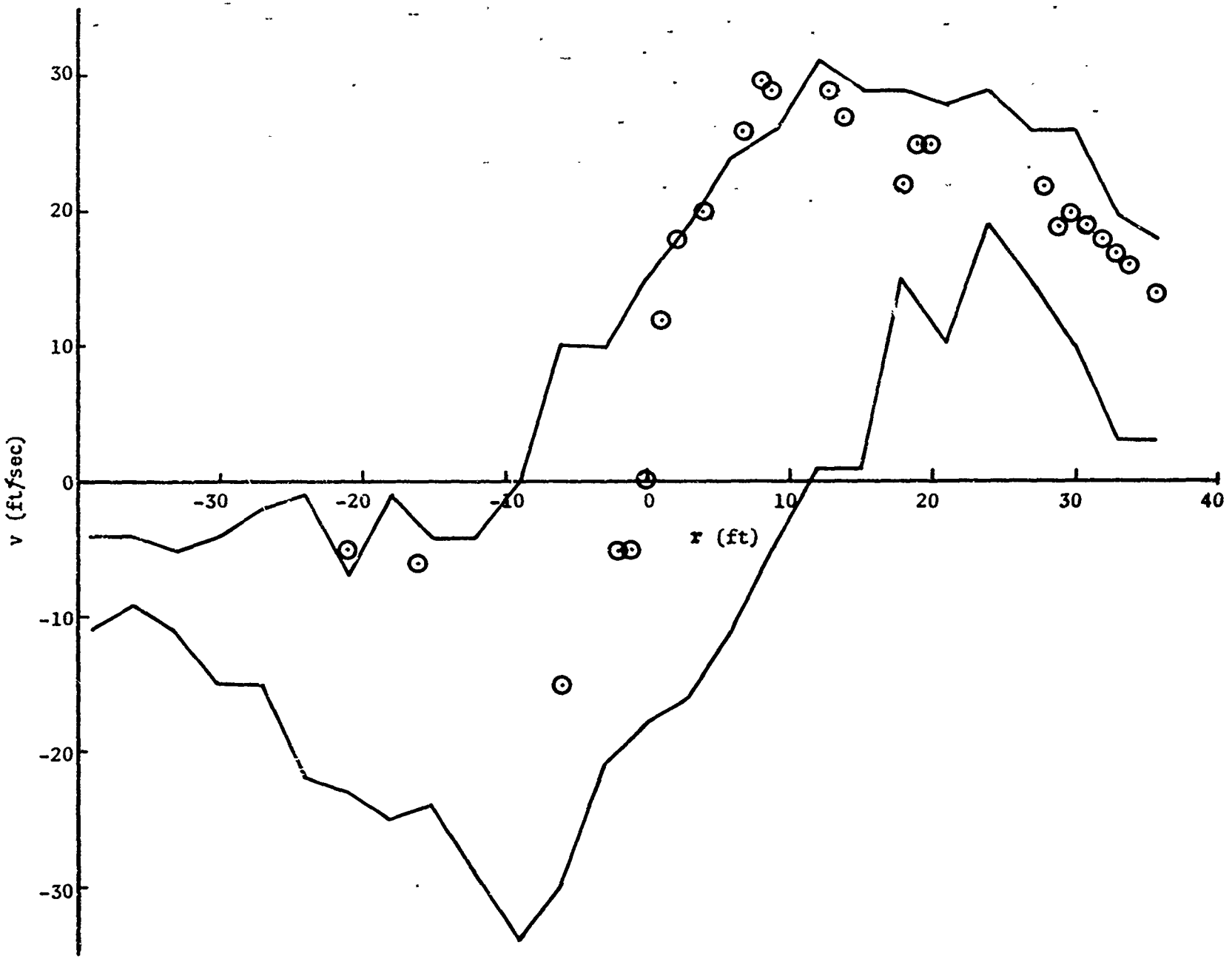


Figure 4-38. Velocity vs Radial Distance for C-141, Run 2-2

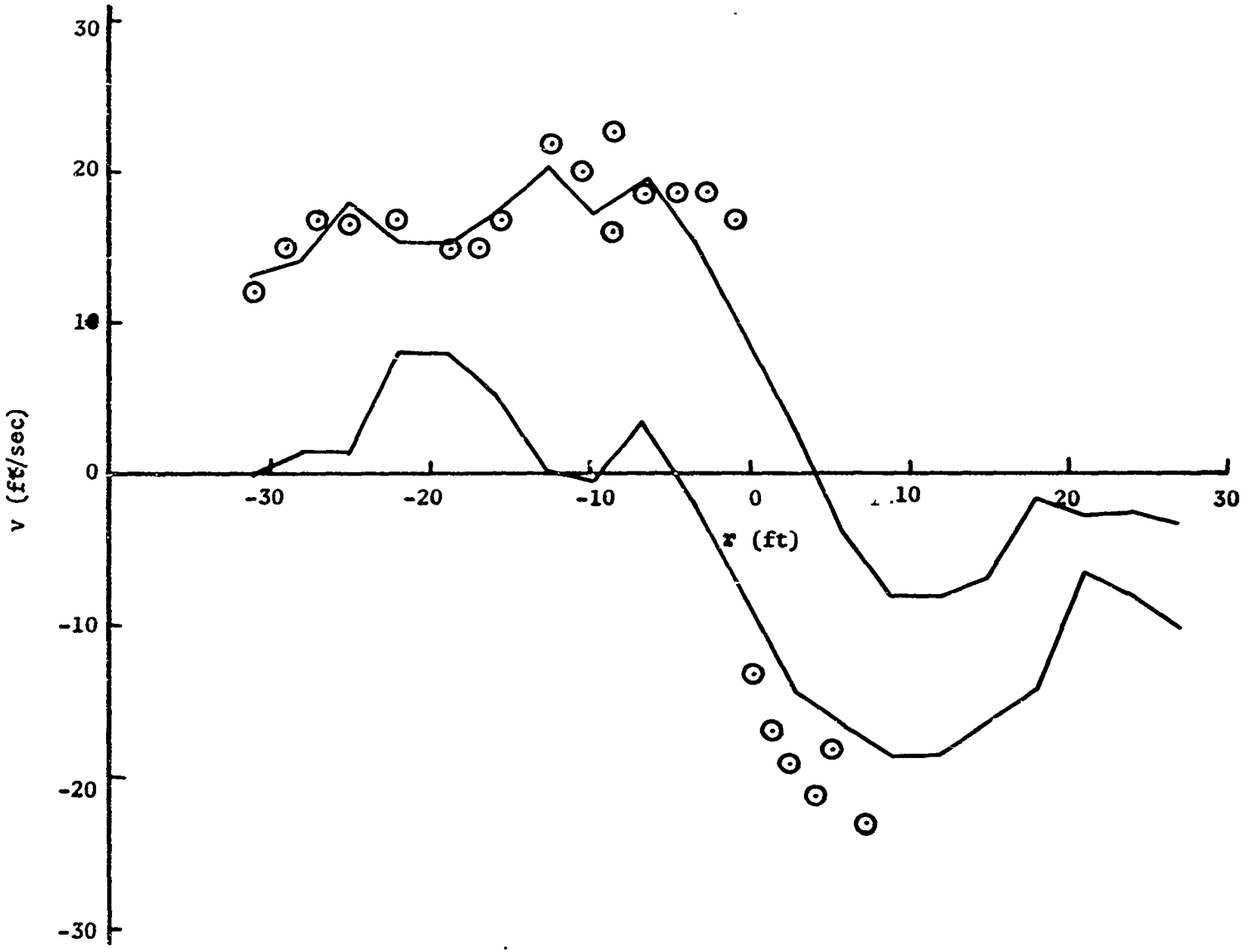


Figure 4-39. Velocity vs Radial Distance for C-141, Run 4-1

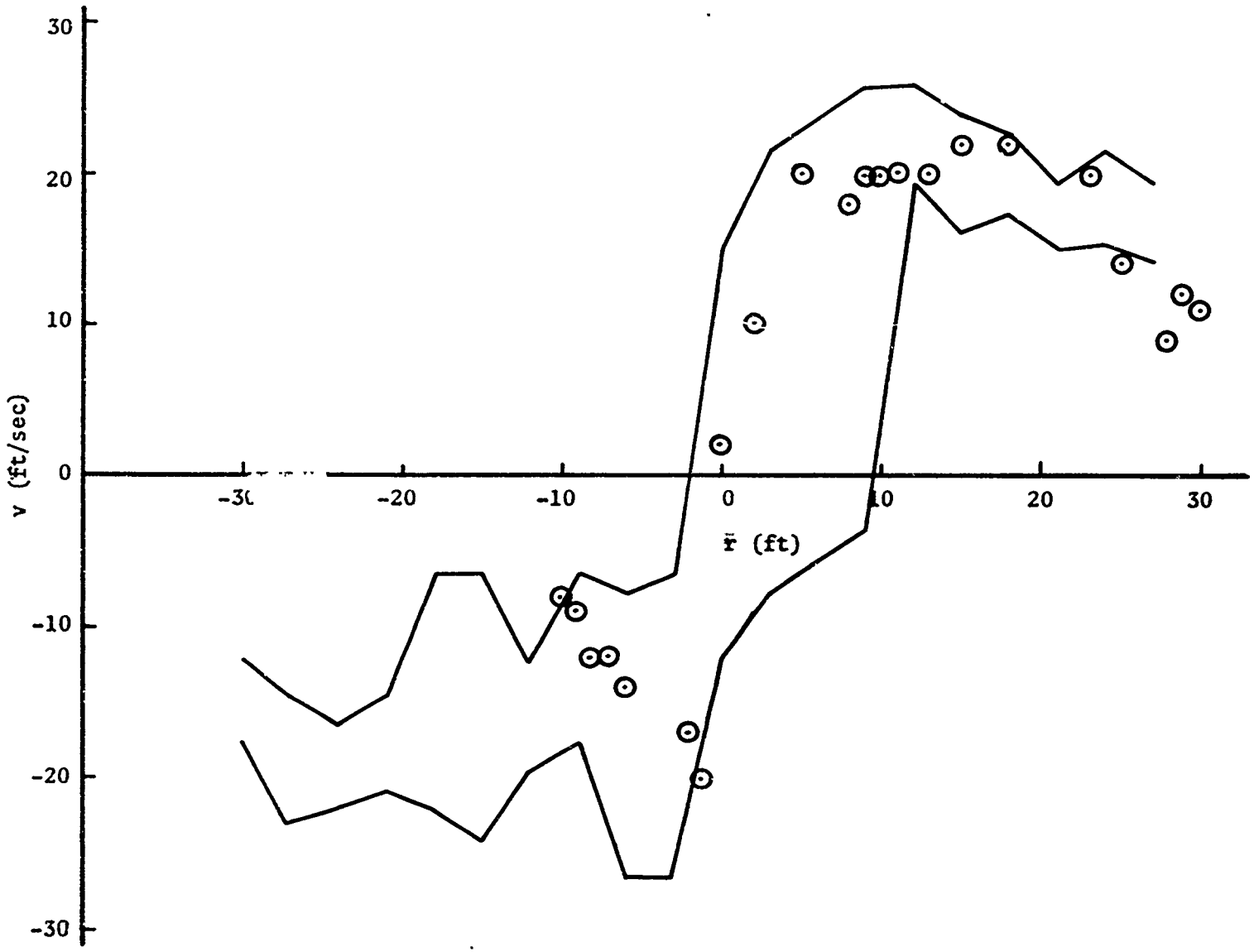


Figure 4-40. Velocity vs Radial Distance for C-141, Run 4-2

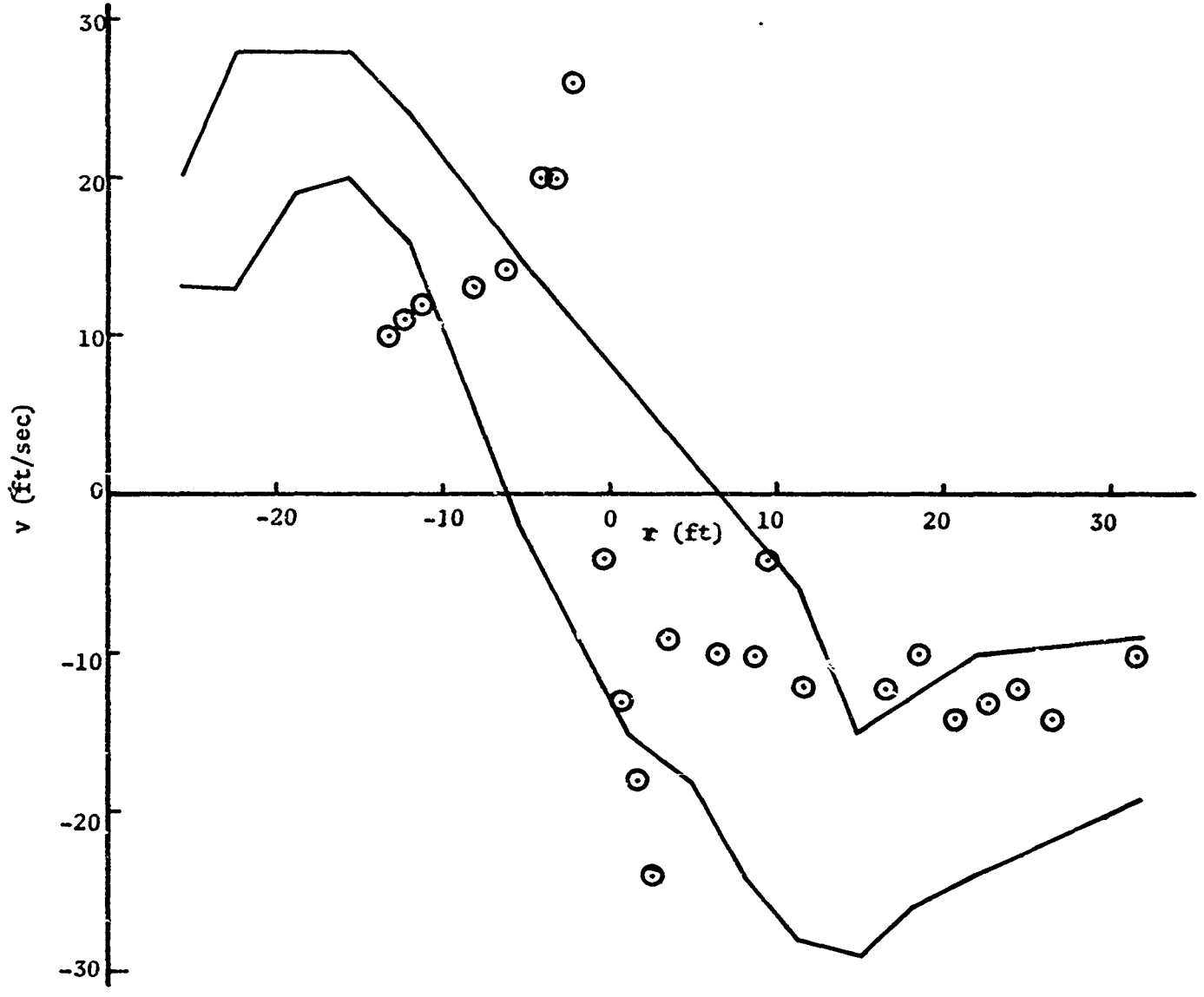


Figure 4-41. Velocity vs Radial Distance for C-141, Run 6-1

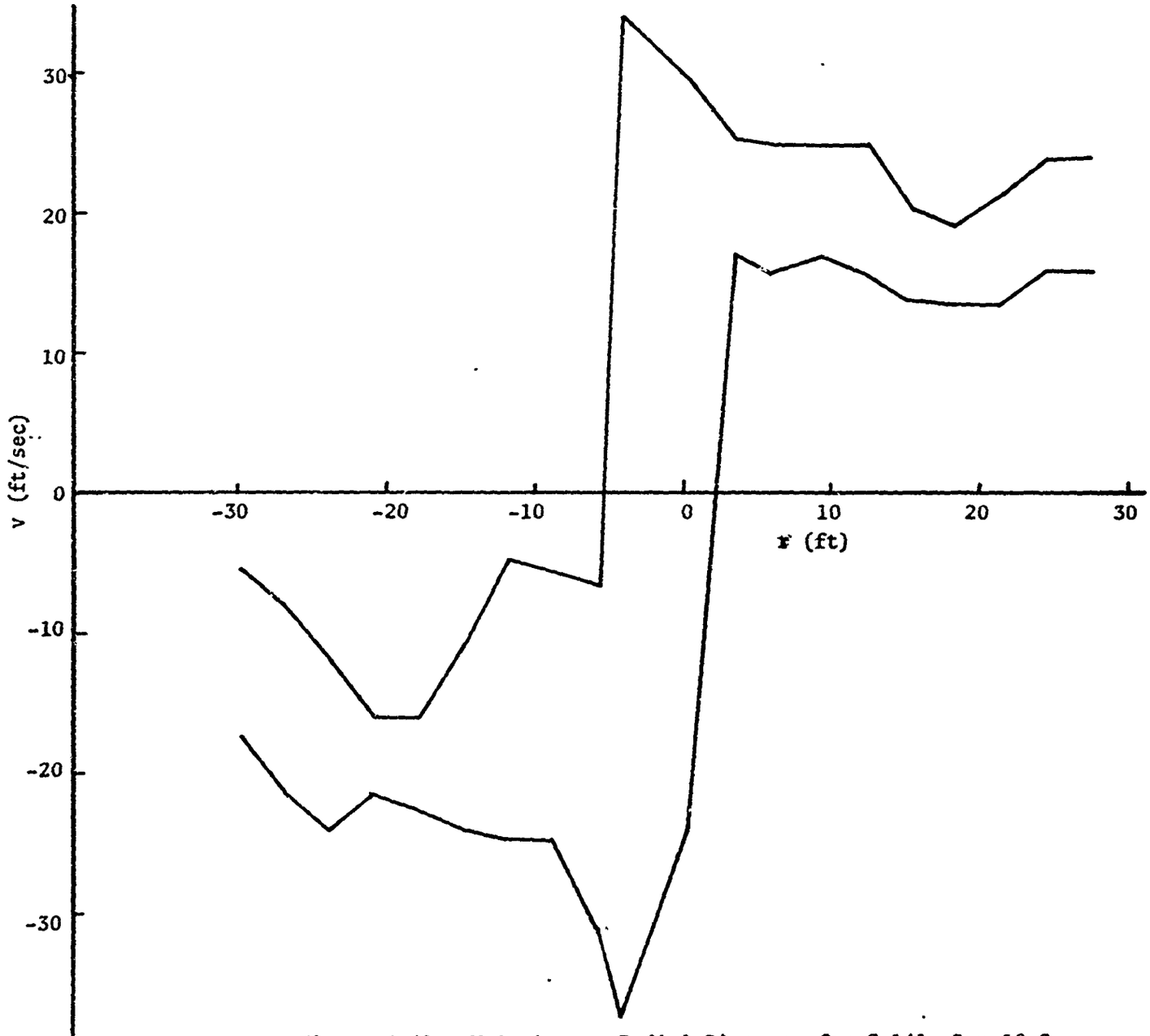


Figure 4-42. Velocity vs Radial Distance for C-141, Run 10-2

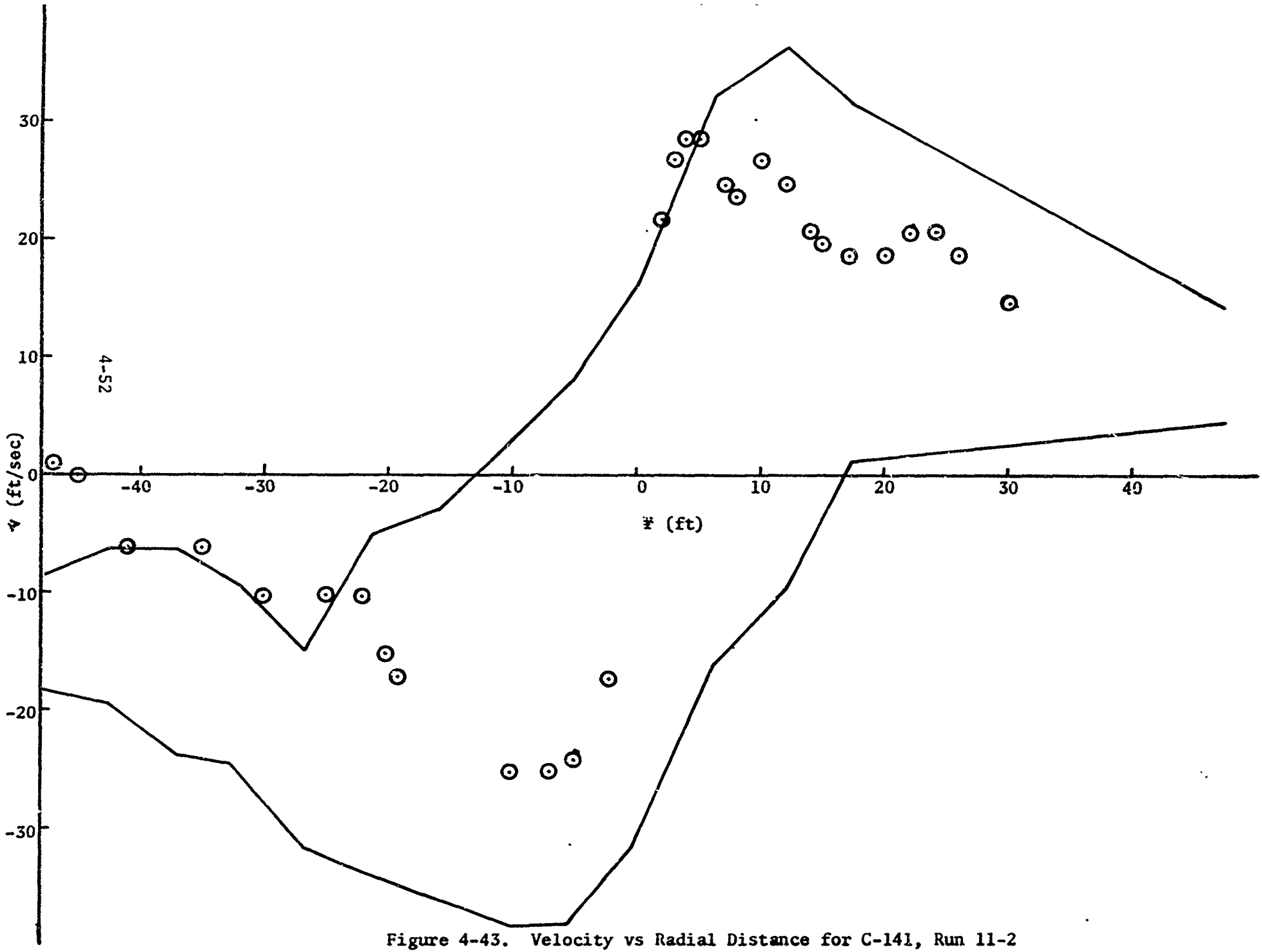


Figure 4-43. Velocity vs Radial Distance for C-141, Run 11-2

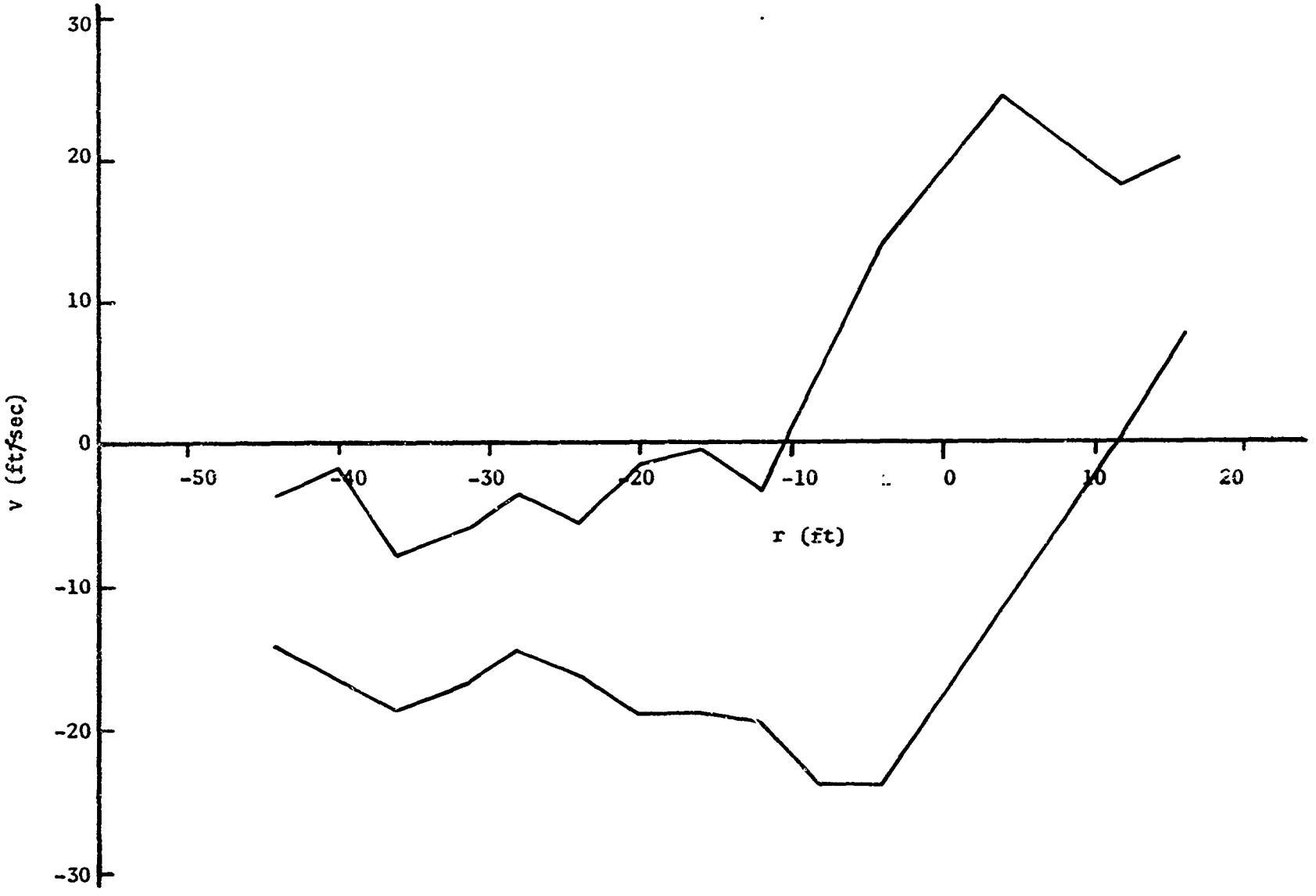


Figure 4-44. Velocity vs Radial Distance for C-141, Run 12-2

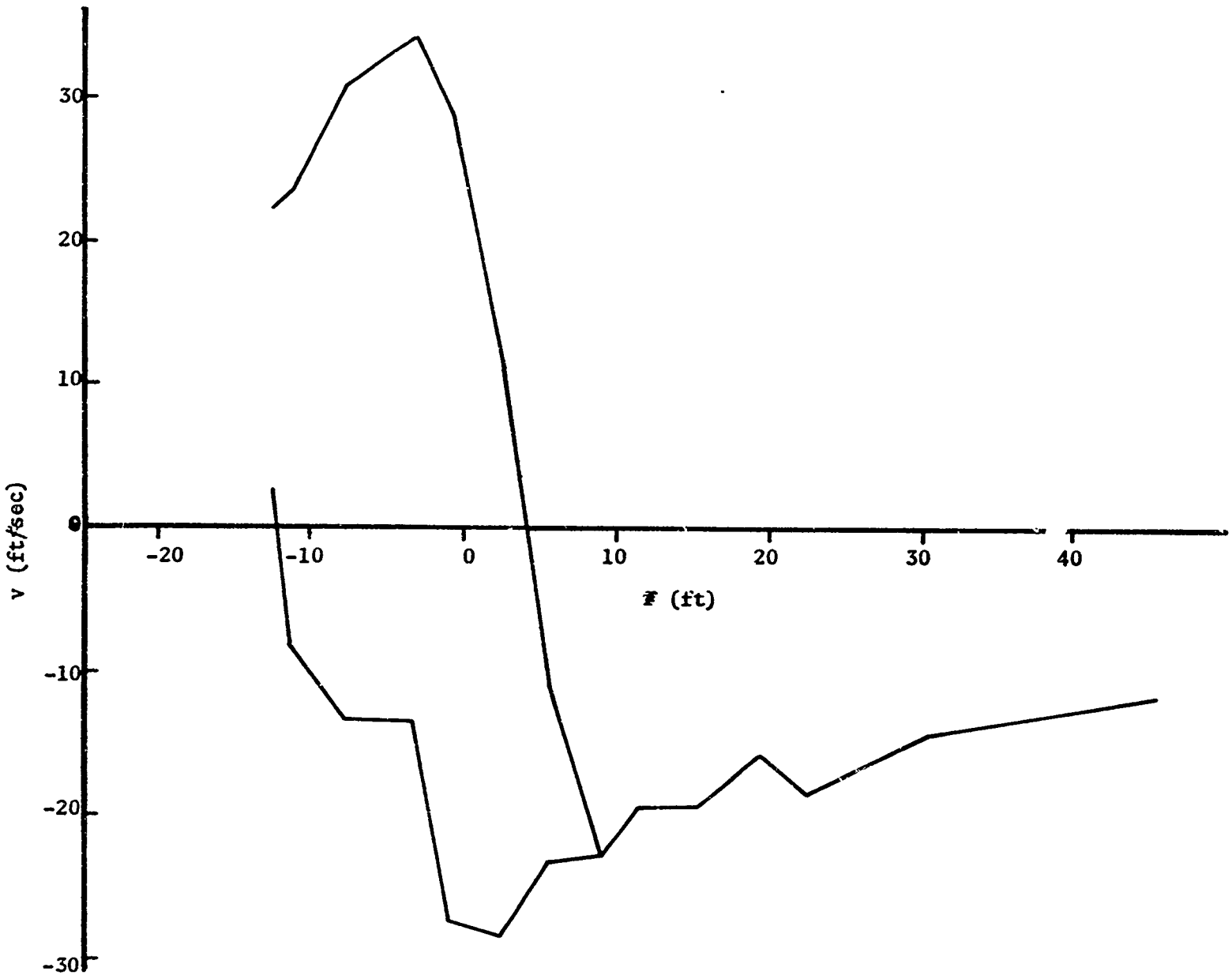


Figure 4-45. Velocity vs Radial Distance for C-141, Run 16-1

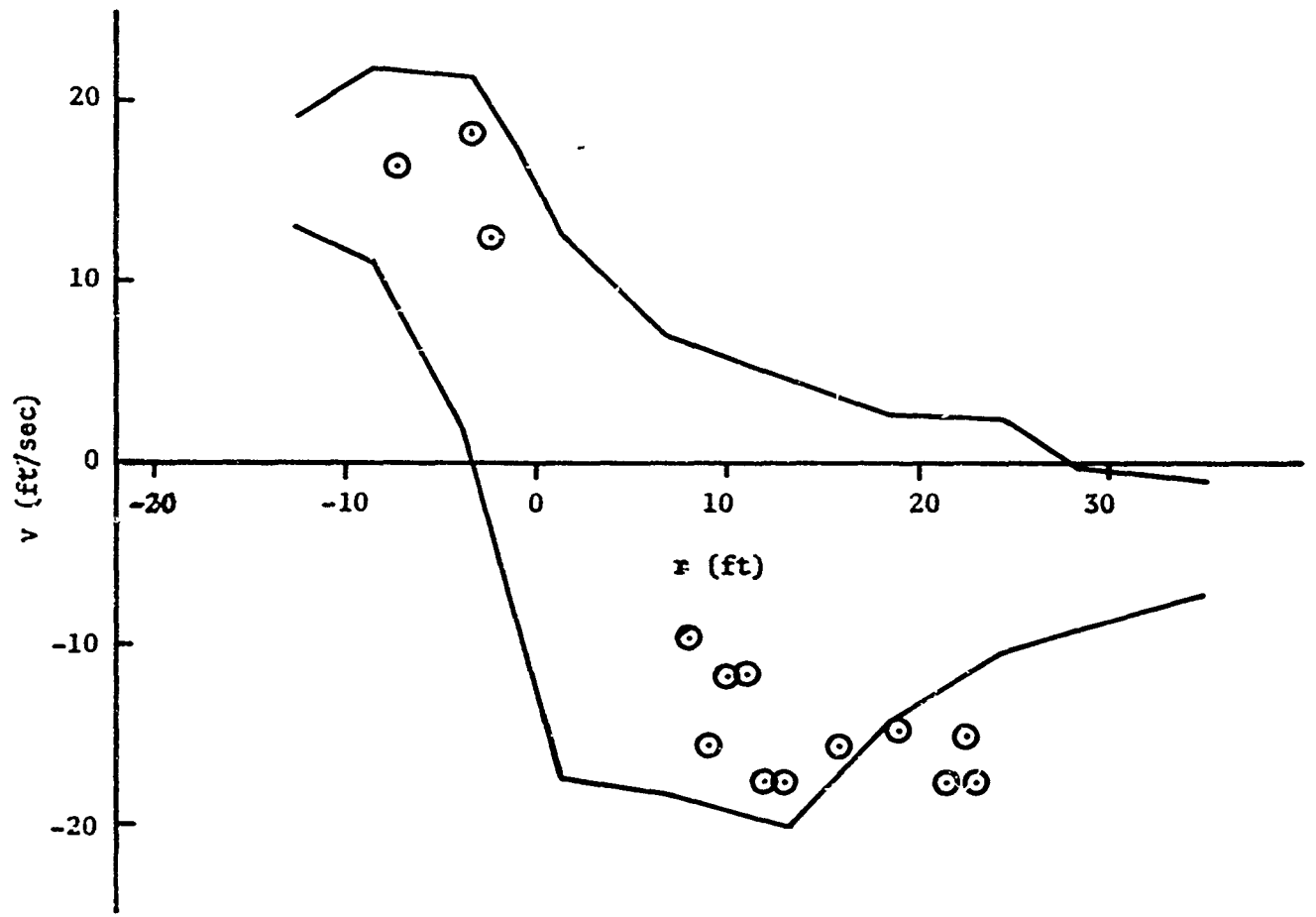


Figure 4-46. Velocity vs Radial Distance for C-141, Run 18-1

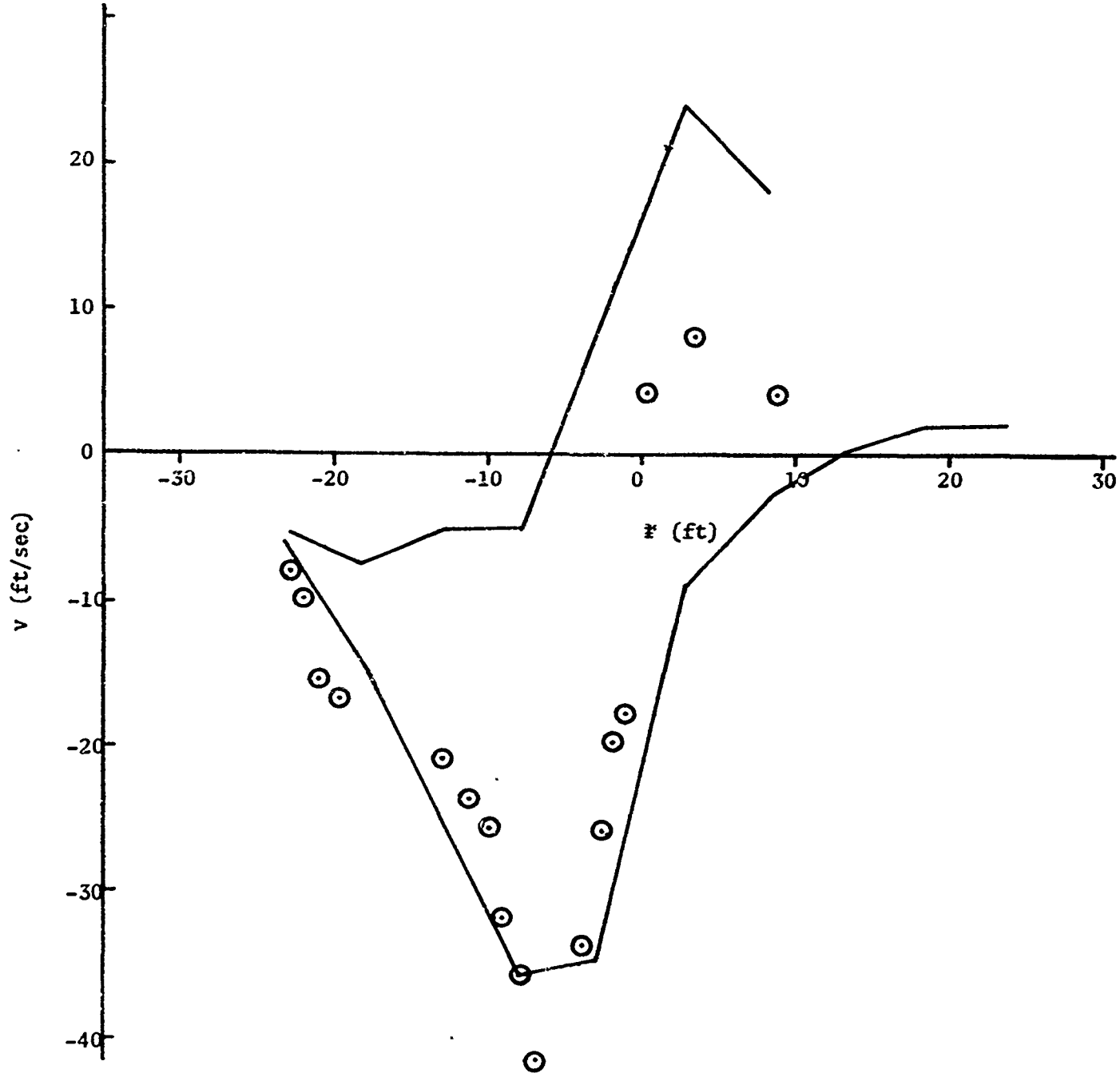


Figure 4-47. Velocity vs Radial Distance for C-141, Run 18-2

In general, the agreement between the two sources of data is again good. The scale of the C-141 vortex is seen to be quite large, and the maximum vortex velocity is quite consistently found to be around 30 ft/sec by both sensors. In a couple of cases, however, some discrepancy in detail does appear. For example, in Figure 4-41, the acoustic data look similar to a number of others, while the probe data show the maximum velocity very close to the center and a very rapid drop-off beyond there. This latter behavior does not seem reasonable (for example, the circulation may be seen to drop sharply beyond the radius of maximum velocity) and it is suggested that further examination of the original data is warranted.

## 4.4 C-5A Results

The third aircraft that was scheduled for these tower tests, and the one that was to represent the class of large heavy aircraft that pose the most serious vortex threat, was the C-5A. A series of runs was accomplished on the one day that aircraft was made available. Unfortunately, from the point of view of interpreting the data, there was virtually no wind during those runs. Since the uniform translational motion caused by the wind plays a large part in identifying the center and establishing the scale of the vortex in the tower configuration, interpretation of the observables in terms of vortex structure is rendered quite difficult by the absence of steady wind and the consequent erratic motion of the vortex. Further tests to compensate for this lack of data that could be studied with confidence would not be run because the aircraft became unavailable due to other Air Force requirements.

Two samples of the data taken during the C-5A tests are shown in Figures 4-48 and 4-49. They are similar in format to the curves of vortex velocity vs distance for the C-141. The character of the vortex is found to be much like that of the C-141, with a very large

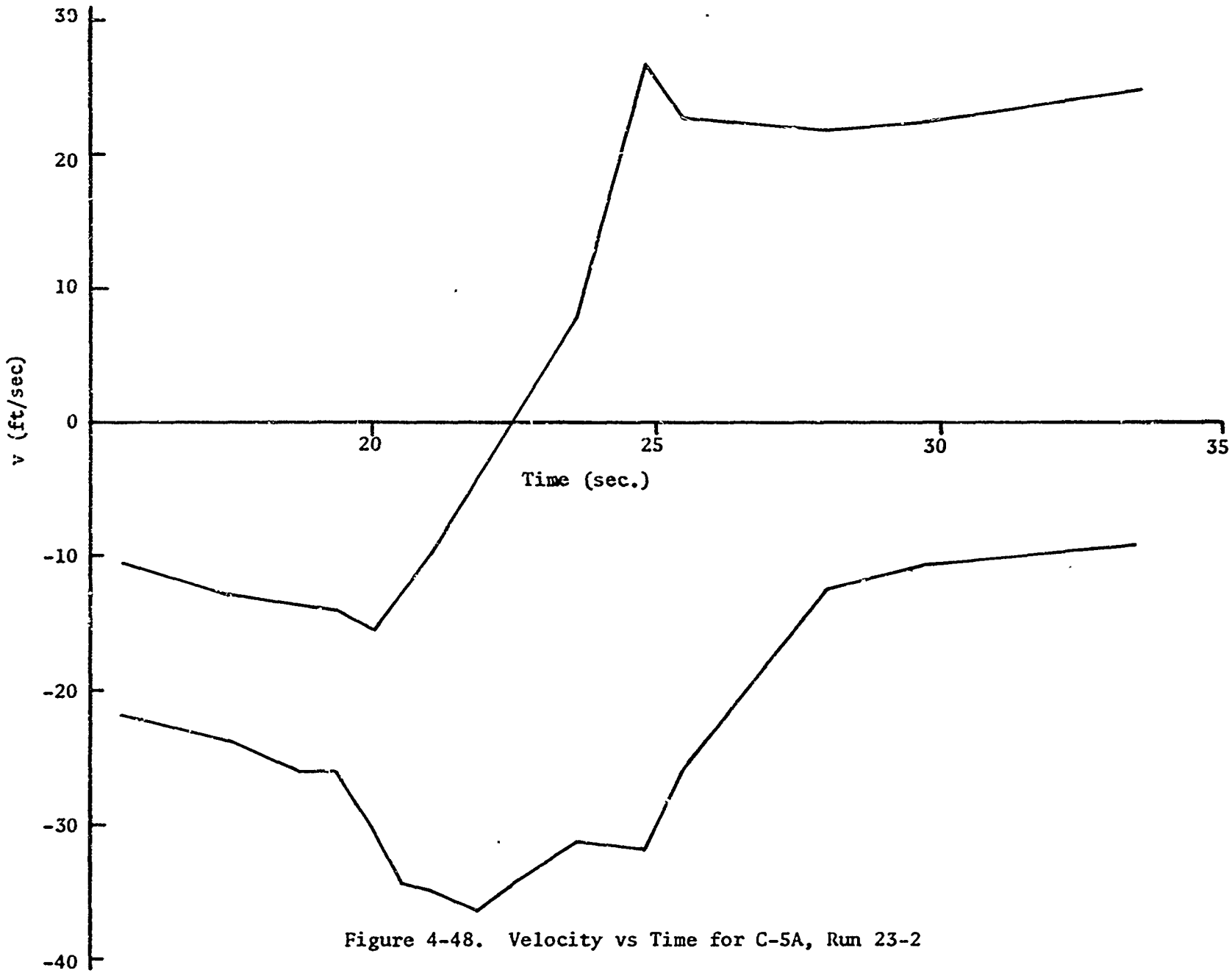


Figure 4-48. Velocity vs Time for C-5A, Run 23-2

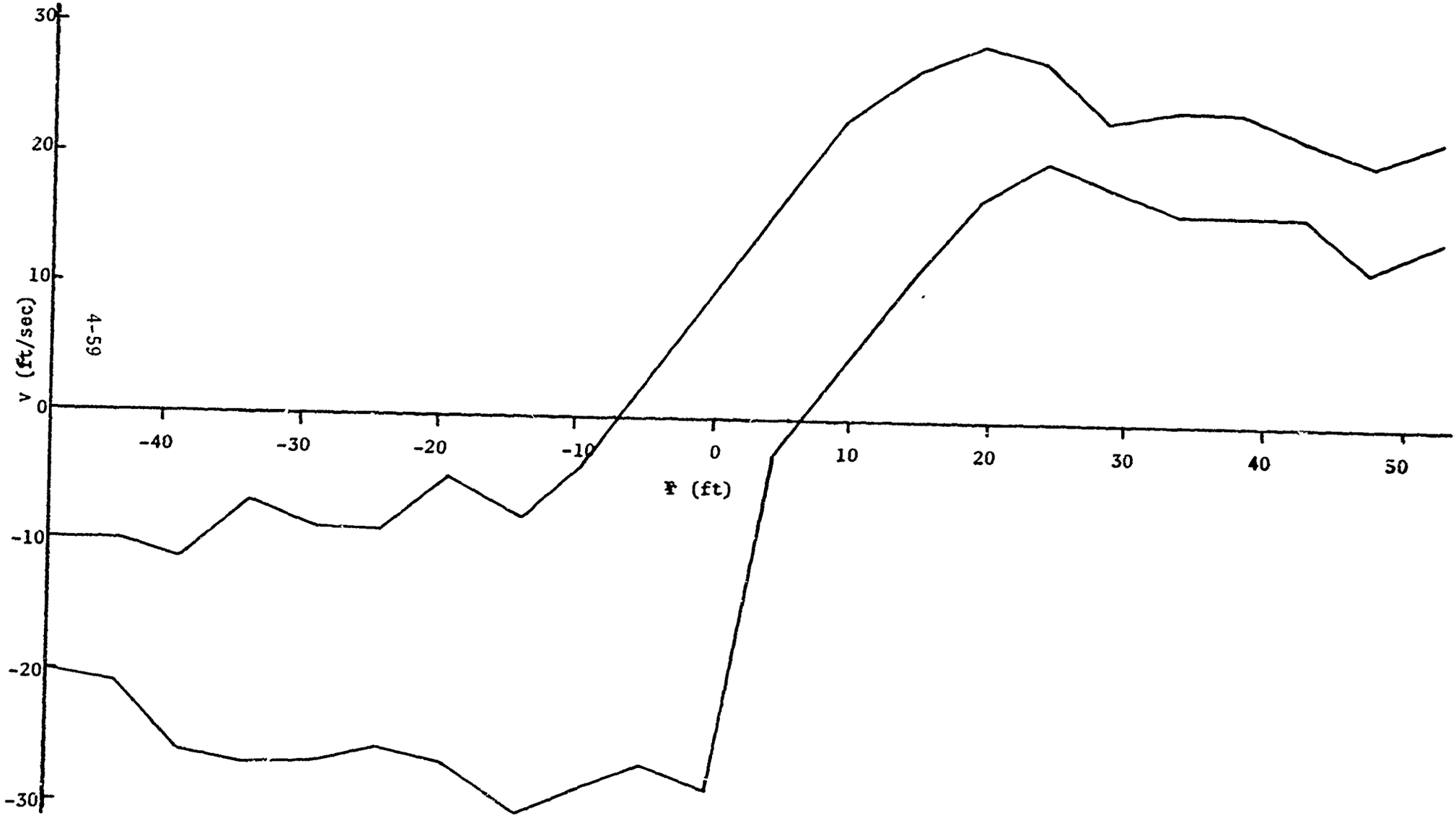


Figure 4-49. Velocity vs Radial Distance for C-5A, Run 32-2

core and peak velocities of about 30 ft/sec. In Figure 4-48, the vortex velocities of run 23-2 are shown plotted against time, since the lack of any consistent wind made the conversion to distance impossible in this case. In many other cases, an almost total lack of wind led to very erratic dependence of observed velocity vs time. One example was obtained in which the wind appeared to be steady enough to convert the time axis to distance. The vortex velocities of run 32-2 are therefore shown plotted against radial distance in Figure 4-49. It can be seen that the spatial extent over which tangential velocities remain significant is over 100 ft in diameter.

## 4.5 Other Aircraft Results

Although the original test schedule called for observation and data analysis of runs of only the three aircraft just discussed, a number of runs by other aircraft were observed, since the personnel and equipment were prepared for operation at those times. The two other aircraft were the CV-880 and the DC-9. A limited amount of data processing and analysis have been carried out for these runs.

Four examples of the processed results of CV-880 run are shown in Figures 4-50 through 4-53. The processing was again the same as was done for the C-141 data. The shape of the velocity vs distance curves is very similar to that observed for the C-141, but examination of the figures reveals that both the core size and the peak velocities are smaller than those for the C-141. As before, the agreement with the corresponding NAFEC probe data is quite good.

A number of DC-9 runs were observed while they were being conducted for other purposes at NAFEC. All of these incidentally were accompanied by smoke grenades for flow visualization. Examples of the observed velocity vs distance curves are shown for three of the vortices in Figures 4-54 through 4-56.

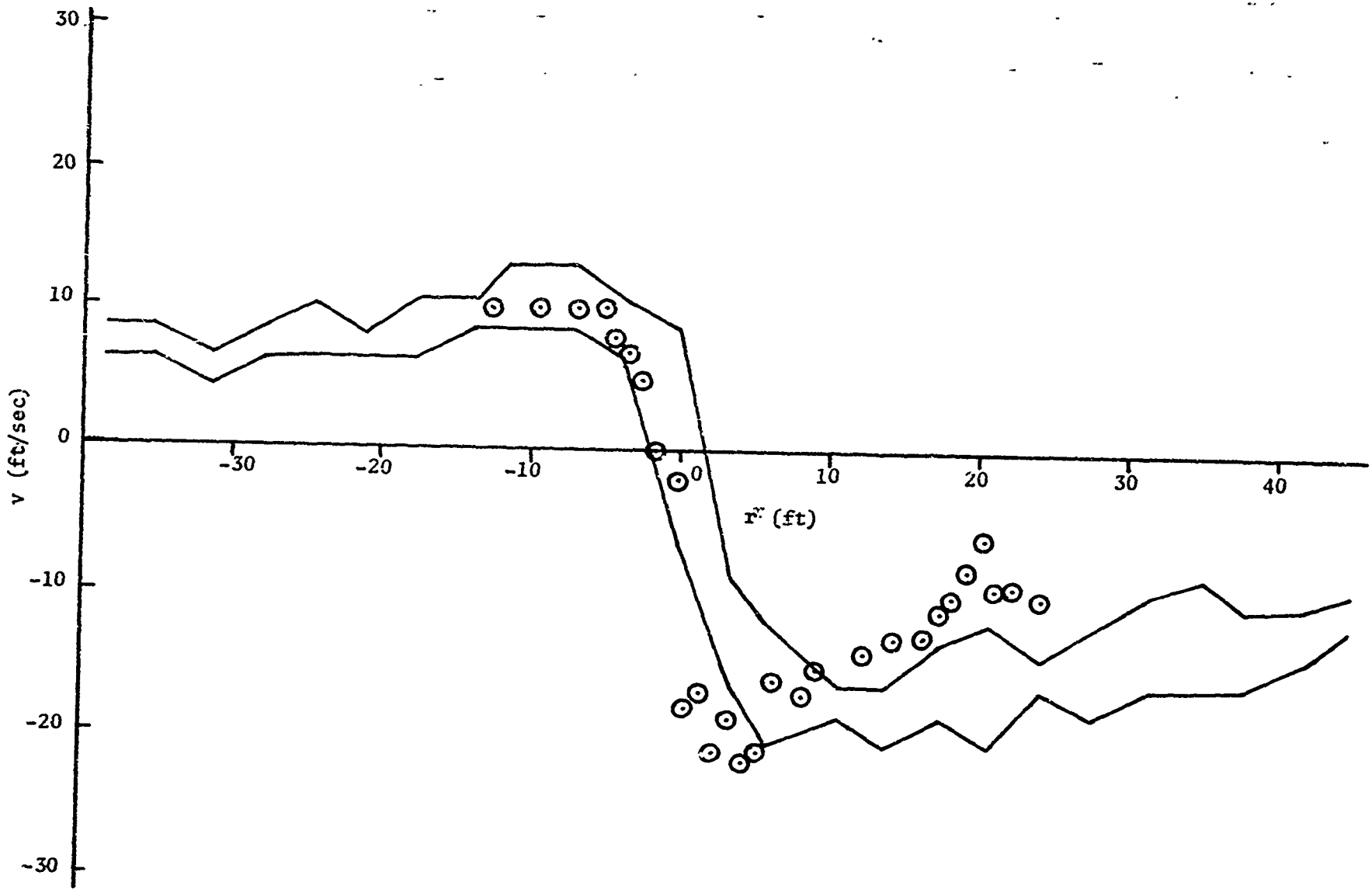


Figure 4-50. Velocity vs Radial Distance for CV-880, Run 32-1

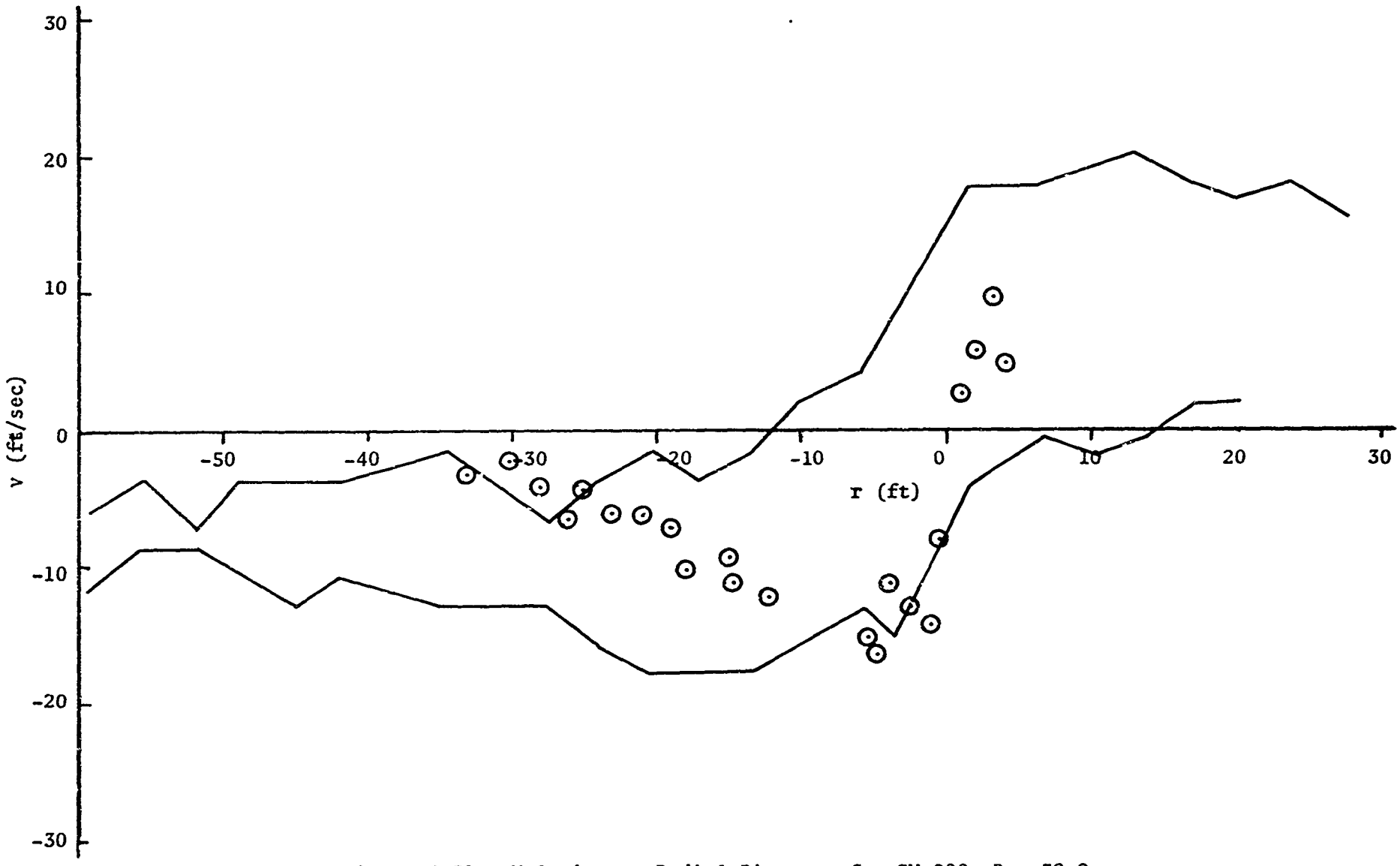


Figure 4-51. Velocity vs Radial Distance for CV-880, Run 32-2

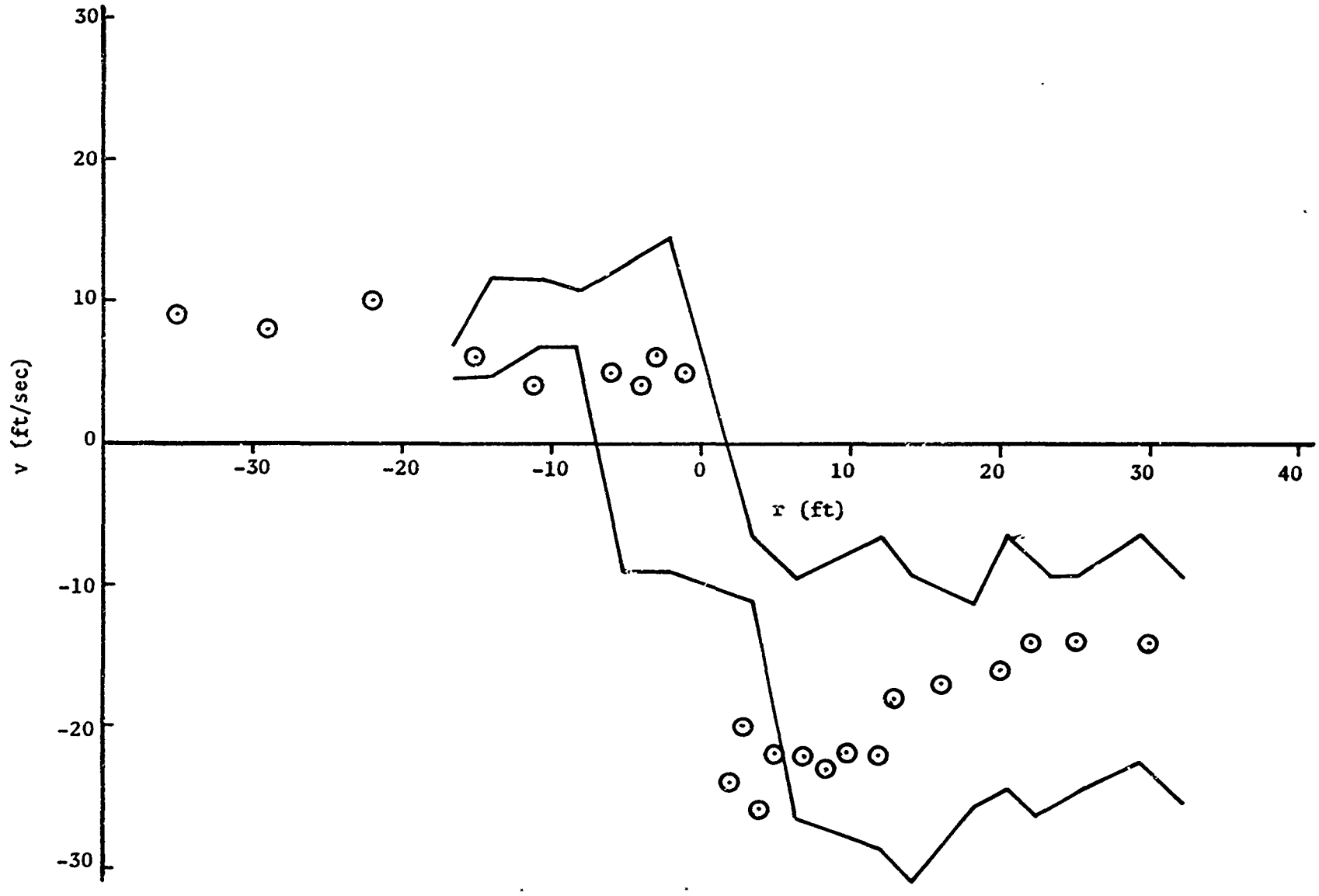


Figure 4-52. Velocity vs Radial Distance for CV-880, Run 36-1

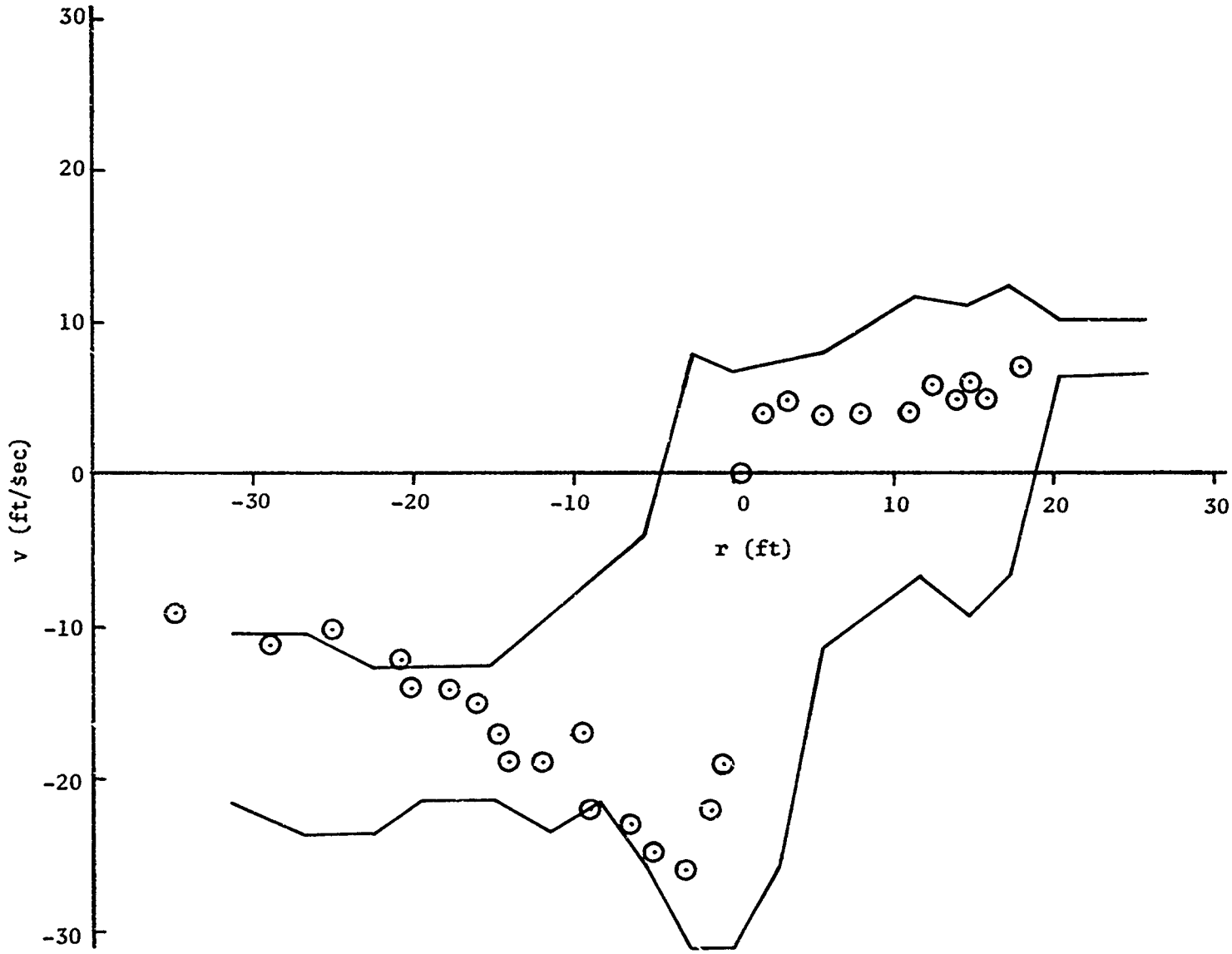


Figure 4-53. Velocity vs Radial Distance for CV-880, Run 36-2

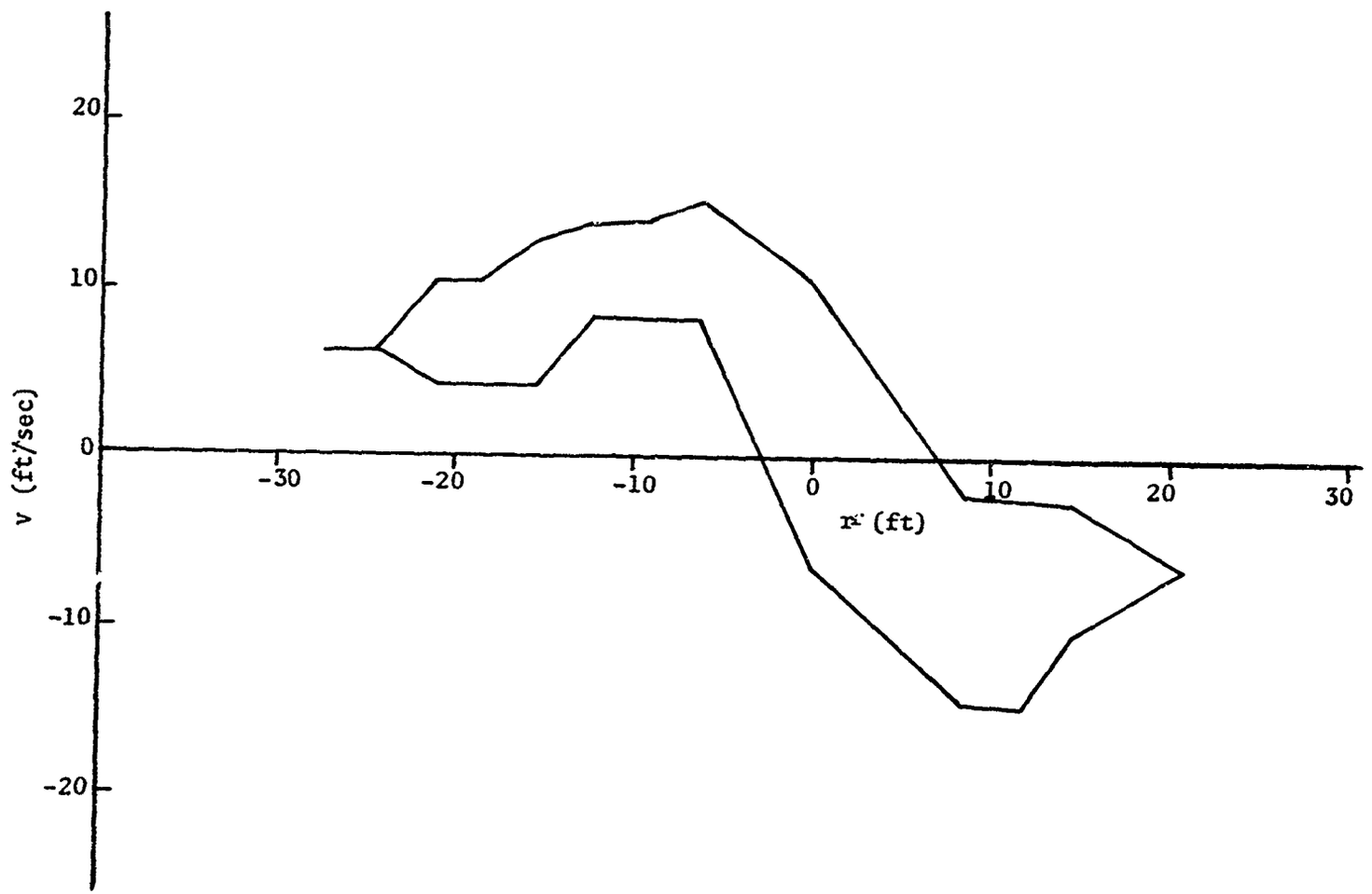


Figure 4-54. Velocity vs Radial Distance for DC-9, Run 12-1

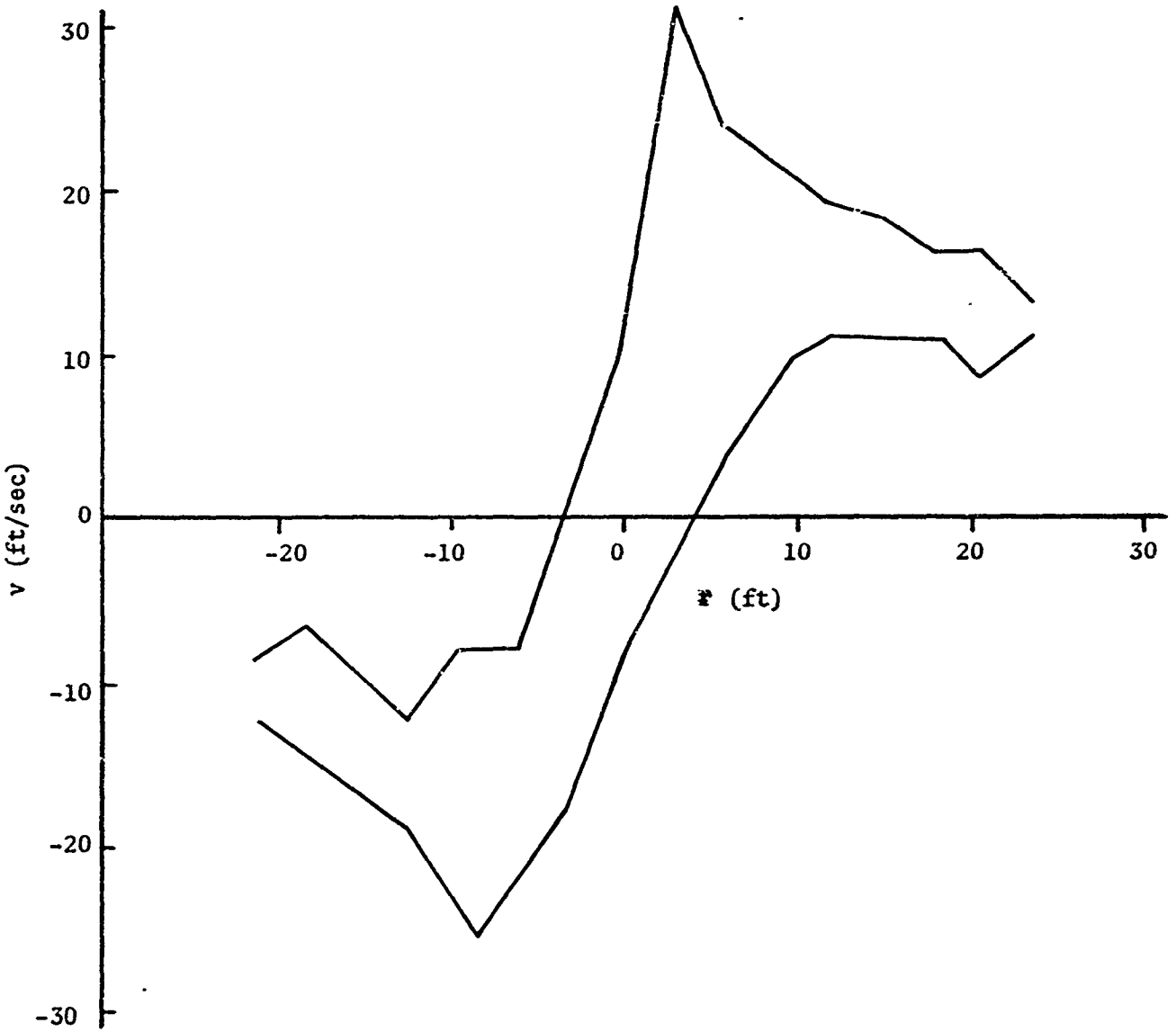


Figure 4-55. Velocity vs Radial Distance for DC-9, Run 12-2

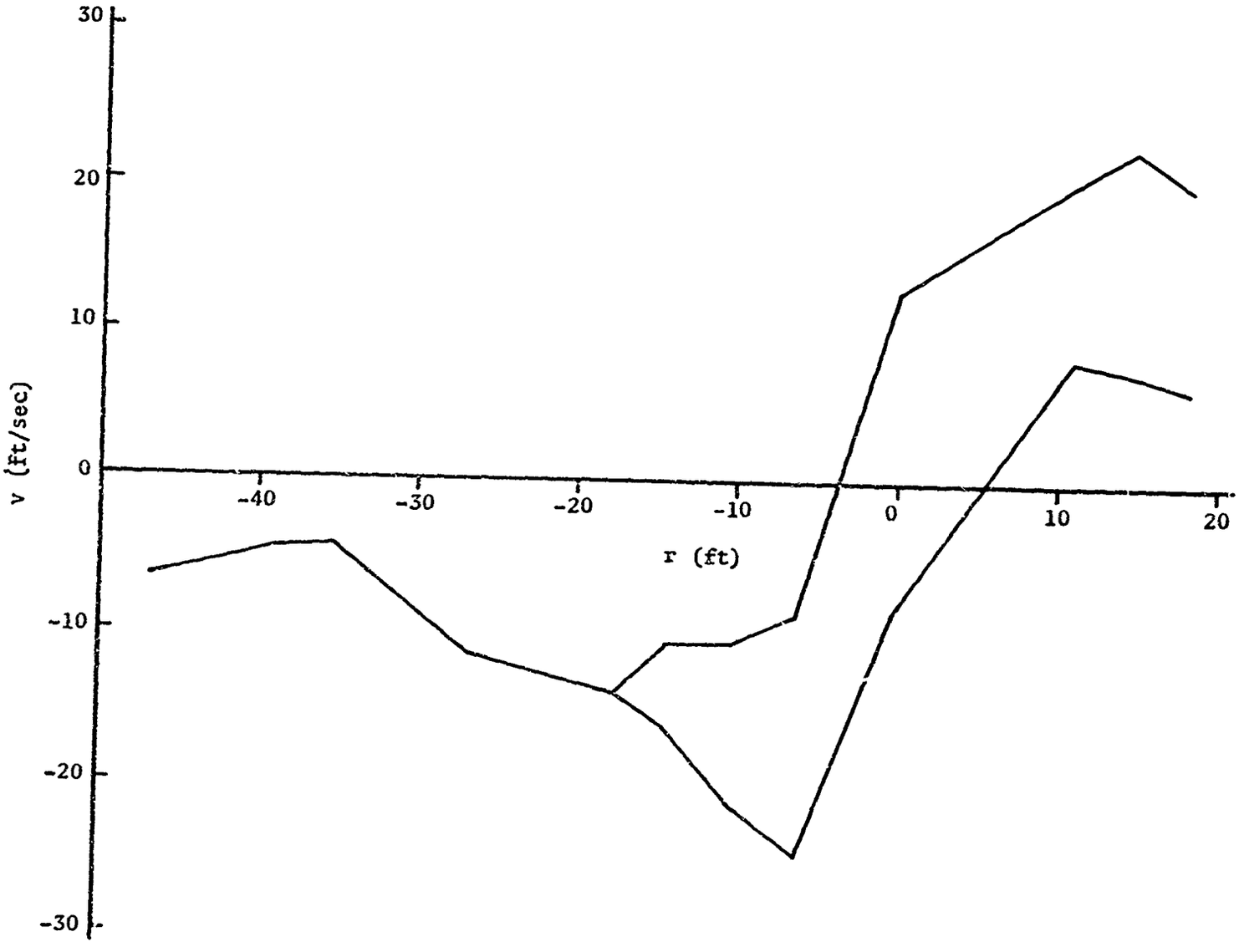


Figure 4-56. Velocity vs Radial Distance for DC-9, Run 23-2

## 4.6 Discrimination Results

The emphasis in presenting the data of these current tower tests has so far been on their physical interpretation, correlation with the model, and comparison with the corresponding NAFEC probe data. Let us now turn to the question of deducing the circulation as an indication of vortex strength and hazard, in short, to discrimination.

Before examining the available data in detail, it can be noted immediately that the tests fell considerably short of providing the broad range of vortex strength that could beused in a definitive study of discrimination capability. The original test schedule called for a 100,000 lb aircraft, the DC-7, a 300,000 lb aircraft, the C-141, and a 600,000 lb aircraft, the C-5A. Very little data that can be studied with high confidence were obtained for the C-5A, for reasons discussed in Section 4.4. The C-141, in fact, flew at a weight only slightly in excess of 200,000 lbs. Most of the data then correspond to a total range of circulations that is considerably less than the factor of 3 or so that was anticipated for this series of tests.

Returning first to the DC-7 results, deduction of circulation is a simple matter, given the plots of vortex velocity vs radius of Figures 4-8 to 4-31. The quantity $r \cdot v(r) = \Gamma(r)/2\pi$ can be directly replotted, and two examples are given in Figures 4-57 and 4-58, taken from Figures 4-10 and 4-14 respectively. The question of the detailed shape of the buildup of circulation at small radii is not decisively answered by these and the other similar curves; virtually every curve however shows a rather consistent value at radial distances of 10 ft or more, with variations of perhaps 10 percent or so about the mean trend. In order to summarize the results succinctly, the value of circulation (divided by $2\pi$) at 20 ft was chosen from each curve as a value representative of both the estimated circulation and the threat over the proper scale for a "typical" small encountering aircraft.

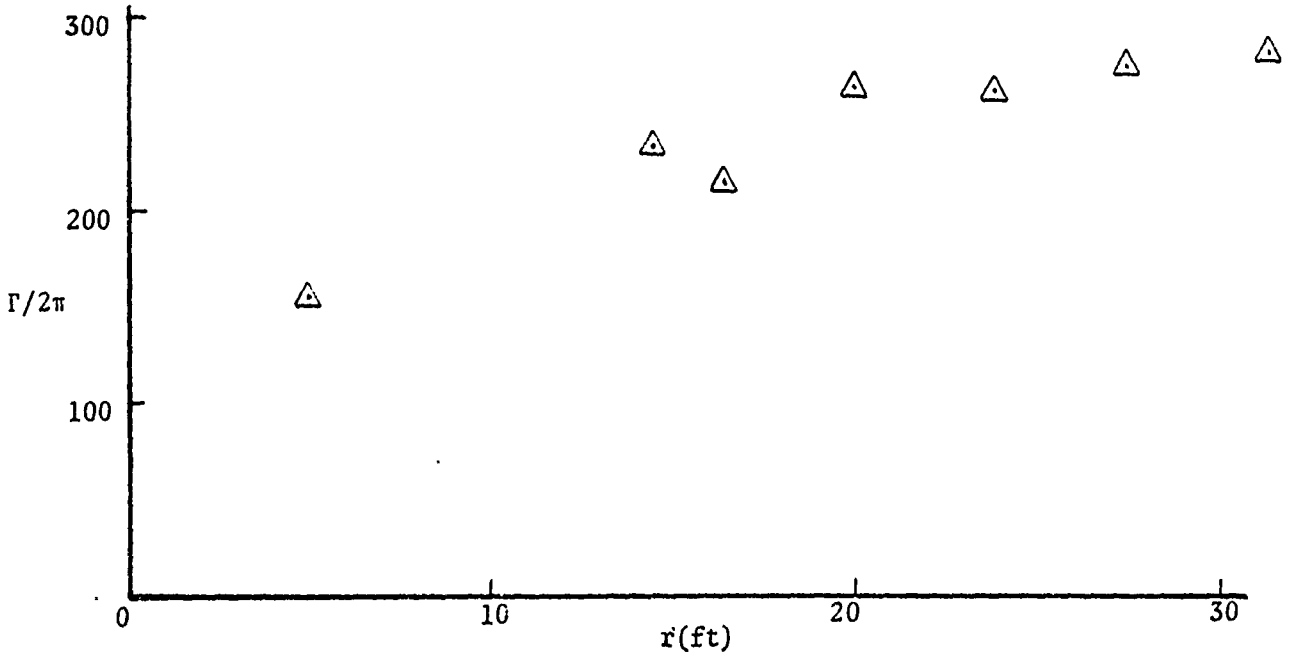


Figure 4-57. Circulation vs Radius for DC-7, Run 96-1

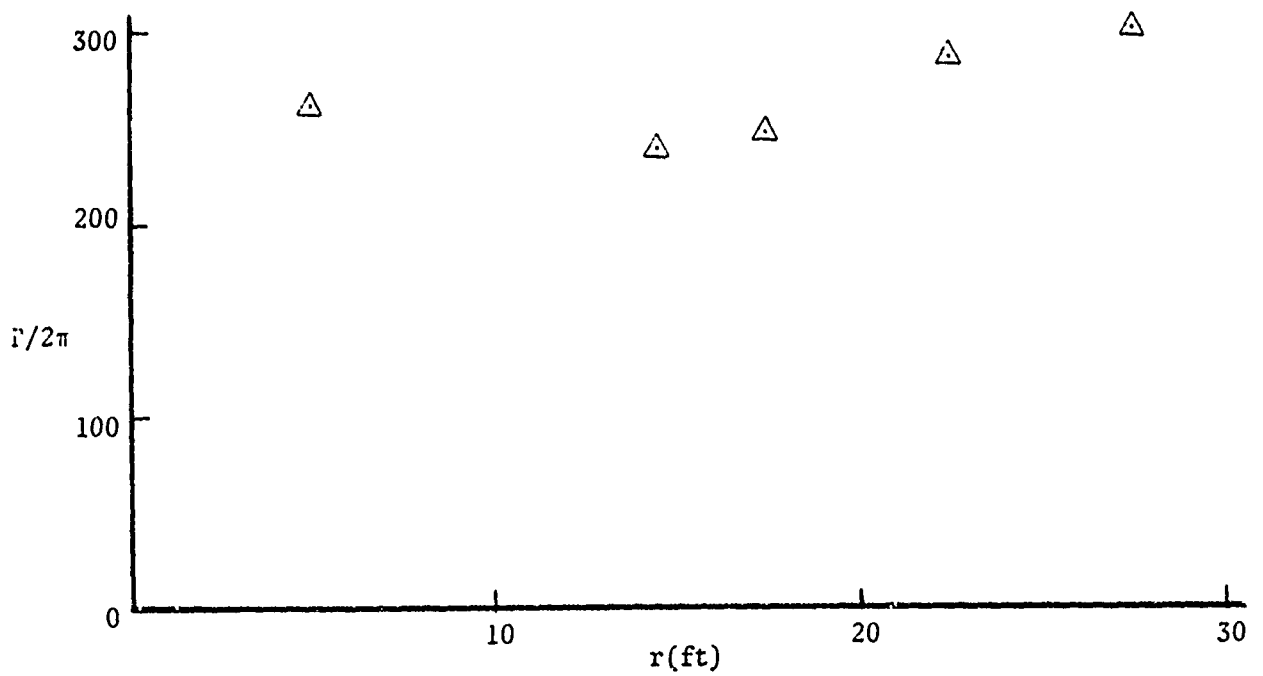


Figure 4-58. Circulation vs Radius for DC-7, Run 103-1

These values of circulation are listed in Table 4-1. All of the listed runs were in the landing configuration. The circulation values average about 270 (compared with a "nominal" value from equation 2-3 of about 320), and have a standard deviation less than 20 percent of that value. It would be most difficult to state without a great deal of further analysis and comparison with the NAFEC data how much of this variation is due to measurement errors and how much to the actual difference among different vortices. In connection with the latter point however, it should be recalled that all of these tests were conducted under relatively similar condicitons, and core should be exercised about drawing general conclusions as to the variations that might be found in vortex circulations under all environmental conditions, and at all altitudes and ages of interest in operational situations.

An alternative technique for estimating the circulation at 20 ft was employed on the data presentation format used for the remaining aircraft. It has been noted that the range of velocities observed at a given distance from the center of the observation volume corresponds to the variation from the minimum velocity at the edge further away from the core to the maximum velocity at the edge nearer the core. Thus, given the assumption that the radius of the observation volume is 5 ft, the maximum velocity observed when the center of the vortex is 25 ft from the center of the observation should serve as an estimate of the velocity at a radius of 20 ft. The circulation is then determined by multiplying this value by 20.

This simple procedure was followed for all of the C-141 data in Figures 4-37 through 4-43. The two values of maximum velocity 25 ft on either side of the center were averaged to yield a single value, which was then used to deduce the circulation. The remaining C-141 data were not included because at least one of the two data points 25 ft from the center was not available. Those estimates would have been of lower confidence because of possible residual velocity bias.

TABLE 4-1. ESTIMATED CIRCULATIONS AT $r = 20$ ft FOR DC-7 VORTICES

| Run | $\Gamma/2\pi$ ($ft^2/sec$) |
|---|---|
| 95-1 | 200 |
| 95-2 | 310 |
| 96-1 | 250 |
| 96-2 | 260 |
| 97-1 | 250 |
| 97-2 | 190 |
| 103-1 | 270 |
| 103-2 | 300 |
| 105-1 | 320 |
| 105-2 | 280 |
| 107-1 | 280 |
| 107-2 | 280 |
| 109-1 | 360 |
| 109-2 | 350 |
| 115-1 | 320 |
| 129-1 | 170 |
| 129-2 | 270 |
| 151-1 | 240 |
| 151-2 | 330 |
| 157-1 | 230 |
| 165-1 | 310 |
| 165-2 | 260 |
| 169-1 | 270 |
| 169-2 | 270 |

The resulting estimates of circulation are shown in Table 4-2. They average 415 $ft^2/sec$, compared with the nominal value of 560 $ft^2/sec$, and have a standard deviation of nearly 25 percent of the mean. It might be pointed out that, while quantitative estimates of circulation for the two vortices of run 18 could not be made with high confidence, they appear to have very much lower circulations than the average. This is particularly true for the second vortex, which may have a value near 200 $ft^2/sec$.

When this process is carried out for the one C-5A run that appears to have valid velocity-vs-distance data, a resulting value of 540 $ft^2/sec$ was obtained. It should be noted however that if the process is carried out again for a radius of 40 ft rather than 20 ft, a circulation in excess of 800 $ft^2/sec$ is obtained. The nominal value obtained from equation 2-3 is 810 $ft^2/sec$.

The procedure followed for the C-141 runs was duplicated for the CV-880 data. The estimates of circulation for the three runs which qualified are shown in Table 4-2. They are all near their mean value of 300 $ft^2/sec$. The nominal figure for these CV-880 runs is 320 $ft^2/sec$.

Finally, circulation estimates were obtained from the two DC-9 vortices for runs 12-2 and 23-2. These two values, averaging 260 $ft^2/sec$, can be compared with the nominal value, which is also 260 $ft^2/sec$. All of these circulation estimates are entered into Table 4-2.

In general, it can be seen that the procedures adopted for estimating circulation do order the observed aircraft according to the expected vortex strengths. The quantitative agreement with predicted circulation values is, in fact, quite good.

TABLE 4-2. ESTIMATED CIRCULATIONS AT r=20 ft

| Aircraft | Run | $\Gamma/2\pi$ ($ft^2/sec$) |
|---|---|---|
| C-5A | 32-2 | 540 |
| C-141 | 2-1 | 340 |
| | 2-2 | 450 |
| | 4-1 | 250 |
| | 4-2 | 410 |
| | 6-1 | 430 |
| | 10-2 | 450 |
| | 11-2 | 580 |
| CV-880 | 32-1 | 270 |
| | 32-2 | 310 |
| | 36-2 | 310 |
| DC-9 | 12-2 | 240 |
| | 23-2 | 270 |

## 5. EXTENDED TRACKING TESTS

The overall aim of the work covered in this report and its predecessor[2] is to demonstrate two general capabilities. The first, the ability to measure vortex characteristics quantitatively and relate them to a model, has been covered in Sections 2, 3 and 4. The second is the ability to observe and track vortices at altitudes and under conditions of operational interest.

In the earlier tests in the fall of 1971, tracks were obtained at altitudes of several hundred feet, and an analysis was made (in Section 7 of reference 2) of what system improvements would be expected to lead to adequate system coverage. In brief, an estimated 26 dB was quoted as the improvement in performance required for confident tracking of vortices from large aircraft at altitudes up to 1700 ft. A set of specific (and attainable) system upgradings was given that should lead to an enhancement in performance by that amount. During the short interval between that time and the current test series, modifications in the equipment were made (principally in reducing receiving antenna sidelobes) that improved system performance by perhaps 10 to 15 dB.

The current contract calls for tracking tests to be conducted at NAFEC to demonstrate the tracking capability of the improved system. The original schedule called for a large aircraft representative of the true threat (in particular, the Air Force C-5A used in the tower tests) to be an important part of the tracking tests. This however was not to be, for reasons already given in Section 4. The tracking tests that were actually run involved a DC-6 and a CV-880, both of which generate vortices on a much smaller scale than the large aircraft of major concern. It might be expected therefore that tracking of these vortices would be somewhat degraded from that of the large vortices, but by an amount that would be difficult to determine.

This section describes the tracking tests and their results. Section 5.1 gives details of the experimental equipment and system set-up for the

NAFEC tests. Section 5.2 describes the various tracking modes and the corresponding beam configurations, wave forms and data collection technique. Section 5.3 describes the data analysis, and reports the experimental results.

## 5.1 Experimental Equipment and System Set-Up

In contrast with the low-altitude (∿100 ft) tower tests which employed a single vertical transmitter beam intersected by ten receiver beams, the tracking tests employed an 88-element phased array operating simultaneously at two frequencies (5500 and 4500 Hz). In the first, or ARRAY mode, the output beam pattern consists of two beams displaced in elevation by about 16 degrees, each transmitting a continuous (CW) signal at one of the above frequencies. The beam pairs are changed in time sequence to four different positions with respect to the array elevation axis (see positions 1 through 4 for the two beams in Figure 5-1, a representative beam configuration). Thus, one complete sweep of the respective beam positions for the two beams includes 8 beam positions (four at each frequency, labeled L for lower frequency and H for higher frequency). In the second, or BROAD BEAM mode of operation the array produces a single wide beam with a $30^{\circ}$ beamwidth. Again a dual frequency transmission is employed, but in this mode the two frequencies illuminate the same (relatively large) volume. The lower frequency transmission is a continuous (CW) signal as in the ARRAY mode, while the higher frequency transmission is a low-PRF pulsed mode. These waveforms and their application to the tracking task are described in detail in the next section.

As shown in Figure 5-1, the receiver antenna employed in the tower tests is again used for the tracking tests, but with twelve operating beams and with the fan of beams having an angular extent of $\pm 18^{\circ}$ centered at an elevation angle of $90^{\circ}$. The phased array transmitter beams are directed to intersect these receiver beams, with the highest intersection located above the altitude of the aircraft flight path. Figure 5-1

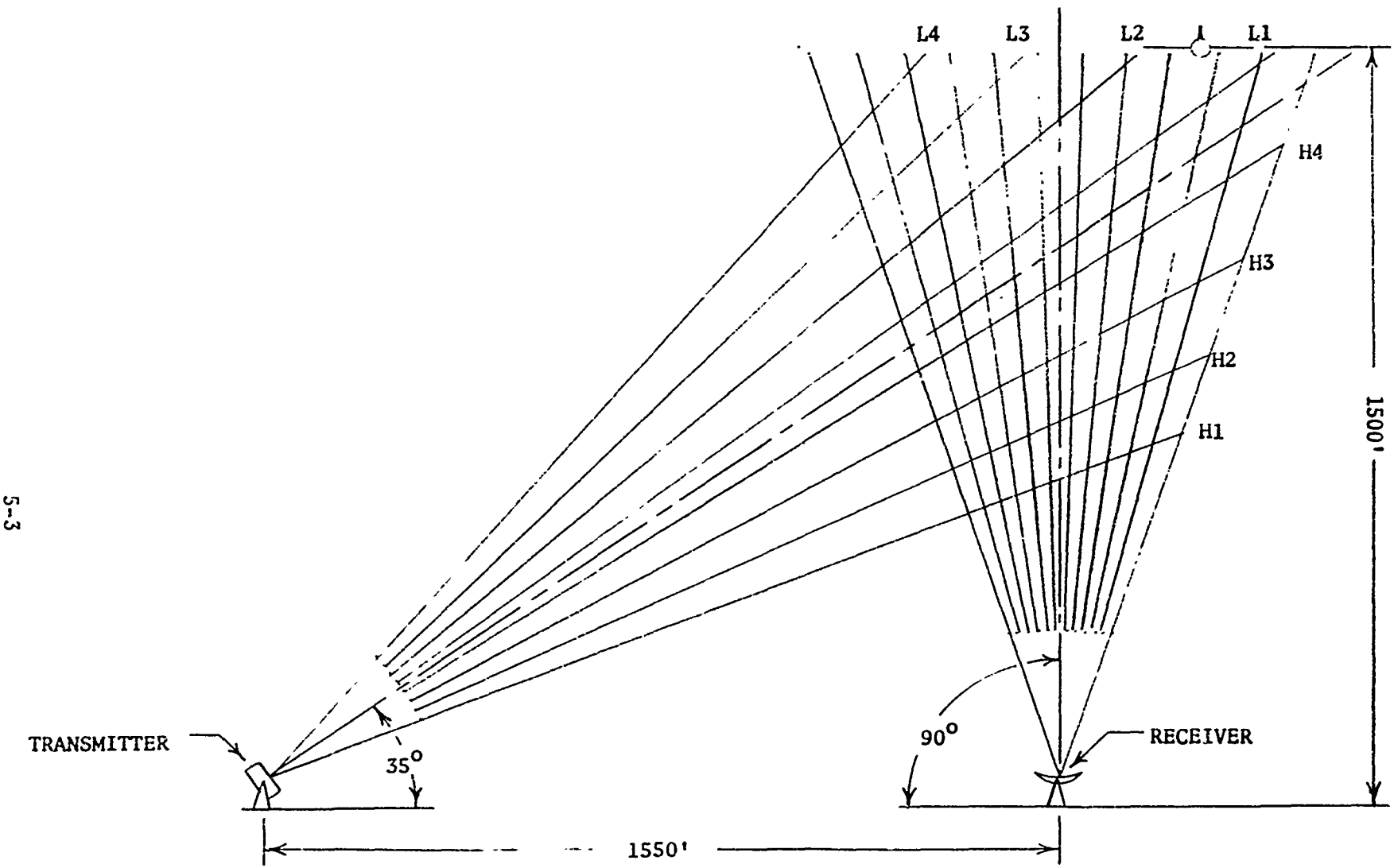


Figure 5-1. Experimental Set-up for Vortex Detection and Tracking Tests

positions operated at 4500 Hz. The transmission timing sequence for the ARRAY mode is shown schematically in Figure 5-2a. Transmission of the CW signal at each beam position lasts 0.4 sec, with a subsequent dead time of 0.4 sec after completing the transmission cycle through all beam positions. Similarly, Figure 5-2b illustrates the transmission timing sequence in the BROAD BEAM mode.

Data collection from the tracking tests is completely analogous to that for the tower tests. Each of the twelve receiver channels is recorded separately and simultaneously on 14-track analog tape for the desired duration of each aircraft fly-by. The remaining analog tape channels are used to record timing signals and voice information from the test director. On-site data validation of the ARRAY mode transmission is provided by real-time and play-back analysis of the data recorded in the various receiver channels. Specifically, the received signal is passed through an analog spectrum analyzer, with spectral broadening of the feed-through signal indicating the presence of vortex-induced acoustic scattering in the selected receiver channel.

## 5.3 Data Analysis and Experimental Results

Detailed analysis of the ARRAY mode tracking data requires spectral analysis of the return signals from each transmitter/receiver beam intersection. Each intersection is identified by a specific time delay corresponding to the acoustic propagation time from the transmitter to the intersection volume and then down to the receiver. With this time-delay identification of each beam intersection, the detailed detection and tracking analysis employed the following procedures. Each receiver beam (analog tape channel) was analyzed separately. Specifically, four tunable time-delay circuits were employed to initiate the coherent integrations necessary for the spectral analysis of the return from each transmitter/receiver beam intersection. Time delays equivalent to the signal propagation time for the respective beam intersections

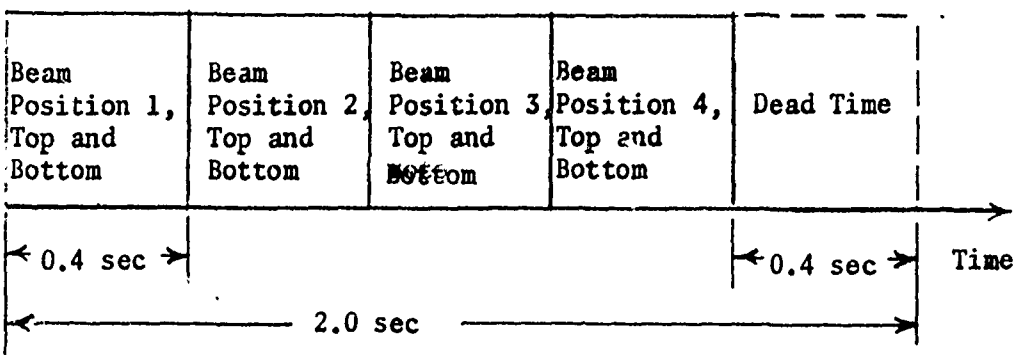


Figure 5-2a. Transmission Timing Sequence for ARRAY Mode

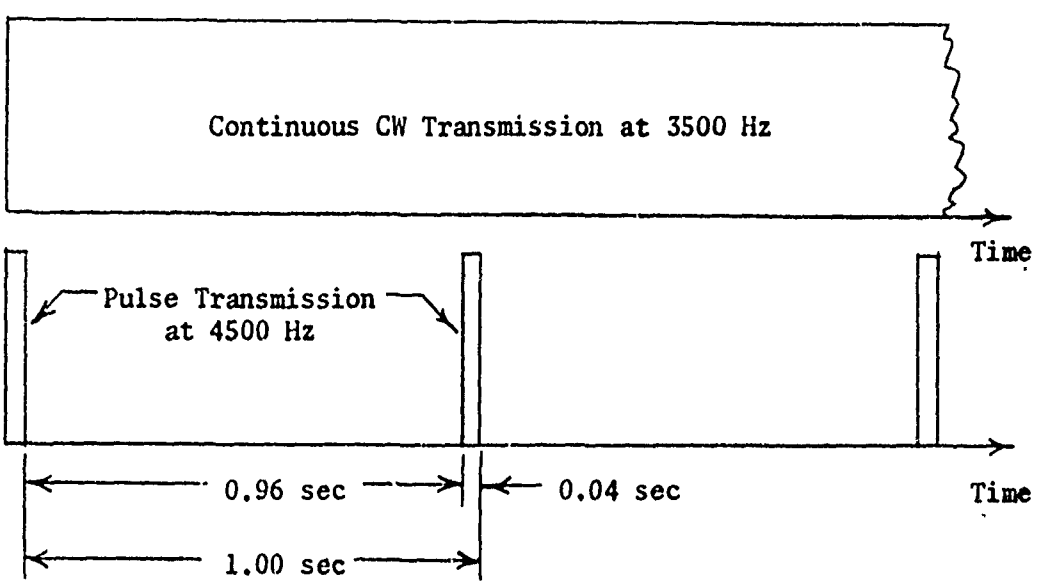


Figure 5-2b. Transmission Timing Sequence for BROAD BEAM Mode

were set in these circuits, coherent integration of the returns signals was initiated for each intersection at the end of the corresponding time delay, with an integration period equal to transmitted pulse length, 0.4 sec. The resulting spectra from each transmitter/receiver beam intersection were monitored as a function of time after the aircraft passage, with vortex detection following readily from the doppler-broadened spectra (broadened with respect to the feed-through signal width) caused by the rotational vortex velocity field. Each detection time was noted with respect to $T_c$, the time of aircraft passage, and the resulting tracks were obtained by carrying out this procedure in each receiver beam.

BROAD BEAM pulse transmissions are analyzed somewhat differently. Time, as well as frequency-domain (velocity spectrum) analysis is used, again with each receiver beam being analyzed individually. With the low-PRF pulse transmissions, each pulse triggers a time-domain sweep of the received signal in the particular beam being analyzed. A vortex detection as indicated by a pulse return at a time delay corresponding to the total acoustic propagation time. Noting this time delay and comparing it to the contours of constant propagation time (ellipses with foci at the transmitter and receiver, see Figures 5-3 through 5-9) the vortex location (elevation) can be determined in the beam. The CW transmission is then used for spectral analysis of the vortex-induced acoustic scattering at the time when the pulses are received. Integration times for this velocity spectrum analysis are selected to provide the desired velocity resolution of a few feet per second. The pulse mode vortex detection is verified by observation of the characteristic time history of vortex spectral broadening of the transmitted signal. (See Figures 4-1 through 4-6 and Figures 4-33 through 4-36.) Thus, the pulse mode is used to determine the vortex position (time delay) within a receiver beam, while the CW transmission is used to determine the vortex spectrum and correspondingly, the vortex circulation and hazard level.

Tracking tests were conducted on 20 June with a DC-6. (DC-7 and CV-880 aircraft were specified for these tests after it became known that larger aircraft would not be available. Neither of these aircraft could be flown for the tests on the date arranged, so the DC-6 was substituted.) On both days, a sequence of runs was made consisting of four successive flights at each of four altitudes, 600, 900, 1200 and 1500 ft. The ARRAY mode was operated on three out of each group of four flights at a given altitude. It is these runs that were analyzed in detail as just described. As anticipated from the short duration of the pulses and hence lower signal energy, the pulse transmissions yielded lower signal-to-noise ratios than did the ARRAY-mode transmissions. The resulting detections for the BROAD-BEAM tests were correspondingly weaker and less confident, and were not analyzed in detail.

Figures 5-3 through 5-6 show the tracks obtained for a sampling of the DC-6 runs. Figure 5-3 shows the vortex track obtained for run H-3 at an aircraft altitude of 600 ft (nominal position shown in the figure). The numbers next to the end locations are the initial ($T_i$) and final ($T_f$) times at which observations of the track were made. Figure 5-4 shows a vortex track for run H-7 at 900 ft altitude. Figure 5-5 shows a vortex track for run H-9 at 1200 ft altitude, and Figure 5-6 shows a vortex track for run H-14 at an aircraft altitude of 1500 ft. In the last two high-altitude tracks, the initial vortex detections were made at altitudes of about 1000 and 1200 ft. with a possible additional detection of 1300 ft for run H-14.

Figures 5-7 through 5-9 show tracks obtained on the vortices from the CV-880 aircraft. Figures 5-7 and 5-8 show tracks for runs H-58 and H-59, with a nominal aircraft altitude of 900 ft, while Figure 5-9 illustrates a vortex detection at 900 ft from an aircraft flying at 1200 ft on run H-60. It was anticipated prior to these tracking tests that the vortex tracks from the CV-880 would be poorer than those of

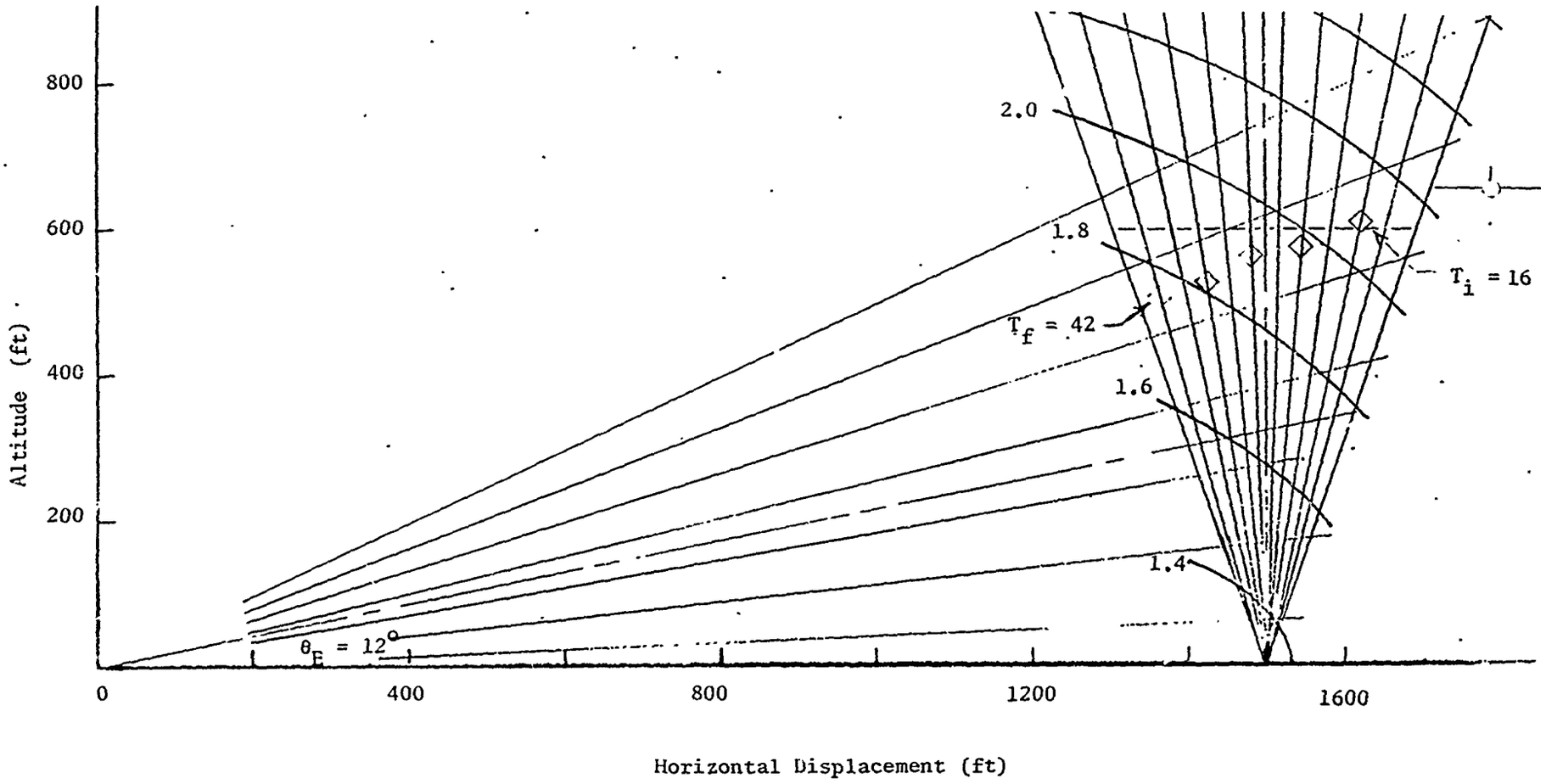


Figure 5-3. DC-6, Run H-3, Vortex Track from Aircraft at 600 ft.

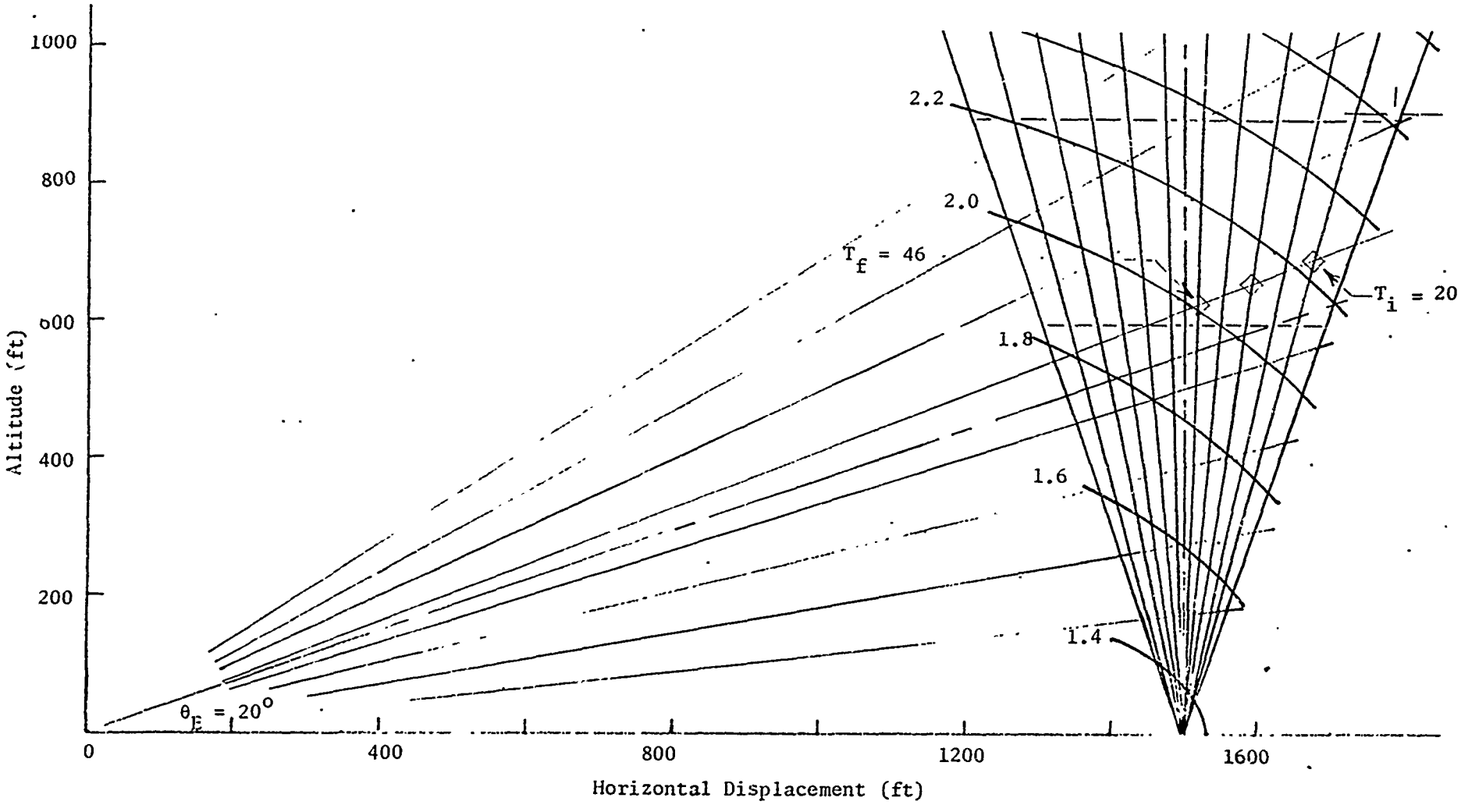


Figure 5-4. DC-6, Run H-7, Vortex Track from Aircraft at 900 ft

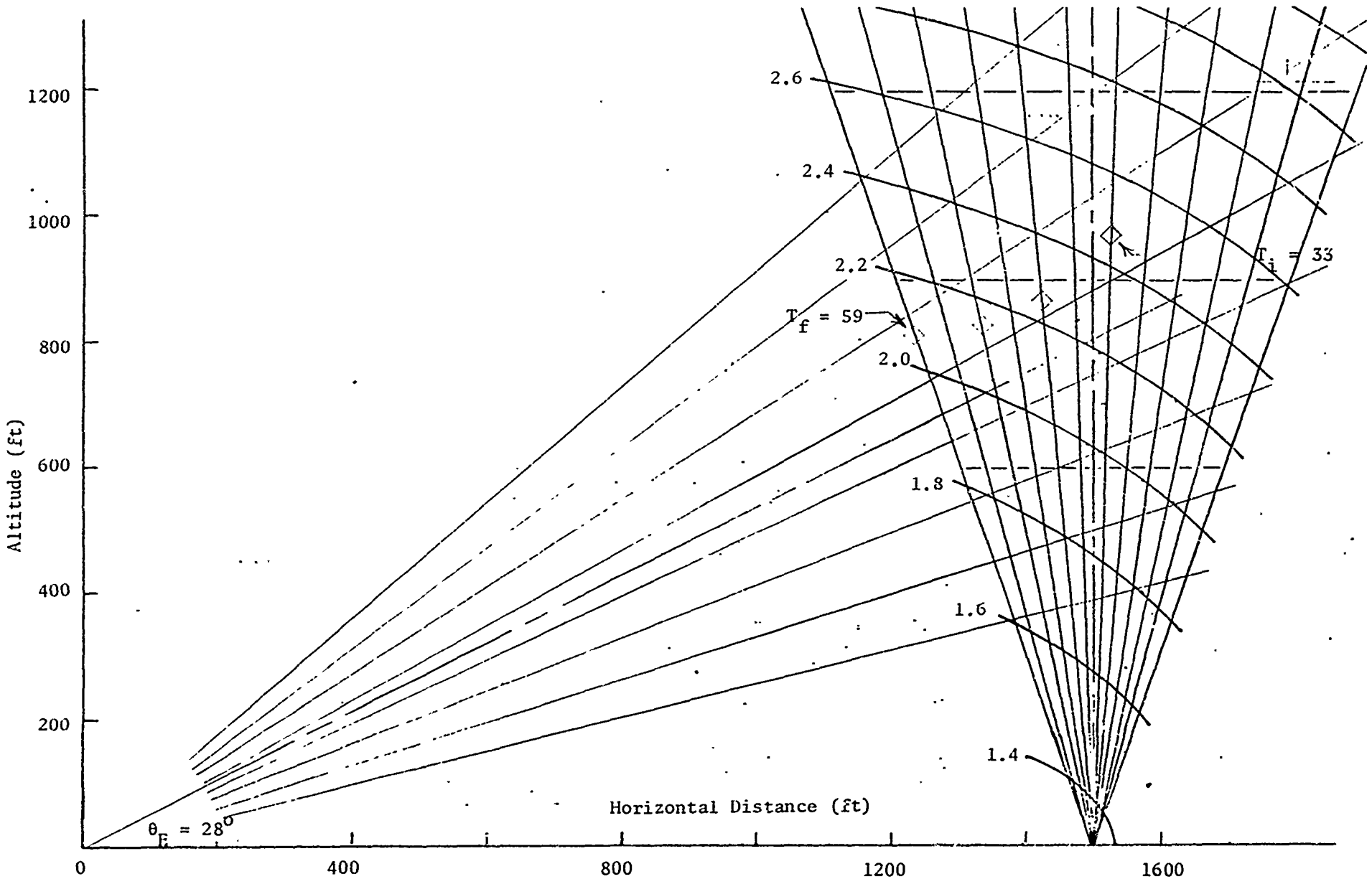


Figure 5-5. DC-6, Run H-9, Vortex Track from Aircraft at 1200 ft

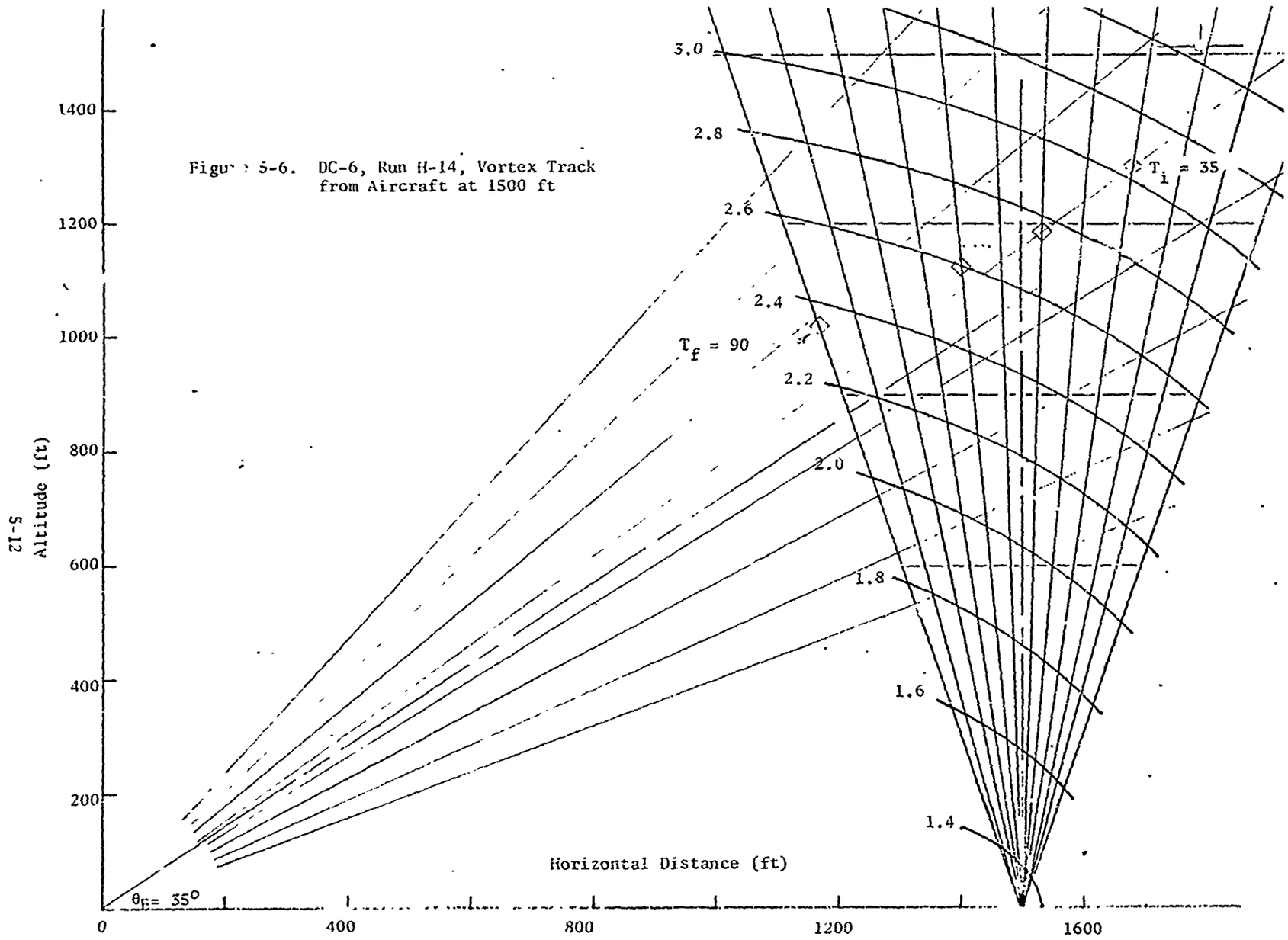


Figure 5-6. DC-6, Run H-14, Vortex Track from Aircraft at 1500 ft

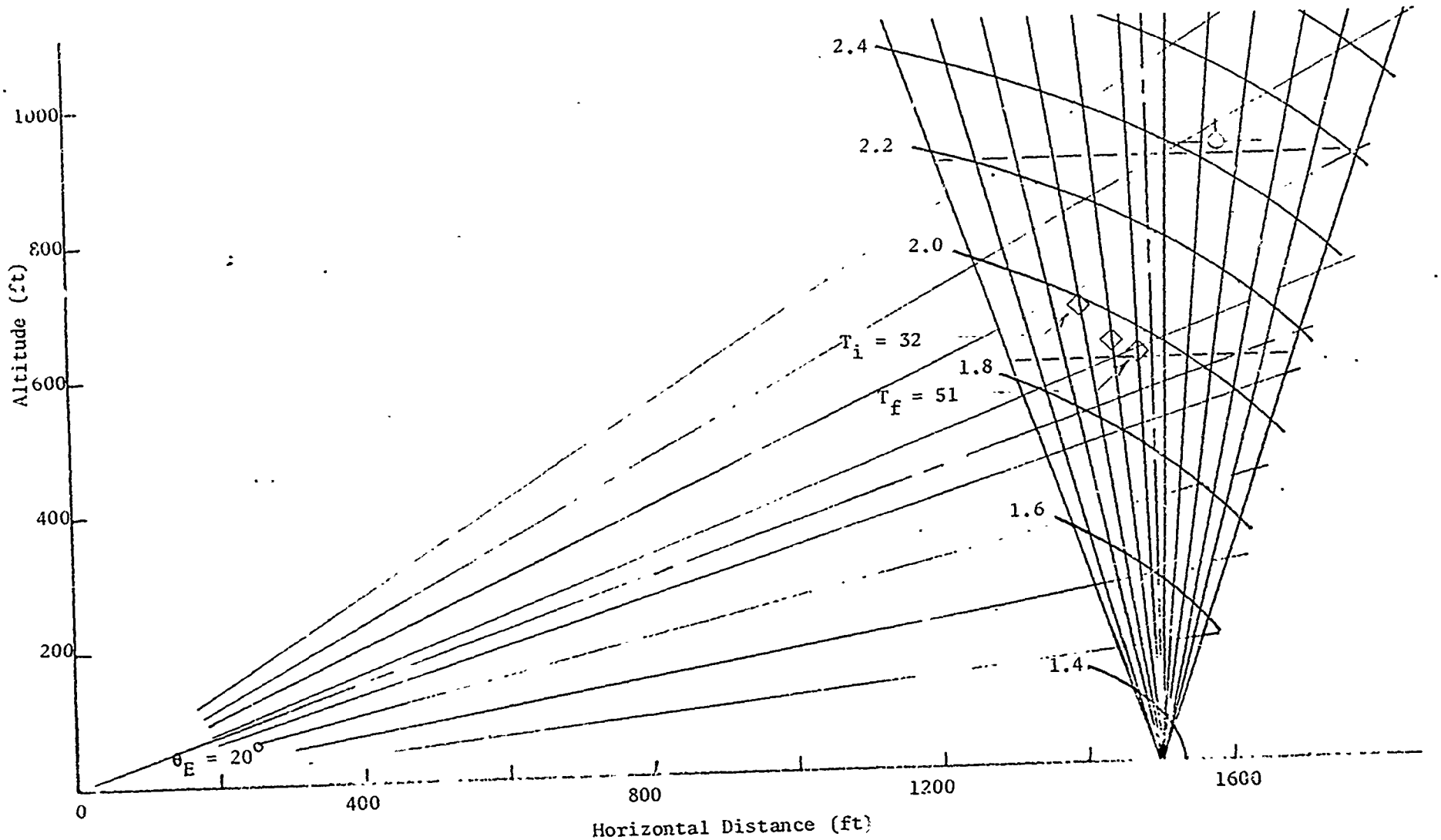


Figure 5-7. CV-880, Run H-58, Vortex Track from Aircraft at 900 ft

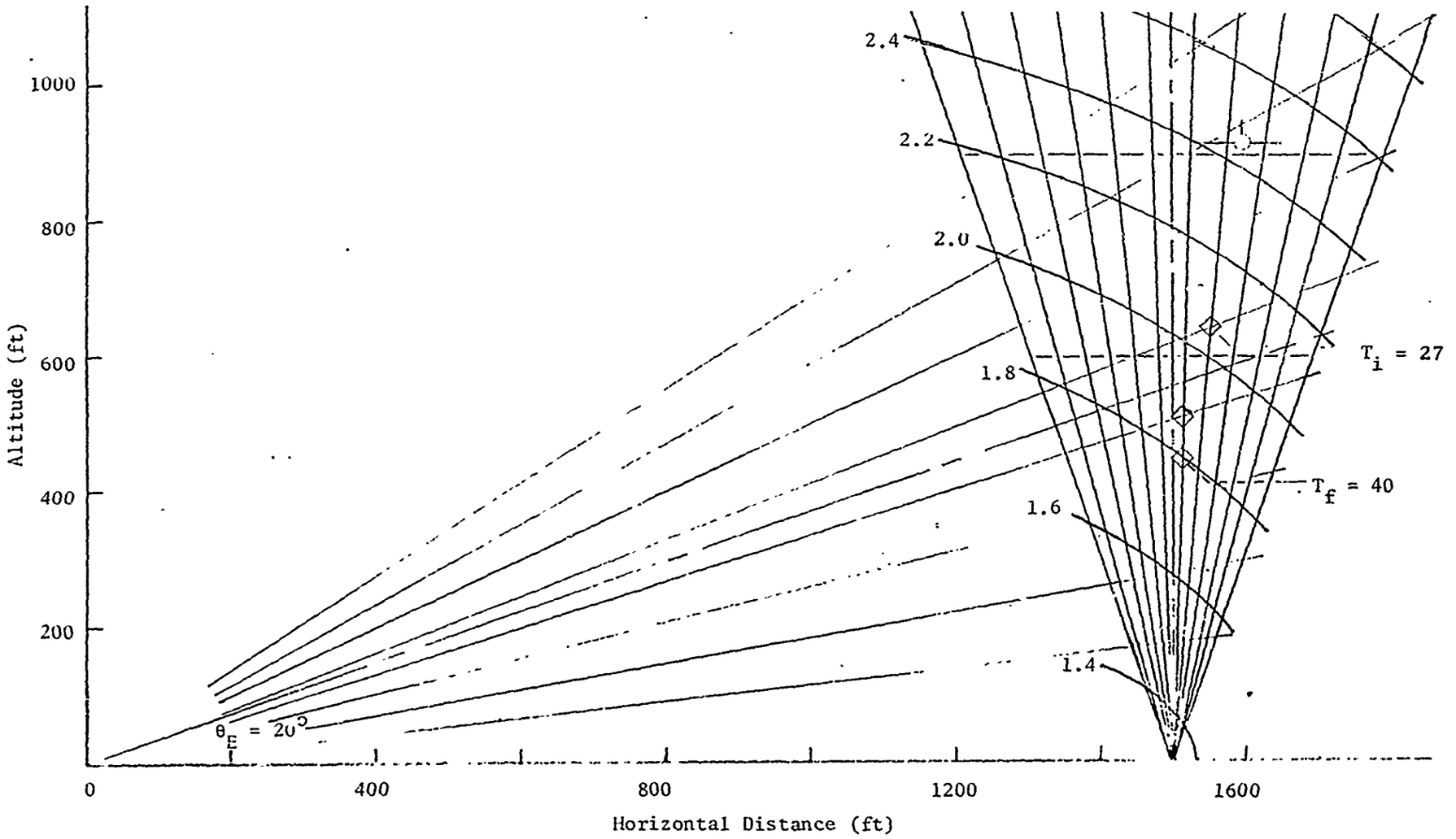


Figure 5-8. CV-880, Run H-59, Vortex Track from Aircraft at 900 ft

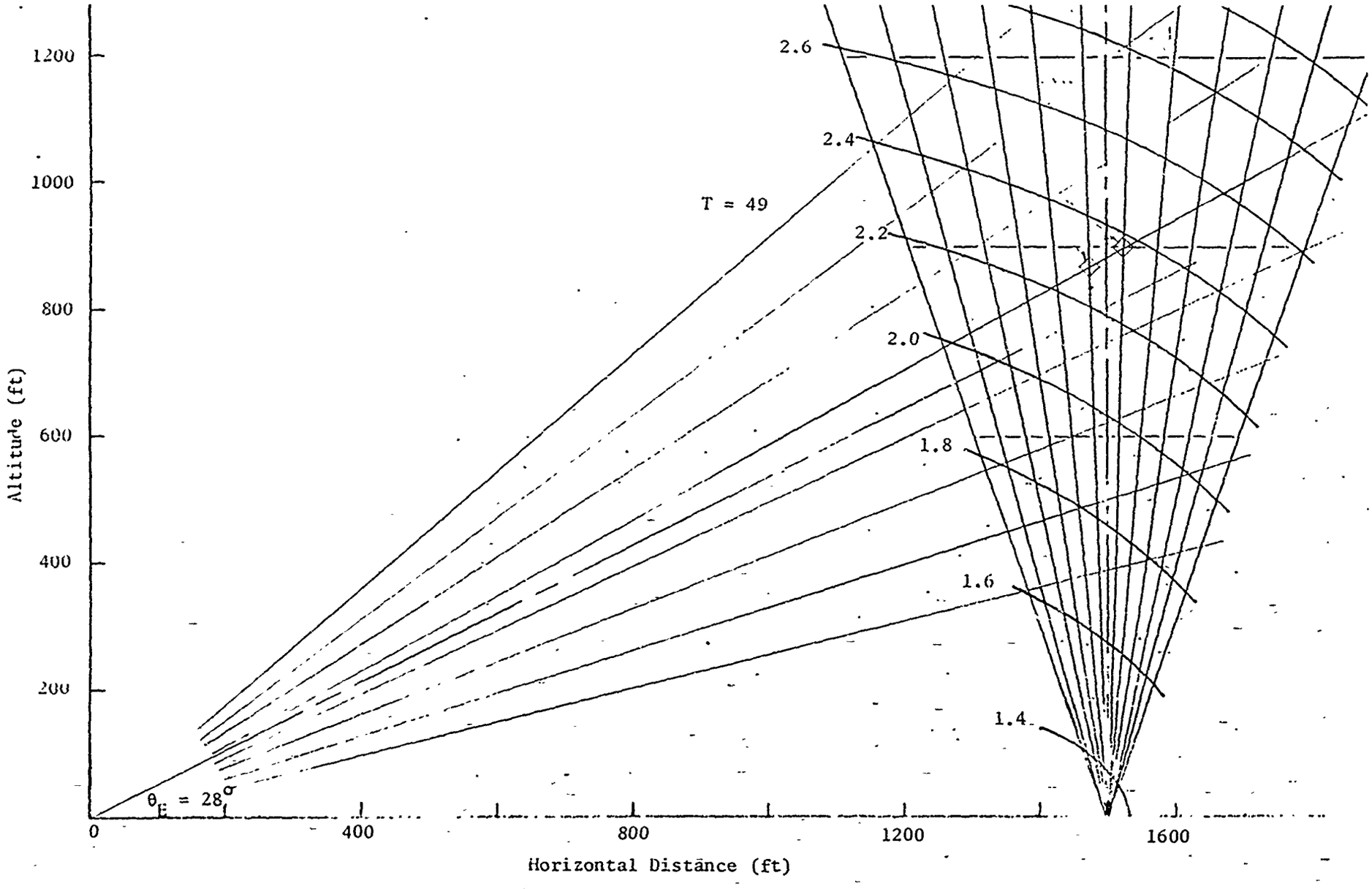


Figure 5-9. CV-880, Run H-60, Vortex Detection from Aircraft at 1200 ft

the DC-6. This results from two important effects. First, the CV-880 is a very noisy aircraft and, as a result, sustained, high noise levels prevent early high-altitude detection of the vortices. Second, the CV-880 vortex appears to be an anomalously weak acoustic scatterer, for reasons not understood at present. Cross sections from CV-880 vortices have been found in a preliminary analysis to be 7 to 10 dB lower than those of the DC-7 or C-141. The received acoustic signal is correspondingly reduced by this amount, resulting in poorer signal-to-noise ratios and a more difficult detection problem.

It may be noted in the preceding figures, that initial vortex detection occurred at times ranging from 15 to 40 sec after the aircraft passage. This observation is primarily a result of high levels of broad-band aircraft noise, increasing the backgorund noise level and thus decreasing signal-to-noise ratios for vortex detection. As noted above, this problem is particularly acute with the CV-880 aircraft. With the short period of time available for this tracking data analysis, no effort was made to quantize the noise level history of the passing aircraft, and confirmed vortex detections were limited to high signal-to-noise detections. Future work should include an analysis of the effect of aircraft noise on vortex detection, an effort to select a more favorable transmitter-receiver geometry for sidelobe noise suppression, and improved receiver designs to further reduce azimuthal receiver sidelobes. These measures would substantially reduce the delay after aircraft passage at which confident track can be established.

In summary, the major goal of detecting and tracking vortices at altitudes well over 1000 ft has been achieved despite the fact that large aircraft representative of the true operational threat did not participate in these tests.

## 6. PRELIMINARY SYSTEM ANALYSIS

The goal of the entire wake turbulence detection program of which the work covered in this report forms a part is an effective operational system that will permit increased runway usage with minimal hazard. Most of the work covered by this contract is directed toward an understanding of the physical vortex phenomena and the means by which relevant hazard-related parameters may be deduced from the scattered acoustic signals. A complete description of a system that utilizes this information to achieve the goal just described is beyond the scope of the current effort; indeed, the system requirements that must be satisfied by the candidate design have not yet been defined. A number of observations that relate to the system application of acoustic radar can however be made at this time, and this section is devoted to a discussion of some of those points. It is hoped that this discussion may even help formulate some of the system requirements, although it is clear that a much greater effort is needed (and should be expended in the near future) to define adequately the system requirements and design.

## 6.1 System Definition Approach

In order to select a baseline system configuration of the ground-based acoustic vortex detection system capable of providing wake vortex surveillance along the ILS corridor associated with an airport runway, the following approach would normally be taken:

Development of system requirements

Identification of system functions

Identification of major subsystems

Analysis of subsystem candidates

Selection of the baseline system

The procedure is illustrated schematically in Figure 6-1.

System requirements are needed first of all because they impose the design constraints that all candidate systems must meet, and they form the basis of comparisons between alternative approaches. A preliminary attempt is therefore made in this section to identify some of them. The set of system requirements presented here is not intended to be definitive, and further iterations will be required before the final set of requirements is generated.

The identification of the system functions has the purpose of determining the different steps that are to be implemented in order to satisfy the vortex detection system requirements.

The identification of major subsystems consists of determining the major hardware groups forming the system, i.e., sensor subsystem, data processing, display subsystem, computer requirements and software. Identification of specific hardware is not accomplished at this stage. Also, it is of interest to note that there is not necessarily a one-to-one relation between functions and elements. One function might require the utilization or participation of more than one element of the system in

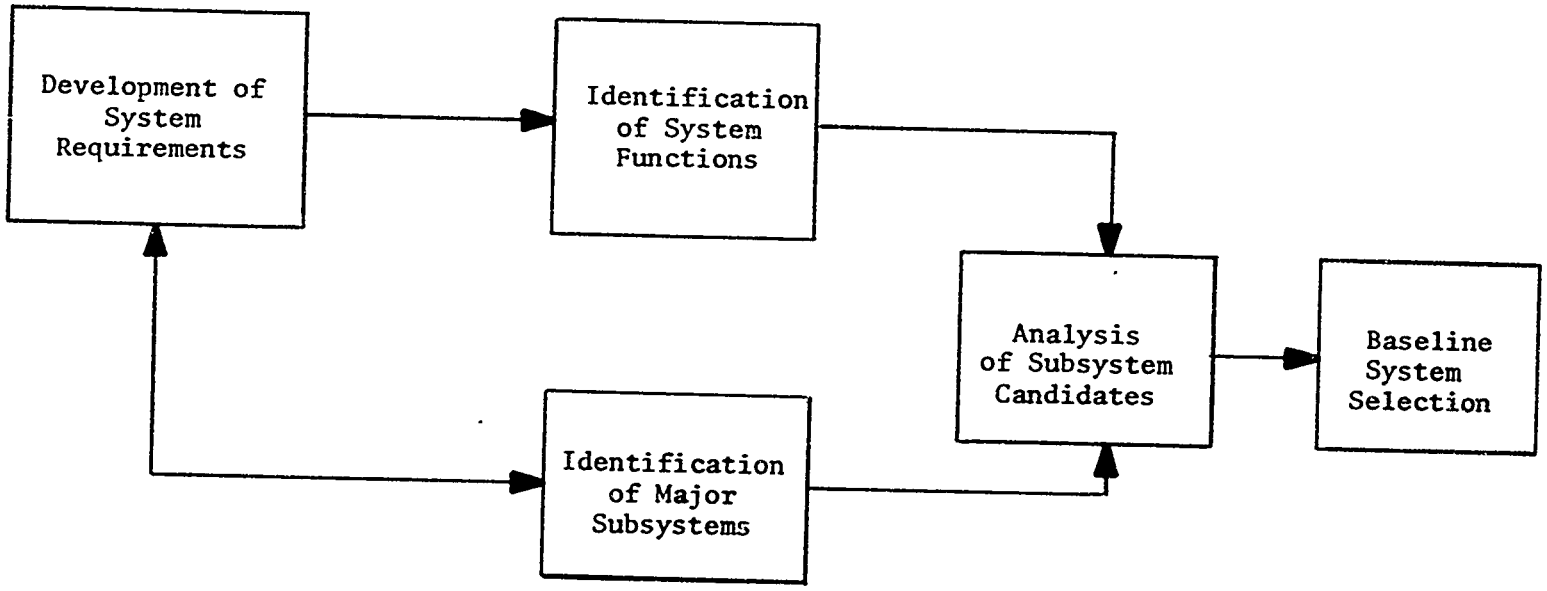


Figure 6-1. System Selection Approach

order to be accomplished. For example, tracking is a function that requires processing and correlation by the computer, but may in some cases require action by the operator through a display and possibly further operation of the sensor to provide additional data. On the other hand a single element, such as the computer, may participate in several functions.

In general, this process is accomplished through a trade-off analysis. In some cases however, assignment of a subsystem requirement can be made on the basis of experience with similar systems rather than requiring a more extensive trade-off analysis. Examples of such assignments might be for subsystem reliability or maintainability. It is during this phase of system development that the lower functions are correlated with elements of the subsystems.

Finally, the baseline system selection is a result of work performed during the development of subsystems requirements. Other considerations, such as cost, availability of components, commonality, system growth potential, and related issues have received only the most cursory consideration in this effort.

## 6.2 System Requirements

A preliminary attempt has been made to generate specifications to be used as general ground rules for designing a ground-based acoustic detection system. The specifications have been organized under four headings, as follows:

General System Requirements

Surveillance Volume Requirements

Hazard Chacteristics

Environmental Conditions

Each in turn is treated in the following group of subsections.

6.2.1 General System Requirements

a. The vortex detection system has the purpose of generating vortex wake data which will be used by the ATC to control airplane landing separation. The system shall be able to detect, acquire and track vortices generated within a single airport runway ILS approach airspace.

b. The system shall consist of acoustic radar (transmitter and receiver) sets installed, as a minimum, at the outer marker, middle marker and at a distance compatible with an aircraft altitude of 100 ft. Additional installations may be deemed necessary by studies of meteorological effects, vortex dynamics and operational needs.

c. The system shall be able to locate and track vortices with an accuracy of 100 ft, and shall put out an indication of the hazard presented by the vortex to an encountering aircraft. This information shall be available in a format and on a time scale compatible with the operational doctrine to be followed (but not yet formulated).

6.2.2 Surveillance Volume Requirements

a. The vortex detection system shall perform surveillance of vortices generated by airplanes flying along an ILS corridor. The ILS corridor standard characteristics are presented in Figure 6-2. The geometrical dimensions of the typical ILS corridor to be used in this phase for generation of subsystem requirements are shown in Figure 6-3.

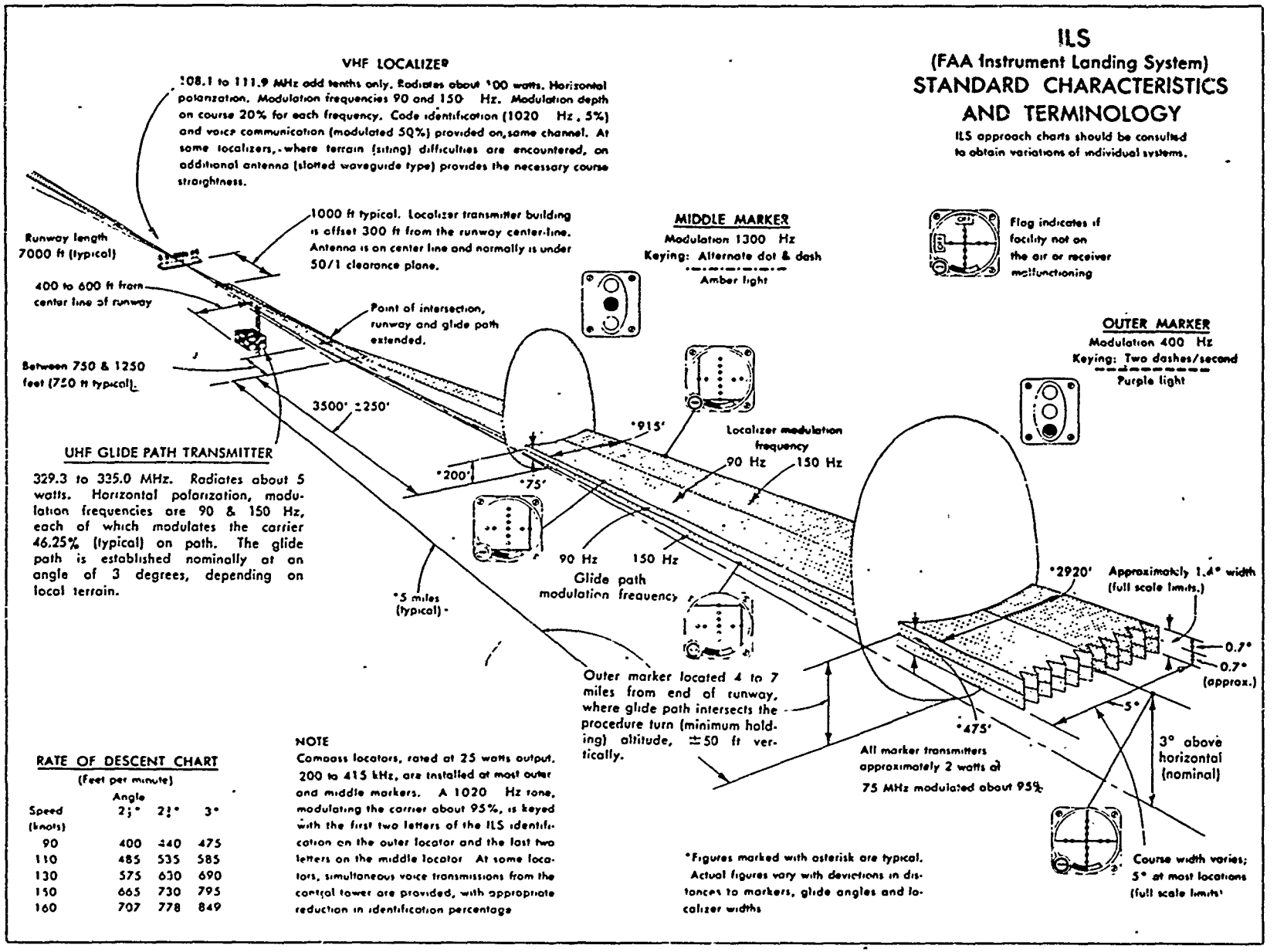


Figure 6-2. Standard ILS Corridor

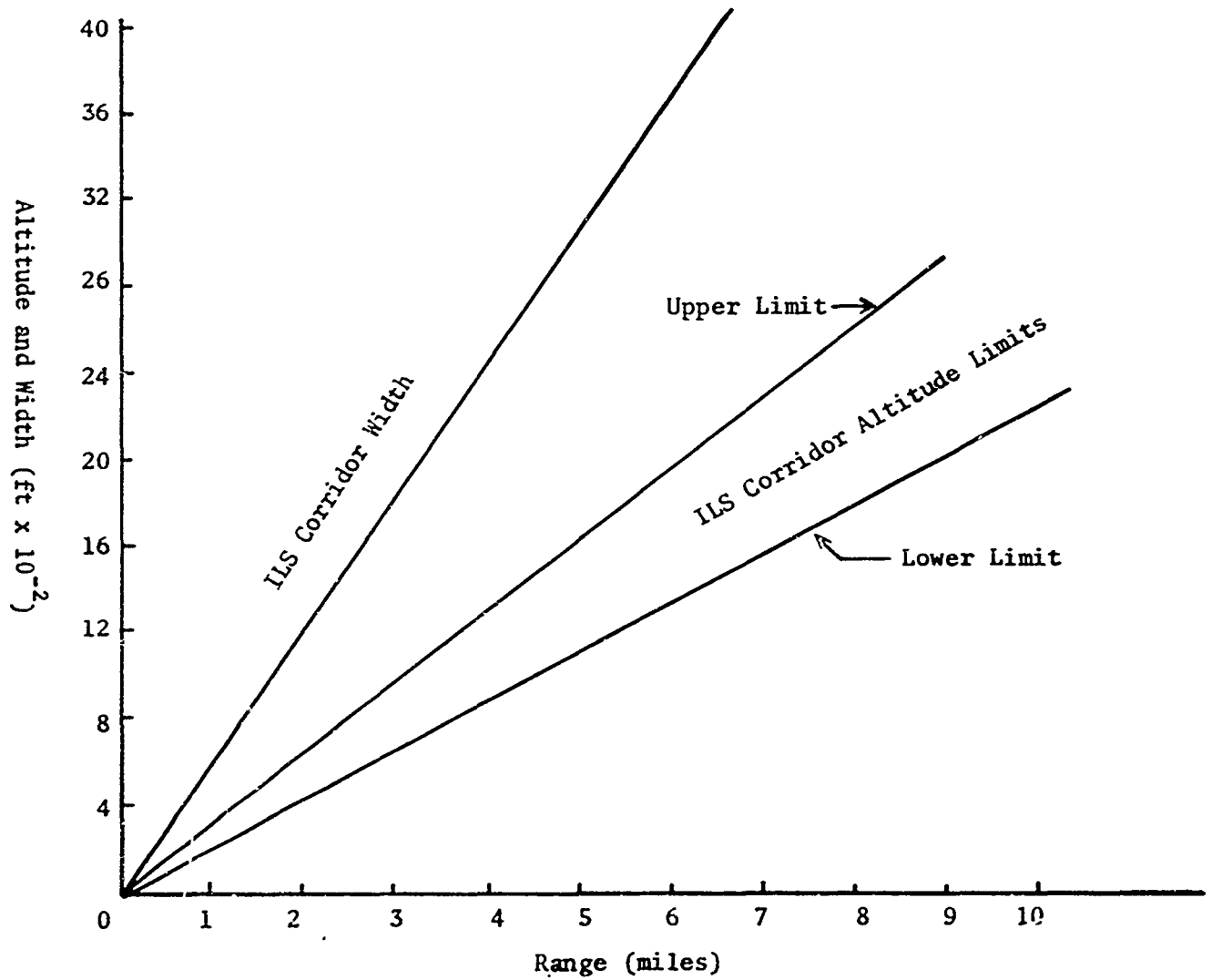


Figure 6-3. ILS Corridor Dimensions

b. The utilization of the runway associated with the ILS corridor to be instrumented shall be limited to the wind envelope presented in Figure 6-4.

### 6.2.3 Hazard Characteristics

a. The system shall measure vortex circulations greater than 1250 $ft^2/sec$ to within ±30 percent. Generally speaking, this covers aircraft with weights of 100,000 lbs and more.

b. The vortex wake shall be assumed to decay almost instantaneously after being generated in a wind of 30 mph or more.

c. For nominal design purposes, the vortex pair may be taken to be initially separated by distances between 75 and 200 ft, to sink at a rate of 4 to 10 ft/sec and to be convected by the wind. It is to be understood that specific instances may vary widely and differ considerably from nominal.

### 6.2.4 Environmental Conditions

The vortex detection system shall be capable of withstanding the range of environments and conditions encountered during operation at airports. The equipment shall meet standard Government specifications with respect to operation in such environments and conditions.

## 6.3 System Functions

Before a system can be designed properly, the requirements that the system must satisfy from the functional point of view must be clearly identified. The preliminary analysis for the vortex detection system will be performed by identifying top and first level functions. Second and lower level functional requirements need not be identified at the current stage of system design.

The vortex detection system shall perform the top-level functions of searching, detecting, acquiring and tracking vortices generated by

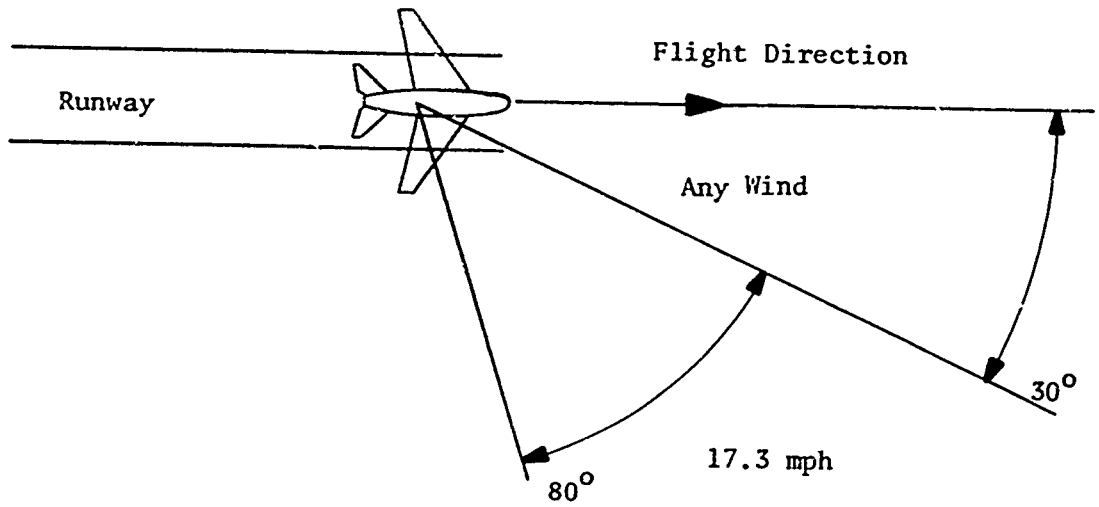


Figure 6-4. Wind Envelope for Runway Use

one airplane that may pose a hazard to another aircraft, then evaluating that hazard and communicating or displaying the information to the user.

The search function is implemented by the acoustic transmitter and receiver beams that cover the surveillance volume of interest. The search function requires performing the first-level functions of

Specify Scan Mode

Initiate Scan

Terminate Scan

Select Scan Rate

Select Transmitted Signal Parameters

The detection function is accomplished when the return signal exceeds the detection criteria. First-level functions associated with this function may include, but are not limited to,

Set thresholds

Determine noise power

Select detection criteria.

The acquisition function consists of determining whether or not the detected signals are associated with a vortex. First-level functions associated with the acquisition function may include

Magnitude comparison

Spectrum broadening comparison

Vortex location determination

Tag returns.

The tracking function is exercised by the system from the moment that returns are identified to be associated with a vortex. The track function may include the first-level functions

Initiate tracks

Select initial track correlation boxes

Estimate vortex state

Predict future vortex state

Compute track correlation boxes

Select criteria for track termination

Compare vortex state with track termination criteria

Terminate tracks.

The evaluation function has the purpose of determining whether or not the safe flight of an airplane during landing will be jeopardized by a vortex wake hazard generated by a preceding airplane. This function may be implemented by the first-level functions

Compute times of airplane crossing specified stations

Predict vortex state (position, velocity and circulation) at the stations at those times

Correlate vortex and airplane predicted position

Correlate vortex circulation with encountering airplane

Estimate hazard.

The final function consists of communicating the information so that appropriate action may be taken. This may take the form of a special-purpose, self-contained display or merely of an input to another, more general ATC system. No attempt is made here to identify the top and first-level functions that an ATC system shall perform in order to

make maximum utilization of vortex wake data in the safe control of airplanes during the terminal approach phase.

## 6.4 System Description

A preliminary design of a terminal vortex detection system is envisioned which includes a sensor subsystem, a communication subsystem, processing subsystem and display subsystem, shown schematically in Figure 6-5. Two display options are indicated, depending on how the output is to be used. The display subsystem is shown for autonomous operation of the vortex system. Alternatively, when it is to be integrated into a larger ATC system, the display subsystem is replaced with a buffer which serves as the interface between the vortex detection system and the terminal air traffic control system.

The sensor subsystem consists of all the radar sets that have been installed in an airport to detect vortices. The main function of this subsystem is to gather vortex data. The radar transmitter is formed by the following hardware groups:

Radar pedestal

Antenna dish

Power supply

Transmitter electronics

Connector group

Driver and horns

Control group

The radar receiver is formed by the following hardware groups:

Radar pedestal

Antenna dish

Microphones

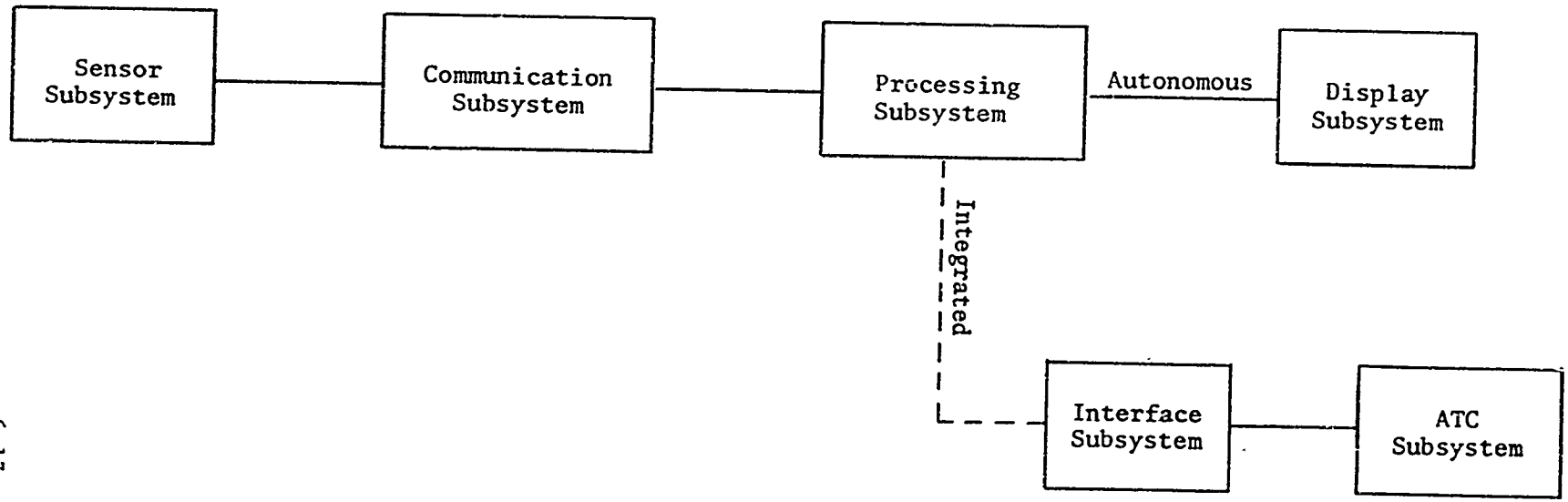


Figure 6-5. Vortex Detection System

Receiver electronics

Power supplies

Connectors.

The Communication Subsystem consists of all the communication gear and transmission lines that are required for sending pertinent data to the processing subsystem.

The Processing Subsystem consists of the special and general purpose computers which are needed to generate the vortex spectrum, to calculate the vortex position, to estimate and predict the vortex state, to assess the hazard and to format the output data.

The Display Subsystem consists of the CRT displays and keyboards required to perform the interface between the operators and the system in the autonomous mode of operation. The Interface Subsystem consists of the buffer and control units required for interfacing with an existing terminal traffic control installation in the integrated mode.

## 6.5 Baseline System Definition

### 6.5.1 Radar Station Selection

In order to study the coverage problems along the ILS corridor of a single runway, four sensor units located at the outer marker, at half the distance between the outer and middle markers, at the middle marker and at the threshold were selected as a baseline case. Selection of these radar locations satifies system requirements and at the same time affords coverage of virtually all altitudes in the ILS approach corridor within the outer marker.

Assuming (see Figure 6-2) that the threshold and the middle and outer markers are located about 1/4 mile, 1 mile and 5 miles respectively from the intersection of the runway and glide slope, the

remaining sensor unit is then to be 3 miles from that point. The width and the altitudes of the boundaries of the ILS corridor at these stations can be obtained from Figure 6-3. Table 6-1 presents these values for the areas selected for radar coverage analysis.

The position of the antennas for the radar set located at the threshold is constrained by the limitations on structures in the vicinity of a runway. In this study it has been assumed that the runway is 150 ft in width and that no equipment can be installed within 50 ft of the runway edges. Thus, radar antennas can only be installed outside of a distance of 125 ft from the runway centerline.

### 6.5.2 Sensor Location Constraints

The location of the receiver and transmitter antennas and their number will depend on the dimensions of the radar coverage boundaries and the altitude of the coverage volume as constrained by the maximum acceptable antenna elevation and azimuth angular coverage, scattering angles, S/N ratio for detection and single-look vortex position determination accuracy.

Table 6-2 presents parameter limitations which constrain the location of transmitters and receivers at the selected radar stations. The constraints can be grouped under the general heading of constraints due to antenna design, constraints due to the physics of the problem and constraints due to system requirements.

Under the first type of constraint we encounter those factors bounding the search elevation boundaries of the receivers and transmitter. These limits are related to radar sidelobe supression and beamwidth requirements. The second constraint is associated with the angular dependence of the vortex scattering cross-section. In order to avoid scattering angles of $90^{\circ}$ and $180^{\circ}$, which are expected to show weaker scattering, the allowed ranges have been taken from $30^{\circ}$ to $70^{\circ}$

TABLE 6-1. COVERAGE SECTIONS AT RADAR STATIONS

| Sensor Unit | Distance (miles) | Width of the Section (ft) | Lower Boundary Altitude (ft) | Upper Boundary Altitude (ft) | Section Height (ft) |
|---|---|---|---|---|---|
| 1 | 0.25 | 150 | 57 | 81 | 24 |
| 2 | 1 | 600 | 228 | 324 | 96 |
| 3 | 3 | 1800 | 684 | 972 | 288 |
| 4 | 5 | 3000 | 1140 | 1620 | 480 |

TABLE 6-2. RADAR UNIT CONFIGURATION CONSTRAINTS

| Basic Limitation | Constraint | Magnitude |
|---|---|---|
| Antenna Design | Elevation Coverage (1 receiver) | $\leq 40^{\circ}$ |
| Vortex Physics | Scattering Angles | |
| | High Altitude Detection | $30^{\circ}$ - $70^{\circ}$<br>$110^{\circ}$ - $150^{\circ}$ |
| | Low Altitude Detection | $15^{\circ}$ - $75^{\circ}$<br>$105^{\circ}$ - $160^{\circ}$ |
| System Requirements | S/N Ratio | $\geq 13$ dB |
| | Single-Look Vortex Position Determination | $\leq 100$ ft at outer marker |

and from $110^{\circ}$ to $150^{\circ}$. At low altitudes, the shorter range allows the scattering angles to vary between $15^{\circ}$ to $75^{\circ}$ and $105^{\circ}$ to $160^{\circ}$ without excessive S/N degradation.

### 6.5.3 Approaches to Vortex Position Determination

Three basic methods of locating a vortex have been considered. The first method determines the vortex location by two angular measurements. The second determines the location of the vortex by one angular measurement and one time delay. The third method is based on the measurement of two time delays. The first two methods require one transmitter and one receiver to determine the vortex location. The third method requires an additional receiver.

6.5.3.1 Location by Two Angles. This method requires one transmitter T and one receiver R (see Figure 6-6). To locate a vortex V, one measures the two angles $\theta_1$ and $\phi$ of transmission and reception, respectively. The coordinates $x_o$ and $z_o$ of the vortex are given by

$$x_o = \frac{\cos\theta_1 \sin\phi}{\sin(\theta_1+\phi)} d$$

$$z_o = \frac{\sin\theta_1 \sin\phi}{\sin(\theta_1+\phi)} d \qquad (6\text{-}1)$$

6.5.3.2 Location by One Angle and One Time Delay. The second method also makes use of a single transmitter and a single receiver; but rather than measuring two angles, the vortex location is determined by one angle, for example, the angle of transmission $\theta_1$, and the total time of propagation of a pulse emitted at T and received at R. Assuming constant speed of propagation c, the total path length $r_o + r_1$ (see Figure 6-6) is related to the time interval t by

$$r_o + r_1 = ct = k \qquad (6\text{-}2)$$

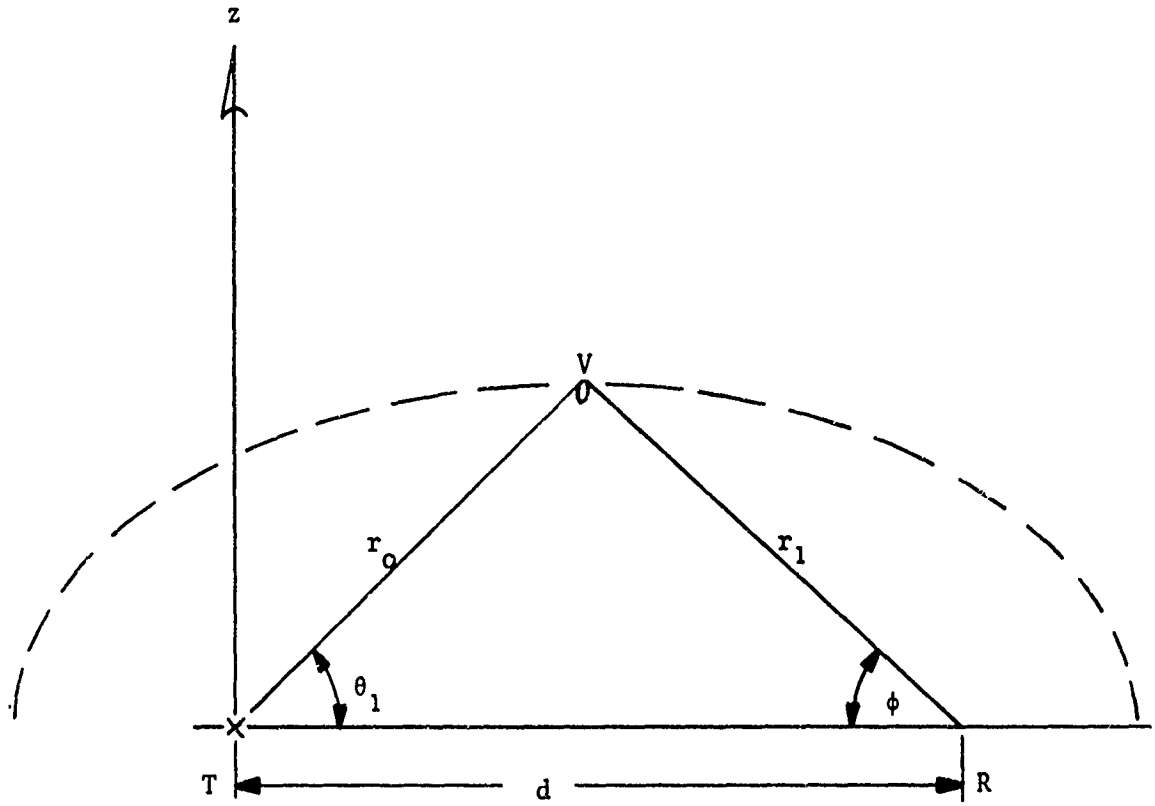


Figure 6-6. Vortex Location Configuration Utilizing a Transmitter and One Receiver

This is the equation of an ellipse. The coordinates of the position of the vortex V are obtained by solving the intersection of this ellipse with the straight line that passes through the transmitter and whose slope is tan $\theta_1$. The solution for $x_o$ and $z_o$ is

$$x_o = \frac{(k^2 - d^2)}{2} \left[ \frac{\cos \theta_1}{k - d \cos \theta_1} \right]$$

$$z_o = \frac{(k^2 - d^2)}{2} \left[ \frac{\sin \theta_1}{k - d \cos \theta_1} \right] \qquad (6\text{-}3)$$

6.5.3.3 Location by Two Time Delays. The third method requires two receivers instead of one (see Figure 6-7). The times of propagation $t_1$ and $t_2$ for the signal to travel the paths $TVR_1$ and $TVR_2$ are measured. The coordinates of the point are given by the intersection of the two ellipses.

$$r_o + r_1 = ct_1 = k_1$$

$$r_o + r_2 = ct_2 = k_2 \qquad (6\text{-}4)$$

Solving the above pair of equations for the coordinates of the point V yields

$$x_o = \frac{1}{2} \frac{r_1^2 k_2 - r_2^2 k_1}{d_2 k_1 - d_1 k_2}$$

$$z_o = \frac{1}{2} \frac{r_1 r_2}{d_2 k_1 - d_1 k_2} \sqrt{(d_2 - d_1) - (k_2 - k_1)} \qquad (6\text{-}5)$$

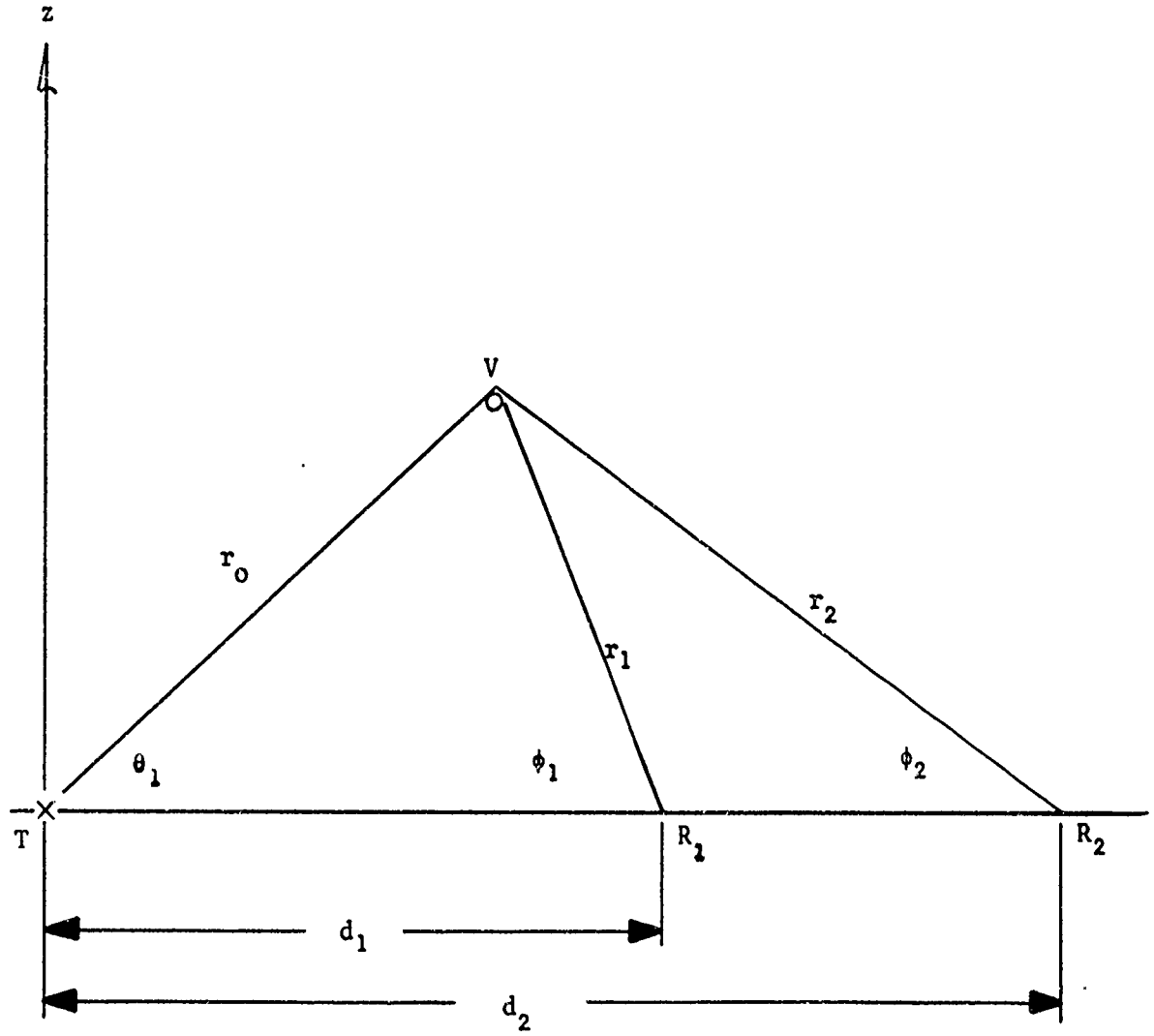


Figure 6-7. Vortex Location Configuration Utilizing a Transmitter and Two Receivers

where $d_1$ and $d_2$ are the distances from the transmitter T to the receivers $R_1$ and $R_2$ respectively and

$$r_i = (k_i - d_i) \qquad i = 1,2$$

### 6.5.4 Vortex Location Error Analysis

A study has been conducted by Xonics, under Univac's prime FAA Contract (DOT-FA70WA-2289) on ARTS-III enhancement, to 1) determine the use of meteorological data in conjunction with wake vortex observations to improve the capability of hazard resolution, and 2) determine methods of digitizing meteorological data (such as barometric pressure, temperature and wind) and of processing that data in conjunction with wake turbulence data for more effective use as an input to air traffic control. The results of the study were documented in reference 16.

In performing the first task of the study, an analysis of errors induced by atmospheric effects for the three methods of vortex location was conducted. It was concluded that for most conditions of practical interest, the three methods have approximately the same accuracy in determining the position of a vortex. This result is true for the methods that use angular information for beamwidths up to about $3.5^{\circ}$. Based on this result, it appears that the selection of the method of vortex location is not strongly affected by accuracy considerations.

### 6.5.5 Sensor Unit Configuration

Since any of the sections considered for coverage can be scaled from one of them by multiplying its dimensions by the ratio of the distances from the threshold point, it is sufficient to study the coverage problem in one section; and by scaling, determine the location of transmitter and receiver antennas in the others. The section located 3 miles from the threshold point has been selected to perform the coverage study.

Two sensor unit configurations will be considered for satisfying the coverage requirements at any section along the ILS corridor. The first consists of one transmitter and one receiver. The second consists of one transmitter and two receivers.

6.5.5.1 One Transmitter and One Receiver Configuration. For reasons of symmetry, the transmitter and the receiver in this case are taken to be symmetrically located about the ILS corridor center line. It can be shown geometrically that a solution which satisfies the constraints given in Table 6-2 is given by transmitter and receiver locations 1800 ft either side of the runway centerline extension (see Figure 6-8). The figure shows that the scattering angles vary for this configuration from $42^{\circ}$ to $69^{\circ}$, the transmitter and receiver elevation coverage requirement is $33^{\circ}$, and the minimum elevation of the transmitter or receiver beam is $14^{\circ}$.

6.5.5.2 One Transmitter and Two Receivers Configuration. For reasons of symmetry, the transmitter in this case will be located at the center (see Figure 6-9). The receiver antennas are also symmetrically placed about the ILS corridor center line. In order to satisfy the scattering angle constraints given in Table 6-2, they should be located at a distance from 660 ft to 1040 ft from the transmitter.

The needed elevation coverage for the receiver located at 660 ft is 65 degrees and for the receiver located at 1040 ft is 50 degrees. Therefore, no total section coverage is possible in either case if the 40-degree receiver elevation constraint is to be met. The minimum coverage loss when meeting the receiver elevation coverage constraint is achieved by placing the receivers 1040 ft on either side of the centerline. The coverage loss in this case is approximately 12 percent.

The transmitter elevation coverage requirement is 102 degrees. The minimum elevation of a transmitter beam is 39 degrees while the minimum elevation for a receiver beam is 32 degrees.

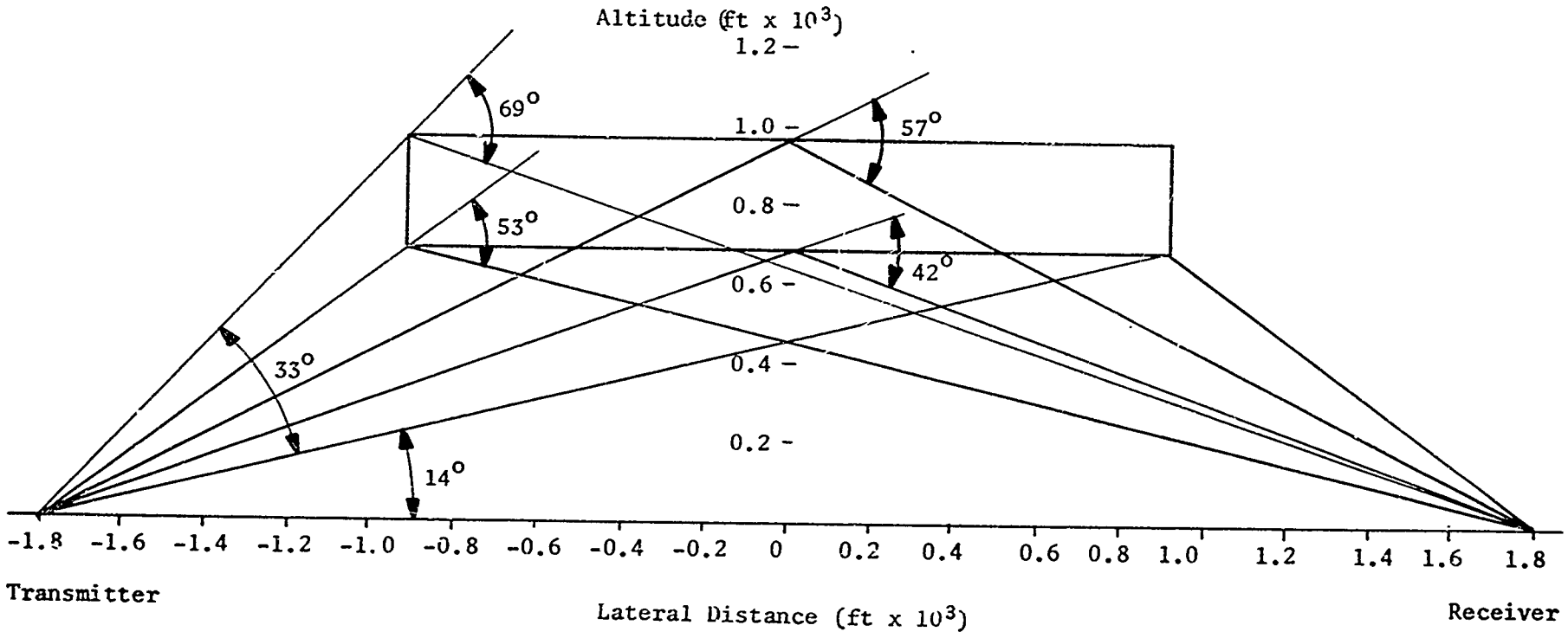


Figure 6-8. One Transmitter and One Receiver Configuration

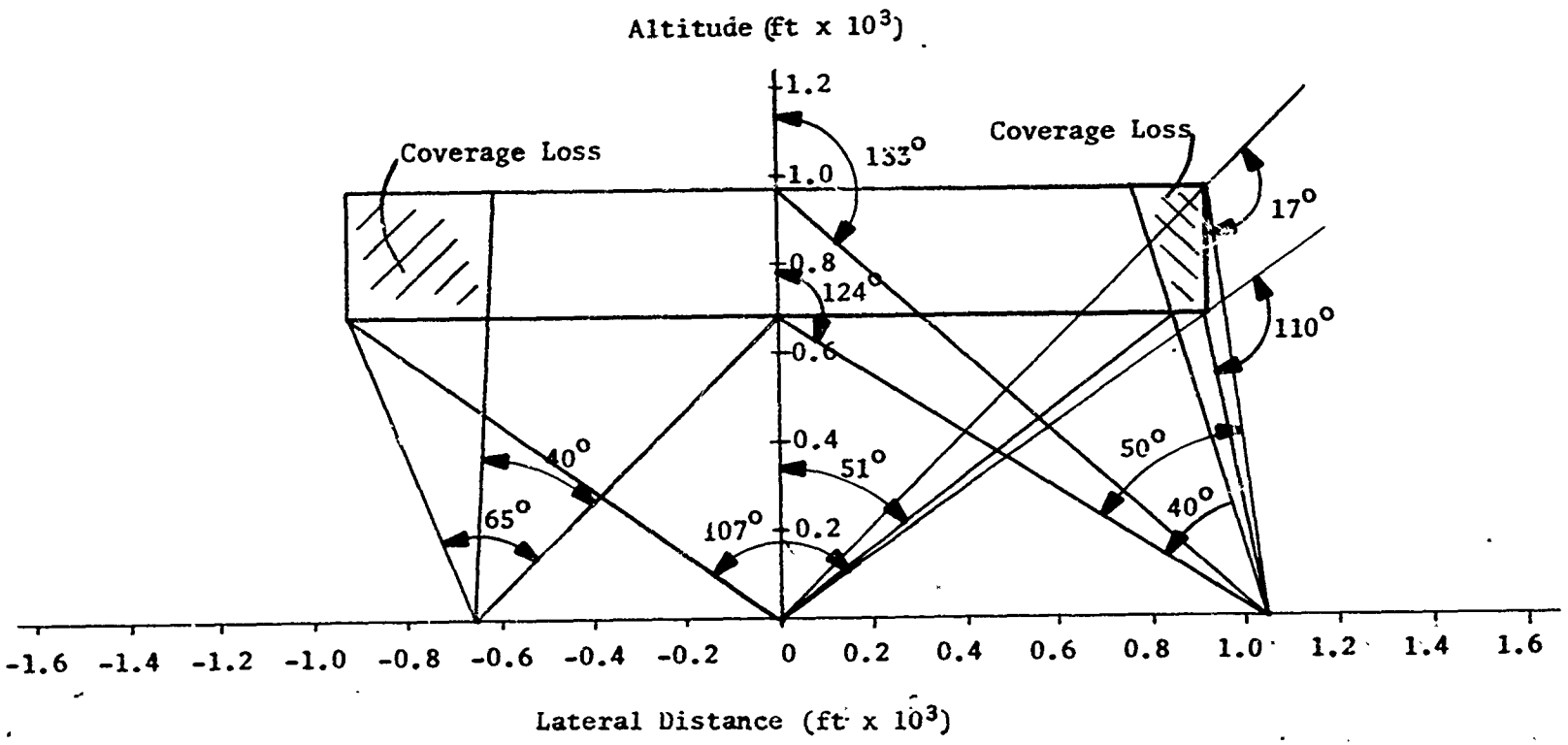


Figure 6-9. One Transmitter and Two Receivers Configuration

6.5.5.3 Sensor Geometry at Other Stations. As explained at the beginning of this section, once the coverage analysis have been performed at any section of the ILS corridor, the geometric location of radars at any other station is obtained readily by scaling the results.

Table 6-3 summarizes the radar antenna locations at all stations for the radar configuration consisting of one transmitter and one receiver. The transmitter and receiver for the threshold position are located at a distance of 145 ft from the runway centerline, and consequently they meet the installation requirement specified in Section 6.5.1.

Table 6-4 gives the receiver antenna locations for the radar configuration consisting of one transmitter and two receivers. The threshold station has not been included in the table because the tristatic configuration does not meet the sensor location requirement relative to the runway centerline of Section 6.5.1. In addition the bistatic configuration is more cost-effective at the close-in station, as will be shown in the following paragraphs.

6.5.5.4 Baseline Sensor System Configuration. It was pointed out earlier in this section that only the configuration of one transmitter and one receiver satisfies the constraints at the threshold. The selection of radar configurations at the other stations is still open. An analysis was carried out to determine the vortex height at which the radar configuration consisting of one transmitter and one receiver will have, at the receiver output, the same S/N as the output of the radar configuration consisting of one transmitter and two receivers for a vortex altitude of 1700 ft. The analysis was made for the geometrical conditions in both cases that yielded the poorest signal-to-noise ratio. This is found to be the case where the vortex is located in either of the higher corners of the section under coverage. For the purpose of this analysis, it was assumed that the attenuation was

TABLE 6-3. ONE RECEIVER AND ONE TRANSMITTER ANTENNA LOCATION

| Sensor Station | Transmitter Distance (ft) | Receiver Distance (ft) |
|---|---|---|
| Threshold | 145 | 145 |
| Middle Marker | 680 | 680 |
| 3 Miles | 1800 | 1800 |
| Outer Marker | 2900 | 2900 |

TABLE 6-4. ONE TRANSMITTER, TWO RECEIVERS ANTENNA LOCATIONS

| Sensor Station | Receiver Displacement (ft) |
|---|---|
| Middle Marker | 404 |
| 3 Miles | 1040 |
| Outer Marker | 1670 |

1 dB/100 ft, that the vortex filled the scattering volume and that the scattering cross section was independent of the scattering angle. Given these assumptions, the solution is essentially the configuration at low scattering angle that gives the same range as that at high scattering angle, so that in fact the solution is very insensitive to the first two assumptions. The results of the analysis show the equivalent altitude for the one-receiver configuration to be 700 ft. Since it is apparent that tracking at 1700 ft altitude is a fairly stringent requirement for even the optimal configuration, 700 ft may be taken as a rough upper altitude limit for the single-receiver configuration.

The tristatic radar system should prove to be more expensive than the bistatic system because of the larger number of sites involved; the bistatic configuration will probably be preferable when it satisfies performance requirements (output S/N ratio). Therefore, the most effective acoustic detection system tentatively is concluded to be the system that uses the bistatic configuration at the threshold and at the middle marker, and the tristatic configuration at the further stations.

## 6.6 Sensor Characteristics

A preliminary determination of the transmitter and receiver characteristics for a track-while-scan sensor subsystem has been performed. For both radar configurations the scanning is done by a single-beam transmitter that sweeps the section at a specified rate. In both configurations, the receiver antennas are multi-beamed and fixed.

The sensor characteristics to be determined for both sensor configurations are presented in Table 6-5. In order to obtain the sensor characteristics, the criterion used as the basis for the selection of these parameters was taken to be the maximization of the ratio of

received power to background noise power. The received power to background noise power ratio is given by

$$\frac{P_R}{P_N} = \frac{P_T\, G_T\, A_R \sigma}{(4\pi)^2\, R_1^2\, R_2^2\, P_N}\, e^{-\alpha(R_1+R_2)} \tag{6-6}$$

where

$P_R$ = received power

$P_T$ = transmitted power

$G_T$ = gain of the transmitting antenna

$A_R$ = effective area of the receiver

$\sigma$ = the vortex cross-section

$\alpha$ = the atmospheric attenuation coefficient

$R_1$ = distance from the transmitter to the vortex

$R_2$ = distance from the vortex to the receiver

$P_N$ = background noise power

TABLE 6-5. SENSOR SUBSYSTEM CHARACTERISTICS

| Transmitter | Receiver |
|---|---|
| Beamwidth | Beamwidth |
| Dish Size | Dish Size |
| Illumination Frequency | Integration Time |
| Scan Rate | Number of Beams |

The geometric quantities in equation (6-6) have already been optimized, and the remaining quantities are found to depend on operating frequency. This can be expressed explicitly as

$$\frac{P_R}{P_N} = C \frac{\Delta\theta \, e^{-\alpha R}}{P_N} \tag{6-7}$$

using the fact that

$$G_T = \frac{4\pi}{(\Delta\theta)^2} \tag{6-8}$$

and taking the cross-section $\sigma$ to be proportional to $(\Delta\theta)^3$. This latter proportionality results from the assumptions that a vortex fills the beam in both the longitudinal and the lateral direction, and that the cross-section of a given volume is essentially independent of frequency.

Of the terms in equation (6-7), it is known that $P_N$ decreases by perhaps 5 to 10 dB per octave in the range of several kHz (which tends to raise the operating frequency), and $\Delta\theta$ decreases linearly with increasing frequency (which tends to lower the operating frequency). Both terms are however strongly dominated by the exponential attenuation term at higher frequencies and long ranges, so that for altitudes of perhaps 1000 ft or more, frequencies of around 4 kHz or less are required.

The maximum acceptable $\Delta\theta$ is constrained by the single-look accuracy requirement on the determination of the vortex location. The scan rate is a compromise between system reaction-time requirements and tracking accuracy. Once the scan rate $\dot{\theta}$ and the beamwidth $\Delta\theta$ are determined, the dwell time is obtained from the ratio $t_I = \frac{\Delta\theta}{\dot{\theta}}$. The dwell time fixes the maximum integration time, which in turn determines the velocity resolution. The antenna diameter is related to the wavelength $\lambda$ and the beamwidth by the familiar expression

$$D = \frac{\lambda}{\Delta\theta} \tag{6-9}$$

Based on all of the foregoing factors and considerations, nominal specifications have been determined for the sensor units that will gather vortex data with sufficient strength and accuracy to satisfy the requirements. Table 6-6 lists the sensor parameters for the unit to be installed at the outer marker that consists of one centrally located transmitter and two outlying receivers. Table 6-7 gives the same information for the middle marker unit, which consists of a single transmitter and receiver symmetrically displaced about the ILS centerline. It can be seen from both Tables 6-6 and 6-7 that the sensor parameters are not vastly different from those already used in the acoustic radar tests, and they do not therefore require a great extrapolation from current practice.

TABLE 6-6. RADAR CHARACTERISTICS FOR UNIT AT OUTER MARKER

| | |
|---|---|
| Transmitter | |
| Beamwidth | $3^{o}$ |
| Scan Rate | $15^{o}$/sec |
| Scan Time | 6.8 seconds |
| Illumination Frequency | 3 kHz |
| Dish Diameter | 8 ft |
| Receiver | |
| Integration Time | 0.2 sec |
| Number of Beams | 10 |
| Average Beamwidth | $4^{o}$ |
| Dish Diameter | 6 ft |

TABLE 6-7. RADAR CHARACTERISTICS FOR UNIT AT MIDDLE MARKER

| | |
|---|---|
| Transmitter | |
| Beamwidth | $2^{o}$ |
| Scan Rate | $10^{o}$/sec |
| Scan Time | 3.3 seconds |
| Illumination Frequency | 6 kHz |
| Dish Diameter | 6 ft |
| Receiver | |
| Integration Time | 0.2 sec |
| Number of Beams | 11 |
| Average Beamwidth | $3^{o}$ |
| Dish Diameter | 5 ft |

## 7. CONCLUSIONS

The work described in this report was performed under FAA Contract No. DOT-FA72WA-2843. Briefly stated, the program called for a short-term, concentrated effort principally aimed at demonstrating two aspects of the capability of the Xonics acoustic vortex sensor. The first was the capability to measure quantitatively the significant vortex rotational velocities, correlate these measurements with a model, and deduce from the combined picture an estimate of vortex strength. The second was the capability to detect and track vortices at altitudes above 1000 ft, and if possible as high as 1700 ft, the maximum aircraft altitude at the outer marker.

Both goals were unfortunately compromised by the very limited availability of the Air Force C-5A, which was to represent in both sets of tests the class of large aircraft that produce the threat of most concern. Within the limitations of conducting the tests with the available smaller aircraft however, all of the goals of the program were met.

In particular, the principal conclusions are:

1. A relatively simple model of vortex structure and acoustic scattering accounts for the major features observed in the acoustic doppler spectra obtained from the field tests.
2. Modifications to the simple model that correspond to a number of (possibly realistic) deviations from the simplified assumptions of the model do not substantially affect the key features of the spectra related to threat estimation.
3. Discrimination procedures to determine the circulation, hence hazard, of a vortex produce consistent results for both vortices whose core structures are small with respect to the acoustic observation volume and those that are comparable to

or larger than the observation volume. Variations with aircraft configuration that have been noted for some vortex characteristics are not found in the discriminant estimates.

4. The estimated circulations for different aircraft are ordered according to the size of the generating aircraft, and correspond reasonably well to the theoretical values.

5. Tracking of vortices has been accomplished for altitudes of the generating aircraft (in this case a DC-6) up to 1500 ft.

6. A preliminary system analysis indicates that a single runway approach can be covered by three or four sensor units whose characteristics are not greatly different from those employed in these tests.

## REFERENCES


1. Proudian, A., M. Balser and A. Nagy, *"First Observations of Aircraft Vortices by Xonics Acoustic Radar"*, Xonics TR-14 (9 December 1971).

2. Balser, M., A.E. Nagy and A. P. Proudian, *"Vortex Observations by the Xonics Acoustic Radar at NAFEC"*, Report No. FAA-RD-71-103 (December 1971).

3. Goldstein S., "Modern Developments in Fluid Dynamics", Oxford Press (1938), also Dover (1965), Section 12.

4. Donaldson, C. du P., *"A Brief Review of the Aircraft Trailing Vortex Problem"*, AFOSR-TR-71-1910, (1971).

5. Garodz, Leo J., *"Investigation of the Relatively Long Time-History Vortex Characteristics of the Convair CV-880 Airplane in Terminal Area Type Flight Operations"*, Data Rept. Proj. No. 504-303-03X, NAFEC, November 1970.

6. Maxworthy T., *"The Structure and Stability of Vortex Rings"*, J.F.M., 51, 15 (1972).

7. Lamb, H., Hydrodynamics, Sixth Ed. Cambridge Press (1932), Dover (1946) p.592.

8. Betz, A., *"Behavior of Vortex Systems"*, Zeit. für angewandte Math. und Mech., 12, No. 3, June 1932. Also NACA Tech. Memo 713, June 1933.

9. Hoffmann, E.R. and P.N. Joubert, *"Turbulent Line Vortices"*, J.F.M., 16, pp. 395-411 (1963).

10. McCormick, B.W., J.L. Tangler and H.E. Sherrieb, *"Structure of Trailing Vortices"*, J. Aircraft, 5, No. 3, pp. 260-267.

11. Logan, A.H., *"Vortex Velocity Distributions at Large Downstream Distances"*, J. Aircraft, 8, No. 11, 930 (November 1971).

12. Olsen, J.H., A. Goldburg and M. Rogers, "Aircraft Wake Turbulence and Its Detection", Plenum Press (1971), paper by H.N. Olsen entitled "Results of Trailing Vortex Studies in a Towing Tank".

13. V.I. Tatarsky, Wave Propagation in a Turbulent Medium, Dover Publications 1961.

14. Naudascher, E., *"Flow in the Wake of Self-Propelled Bodied and Related Sources of Turbulence"*; Journal of Fluid Mechanics (1965) 22, pt. 4. pp. 625-656.

15. Aircraft Wake Vortex Sensing Systems, Annual Report, TSC, 30 June, 1971, p.3.

16. *"Integration of Meteorological Sensors into the ARTS-III System"*, Xonics TR-10 (15 December 1971).